Experiments towards strong coupling and ground state cooling in an atom-optomechanical hybrid system

Dissertation

zur Erlangung des Doktorgrades
an der Fakultät für Mathematik, Informatik und Naturwissenschaften
Fachbereich Physik
der Universität Hamburg

vorgelegt von
Christian Felix Klein
aus Hamburg

Hamburg
2024

Gutachter der Dissertation:	Prof. Dr. Klaus Sengstock Prof. Dr. Roland Wiesendanger
Zusammensetzung der Prüfungskomission:	Prof. Dr. Klaus Sengstock Prof. Dr. Roland Wiesendanger Prof. Dr. Roman Schnabel Prof. Dr. Ludwig Mathey Prof. Dr. Ralf Riedinger
Vorsitzender der Prüfungskomission:	Prof. Dr. Roman Schnabel
Datum der Disputation:	04.12.2024
Vorsitzender des Promotionsausschusses:	Prof. Dr. Markus Drescher
Leiter des Fachbereichs:	Prof. Dr. Wolfgang Parak
Dekan der Fakultät für Mathematik, Informatik und Naturwissenschaften:	Prof. Dr. Ing. Norbert Ritter

Abstract

Modern experimental quantum physics experienced a rapid development in the past decades. The high degree of control and state of the art experimental techniques motivated the research field of hybrid quantum systems. Hybrid quantum systems combine different hybrid partners that can acquire quantum properties on their own to exploit their individual advantages.
Here we report on the latest results at our experiment that aims to realize strong hybrid coupling between a micromechanical Si_4N_3 trampoline resonator and laser-cooled ^{87}Rb atoms. The coupling is mediated via a coherent light field that is reflected from the resonator and forms an optical 1D lattice potential for the atoms.
Due to optical losses on the beam path, the coupling lattice is asymmetrically pumped. This leads to the emergence of atomic density waves in the lattice which has a detrimental effect on the coupling for attractive lattice potentials. We numerically simulated this phenomenon and found that introducing an additional pump-asymmetry-compensation beam can remove the asymmetry-induced instability. As a result we implemented a compensation lattice which allowed us to operate in the previously inaccessible regime of attractive coupling lattice potentials where we reached a maximal cooperativity $C_{\mathrm{hybrid}} = (100 \pm 25)$ at room temperature.
In a parallel endeavor we successfully implemented a new fiber cavity with $\mathcal{F} = 785$ to significantly improve the coupling between atoms and the mechanical resonator. In this configuration we reached a maximal cooperativity of $C_{\mathrm{hybrid}} = (5900 \pm 1300)$ at room temperature. Furthermore we show experimentally that increasing the finesse of the cavity even further to $\mathcal{F} = 14500$ does not improve the coupling strength in good agreement with theoretical predictions such that further improvements by tuning the finesse are not feasible.
Lastly we realized a quantum-non-demolition measurement technique to perform rapid state tomography of a mechanical resonator. Here the interaction between the resonator and the light field takes place on time scales much smaller than the mechanical oscillation period, which allows for back-action evading measurements of the resonator state with sub-standard-quantum-limit resolution. We calculated a finesse of $\mathcal{F} = 14500$ to resolve the resonator ground state and manufactured as well as implemented a corresponding new fiber cavity into the experimental setup. We conducted pulsed measurements with cavities of $\mathcal{F} = 785$ and $\mathcal{F} = 14500$. While the medium finesse configuration allowed to resolve the resonator state with an imprecision of 16 zero-point motions, the first experiments using the high finesse configuration suggest that further experimental modifications are necessary to acquire meaningful results.

Zusammenfassung

Die moderne Quanten-Experimentalphysik hat in den vergangenen Jahrzehnten große Fortschritte gemacht. Die vielfältigen Möglichkeiten Quantensysteme zu manipulieren, kombiniert mit modernsten, experimentellen Techniken motivierten das Forschungsfeld der hybriden Quantensysteme. Hybride Quantensysteme kombinieren verschiedene Subsysteme mit dem Ziel deren jeweilige Vorteile zu vereinen.
In dieser Arbeit präsentieren wir die neuesten Ergebnisse unseres Experimentes, dessen Ziel die Realisierung starker Kopplung zwischen einem mikromechanischen Si_4N_3 Trampolin-Resonator und lasergekühlten ^{87}Rb Atomen ist. Die Kopplung wird über ein kohärentes Lichtfeld vermittelt, das vom Resonator reflektiert wird und ein optisches 1D-Gitterpotential bei den Atomen bildet.
Aufgrund optischer Verluste auf dem Strahlweg wird das Kopplungsgitter asymmetrisch gepumpt. Diese Pump-Asymmetrie führt zur Entstehung atomarer Dichtewellen im Gitter, die einen destruktiven Effekt auf die hybride Kopplung in attraktiven Gitterpotenzialen haben. Wir haben dieses Phänomen in einer numerischen Simulation modelliert und herausgefunden, dass die hybride Instabilität durch einen zusätzlichen Kompensationsstrahl unterdrückt werden kann. Infolgedessen haben wir ein Pump-Asymmetrie kompensiertes Gitter implementiert. Dies erlaubte uns im vormals nicht zugänglichen Regime attraktiver Gitterpotentiale zu arbeiten und eine Kooperativität von $C_{\mathrm{hybrid}} = (100 \pm 25)$ zwischen beiden Systemen zu erreichen.
Um die Kopplungsstärke zu erhöhen, haben wir erfolgreich eine neue Faser-Cavity mit einer Finesse von $\mathcal{F} = 785$ im System eingebaut. In dieser Konfiguration war es möglich eine maximale Kooperativität von $C_{\mathrm{hybrid}} = (5900 \pm 1300)$ zu erreichen. Des Weiteren konnten wir, in guter Übereinstimmung mit theoretischen Vorhersagen, experimentell nachweisen, dass eine weitere Erhöhung der Finesse auf $\mathcal{F} = 14500$ zu keiner weiteren Verbesserung der Kopplungsstärke führt.
Zusätzlich präsentieren wir eine Methode zur „rückwirkungsfreien“ Messung des Resonatorzustandes, die eine vollständige Zustandstomographie im Phasenraum ermöglicht. In diesen Messungen findet die Lichtfeld-Resonator Wechselwirkung auf Zeitskalen statt die viel kürzer sind, als eine Oszillationsperiode des Resonators. Dies erlaubt die Vermessung des Zustandes mit einer Auflösung unterhalb des Standard-Quanten-Limits. Um den Grundzustand des Resonators aufzulösen, haben wir eine notwendige Finesse von $\mathcal{F} = 14500$ errechnet. Im Rahmen dieser Arbeit wurden Cavities entsprechend dieser Spezifikation gefertigt und in das Experiment implementiert. Messungen wurden bei Finessen von $\mathcal{F} = 785$ und $\mathcal{F} = 14500$ durchgeführt. Während das System den Resonatorzustand bei der niedrigeren Finesse mit einer Präzision der 16-fachen Grundzustandsbreite auflösen konnte, zeigten die ersten Experimente mit der Hochfinesse-Cavity, dass weitere experimentelle Verbesserungen notwendig sind, um aussagekräftige Ergebnisse zu erhalten.

Publikationen

Im Rahmen dieser Arbeit sind die folgenden Veröffentlichungen entstanden.

Publications

The following research articles have been published in the course of this thesis.

- P. Rohse, J. Butlewski, F. Klein, T. Wagner, C. Friesen, A. Schwarz, R. Wiesendanger, K. Sengstock and C. Becker: “A cavity optomechanical locking scheme based on the optical spring effect", Review of Scientific Instruments **91**, 103102 (2020), ISSN 10897623.

Contents

Chapter 1

Introduction

The discovery of quantum mechanics in the early 20th century heralded a new era of physics and provided us with a fundamentally different conception of our world. Quantum mechanics erased the idea of a deterministic world in which it would be possible to describe and predict the behavior of any physical system precisely given enough knowledge about it. While being heavily debated in the first decades of its creation [1], involving some of the most prestigious physicists of that time, it quickly became one of the most successful and fundamental theories of modern physics besides the theory of general relativity.

The evolution of experimental quantum physics reflects this success. Beginning with famous experiments to verify the quantum nature of matter [2–5] and gaining insight into the microscopic world [6, 7], the aspiration nowadays shifted towards creating and controlling of new quantum systems. Quantum theory branched out and formed new physical disciplines that accounted for the increasing depth and complexity it provided. Nowadays, this deep understanding even allows for the design of systems on the quantum level, be it in the creation of new quantum materials [8, 9], the setup of tailored platforms for high-precision sensing [10–12] or in the realization of quantum systems to store [13, 14] or even process information.

A major obstacle all modern quantum technologies must overcome is their scalability up to a system size that enables us to benefit from their unique properties in daily life applications. Quantum properties can only emerge in a coherent system. While quantum objects live in a superposition of coherently overlapped states, they maintain their quantum properties only until any decoherence is introduced [15]. Decoherence can emerge due to a measurement or coupling to classical noise [16]. As such, any quantum system converges towards a classical system upon a certain size which is widely known as the correspondence principle.

The boundary at which this happens is not fixed. If at all, it has been shifted to allow for larger system sizes by trying to suppress any influence that disturbs the underlying quantum system. This can be achieved i.e., by cryogenic cooling or by introducing highly confined and isolated systems that hardly couple to the classical environment [16].

Another major challenge is the combination of different quantum systems. While there have been rapid advancements in the creation of quantum systems that serve a particular purpose for quantum simulation [17–21], quantum computing [22–26], quantum

memory or for information transfer and cryptography [27, 28], most systems lack any compatibility with each other. This partly arises from the different quanta that are used for particular tasks. Atomic states, for example, Rydberg states [29], are particularly suited for use in quantum gates. Quantum information transfer over long distances can be done particularly well with photons [30], while spin states are promising candidates to use in quantum memories [31]. The combined use of these systems would require a coherent state transfer and thus a hybridization of the system as a whole.
These challenges are linked to the question of whether it is possible to combine quantum systems of different kinds and to which degree. Hybrid quantum systems are used as an experimental platform to investigate these questions and give insight into the fundamental physics behind phenomena such as quantum state transfer [32–39], teleportation [40] and quantum entanglement [41–44].
Two particularly suited hybrid partners are ultracold atoms and micromechanical resonators. While ultracold atoms offer exceptional control and access to their internal and external states [45], micromechanical resonators excel in their customizability. They can be designed to realize various hybrid systems that couple optically, capacitively, via magnetic fields [46–48], via microwaves [44] or Van-der-Vaals forces [40, 47, 49, 50]. They can be prepared in their motional ground state [43, 46, 49–54] by continuous radiation pressure cooling or using pulsed, backaction-evading measurement protocols. Specific designs allow hybrid atom-optomechanical coupling to motional or internal [38, 55] degrees of freedom.

An atom-optomechanical hybrid system

The *NanoBEC* experiment aims to realize a strongly coupled quantum hybrid system. It consists of ultracold ^{87}Rb atoms and a cryogenically cooled, micromechanical trampoline resonator inside a Fiber Fabry-Pérot microcavity (FFPC) in the Membrane-in-the-Middle (MiM) configuration that couples via a light field as depicted in Fig. 1.1(A). Due to its short length, the linewidth of the cavity exceeds the resonance frequency of the trampoline resonator by orders of magnitude ($\kappa_{\mathrm{cav}} \gg \omega_{\mathrm{m}}$), placing the system in the unresolved-sideband-regime. Hence, the cavity response to the membrane motion can be approximated as instantaneous [56]. This renders it particularly suitable for experiments with low-frequency resonators, pulsed experiments, and hybrid experiments that require high coupling strengths between their constituents [56].
The main goal of this experiment is to enter the strong coupling regime. In this regime, the system can be described with a fully quantized Hamiltonian H_{int} where any single photon light field excitation due to the motional state of the atoms corresponds to a phononic excitation of the resonator [53]. This would allow for coherent energy transfer between both systems and would render quantum state transfer between both systems possible [57].
Fulfilling the strong coupling condition is a challenging task. It requires the coupling rate between both sub-systems to be larger than the sum of all decoherence rates [57, 58]. This condition is expressed by the cooperativity parameter C_{hybrid}. Strong coupling requires the cooperativity to exceed the thermal phonon occupation of the resonator ($C_{\mathrm{hybrid}} \gg \bar{n}_{\mathrm{th}}$).

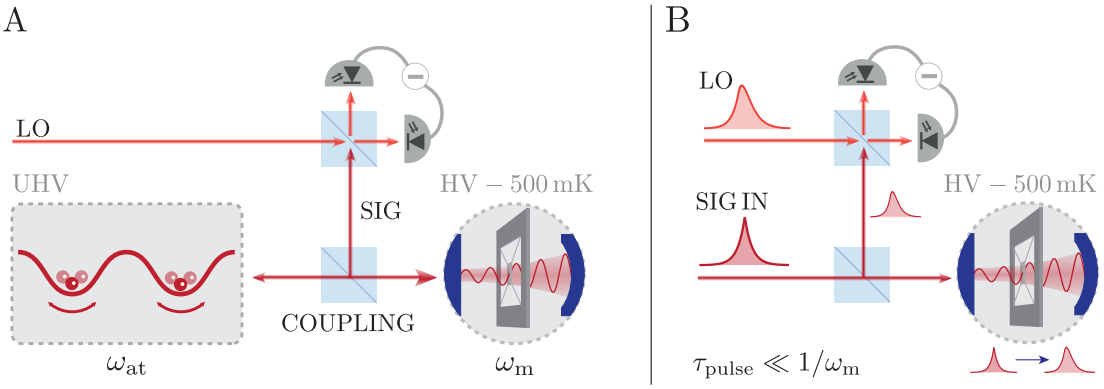

Figure 1.1: Sketch of the experimental configurations: (A) *Hybrid Coupling*: Ultracold atoms are coupled resonantly to a micromechanical resonator using an optical lattice. The coupling arises if the resonance condition is fulfilled ($\omega_m = \omega_{at}$). The resonator state is detected by continuous balanced homodyne detection. (B) *Pulsed experiments*: The resonator is prepared in a conditional squeezed state by using a quantum-non-demolition (QND) measurement protocol. Therefore, very short detection light pulses ($\tau_{pulse} \ll 1/\omega_m$) are used to take snapshots of the quasi-stationary states of the resonator. These allow for a reconstruction of the resonator state with sub-standard-quantum-limit (SQL) precision. Figure (B) based on Ref. [59].

In pursuit of fulfilling this condition, many efforts were made to optimize the cooperativity parameter at the experiment, ranging from the integration of the optomechanical system into a high-vacuum cryogenic environment [60, 61] over customized designs of the micromechanical resonator to the implementation of radiation pressure cooling protocols that allow for cooling near the resonator ground state [57, 62]. While these efforts yielded an overall improvement of the cooperativity, it remained orders of magnitude too small to access the strong coupling regime [63].

During this work, we tried to further improve the cooperativity by addressing two properties of the hybrid system that remained unchanged until now.

Since the cooperativity linearly scales with the number of atoms that couple to the resonator, the system would benefit from a red-detuned coupling lattice (relative to the atomic transition) which attracts the atoms and thus provides higher atomic densities. Previous experiments from independent groups showed this operating regime to be inaccessible, as it consistently drives the optomechanical system into limit cycles [62, 64]. In 2011, J.K. Asboth *et al.* provided a theoretical model of this phenomenon in the form of density waves that arise in asymmetrically pumped optical lattices with high atomic densities [65, 66]. This “dynamic instability” leads to a phase lag in the coupling lattice that induces a positive feedback loop between the resonator and the atomic motion. Since the asymmetry of the coupling lattice is an inherent property of such systems, most coupling experiments are done in blue-detuned coupling lattices where this effect does not occur.
To enter this regime nonetheless, we implemented an auxiliary branch to compensate for the pump asymmetry in our system. We verified the feasibility of this approach with a numerical simulation that describes the lattice dynamics for different pump asymmetries and under the influence of a pump asymmetry compensation beam. This allowed

us to perform coupling experiments in a previously inaccessible regime, yet the overall cooperativity was worse than in a blue-detuned coupling lattice. The pump asymmetry compensation (PAC) experiments were done together with J. Butlewski and are described in detail in his thesis [63]. We restrict ourselves to presenting the core results in this thesis.

Finally, we optimized the fiber cavity finesse. While it strongly affects the cooperativity ($C_{\mathrm{hybrid}} \propto \mathcal{F}^2$), it also influences the shot-noise related decoherence rates in the optomechanical system. Thus, it is supposed to have an optimum value for our specific setup at $\mathcal{F}_{\mathrm{opt}} = 600$ [55]. In this thesis, we exchanged the previously used fiber cavity ($\mathcal{F}_{1,\mathrm{empty}} = 60 \pm 2$) for a fiber cavity with higher finesse[1] ($\mathcal{F}_{2,\mathrm{empty}} = 785 \pm 15$). By adjusting the resonator position in the intra-cavity field, the finesse can be adjusted to 600 and 1500. Coupling experiments were done for $\mathcal{F} = 650 \pm 50$ and $\mathcal{F} = 1500 \pm 100$. As presented in Fig. 1.2, this modification significantly increased the cooperativity of the hybrid system by a factor of 30 for the lower finesse. Furthermore, the experiments show a backaction-induced decrease in cooperativity at higher finesses in good agreement with theory, rendering a fundamental limit to the cooperativity that can be achieved with this setup.

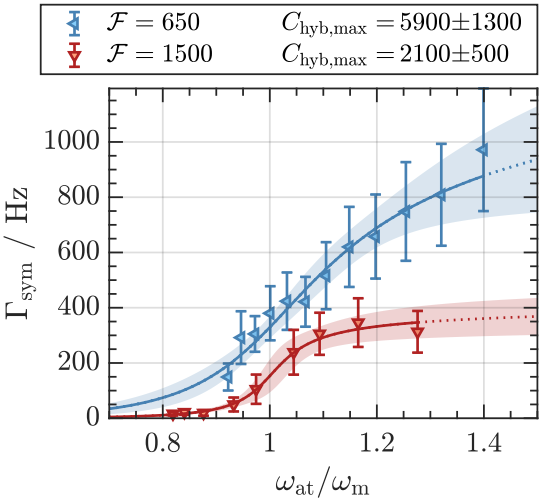

Figure 1.2: Hybrid Coupling at optimized finesse: Sympathetic cooling rates as a function of the atomic trapping frequency in units of ω_{m}. The measurements were conducted at $\mathcal{F} = 650 \pm 50$ (blue) and $\mathcal{F} = 1500 \pm 100$ (red). The maximum obtained hybrid cooperativity at $\mathcal{F} = 650$ is by a factor of 30 higher than in previous measurements for the lower finesse $C_{\mathrm{hybrid,old}} = 190 \pm 40$. For higher finesses, the cooperativity decreases again.

QND measurements of the optomechanical system

Apart from their excellent properties as hybrid partners, micromechanical resonators are objects of current research interest [68]. When prepared in their ground state, they serve as powerful platforms for quantum entanglement experiments [43, 69, 70], and can even be controlled at the quantum level with sophisticated feedback techniques [71]. Due to the cryogenic environment and high degree of control, our experiment is ideally suited to prepare our resonator in its motional ground state despite its low eigenfre-

[1] Produced during Ref. [67].

quency. Previous experiments allowed for continuous radiation pressure cooling near the motional ground state of the resonator, reaching a minimal phonon occupation of $\bar{n}_{\mathrm{th}} = 3.8 \pm 0.1$ [62].

An alternative method for preparing any oscillator in a (conditional) ground state was proposed in 2011 by Vanner *et al.* [59] and is depicted in Fig. 1.1(B). Here, the quadratures of the resonator are treated as quantum-non-demolition (QND) observables. By using very short light pulses that fulfill the condition $\tau_{\mathrm{pulse}} \ll 1/\omega_m$, snapshots of the quasi-steady state of the oscillator are taken. At the same time, the back-action from the measurement on the system is minimized. The information acquired from the snapshots allows for reconstruction of the resonator state with sub standard-quantum-limit (SQL) precision. In the context of mechanical resonators, the SQL is resembled by the zero-point motion x_{zpm}. This quantity describes the motion the resonator undergoes upon excitation by one phonon. QND measurements of micromechanical resonators were initially realized in a proof-of-principle experiment in 2013 by the same group [72] and successfully applied on the quantum scale in 2018 [73, 74]. They resemble a powerful method in high-precision metrology [10, 11, 75]. The precision of the measurements is quantified by the measurement strength parameter χ that relates the acquired information per pulse to the noise introduced to the measurement device. Squeezing below the standard quantum limit was never accomplished as the required measurement resolution $\chi > 1$ was inaccessible in the systems mentioned above. We determined a finesse of $\mathcal{F} = 14500$ to be necessary to reach the required resolution. Thus, we designed new high-finesse fiber cavities with $\mathcal{F}_{\mathrm{empty}} = 14500 \pm 1500$ and overhauled the detection, introducing an all fiber based setup. While operation at $\mathcal{F} = 1500$ allowed us to squeeze the resonator state to a width of $(16 \pm 1)\, x_{\mathrm{zpm}}$, measurements at $\mathcal{F} = 14500$ did not provide enough statistics such that further experimental modifications are necessary to acquire meaningful results.

This thesis is structured as follows:

Chapter 2 - The atom-optomechanical hybrid system

In this chapter, we describe the experimental platform in detail. The new cavities used in this work require an updated description of the optomechanics of the system. Furthermore, we give an overview over the atomic part of the experiment, used for the hybrid coupling. The homodyne detection was rebuilt to reach better detection efficiency, higher stability, and lower detection noise. We decided to implement an all fiber based detection setup. We introduce and characterize this setup and compare it to the previously used free-space setup. Finally, we discuss the production and characterization of new fiber cavities with $\mathcal{F}_{\mathrm{empty}} = 785$ and $\mathcal{F}_{\mathrm{empty}} = 14500$ for the pulsed experiments that have been performed in this work. This chapter is structurally oriented along previous theses [62, 63, 76].

Chapter 3 - Towards a strongly coupled atom-optomechanical hybrid system

This chapter summarizes the results of our hybrid coupling experiments. After a short introduction to sympathetic cooling as a benchmark for determining the cooperativity parameter, we present the core results of our measurements on Pump Asymmetry Compensation. Furthermore, we show how the exchange of the fiber cavity significantly increases the cooperativity of the system. We verify that any further improvement by increasing the finesse is not feasible, which is in good agreement with theory and poses a limit on the cooperativity that can be reached in this kind of system.

Chapter 4 - Rapid state preparation using QND measurement techniques

This chapter is dedicated to ground state preparation of the micromechanical resonator by a pulsed QND measurement protocol. We introduce the concept of back-action evading QND measurements and how they apply to our system. We discuss the upgrades implemented on our system to be able to resolve the oscillator state with sub-SQL precision and present the outcome of these efforts.

Chapter 2

The atom-optomechanical hybrid system

In this chapter, we describe the experimental platform on which all experiments in this thesis were conducted. The hybrid experiment consists of a cryogenically cooled, micromechanical resonator in a FFPC and a ^{87}Rb *BEC system. While the BEC system has not been changed compared to previous theses, extensive modifications have been made on the optomechanical side of the system. This includes the increase of the fiber cavity finesse to values of* $\mathcal{F}_{\text{empty}} = 785 \pm 15$ *and* $\mathcal{F}_{\text{empty}} = 14500 \pm 1500$ *and the implementation of an all fiber based homodyne detection. These modifications require a new characterization of the optomechanical system, which is presented in this chapter. Furthermore, we give a brief overview of the atomic system and will discuss the design considerations and production of the newest high finesse cavities.*

The research field of hybrid quantum systems has evolved rapidly in recent years leading to a wide variety of possible hybrid partners. Quantum hybrid systems have been realized in many different setups by coupling superconducting circuits and microwave resonators [33, 77, 78], mechanical resonators with semiconductor quantum dots [79, 80] and by the creation of atom-optomechanical systems [46, 58, 81, 82]. Beneficial properties for creating a quantum hybrid system are long coherence times in and between the individual systems and similar excitation frequencies between both partners.
Ultracold atoms are particularly suited as hybrid partners due to the high degree of control possible with state of the art technology. This allows for preparation of internal [83, 84] and motional [85, 86] states of an atomic system with high lifetimes on the order of multiple seconds. Micromechanical resonators are highly customizable platforms that can be tailored to a specific coupling mechanism. The figure of merit of these devices is the $Q\omega$ product of the resonators eigenfrequency and quality factor which characterizes the coherent oscillations the resonator undergoes after an initial excitation. The increasing manufacturing capabilities nowadays allow for high Q micromechanical resonators with GHz frequencies, rendering ground state preparation of these devices possible even at room temperature [87–89]. Here, we describe the experimental setup of the individual hybrid partners, starting with the cold atom apparatus, the coupling

lattice, and the detection where the focus lies on the new fiber based detection setup. Furthermore, we introduce the optomechanical system and discuss the new fiber cavities in more detail. For extensive information on the initial design considerations, also refer to [90, 91].

2.1 Cold atom apparatus

To prepare the atomic part of the hybrid system, we use a ^{87}Rb BEC machine that was designed and set up by A. Bick and C. Staarmann. While a detailed description and characterization of the system is provided in their respective theses [90, 91], we give an overview of the most important parts of the experiments conducted in this thesis.
Initial design considerations aimed at a system that provides short cycle times while reaching high atom numbers in the Magneto-Optical-Trap (MOT) and for the BEC. This is necessary because the coupling strength scales proportionally to the number of atoms [53, 58]. Our system meets these requirements by using a two-stage MOT setup with a 2D-MOT from which the atoms are transferred to the 3D-MOT by an optical pushing beam. Both glass cells of the experiment are separated by a differential pumping stage which allows for high vapor pressures in the 2D-MOT glass cell while providing an excellent background pressure. This benefits high BEC lifetimes in the 3D-MOT glass cell. Figure 2.1 depicts the transitions of ^{87}Rb and the individual components of the apparatus that address the respective transitions.

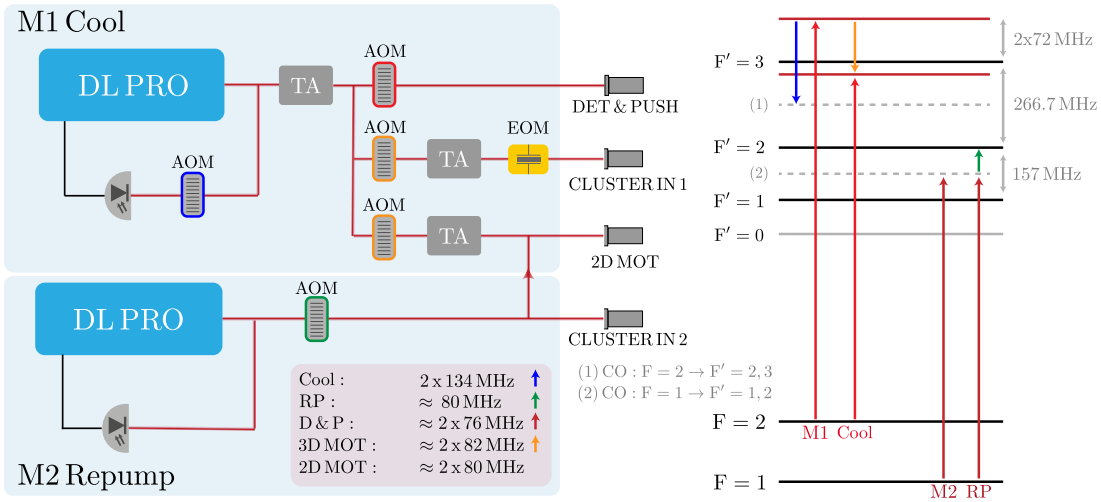

Figure 2.1: Sketch of the laser system and the addressed hyperfine states of ^{87}Rb: The laser system consists of a cooling laser (M1) and a repumping laser (M2) that are locked via a doppler-free spectroscopy branch to the respective crossover resonances (1) and (2) depicted by the dashed gray lines. The cooling laser is amplified by a tapered amplifier (TA) and split up into three branches for the pushing and detection beam (DET), 3D-MOT (CLUSTER IN 1) and 2D MOT where the intensity is amplified by additional TAs and tuned to the hyperfine resonances depicted on the right side of the picture by the respectively colored acousto-optic-modulators (AOM). The repumper is split into branches for the 2D and 3D MOT to account for the non-closed level structure. Figure adapted from Ref. [90].

The atoms are cooled on the transition $|5^2S_{1/2}, F = 2\rangle \rightarrow |5^2P_{3/2}, F' = 3\rangle$. Since this transition does not create a closed cycle the atoms have to be repumped on the $|5^2S_{1/2}, F = 1\rangle \rightarrow |5^2P_{3/2}, F' = 2\rangle$ transition. The cooling laser (M1) is locked to the $F = 2 \rightarrow F' = 2, 3$ crossover resonance via a 2x134 MHz double pass acousto-optic-modulator (AOM) and split into three branches. While for the detection and pushing branch it is tuned on resonance by a double pass AOM, it is slightly red detuned to the $F' = 3$ level for the 2D- and 3D-MOT branch. These branches are fed into a fiber cluster where they are split and adjusted in their polarization. The repumper (M2) is locked to the $F = 1 \rightarrow F' = 1, 2$ crossover resonance and tuned to the $F' = 2$ level via a single pass AOM. It is overlapped with the 2D- and 3D-MOT beams.

The 2D-MOT is created in the upper glass cell by two elliptical, retro-reflected beams that catch atoms from the background gas. A near detuned pushing beam transfers the atoms from the 2D-MOT into the lower glass cell. Because of this setup the 3D-MOT can operate at low background pressures ($p < 10^{-11}$ mbar) and has fast loading times of a few seconds.

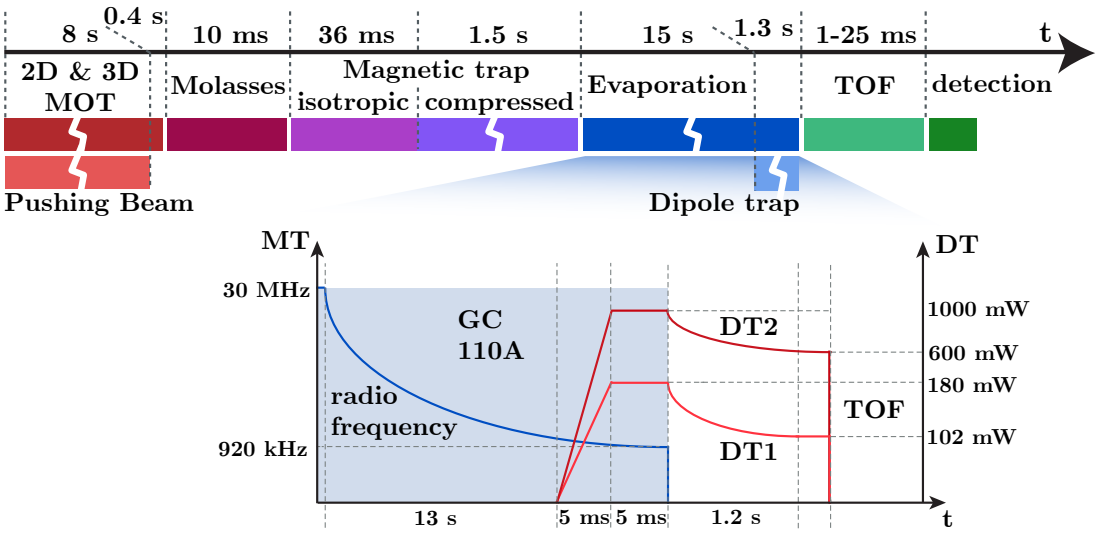

Figure 2.2: Experimental sequence for BEC creation: After the initial MOT loading and a short molasses phase where the atoms are cooled to sub-doppler temperatures, the atoms are loaded into a magnetic trap in which they are cooled by radio-frequency (RF) evaporation. The evaporation is depicted in the lower graphic in more detail and depends on whether a BEC in a magnetic trap (MT) or a BEC in a dipole trap (DT) is created. During evaporation, the gradient coils (GC) are switched on and the RF-frequency is ramped down exponentially from 30 MHz to 920 kHz (960 kHz for the DT sequence). For the MT-BEC sequence, the gradient coils are switched off after the evaporation and a time-of-flight (TOF) image is taken. In case of the DT-BEC, the atoms are loaded into the crossed dipole trap by linearly ramping DT1 and DT2 to 180 mW and 1000 mW. After the GC are switched off, DT1 and DT2 are ramped down to 102 mW and 600 mW respectively. Figure from Ref. [63].

BEC in magnetic trap:
The experimental setup allows for the creation of large BECs ($N_{\mathrm{atoms}} \approx 1.4 \cdot 10^5$) in a magnetic trap with cycle times under 30 seconds. The experimental sequence is depicted in Fig. 2.2. After an initial MOT loading time of a few seconds, where the atoms are cooled to the doppler temperature $T_{\mathrm{D}} = \hbar\Gamma/2k_{\mathrm{B}} = 146\,\mu\mathrm{K}$, they reach a temperature of $10\,\mu\mathrm{K}$ in the molasses phase of the sequence. Thereafter the atoms are loaded into an isotropic magnetic trap (4D magnetic cloverleaf trap [91]) which is overlapped with a homogenous Helmholtz field. By ramping down the Helmholtz field, the magnetic trap is compressed. The temperature is further reduced by RF-evaporation cooling of the atoms, transitioning the trapped atoms into a BEC. After evaporation, the magnetic trap is switched off and an absorptive time-of-flight (TOF) image is taken.

BEC in dipole trap:
The magnetic trap only allows for trapping atoms in a certain m_{F}-state ($m_{\mathrm{F}} > 0$). For experiments that realize the coupling via internal states, the atoms need to be trapped independently of their m_{F}-states. This is realized by trapping the atoms in a far red detuned crossed dipole trap that is created from a Nd:YAG laser at $\lambda_{\mathrm{DT}} = 1064\,\mathrm{nm}$. The dipole trap is formed by two circular shaped beams with diameters $\mathrm{w}_{\mathrm{DT1}} = 52\,\mu\mathrm{m}$ and $\mathrm{w}_{\mathrm{DT2}} = 242\,\mu\mathrm{m}$ at final evaporation beam powers of 102 mW and 600 mW. This yields different trapping frequencies along the different axes of the dipole trap. While in the y and z-direction, the trapping frequency is $(\omega_{\mathrm{y}}, \omega_{\mathrm{z}}) = 2\pi \cdot (144, 105)\,\mathrm{Hz}$. In the x-direction it yields $\omega_{\mathrm{x}} = 2\pi \cdot 12\,\mathrm{Hz}$ [91]. Furthermore, the dipole trap leads to a cigar shaped BEC that is elongated along the x-direction. This is beneficial for coupling experiments since the coupling lattice beam is co-propagating in this direction such that more atoms can participate in the coupling. The dipole trap sequence is mostly similar to the sequence for a BEC in the magnetic trap. At the end of the RF-evaporation the dipole trap is ramped up and the atoms are loaded into the dipole trap. After the gradient fields are switched off, the power of the dipole trap beams is exponentially ramped down until an almost pure BEC with $N_{\mathrm{atoms}} \approx 5 \cdot 10^4$ remains. The BEC in the dipole trap has a very long lifetime ($\tau_{1/e} \approx 17\,\mathrm{s}$) and is also used for the lattice calibration as described in Section 2.2.1.2.

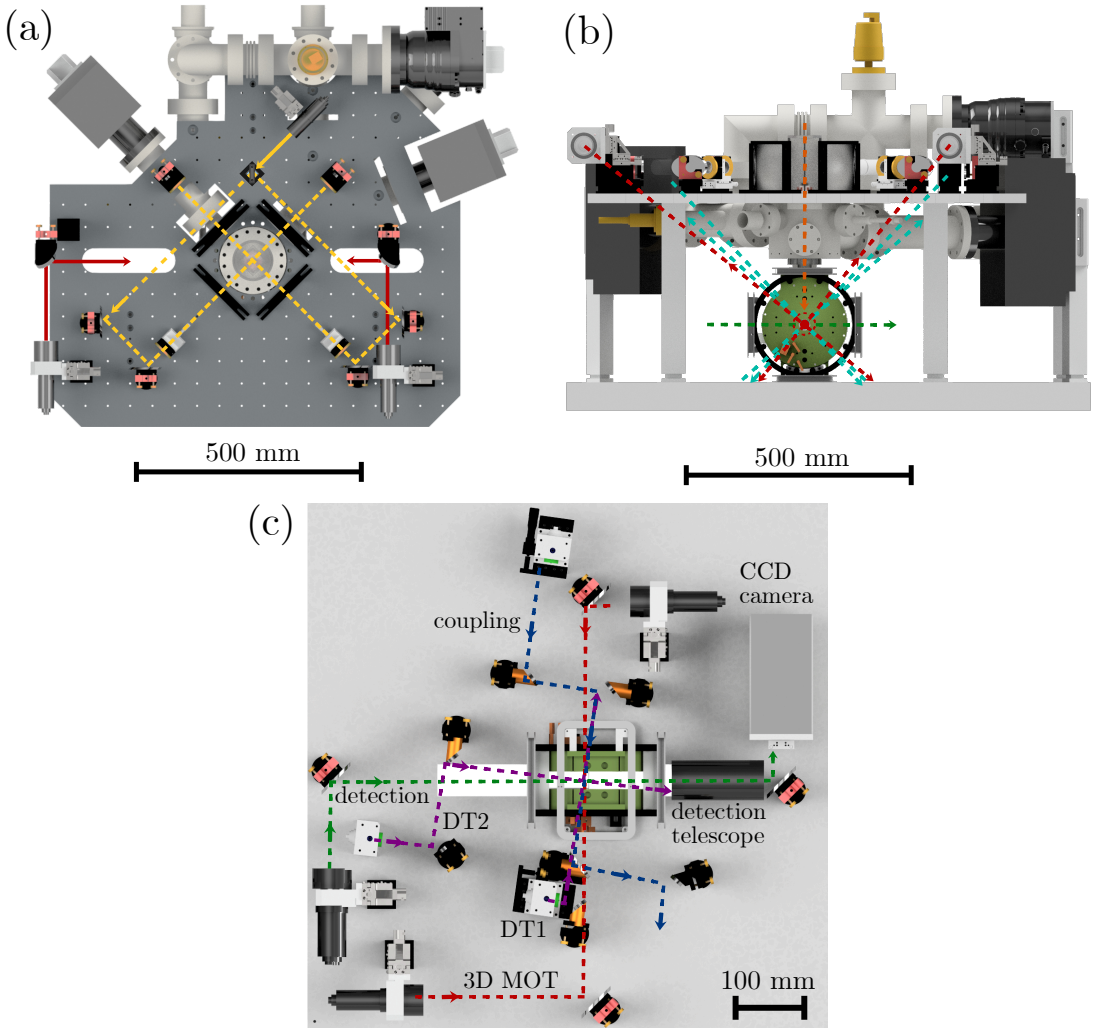

Figure 2.3: 3D Sketch of the BEC machine: (a) Top down view on the upper part of the 2D-MOT / 3D-MOT setup. The dashed yellow lines show the path of the 2D-MOT beams while the red lines denote the 3D-MOT beams that are directed to the lower glass cell. (b) Side view of the setup. The atoms are transferred from the upper 2D-MOT to the 3D-MOT by a resonant pushing beam (dashed orange line) and trapped in the 3D MOT by red detuned 3D MOT beams (dashed red lines). The turquoise dashed lines show the beam path of the 2D trapping lattice. The coupling beam path is shown as dashed green line. (c) Top down view on the lower part of the setup. The purple lines show the beam path of the crossed dipole trap (DT1 and DT2). The DT1 beam is co-propagating with the coupling lattice beam (blue dashed line). At the end of the sequence the BEC is imaged via the detection beam (green dashed line) by absorption imaging on a CCD camera. Figure from Ref. [63].

2.2 Hybrid coupling laser system

The coupling is mediated via light that couples to both hybrid partners. The atoms are loaded into an optical 1D-lattice that is created when the light incident on the atoms is reflected from the MiM-system [52]. For reasons described later in this thesis the coupling lattice laser is moderately detuned with respect to the D_2 $F = 2 \rightarrow F' = 3$ transition. It creates optical potential wells along the lattice axis, separated by $d_{pot} = \lambda_{coupl}/2$. The lattice trapping frequency ω_{lat} has to be matched with the eigenfrequency of the resonator ω_m to achieve coupling. Figure 2.4 shows a sketch of the coupling laser system.

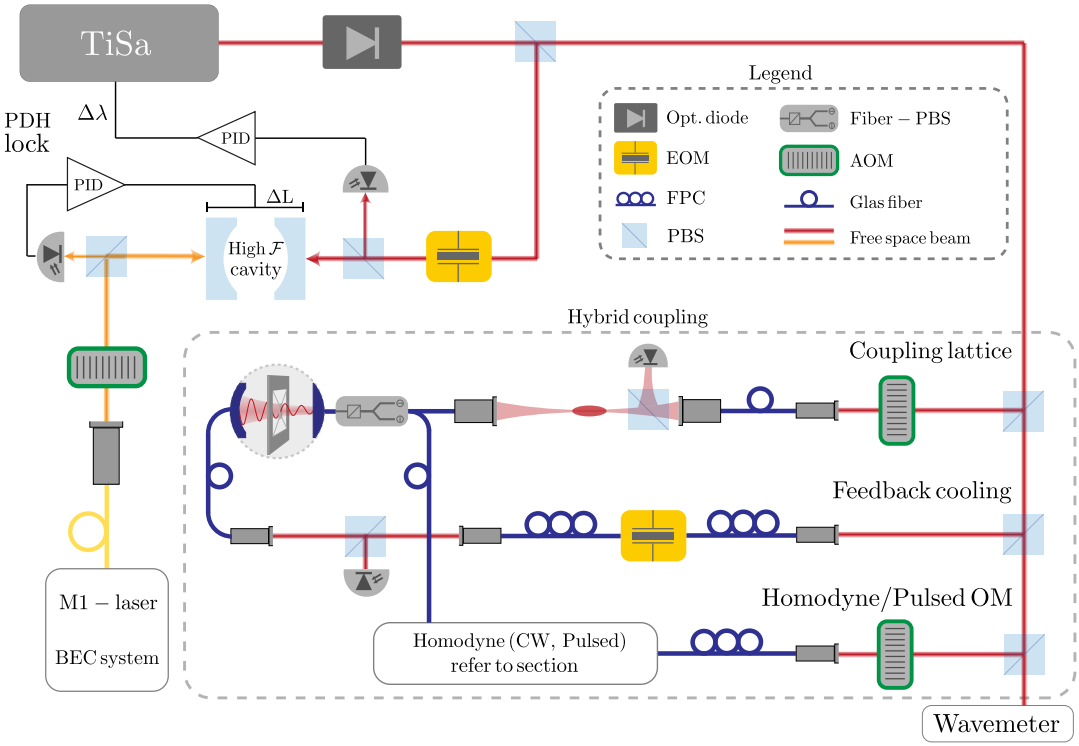

Figure 2.4: Sketch of the hybrid coupling setup: The Titanium-sapphire (TiSa) laser (red ray) is split into five branches. A small amount of the beam is split off into the transfer lock branch where it is coupled into a reference cavity (Toptica FPI100, $\Delta\nu = 3\,\mathrm{MHz}$) together with the cooling laser beam (orange ray). The length of the reference cavity is locked to the frequency stabilized cooling laser. The TiSa is subsequently locked to the reference cavity. The cooling laser beam can be frequency shifted by a 80 MHz double pass AOM to tune the TiSa frequency via the transfer lock. The majority of the beam power goes into the laser system that is used for the hybrid coupling experiments (grey dashed box). The coupling lattice branches contains a single pass 110 MHz AOM for intensity regulation and fast switching. The homodyne branch contains a 80 MHz AOM. The coupling lattice beam is focused onto the atoms via a telescope that is directly appended to the glass fiber. It is reflected from the MiM-system and creates an optical 1D lattice. The feedback cooling branch couples to the MiM-system from the opposite side of the fiber cavity. The motional state is read out via balanced homodyne detection. Since this part is distinct for different experiments, a detailed drawing is depicted in the corresponding Sections 2.4 and 4.2.3. The remaining beam is directed into a wavemeter (HighFinesse WS6-600).

We briefly outline the essential components of the setup with and then focus on the coupling lattice setup.

Titanium-sapphire laser The lattice beam is derived from a Titanium-Sapphire (TiSa) laser[2] that can be tuned over a frequency range of 25 THz, covering the resonances of the rubidium D_1 and D_2 line at a vacuum wavelength of $\lambda_{D_1} = 794.8\,\text{nm}$ and $\lambda_{D_2} = 780\,\text{nm}$ [92]. Despite the large frequency range, it is possible to stabilize the laser to a specific frequency with an accuracy of 50 MHz. This is possible via a combination of multiple locks that together provide a large locking bandwidth. The MBR 110 utilizes an etalon lock for compensation of small frequency deviations by locking the etalon transmission signal to the laser frequency. Larger frequency drifts are compensated by the internal servo lock that references the laser to a low finesse $\mathcal{F}_{\text{ref}} \approx 25-50$ cavity and stabilizes its frequency with respect to the cavity resonance via a dither lock [57]. The combination of these locks results in a bandwidth for small disturbances up to 100 kHz[3].

Transfer lock
Fulfilling the resonance condition between both hybrid partners requires for accurate tuning of the coupling lattice frequency. The TiSa can be locked to an external reference with a 6 dB locking bandwidth of 12 Hz. This feature is used for the transfer lock that allows to stabilize the TiSa frequency to the cooling transition of the rubidium D_2 line with an accuracy of 3 MHz. As depicted in Fig. 2.4 both the TiSa and the M1 cooling laser are coupled into the same high finesse cavity[4] ($\Delta\nu = 3\,\text{MHz}$) from opposite sides. Sidebands are modulated onto the TiSa laser light via a 10 MHz EOM. The cavity signal is used to derive a Pound-Drever-Hall (PDH) signal. While the reference cavity is stabilized onto the M1 cooling laser, the TiSa laser frequency is stabilized onto the reference cavity. This allows us to lock the TiSa laser onto the atomic resonance in units of FSR of the reference cavity. The FSR of the reference cavity was determined in previous theses [57, 62] to $\Delta\nu = n_{\text{FSR}} \times (997.544 \pm 0.004)\,\text{MHz}$ The transfer lock is essential for the precise calibration of the wave meter and the coupling lattice depth. When activated it diminishes slow drifts of the TiSa laser (up to 50 MHz in 5 minutes without the lock). For the coupling experiments with the new cavities it became necessary to tune and stabilize the frequency with a precision of $< 10\,\text{MHz}$ near the atomic resonance. Thus, the transfer lock was modified and an additional double pass AOM between the M1 cooling laser and the reference cavity was implemented. This allows us to use the transfer lock to carefully tune the coupling lattice detuning close to the atomic resonance between $\Delta_{\min\,(2,3)} = (22 \pm 3)\,\text{MHz}$ and $\Delta_{\max\,(2,3)} = (182 \pm 3)\,\text{MHz}$.

Homodyne detection
The motional state of the resonator is detected by phase sensitive homodyne detection. Homodyne detection is particularly insensitive to common mode noise on the light and offers excellent signal to noise ratios [93, 94]. The homodyne detection beam is split into two branches one of which serves as local oscillator (LO) while the other one interacts with the resonator. Via lock-in detection at the resonator eigenfrequency, the

[2] *Coherent MBR 110*
[3] According to the manufacturer *Coherent*.
[4] *Toptica FPI 100*

interference signal between both beams is detected. The homodyne detection branch contains an AOM that uses a similar electronics configuration as the coupling lattice AOM to regulate the homodyne beam intensity. Dependent on the conducted experiments (i.e., coupling experiments or pulsed experiments) this part of the experiment is built differently[5]. All recent experiments were conducted with a fiber based instead of a free space homodyne detection setup[6].

Feedback cooling
Feedback cooling is done by acquiring the position of the resonator via balanced homodyne detection and deriving a phase shifted feedback signal that counteracts the resonators motion. For this, fast processing of the signal as well as an excellent detection noise floor is necessary [95]. The feedback cooling branch couples the TiSa light into a fast fiber EOM[7] via a polarization maintaining (PM) fiber. Behind the EOM we measure the intensity of the feedback beam and regulate it via the EOM bias input. To achieve the highest possible modulation depth, the working point of the EOM is chosen such that it operates at half of the maximum transmission. Feedback cooling is only relevant for the experiments on pump asymmetry compensation. For a thorough theoretical description of the feedback cooling mechanism we refer to Appendix C.

2.2.1 Coupling lattice

The coupling lattice has to be intensity stabilized and able to be switched on and off reproducibly on the order of 100 ns. This is realized via a 110 MHz single pass AOM[8] in the coupling lattice branch that is driven by a RF-modulation that can be regulated in power and switched via a high speed RF-switch. Additionally, the lattice beam can be blocked with a shutter in front of the fiber to ensure that no stray light can disturb the experimental sequence. The setup allows for the generation of short pulses with minimal pulse widths of 100 ns with low cycle to cycle pulse power deviations of only 0.3 % [57]. These are necessary properties for the calibration of the lattice via Kapitza-Dirac diffraction (Sec. 2.2.1.2). The coupling lattice light is transferred to the lower lab via a single mode (SM) fiber.

[5] Figure 2.4 depicts the configuration for the hybrid coupling experiments. The configuration for pulsed measurements is slightly different and described in the respective Chapter 4.

[6] A description of the free space setup that has been used for the PAC experiments can be found in Appendix A.1.

[7] *Jenoptik AM785b*

[8] The AOM operates at 120 MHz.

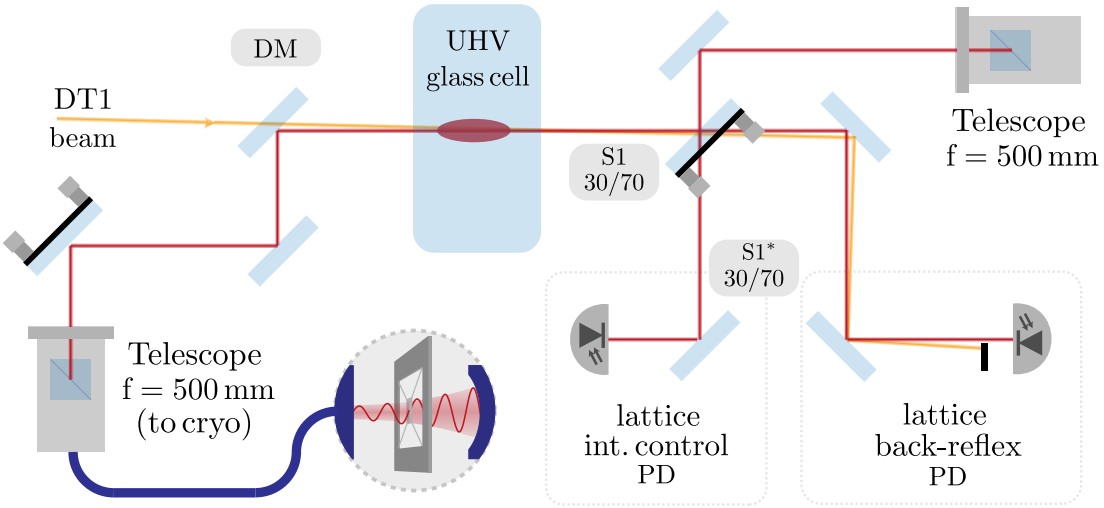

Figure 2.5: Sketch of the coupling lattice setup: The coupling lattice beam is focused onto the atoms by a telescope (*Schäfter & Kirchhoff fiber collimator 60FC-L-4-M20L-02 and focusing lens 13M-S500-05-S)* at a working distance of 49.2 cm and re-coupled into the cryostat via a second, identically configured telescope. It is reflected from the MiM-system and forms a standing wave. The lattice beam is passing through a R:T = 30:70 beamsplitter and directed onto a photodiode for the lattice intensity control. The back-reflected beam is monitored on the lattice back-reflex PD. The beam can be fine adjusted onto the atoms and onto the cryo telescope by micrometer screws at the respective positions. The dipole trap is aligned along the coupling lattice and passes through the same dichroic mirror, the coupling lattice beam is reflected at.

2.2.1.1 Lattice setup

Figure 2.5 depicts a detailed sketch of the coupling lattice as it is used for hybrid coupling experiments[9]. The coupling lattice lights polarization is cleaned by a PBS in the outcoupling telescope and directed onto the atoms via a substrate with a reflectivity of $R_{780} = 30\%$. The transmitted light is used for the intensity control. A second, identical substrate which reflects the lattice light onto the photodiode compensates for the slight wavelength dependency of the substrates reflectivity. The lattice beam passes through the AR coated glass cell and is reflected on the dichroic mirror which transmits the dipole trap wavelength and allows for the parallel adjustments of both beams. The lattice beam is coupled into the cryostat via an identical second telescope. Both the mirrors in front of the glass cell and the telescope are equipped with micrometer screws to allow for precise alignment. The back-reflex from the fiber cavity is monitored on the lattice back-reflex PD. This signal is used for the cavity alignment, for optimization of the incoupling into the cryostat and to adjust the polarization of the reflected light. Due to losses along the path between the atoms and the resonator and because of the finite reflectivity on resonance of the cavity, the back-reflected beam has only 25% - 30 % of the incident power (dependent on the cavity alignment) [62, 63]. Thus, the 1D lattice is pumped asymmetrically, which is an inherent property of our system. This leads to dynamic instabilities in the coupling in regimes with high atomic densities.

[9]For the PAC experiments an additional compensation beam was introduced. For details refer to Appendix A.2 and Ref. [63].

This effect and the efforts we undertook to compensate it are described in more detail in Chapter 3.2.
For the hybrid experiments coupling and detection light has to enter the cavity simultaneously while any crosstalk between both breams is minimized. Via a PBS, homodyne light is coupled into the same fiber at a perpendicular polarization[10].

Coupling between both constituents takes place, if the resonance condition $\omega_{\mathrm{at}} = \omega_{\mathrm{m}}$ is fulfilled. While the resonators ground mode frequency is fixed at $\omega_{\mathrm{m}} \approx 2\pi \cdot 154\,\mathrm{kHz}$ (depending on temperature and alignment), the trapping frequency of the atoms is dependent on the coupling lattices trapping potential depth. Assuming a harmonic potential the trapping frequency is related to the potential depth via [96]:

$$\omega_{\mathrm{at}} = \sqrt{\frac{2V_{\mathrm{lat}}k_{\mathrm{lat}}^2}{m_{\mathrm{Rb}}}} \tag{2.1}$$

Here V_{lat} denotes the lattice depth given in units of the recoil energy E_{rec} with the lattice k-vector k_{lat} and the mass of one rubidium atom m_{Rb} [92]:

$$E_{\mathrm{rec}} = \frac{\hbar^2 k_{\mathrm{lat}}^2}{2m_{\mathrm{Rb}}} \tag{2.2}$$

Solving for V_{lat} leads to a required lattice depth of $V_{\mathrm{lat}} = 441\,E_{\mathrm{rec}}$ to fulfill the resonance condition. The lattice depth scales like $V_{\mathrm{lat}} \propto I_{\mathrm{lat}}/\Delta_{\mathrm{at,L}}$. While most experiments operate in a far detuned regime with relatively high lattice powers to reduce scattering losses, the high sensitivity of the micromechanical resonator to laser induced heating, requires working in a near detuned ($\Delta_{\mathrm{at,L}} < 1\,\mathrm{GHz}$) regime at low lattice powers $P_{\mathrm{lat}} < 1\,\mathrm{mW}$. As discussed in Chapter 3, the upgrade of the fiber cavity finesse to $\mathcal{F}_{\mathrm{empty}} = 785$ further restricts this requirement and the highest cooperativities are achieved for $P_{\mathrm{lat}} < 25\,\mu\mathrm{W}$ requiring lattice detunings of $\Delta_{\mathrm{at,L}} < 200\,\mathrm{MHz}$. Meaningful measurements require the use of the transfer lock, to avoid frequency drifts. To achieve high intensities at the position of the atoms at moderate powers the coupling lattice beam is focused to a small waist size of $\mathrm{w}_{\mathrm{coupl}} = 76\,\mu\mathrm{m}$.

2.2.1.2 Lattice alignment

For the coupling experiments it is crucial that the atoms are illuminated by the coupling lattice beam precisely. Thus, we align the coupling beam to match the position of the crossed dipole trap. This is done by setting the coupling lattice beam far red detuned with $\Delta_{2,1} = -250\,\mathrm{GHz}$ at $P_{\mathrm{lat}} = 3\,\mathrm{mW}$ and blocking the coupling lattice back-reflex beam. At this setting, the beam attracts the BEC without destroying it due to scattering. This dragging effect is used to pull the BEC out of its equilibrium position and align the beam such that it coincides with the crossed dipole trap. The experimental sequence for this alignment is similar to the dipole trap BEC sequence depicted in Fig. 2.2. After the evaporation in the dipole trap, all optical potentials except to coupling beam are turned off. The coupling beam is turned on for 2 ms. The atoms are dragged

[10] While for the PAC experiments, this is done in a free space setup as depicted in Fig. A.1, all coupling experiments with the new cavities rely on a fiber based PBS.

towards the coupling beam and imaged after 21.5 ms TOF. For bad initial alignments, the detuning can be reduced to increase the dragging effect.
After the alignment of the incident beam, the back-reflex beam is unblocked. Maximizing the back-reflex beam power usually already yields a well aligned system, since the incoupling to the cryostat fiber requires and excellent mode match between the fiber and the incident beam mode. Fine adjustments are made using the Kapitza-Dirac diffraction pattern of a pulsed optical 1D lattice and maximizing the lattice depth at a fixed parameter set. The theory of Kapitza-Dirac diffraction [97] is described in detail in previous theses [57] and shall be outlined in most brevity here.

2.2.1.3 Lattice calibration via Kapitza-Dirac diffraction

Starting with a BEC in the dipole trap sequence, a short coupling lattice pulse of $1\,\mu\text{s} - 56\,\mu\text{s}$ is applied to the BEC after the evaporation in the dipole trap. Thereafter the optical potentials are turned off and a TOF image is taken. While the coupling lattice is on, a momentum transfer between the light field and the atoms occurs. Along the lattice axis this redistribution of photons can either lead to an effective momentum transfer of zero or $\pm 2n\hbar k_{\text{lat}}$ ($n = 1, 2, 3, ...$). The atoms undergo Rabi-oscillations between these momentum orders at a lattice depth dependent frequency. For deeper lattices, higher order processes become relevant, leading to interference between the different momentum order oscillations. These oscillations are described by the solution of the time dependent Schrödinger equation of the system. Measuring the population of the momentum orders for different pulse durations allows to numerically calculate the time dependent Schrödinger equation for a BEC in a periodic potential and determine the lattice potential depth [98, 99]. A measurement example is depicted in Fig. 2.6.
The determined lattice depth is compared to the theoretically expected lattice depth, to acquire a calibration factor c_{cal}. For our system of two co-propagating lattice beams with different powers and waists (P_{inc},w_{inc} and P_{ref},w_{ref}) the expected potential is [86, 92, 99]:

$$V_{\text{lat}} = \frac{4c^2\sqrt{P_{\text{inc}}P_{\text{ref}}}}{\text{w}_{\text{inc}}\text{w}_{\text{ref}}}\left[\frac{\Gamma_{\text{D}_1}}{\omega_{\text{D}_1}^3}\frac{1}{\Delta_{\text{D}_1}} + 2\frac{\Gamma_{\text{D}_2}}{\omega_{\text{D}_2}^3}\left(\frac{1}{20\Delta_{\text{D}_2,\text{F}'=1}} + \frac{1}{4\Delta_{\text{D}_2,\text{F}'=2}} + \frac{7}{10\Delta_{\text{D}_2,\text{F}'=3}}\right)\right] \tag{2.3}$$

Here Γ_{D_1} denotes the linewidth of the ^{87}Rb D_1 transition, ω_{D_1} the corresponding optical frequency and Δ_{D_1} the detuning of the lattice light relative to the D_1 transition. Note that hyperfine structure contributions are omitted in this term due to the large detuning ($\Delta_{\text{D}_1} \approx 7\,\text{THz}$) of the coupling lattice light to this transition. The second term accounts for the coupling of the lattice light ot the ^{87}Rb D_2 transition. Here it is necessary to take the individual transition strengths into account [92]. $\Delta_{\text{D}_2,\text{F}'=\text{X}}$ denotes the detuning of the coupling lattice relative to the $|5^2S_{1/2}, F = 2\rangle \rightarrow |5^2P_{3/2}, F' = X\rangle$ transition. When referenced to the M1 cooling laser via the transfer lock, the TiSa laser is blue detuned from the $|5^2S_{1/2}, F = 2\rangle \rightarrow |5^2P_{3/2}, F' = 3\rangle$ by $2 \times 71\,\text{MHz}$. Together with the AOM in the coupling lattice and the additional double pass AOM in the transfer lock branch,

the coupling lattice can be set precisely to any of the following values:

$$\frac{\omega_{\text{lat}}}{2\pi} = \frac{\omega_{2,3}}{2\pi} + 2 \times 71\,\text{MHz} + 120\,\text{MHz} + n_{\text{FSR}} \times \text{FSR} - 2 \times (\mathbf{40}\ \ldots\ \mathbf{120})\,\mathbf{MHz} \tag{2.4}$$

The modified transfer lock covers a range of 162 MHz[11]:

$$\Delta_{\text{D}_2,\text{F}'=3} = (22 - 182)\,\text{MHz} \tag{2.5}$$

For the Kapitza-Dirac lattice calibration, the TiSa is transfer locked to the M1-cooling laser and the displayed wavelength on the wavemeter is acquired. This allows for an absolute calibration of the displayed wavelength which is used to determine the theoretically expected lattice depth at a set wavelength and lattice power.
Comparing this result with the measured lattice depth yields the lattice calibration factor:

$$c_{\text{cal}} = \frac{V_{\text{meas}}}{V_{\text{theo}}} \tag{2.6}$$

This calibration is very sensitive to slight misalignment of both incident and back-reflex beam. Thus, it is measured on a daily basis.

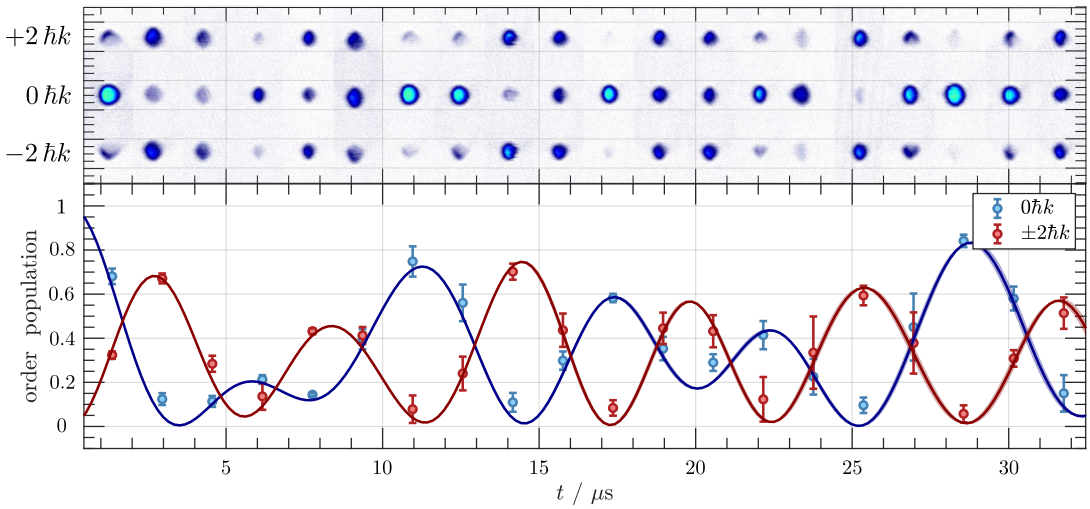

Figure 2.6: Kapitza-Dirac momentum order oscillations: The upper panel depicts the distribution of the atoms in the momentum orders $0\,\hbar k$ and $\pm 2\,\hbar k$ in the TOF-image that corresponds to the respective lattice pulse duration depicted on the x-axis of the lower graphic. The blue datapoints show the measured relative occupation of the 0th momentum order while the red datapoints show the occupation of the ±1st momentum orders. Every datapoint is averaged over four measurements. The numerical solution of the time dependent Schrödinger-equation is fitted [57, 99] (blue and red lines) on the momentum oscillations with the lattice potential V_0 as fit parameter. For the lattice alignment depicted here $c_{\text{cal}} = (90 \pm 0.5)\%$ at a lattice depth of $V_0 = (58.3 \pm 0.3)\,E_{\text{rec}}$. Values between 80 % and 90 % are regularly achieved.

[11] To cover this range we operate the double pass AOM far from its center frequency. While this yields very small diffraction efficiencies, the signal is strong enough to derive a sufficiently large error signal for the PDH lock.

2.3 Optomechanical setup

The optomechanical part of the hybrid system consists of a micromechanical resonator that is placed in a plano-concave fiber Fabry-Pérot-cavity (FFPC) in the MiM configuration. The hybrid coupling scheme imposes special requirements on the optomechanical system. For bidirectional coupling, the light has to be reflected back to the atoms after interaction with the resonator. This requires for an asymmetric cavity where the reflectivity of the cavities incoupling mirror R_1 is smaller than the reflectivity of the outcoupling side R_2. This yields a non-zero reflectivity on resonance. Additionally, the cavity mirror profiles have to be designed such that most of the light coupled into the cavity mode is reflected back into the incoupling fiber mode. Thus, the cavity is built in a plano-concave configuration where the profile of the concave mirror is fabricated according to the mode field diameter of the incoupling fiber. The production of fiber cavities is described in detail in Ref. [67, 100]. For the experiments in this thesis two new fiber cavities at higher finesses were implemented at the experimental setup[12].
The experiments require positioning of the cavity mirrors and the mechanical resonator inside the cavity with a transversal accuracy of 200 nm [57]. While the old setup with $\mathcal{F}_{\text{empty}} = 60$, required a longitudinal accuracy of a few nanometers, the high finesse cavities (particularly at $\mathcal{F} = 14500$) require for a precision of a few tens of picometers due to their narrow linewidth. Thus, the high finesse system benefits from the high passive stability only at cryogenic temperatures. The fiber cavities are aligned to a length between $12\,\mu$m to $24\,\mu$m. Here the planar fiber is aligned closely to the resonator ($d \approx 5\,\mu$m) to acquire better mode match in the planar-planar sub cavity. The distance of the curved fiber differs (dependent on the experiment) between $17\,\mu$m ($\mathcal{F}_{\text{empty}} = 60$) and $6\,\mu$m ($\mathcal{F}_{\text{empty}} = 785$, $\mathcal{F}_{\text{empty}} = 14500$). The necessary precision in alignment is realized via a 5-axis goniometer (Fig. 2.7) that was designed and manufactured in Ref. [60, 61]. A slip-stick piezo design allows to roughly align both fibers with sub-micrometer precision while offering a large travel range of multiple millimeters. The fibers are mounted into piezo tubes that allow to move them continuously with picometer precision.
Both the coupling and the pulsed experiments require the mechanical resonator to operate in the quantum coherent oscillation regime [95] to access the ground state. The resonators quality factor Q and linewidth Γ_{m} depend on the bath temperature. Thus, the whole system is attached to a He^3/He^4 dilution refrigerator that allows to cool the system to a base temperature of $T_{\text{base}} = 500\,\text{mK}$. Beginning in Ref. [63] there were severe issues with our dilution unit ranging from impure He^4 that clogged the systems needle valve and disallowed operation of the system 1K-pot, which is crucial for a proper mixture circulation. Furthermore, blockages occurred during operation indicating leaks in the dilution unit itself. During this thesis we conducted a thorough checkup of the whole system. Multiple leaks were identified and fixed[13]. Even though this allowed to conduct the measurements presented in Chapter 4 at stable, cryogenic temperatures, recurring issues in the liquification process and helium supply required us to conduct the measurements on hybrid coupling at room temperature.

[12] The production and characterization of theses cavities is briefly discussed in Section 2.5 and in Appendix B.5.
[13] An overview over these procedures is presented in Appendix E.

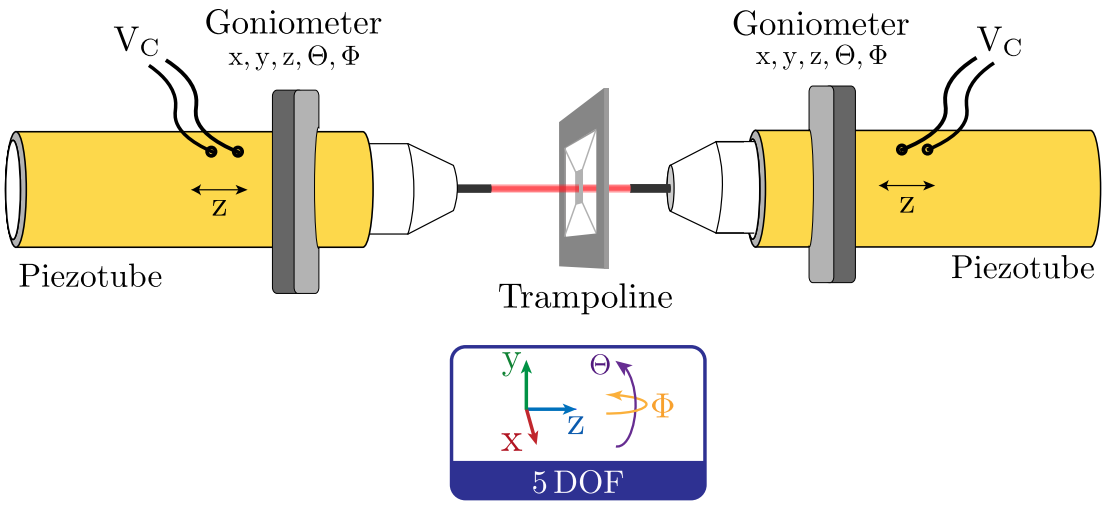

Figure 2.7: Schematic of the MiM setup: The trampoline resonator is placed in the fiber cavity. The coated glas fibers are glued into ceramic ferrules that are mounted to piezo tubes which allow for z-alignment with picometer precision and that can be scanned over a distance of multiple λ, dependent on the system temperature. The piezo tubes are mounted in a 5-axis goniometer that allows positional and angular alignment with sub-micrometer precision. Figure adapted from Ref. [105].

2.3.1 High stress SiN trampoline resonator

From the initial use of high stress SiN membranes for hybrid experiments [101][102] the capabilities and variety of new designs evolved rapidly. In recent years the mechanical quality factor and resonant frequency continuously increased rendering new coupling mechanisms and even ground state preparation at room temperature possible [103]. The MiM configuration comes at an advantage that the optical and mechanical components of the system can be dimensioned independently. This allows us to modify the mechanical properties of the system (e.g. resonator frequency) while leaving the optical properties largely untouched. Due to the small thickness of the resonator material $d = 50\,\mathrm{nm} \ll \lambda$ scattering effects only appear in well defined directions such that MiM configurations with high finesses are realizable with such systems. The positioning of the resonator at a node/antinode of the intracavity field leads to either linear $\sim x_\mathrm{m}$ or quadratic $\sim x_\mathrm{m}^2$ dispersive coupling with the light field allowing for accurate displacement [102] or direct energy measurements [104].

Our system uses a high Q trampoline resonator in a MiM configuration as mechanical hybrid partner. Initially introduced in Refs. [87, 88] they were designed to "enter the quantum regime at room temperature" [87]. Trampoline resonators are tethered high stress, thin silicon-nitride (Si_3N_4) membranes with that yield Q factors on the order of $Q = \omega_\mathrm{m}/\Gamma_\mathrm{m} \approx 10^8$ and low effective masses. Imprinting photonic crystal structures on the central membrane allows to achieve high field reflectivities while maintaining the excellent mechanical quality. These properties promote a very low thermal force noise which is expressed by [95]:

$$S_\mathrm{F}^\mathrm{th} = 4k_\mathrm{B}T_\mathrm{bath}\Gamma_\mathrm{m}m_\mathrm{eff} \tag{2.7}$$

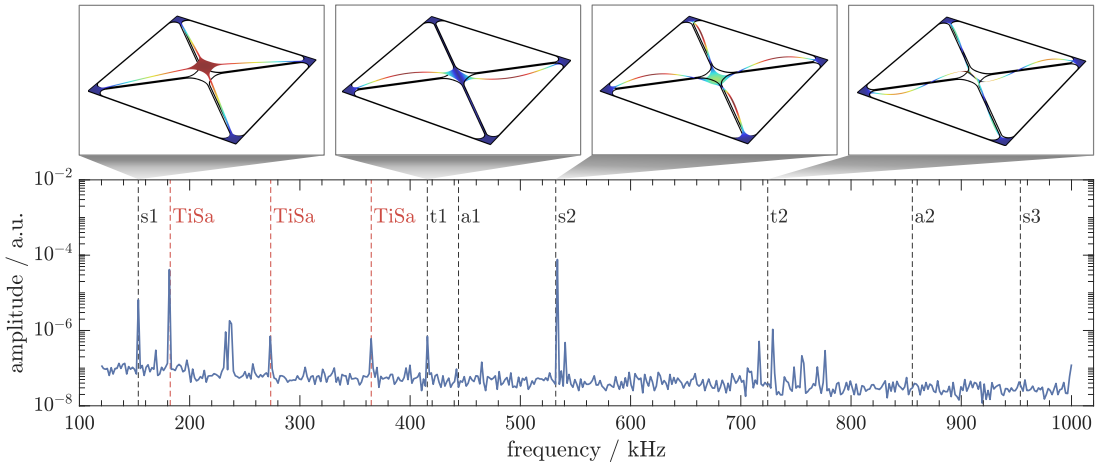

Figure 2.8: Trampoline mode spectrum: Mode spectrum of the trampoline resonator recorded with a spectrum analyzer (Rohde & Schwarz FSP) at a resolution bandwidth of RBW = 100 Hz. Red dashed lines indicate contributions to the spectrum from the etalon lock of the TiSa-laser. Black dashed lines show the different oscillation modes of the resonator where "s" indicated a symmetric (s)-mode, "t" a torsional (t)-mode and "a" an asymmetric (a-mode). The COMSOL simulation results for the first two (s)- and (t) mode are depicted on the top. Simulation written by H. Zhong. Figure from Ref. [63].

To prepare the system in a quantum state, the system has to operate in the quantum-coherent-oscillation-regime (QCO). In this regime the thermal noise introduced to the system during one oscillation period does not exceed the energy of one additional phonon entering the system. This is equivalent to the condition, that the amplitude fluctuation of the resonator due to white noise does not exceed one zero-point motion ($x_{\mathrm{zpm}} = \sqrt{\hbar/m_{\mathrm{eff}}\omega_{\mathrm{m}}}$) within one period. Thus, the condition for reaching the QCO can be derived to be:

$$Q \cdot \omega_{\mathrm{m}} \geq n_{\mathrm{th}} = \frac{k_{\mathrm{B}} T_{\mathrm{bath}}}{\hbar} \tag{2.8}$$

Assuming a thermal decoherence rate $\Gamma_{\mathrm{th}} = n_{\mathrm{th}}\Gamma_{\mathrm{m}}$ from coupling to the thermal bath one can calculate the number of coherent oscillations the system undergoes at a given bath temperature until an additional phonon enters the system using equation 2.9:

$$N_{\mathrm{QCO}} = \frac{\omega_{\mathrm{m}}}{\Gamma_{\mathrm{th}}} = \frac{Q\omega_{\mathrm{m}}\hbar}{k_{\mathrm{B}} T_{\mathrm{bath}}} \tag{2.9}$$

Because we operate the system at different temperatures, this condition is not always fulfilled. Particularly measurements at room temperature are conducted outside the QCO regime. To access the ground state, be it in a pulsed protocol or with continuous cooling schemes, the system has to be in the QCO regime. Table 2.1 compares the mechanical properties at the most common parameters used for our experiments. Unless stated otherwise, these values hold for the measurements conducted in this thesis. The trampoline resonator used in this thesis was designed by H. Zhong [61] using a finite elements simulation and fabricated by *Norcada*. The design aimed for a low effective mass, a high $Q\omega_{\mathrm{m}}$-product and high transmission at $\lambda = 780\,\mathrm{nm}$.

T	ω_m	Q	Γ_m	N_osc
0.5 K	$2\pi \cdot 153.98\,\mathrm{kHz}$	$(8.987 \pm 0.001) \cdot 10^7$	$2\pi \cdot (1.7 \pm 0.4)\,\mathrm{mHz}$	1329
10 K	$2\pi \cdot 152.36\,\mathrm{kHz}$	$(6.832 \pm 0.001) \cdot 10^7$	$2\pi \cdot (2.2 \pm 0.5)\,\mathrm{mHz}$	50
293 K	$2\pi \cdot 154.42\,\mathrm{kHz}$	$(6.662 \pm 0.004) \cdot 10^6$	$2\pi \cdot (23.2 \pm 0.8)\,\mathrm{mHz}$	< 1

Table 2.1: Temperature dependent MiM parameters:
The resonators frequency and Q-factor are temperature dependent. While the QCO is not reached at room temperature, it is accessible at 10 K and at base temperature. The Q-factor is determined by ring-down measurements of the excited resonator. The measurements were taken with the low finesse ($\mathcal{F} = 140$) cavity. Since the resonator experiences optomechanical heating and cooling dependent on the alignment the displayed quality factor is the harmonic mean $Q = 2Q_\mathrm{cool}Q_\mathrm{heat}/(Q_\mathrm{cool} + Q_\mathrm{heat})$. Table from Ref. [63].

The final resonator is made from high-stress (800 MPa), $d = 50\,\mathrm{nm}$ thick Si_3N_4. The central pad is suspended by 4 tethers and has a size of $115 \times 115 \pm 10\,\mu\mathrm{m}$. The resonator is mounted inside a 1 mm × 1 mm window of a rigid silicon frame. The frame has outer dimensions of 5 mm × 5 mm and a thickness of $500 \pm 25\,\mu\mathrm{m}$. It is placed in a copper shuttle under its own weight [63] which allows to exchange the resonator while the experiment is running. Simulations of the trampoline resonator calculate an effective mass of $m_\mathrm{eff} = 3\,\mathrm{ng}$ at an eigenfrequency of $\omega_\mathrm{m} = 2\pi \cdot 154\,\mathrm{kHz}$ for the first symmetric ground mode (s1) which is in good agreement with the measurements.

For most hybrid measurements, the s1-mode is the only relevant mode that is investigated. Higher modes usually do not contribute to the coupling due to the small mechanical linewidths and the large distance of over 350 kHz to the ground mode. In the scenario of pulsed measurements, this is different and as a short pulse contains frequency contributions along the whole mode spectrum of the trampoline. Thus, also higher modes can get excited that broaden the final outcome of a pulsed measurement protocol. The mode spectrum of the resonator is depicted in Fig. 2.8. Besides the s1 mode, the second symmetric mode (s2) is a large contributor to the spectrum for pulsed experiments [63].

2.3.2 Cavity optomechanics of the system

Placing the mechanical resonator inside the cavity creates a coupled system of two harmonic oscillators with eigenfrequencies ω_cav and ω_m that couple via the intra-cavity light field. In a quantum mechanical picture the energy exchange is described via the optomechanical interaction Hamiltonian $\hat{H}_0$ [102]:

$$\hat{H}_0 = \hbar\omega_\mathrm{cav}\hat{a}^\dagger\hat{a} + \hbar\omega_\mathrm{m}\hat{b}^\dagger\hat{b} \tag{2.10}$$

Here $\hat{a}^\dagger(\hat{a})$ are the photonic creation (annihilation) operators of the cavity light field and $\hat{b}^\dagger(\hat{b})$ the respective operators of the resonators mechanical motion. Similar to the "textbook" quantum mechanical harmonic oscillator, we can solve the Schrödinger equation of the mechanical subsystem [106]. The mean phonon occupation of the resonator is given by $\bar{n}_\mathrm{m} = \langle\hat{b}^\dagger\hat{b}\rangle$ with the allowed energies [106] $E_{n_\mathrm{m}} = \hbar\omega_\mathrm{m}\,(n_\mathrm{m} + 1/2)$.

From the solution of the time independent Schrödinger equation and the so acquired normalization constant we get the zero point motion of the mechanical vacuum state $|0\rangle$ to be:

$$x_{\mathrm{zpm}} = \sqrt{\frac{\hbar}{2m_{\mathrm{eff}}\omega_{\mathrm{m}}}} \tag{2.11}$$

The zero-point motion describes the amplitude fluctuation of the resonator due to the occupation with one phonon. In this description of the system, the position and momentum operators $\hat{x}$ and $\hat{p}$ can be expressed by:

$$\hat{x} = x_{\mathrm{zpm}}\left(\hat{b}^\dagger + \hat{b}\right) \qquad \text{and} \qquad \hat{p} = -\mathrm{i}m_{\mathrm{eff}}\omega_{\mathrm{m}}x_{\mathrm{zpm}}\left(\hat{b}^\dagger - \hat{b}\right) \tag{2.12}$$

The coupling between both systems affects the cavity resonance frequency. A Taylor expansion of $\omega_{\mathrm{cav}}(x)$ at $x_{\mathrm{m}} = 0$ yields the following dispersion relation:

$$\omega_{\mathrm{cav}}(x_{\mathrm{m}}) = \omega_{\mathrm{cav}} + x_{\mathrm{m}}\frac{\partial\omega_{\mathrm{cav}}}{\partial x_{\mathrm{m}}} + ... \tag{2.13}$$

This expression contains terms for linear and quadratic coupling to the resonator. Both linear and quadratic coupling can be realized in our system, dependent on the positioning of the resonator in the intra-cavity field. For our experiments, we are interested in the phase of the interacting light which changes linearly with x_{m}. Thus, we omit higher order terms in the following description. The term $G = \partial\omega_{\mathrm{cav}}/\partial x_{\mathrm{m}}$ describes the cavity resonance frequency change upon a mechanical displacement x_{m} and is called the optomechanical coupling of the system. Using expression 2.13 together with 2.10 we obtain a new expression for the systems hamiltonian:

$$\hat{H}_0 = \hbar\omega_{\mathrm{cav}}\hat{a}^\dagger\hat{a} + \hbar\omega_{\mathrm{m}}\hat{b}^\dagger\hat{b} - \hbar g_0\hat{a}^\dagger\hat{a}(\hat{b}^\dagger + \hat{b}) \tag{2.14}$$

$g_0 = Gx_{\mathrm{zpf}}$ corresponds to the cavity frequency shift if the resonator moves by one zero-point-motion x_{zpm}. Since this is equivalent to one photon entering the cavity and coupling to the resonator, this term is called the single photon coupling strength.
The most simple design for such a system would be a moving end mirror Fabry-Pérot cavity. This system yields the simple resonance condition $L_{\mathrm{res}} = 1/2 \cdot n\lambda$ ($n \in \mathbb{N}$) and has a resonance frequency of [107] $\omega_{\mathrm{cav}} = n\pi c/L$, where L denotes the cavity length, and c the speed of light. If one mirror is displaced by a small amount x_{m} the frequency changes by:

$$\omega_{\mathrm{cav}}(x_{\mathrm{m}}) = \frac{n\pi c}{L + x_{\mathrm{m}}} \approx \omega_{\mathrm{cav}}\left(1 - \frac{x_{\mathrm{m}}}{L}\right) = \omega_{\mathrm{cav}} - x_{\mathrm{m}}\frac{\omega_{\mathrm{cav}}}{L} \tag{2.15}$$

Like in equation 2.13 we use a Taylor expansion at $x_{\mathrm{m}} = 0$. Deriving this term yields the frequency shift per displacement $G = -\omega_{\mathrm{cav}}/L$ [107].

The system with a MiM geometry behaves differently. The membrane can be treated as a semi-transparent third mirror that divides the cavity into two subcavities. Dependent on the exact position in the intracavity field either one of the two subcavities is

resonantly enhanced. The implications for the optomechanical properties of the system have been investigated in previous publications [107, 108]. Most relevant are the position dependent change in the reflectivity on resonance and the influence on the cavity linewidth and thus the finesse. Figure 2.9 shows a simulation of the cavity detuning dependent transmission for different positions of the membrane in the intra-cavity field. The slope of the curve corresponds to the optomechanical coupling. While for a central placement (MiM) of the resonator the slopes are symmetric, they develop an asymmetry when the resonator is moved closely to the cavity edge [104, 107].
The optomechanical coupling becomes dependent on the choice of the slope and can be further increased by placing the membrane at the edge (MATE) of the cavity. This setting was investigated in Ref. [104]. For both geometries, the cavity resonance frequency dependent on the resonators intra cavity position x_m behaves differently. The respective cases are described by the following equations [104, 107]:

$$\omega_\mathrm{MiM}(x_\mathrm{m}) = N\omega_\mathrm{FSR} + \frac{\omega_\mathrm{FSR}}{\pi}\left(\mathrm{acos}\left[(-1)^{N+1}|r_\mathrm{m}|\cos(2k_N x_\mathrm{m})\right] - \phi_\mathrm{r}\right) \tag{2.16}$$

$$\omega_\mathrm{MATE}(x_\mathrm{m}) = N\omega_\mathrm{FSR} + \frac{\omega_\mathrm{FSR}}{\pi}\mathrm{atan}\left(\frac{\cos(\phi_\mathrm{r}) + |r_\mathrm{m}|\cos(2k_N x_\mathrm{m})}{\sin(\phi_\mathrm{r}) - |r_\mathrm{m}|\cos(2k_N x_\mathrm{m})}\right) \tag{2.17}$$

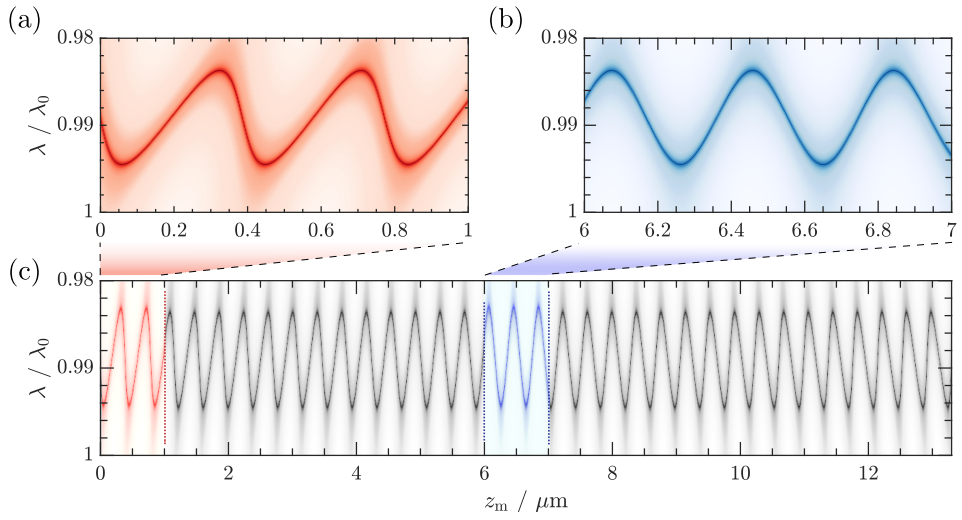

Figure 2.9: Cavity resonance modulation for different membrane positions: Simulation of the cavity resonance modulation for the system with $\mathcal{F}_\mathrm{empty} = 785$ and $L_\mathrm{cav} = 12.9\,\mu$m. We assume $R_1 = 99.97\%$ and $R_2 = 99.25\%$ and a resonators field reflectivity of $r_\mathrm{m} = 0.57$. The slope of the curve at the resonator position z_m resembles the optomechanical coupling strength. (a) Bringing the membrane close to the low reflective mirror causes an asymmetry between the slopes. (b) Resonance modulation with the membrane in the center. The slopes have a symmetric shape. (c) Simulation over the whole cavity length. Darker shades indicate higher transmission. The individual surface profiles of the cavity mirrors are not taken into account in this simulation.

Here N is the cavity resonance number, $\omega_{\mathrm{FSR}} = \pi c/L$ the free spectral range, r_{m} the resonators field reflectivity and $k_N = \pi N/L$ the $N-th$ cavity resonance [104]. The phase shift of the light by reflection off the membrane is described by ϕ_{r}. Figure 2.10 shows plots of both equations 2.16 and 2.17 for different r_{m}. It is beneficial to align the system to this regime to increase the optomechanical coupling.
The MATE geometry presented in Ref. [104] resembles an extreme case because the distance between the membrane and and the cavity mirror is only $1.64 \pm 0.78\,\mu$m in the publication. While the system is in principle stable enough, to operate at these parameters, it comes with a large risk of damaging the resonator since the fibers can slip during the alignment process and the error of the length measurements after alignment is on the same order as the proposed distance [104]. Thus, we choose to position the resonator off center but at a slightly larger distance of $d \approx 4.5\,\mu$m. Here the asymmetry on the cavity resonances is still prominent but not as pronounced as described by equation 2.17.
The optomechanical coupling is determined by measuring the cavity resonance frequency for varying x_{m}. Previously this measurement came with some technical difficulties, that required a special evaluation method that is described in Refs. [57, 62, 63]. Due to the large linewidth of the cavity (multiple GHz, except for $\mathcal{F}_{\mathrm{empty}} = 14500$), it is not possible to scan the laser frequency over the resonance. At the same time, the travel range of the upper fiber piezo in the system was too small to scan over one FSR when the system was operated at base temperature disallowing for a direct measurement of the piezo calibration. For the experiments at room temperature these limitations do not exist and the optomechanical coupling of the MiM system g_{m} can be measured directly with a new method presented in this section.

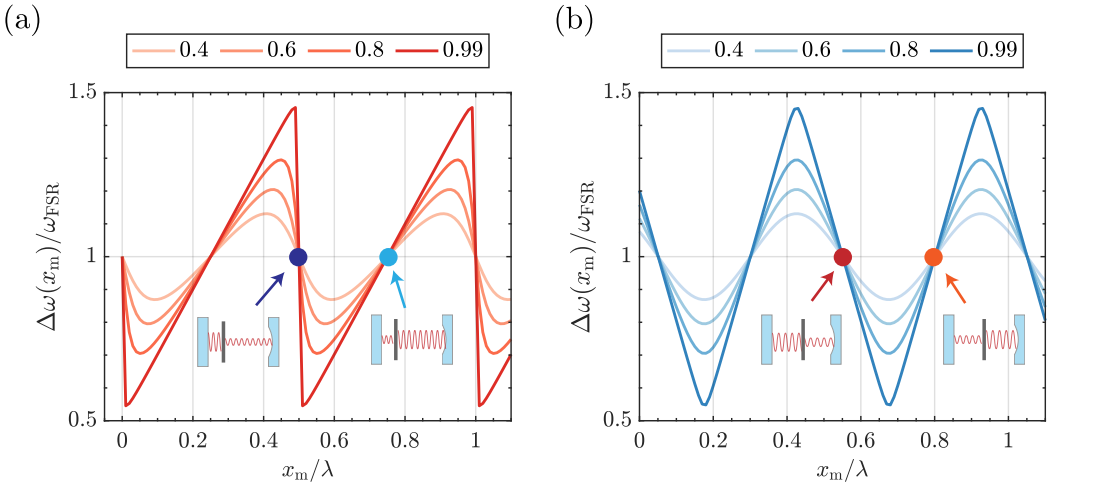

Figure 2.10: Cavity resonances for different geometries:
(a) Resonance behavior and cavity linewidth normalized to the empty cavity for the MATE system according to equation 2.17. The different shades indicate different field reflectivities r_{m}. Close to the edge, the optomechanical coupling is strongly enhanced when choosing the falling slope. (b) Same quantities plotted for the MiM system according to equation 2.16 for different field reflectivities. Figure adapted from Ref. [104].

Additionally, the piezo moving the upper fiber had to be replaced in the last months of this thesis due to a malfunction. The replacement piezo showed a calibration similar to the lower fiber piezo such that the method described here, was also applied at base temperature. The measurement described in the following section was done for the cavity with $\mathcal{F}_{\text{empty}} = 785$[14] [15] .
The optomechanical coupling of the system can be derived from $G = -\omega_{\text{cav}}/L = 187\,\text{GHz/nm}$ of the empty cavity via the relation [107]:

$$\frac{g_{\text{m}}}{G} = \frac{\partial L_{\text{res}}}{\partial x_{\text{m}}} \tag{2.18}$$

This quantity can be measured by symmetrically scanning both fibers around the resonator (emulating a movement of x_{m}) while slowly changing the cavity length by ΔL. This requires accurate knowledge of the piezo calibration $c_{\text{cal}} = \partial x/\partial U$ and a travel range of at least one λ to properly resolve both slopes of the cavity resonance. We determine the piezo calibration by scanning each piezo over at least one FSR which yields a distance of $\lambda/2$ and measure the required voltage to cover this range. These measurements are 10 times averaged and the acquired mean defines the piezo calibration. The calibration values determined with this method are consistent with old measurements [62, 63] but can be acquired much faster.
An overview about the piezo calibrations for different temperatures and the exchanged upper piezo is presented in Appendix B.4. For the setup discussed here, the piezo calibration at room temperature yields $c_{\text{up,293K}} = (2.37 \pm 0.01)\,\text{nm/V}$ and $c_{\text{low,293K}} = (2.95 \pm 0.01)\,\text{nm/V}$. This calibration is also relevant for the homodyne calibration presented in Section 2.4.
We measure $\partial L_{\text{res}}/\partial x_{\text{m}}$ by applying the scheme presented in Fig. 2.11. According to the piezo calibration, a 20 Hz triangular scanning ramp is applied to each fiber such that both fibers move synchronously and in phase by a distance $x(t)$ in the same direction[16]. This yields an effective change of x_{m} in the intra-cavity field. Additionally, the cavity detuning is varied by applying an additional offset scan $\Delta L(t)$ to one of the fibers. This scan is slow (10 mHz) compared to the symmetric scan. The slow movement of the fiber changes the resonance frequency of the cavity which influences the x_{m}-dependent transmission signal. Along each ramp of the fast, symmetric scan, the transmission signal is recorded.

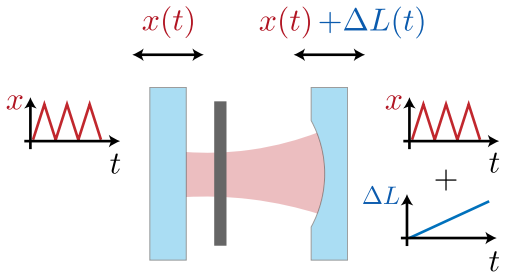

Figure 2.11: Sketch of g_{m} measurement Both cavity mirrors are scanned symmetrically and in phase around the resonator at a frequency of 20 Hz and undergo a movement $x(t)$. One cavity mirror is slowly (10 mHz) scanned with an additional offset to change the cavity length. At each slope of $x(t)$ the transmission dependent on ΔL is measured.

[14] We use $L_{\text{cav}} = 12.9\,(5)\,\mu\text{m}$, $\omega_{\text{cav}} = 2\pi \cdot 384\,\text{THz}$ and $\lambda = 780.24\,\text{nm}$.
[15] For the measurements for the low finesse cavity used for PAC, refer to Ref. [63]. For more information about the system parameters at $\mathcal{F} = 14500$ refer to the respective Chapter 4.
[16] The signal is generated by a 4 channel AWG (TGA 12100) that allows for frequency and phase synchronization between the channels. The output signal is amplified by a factor 50.

The outcome is presented in Fig. 2.12[17]. Each horizontal line corresponds to a scan of x_m over a distance of lambda at a set cavity detuning $\Delta L(t)$. This data requires no additional postprocessing and the optomechanical coupling can be directly extracted from linear fits to the individual slopes. For the hybrid experiments we operate the system at any of these slopes to tune the finesse and optomechanical coupling strength. We find for the configuration with $\mathcal{F}_{\text{empty}} = 785$:

$$\frac{g_{\text{m,high}}}{G} = -1.6 \pm 0.1 \qquad \text{and} \qquad \frac{g_{\text{m,low}}}{G} = 0.58 \pm 0.01 \tag{2.19}$$

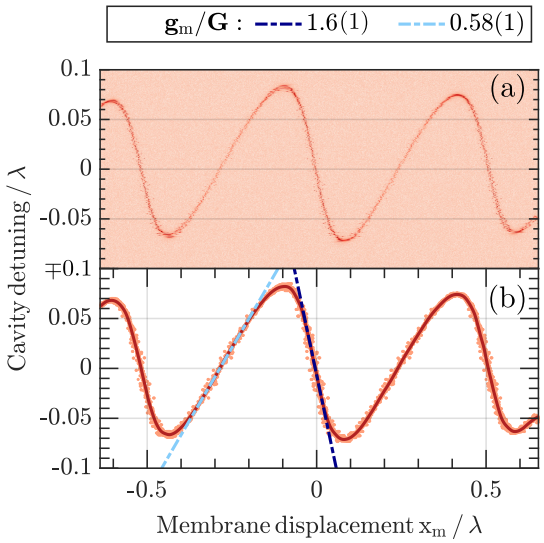

Figure 2.12: Measurement of g_m:
(a) Raw data of the cavity transmission signal for a symmetric scan of both fibers around the resonator with a slow modulation of the cavity detuning. The red shades indicate the cavity transmission (dark corresponds to high transmission) at a resonator position x_m. (b) Extracted resonance curve from upper plot by identifying the points of highest transmission. The optomechanical coupling at each slope is determined by a linear fit (dashed blue lines) through the individual turning points.

[17]The data was recorded with a RTO (*Rohde & Schwarz*): The total measurement time is 40 s at a length of 20 MSa and a sampling rate of 500 kSa/s.

2.3.3 Optical spring effect

In the sections before, we neglected that the resonator position x_m in the intra-cavity field is a dynamic quantity itself [102, 109]. While the resonator motion modulates the cavity frequency with the optomechanical coupling strength $\partial\omega_\mathrm{cav}/\partial x_\mathrm{m}$, pumping the system with a laser that is detuned to the cavity resonance [109] shifts the resonators frequency by $\Delta\omega_\mathrm{m}$. This shift, widely referred to as optical spring effect (OSE), is a consequence of dynamical backaction of the resonator onto itself via the optomechanical coupling g_m. Mathematically the process can be described similarly to feedback cooling[18]. The intra-cavity radiation pressure force influences the susceptibility χ_eff of the resonator yields an altered effective spring constant $k'_\mathrm{m} = m\omega'^2_\mathrm{m} = m(\omega_\mathrm{m} + \Delta\omega_\mathrm{m})^2$ [109]. This frequency shift is linked to a change in the resonators mechanical damping rate by the optomechanical damping rate Γ_opt such that $\Gamma'_\mathrm{m} = \Gamma_\mathrm{m} + \Gamma_\mathrm{opt}$. Dependent on the laser detuning relative to the cavity, Γ_opt can take positive or negative values which comes with optomechanical heating or damping of the resonator. To measure the optical spring effect we tune the cavity close to resonance with the piezo tubes and observe mechanical displacement PSD via lock in detection with our homodyne detection setup (Sec. 2.4). We use the manual scan of our TiSa laser to tune the laser frequency $\Delta = \omega_\mathrm{cav} - \omega_\mathrm{TiSa}$ over a range of up to 40 GHz. For each detuning we measure the frequency shift of the resonator relative to its eigenfrequency and the cavity transmission signal. The transmission curve resembles the resonance of the cavity and is fitted by a Lorentzian curve to determine the cavity linewidth.
The OSE is fitted by equation 2.20 while the optomechanical damping rate can be calculated from equation 2.21 [109]:

$$\Delta\omega_\mathrm{m} = \bar{n}_\mathrm{cav} g_0^2 \left(\frac{\Delta + \omega_\mathrm{m}}{(\Delta + \omega_\mathrm{m})^2 + \kappa^2/4} + \frac{\Delta - \omega_\mathrm{m}}{(\Delta - \omega_\mathrm{m})^2 + \kappa^2/4} \right) \tag{2.20}$$

$$\Gamma_\mathrm{opt} = \bar{n}_\mathrm{cav} g_0^2 \left(\frac{\kappa}{(\Delta + \omega_\mathrm{m})^2 + \kappa^2/4} - \frac{\kappa}{(\Delta - \omega_\mathrm{m})^2 + \kappa^2/4} \right) \tag{2.21}$$

Both quantities scale with the number of intra-cavity photons $\bar{n}_\mathrm{cav}$ and the full width at half maximum (FWHM) cavity linewidth κ. The intra-cavity photon number dependent on the resonator position is expressed by:

$$\bar{n}_\mathrm{cav}(x_\mathrm{m}) = \frac{\bar{n}_\mathrm{cav}^\mathrm{max}}{1 + \left[2(G x_\mathrm{m} + \Delta)/\kappa\right]^2} \tag{2.22}$$

where $\bar{n}_\mathrm{cav}(x_\mathrm{m})$ is the maximum number of photons circulating in the cavity. This implies that the above described effect becomes increasingly relevant for higher finesse optomechanical systems where Γ_opt can exhibit multiple Hz exceeding the mechanical linewidth of the resonator by orders of magnitude. Figure 2.13 shows measurements of the OSE and linewidth for the system with $\mathcal{F}_\mathrm{empty} = 785$ measured at the point of high and low optomechanical coupling[19]. Since the position of the resonator in the cavity

[18] The theory of feedback cooling is described in very detail in previous theses. Thus, it is omitted in this chapter to reduce redundancy. For a detailed description refer to Appendix C and [62, 63, 76].
[19] The corresponding measurement for $\mathcal{F}_\mathrm{empty} = 60$ is presented in Ref.[63].

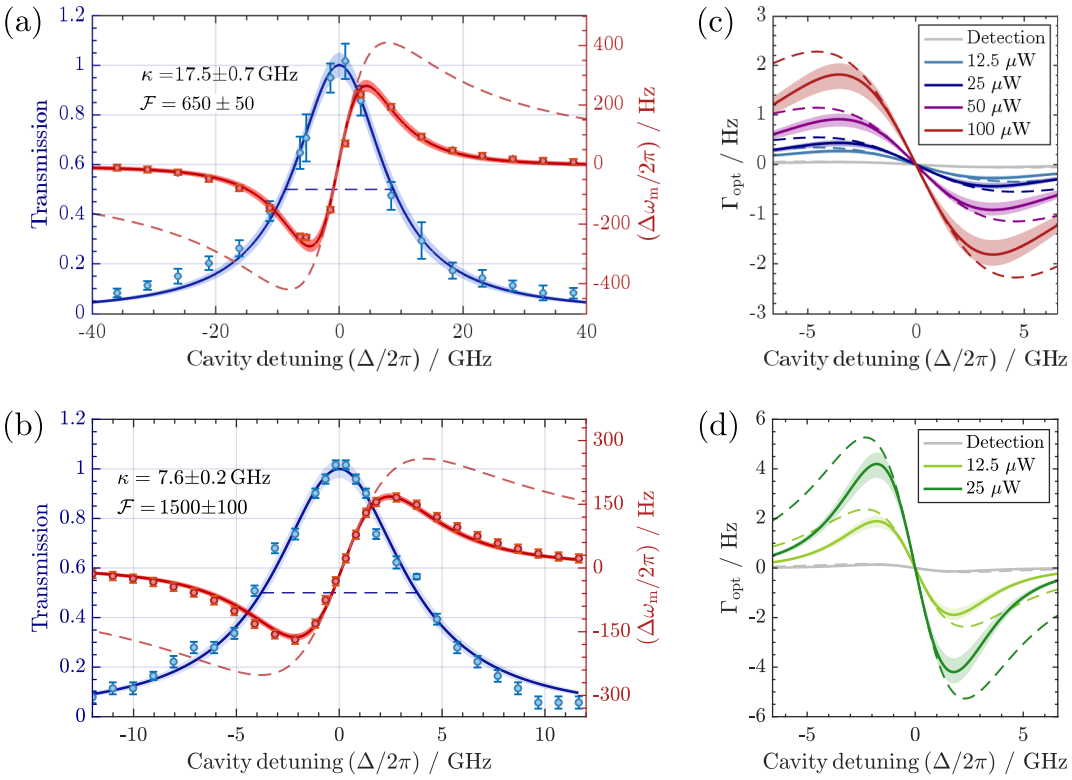

Figure 2.13: Measurement of the optical spring effect:
(a,b) Measurement of the transmission (blue markers) and optical spring effect (red markers) for varying laser-cavity detunings Δ. The transmission curves are fitted with a Lorentzian fit (blue line) while the frequency shifts are fitted with equation 2.20 (red lines). The red dashed lines show the behavior for a constant intra cavity power. The blue dashed line denotes the FWHM of the cavity transmission. (a) Measurement with the resonator aligned to the point of low optomechanical coupling which corresponds to the low finesse adjustment of the cavity. (b) Measurement for the point of high optomechanical coupling.
(c,d) Calculated optomechanical damping rates according to equations 2.21 and 2.25 due to the signal light from the homodyne detection (grey shaded) and for different coupling lattice powers (colored). The measurement for (a,c) was done at $(2.5 \pm 0.5)\,\mu$W signal light. The measurement for (b,d) at $(0.8 \pm 0.2)\,\mu$W. The lighter shades show the 2σ confidence bounds to the fits.

has an influence on the linewidth [104], both working points have a different finesse. From the linewidth measurement and we can determine the systems finesse at a cavity length of $(13.3 \pm 5)\,\mu$m to [107]:

$$\mathcal{F} = \frac{\omega_{\mathrm{FSR}}}{\kappa} = \frac{\pi c}{\kappa L} \quad \text{with} \quad \mathcal{F}_{\mathrm{low}} = 650 \pm 50 \quad \text{and} \quad \mathcal{F}_{\mathrm{high}} = 1500 \pm 100 \tag{2.23}$$

with

$$\kappa_{\mathrm{low}} = 17.5 \pm 0.7\,\mathrm{GHz} \quad \text{and} \quad \kappa_{\mathrm{high}} = 7.6 \pm 0.2\,\mathrm{GHz} \tag{2.24}$$

The optomechanical cooling rate for the system at a given lattice power P_{lat} can be calculated from the previously introduced equations 2.21 and 2.20 by measurement of the optical spring effect[20]. We can use the relation:

$$\frac{\Gamma_{\mathrm{opt,P_{lat}}}}{\Gamma_{\mathrm{opt,P_{HD}}}} = \frac{\Delta\omega_{\mathrm{opt,P_{lat}}}}{\Delta\omega_{\mathrm{opt,P_{HD}}}} \Rightarrow \Gamma_{\mathrm{opt,P_{lat}}} = \Gamma_{\mathrm{opt,P_{HD}}} \frac{\Delta\omega_{\mathrm{opt,P_{lat}}}}{\Delta\omega_{\mathrm{opt,P_{HD}}}} \tag{2.25}$$

In comparison to the old cavity, the optomechanical damping is much stronger. Because of the linear dependency of the optical spring frequency shift upon an incident light power it is possible to extrapolate the optomechanical damping rate of the system for different powers of light that couples into the cavity. While for a light power of $24\,\mu$W [63] the damping rate in the old system was $2\pi \cdot 1.1\,$mHz its equivalent for the new configuration at $\mathcal{F} = 650$ is $2\pi \cdot 640 \pm 50\,$mHz. This not only requires us to operate the system on the optomechanical cooling side at any time, it is also very relevant for hybrid coupling experiments. Because the additional optical damping can be on the same order of magnitude as the sympathetic cooling rate, it has to be accounted for to get comparable measurements of the hybrid cooperativity. According to [101] we can determine a reduced mode temperature of the resonator for an additional damping Γ_{opt} to:

$$T_{\mathrm{mode,opt}} = T_{\mathrm{bath}} \frac{\Gamma_{\mathrm{m}}}{\Gamma_{\mathrm{m}} + \Gamma_{\mathrm{opt}}} \tag{2.26}$$

where T_{bath} denotes the effective bath temperature of the system. This also lead to a reduced initial phonon occupation $\bar{n}$ of the resonator.

$$\bar{n} = \frac{k_{\mathrm{B}} T_{\mathrm{mode}}}{\hbar \omega_{\mathrm{m}}} \tag{2.27}$$

Most of the sympathetic cooling experiments at high coupling lattice powers in Chapter 3 require to operate the system at the point of maximum optomechanical damping. In these measurements we account for the additional damping by using the mode temperature calculated from equation 2.26 as initial system temperature. The optical damping rates for the coupling lattice powers used in Section 3.3 were calculated from the optical spring measurements and are presented in Fig. 2.13 (c,d).

Use of the optical spring lock:
In Ref. [110] the optical spring lock was introduced as a locking scheme to actively stabilize the cavity length in systems with large linewidths. This lock was used for the PAC measurements but not for the hybrid coupling experiments with the cavity presented here since we worked at the point of maximum optomechanical damping, where the slope of the derived error signal is small and the lock unstable.

[20] Assuming a known linewidth κ, detuning Δ and eigenfrequency ω_{m}.

2.4 Detection system

To detect the resonator motion on the quantum level the detection is required to be shot-noise limited and has to offer an exceptionally high signal-to-noise ratio (SNR) [95]. We meet these requirements with coherent, balanced homodyne detection. While conventional optical detection schemes usually acquire information from intensity measurements, coherent detection schemes utilize the mixing of a signal beam with a fixed frequency reference beam (referred to as local oscillator (LO)) to access amplitude and phase quadrature information of the measured signal. The main noise source in these systems is shot-noise introduced by the - usually strong - local oscillator [111] on the photodiode. Furthermore, balanced homodyne detection is insensitive to common-mode noise contributions. Figure 2.14 shows a schematic of the homodyne detection scheme. The signal and LO beams are described by complex field vectors [111], with the real amplitudes A_{SIG}, A_{LO}, their phases ϕ_{SIG}, ϕ_{LO} and their respective optical frequencies ω_{SIG}, ω_{LO}:

$$\vec{E}_{\mathrm{SIG}} = \vec{A}_{\mathrm{SIG}}(t)\exp\left[-\mathrm{i}(\omega_{\mathrm{SIG}}t + \phi_{\mathrm{SIG}}(t))\right] \tag{2.28}$$

$$\vec{E}_{\mathrm{LO}} = \vec{A}_{\mathrm{LO}}(t)\exp\left[-\mathrm{i}(\omega_{\mathrm{LO}}t + \phi_{\mathrm{LO}}(t))\right] \tag{2.29}$$

Both field vectors are mixed with a 2x2 beam splitter resulting in the output fields $\vec{E}_1(t)$ and $\vec{E}_2(t)$. These fields can be calculated from the input fields by the optical transfer function of the splitter with the power-coupling coefficient ϵ [111]:

$$\begin{bmatrix}\vec{E}_1\\ \vec{E}_2\end{bmatrix} = \begin{bmatrix}\sqrt{1-\epsilon} & \mathrm{i}\sqrt{\epsilon}\\ \mathrm{i}\sqrt{\epsilon} & \sqrt{1-\epsilon}\end{bmatrix}\begin{bmatrix}\vec{E}_{\mathrm{SIG}}\\ \vec{E}_{\mathrm{LO}}\end{bmatrix} \tag{2.30}$$

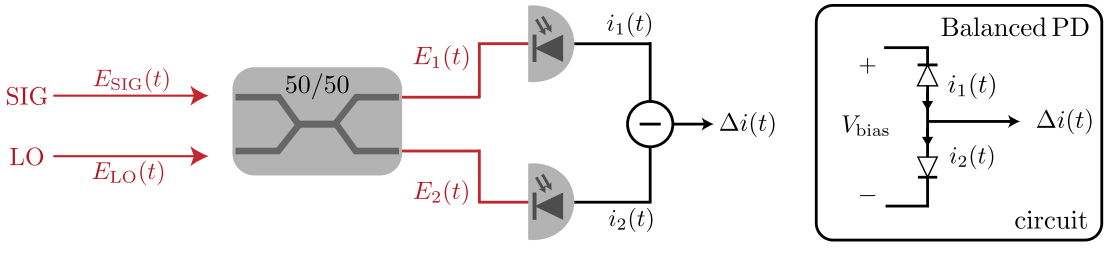

Figure 2.14: Schematic of balanced homodyne detection: A signal beam and a local oscillator beam with the field $E_{\mathrm{SIG}}(t)$ and $E_{\mathrm{LO}}(t)$ are overlapped with a 50/50 beamsplitter. The resulting fields $E_{1,2}(t)$ are directed onto a balanced photoreceiver. Amplitude and phase information are converted into the photodiode currents $i_{1,2}(t)$ that are added to result in the output current $\Delta i(t)$. This current omits direct detection and mixed frequency terms as well as common-mode noise contributions that would occur on a single photodiode coherent detection scheme. Figure based on Ref. [111].

The electronic signal of an interference signal on a single photodiode with responsivity $\mathcal{R}$ is then described by [111]:

$$\begin{aligned} i(t) &= \mathcal{R}\left|\vec{E}_1\right|^2 \\ &= \mathcal{R}\left[(1-\epsilon)\left|A_{\mathrm{SIG}}(t)\right|^2 + \epsilon\left|A_{\mathrm{LO}}\right|^2 + 2\sqrt{\epsilon(1-\epsilon)}\vec{A}_{\mathrm{SIG}}\vec{A}_{\mathrm{LO}}\cos(\omega_{\mathrm{IF}}t + \Delta\phi(t))\right] \end{aligned} \tag{2.31}$$

Here $\omega_{\mathrm{IF}} = \omega_{\mathrm{LO}} - \omega_{\mathrm{SIG}}$ is the frequency difference between the signal and LO beam. The first two terms describe direct detection components. These components are proportional to the power of the respective beams. The third term arises due to the coherent mixing of both beams. Assuming $|A_{\mathrm{SIG}}|^2 \ll |A_{\mathrm{SIG}}A_{\mathrm{LO}}|$ and no LO intensity noise the signal term becomes negligible and the information is contained in the last term which allows to simplify the expression to [111]:

$$i(t) \approx 2\mathcal{R}\sqrt{\epsilon(1-\epsilon)}\cos(\theta)\sqrt{P_{\mathrm{SIG}} \cdot P_{\mathrm{LO}}}\cos(\omega_{\mathrm{IF}}t + \Delta\phi(t)) \tag{2.32}$$

where we used $A = \sqrt{P}$. The term $\cos(\theta)$ arises from the scalar product of the field amplitudes and describes the relative polarization between both fields. The signal $i(t)$ is maximized if $\cos(\theta) = 1$ and the term $2\sqrt{\epsilon(1-\epsilon)}$ is at its maximum. As such, the photo current of the detector is maximized if $\epsilon = 1/2$ and if the polarization between both beam is matched. Under this condition the expression can be further simplified to:

$$i(t) = \mathcal{R}\sqrt{P_{\mathrm{SIG}}(t)P_{\mathrm{LO}}}\cos(\omega_{\mathrm{IF}}t + \Delta\phi(t)) \tag{2.33}$$

In the case of homodyne detection, the signal and LO beam have identical frequencies and $\omega_{\mathrm{IF}} = 0$. Thus, for constant beam powers, the signal becomes purely dependent on the relative phase between both beams.

2.4.1 Noise in homodyne detection

The homodyne detection scheme allows for a phase sensitive low noise measurement of the optomechanical system [93, 112]. The SNR of this detection scheme is dependent on the local oscillator being strong compared to the signal and any other source of noise [93]. The SNR on a single photodiode port relates the received signal $\langle i^2(t)\rangle$ to the thermal $\langle i_{\mathrm{th}}^2\rangle$ and shot noise $\langle i_{\mathrm{sn}}^2\rangle$ contributions [111]:

$$\mathrm{SNR} = \frac{\langle i^2(t)\rangle}{\langle i_{\mathrm{sn}}^2\rangle + \langle i_{\mathrm{th}}^2\rangle} \tag{2.34}$$

where we use [111]:

$$\langle i_{\mathrm{th}}^2\rangle = \frac{4k_{\mathrm{B}}TB_{\mathrm{e}}}{R_{\mathrm{L}}} \qquad \text{and} \qquad \langle i_{\mathrm{sn}}^2\rangle = 2\mathcal{R}\left(\frac{P_{\mathrm{SIG}}(t)}{2} + P_{\mathrm{LO}}\right)B_{\mathrm{e}}\mathrm{e} \tag{2.35}$$

Here e is the elementary charge, B_{e} the electronic bandwidth R_{L} the load resistance and T the detection systems temperature. By using these expressions together with

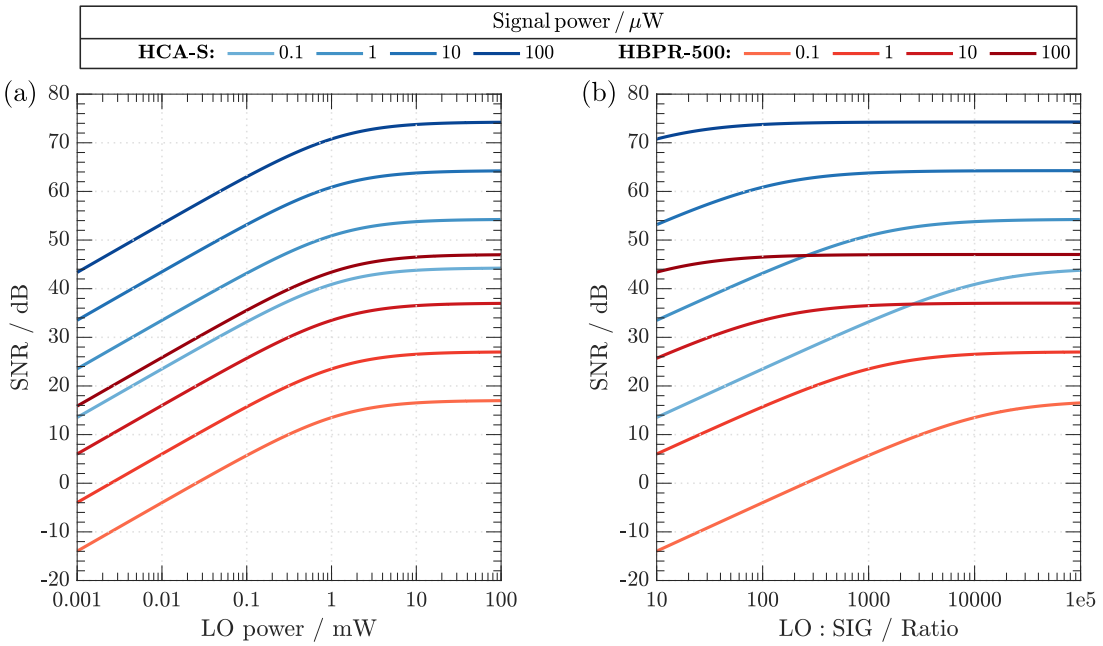

Figure 2.15: SNR in balanced homodyne detection according to equation 2.36:
(a) SNR of the homodyne detection dependent on the LO power. The blue lines show the SNR at different signal beam powers for the 1 MHz *FEMTO HCA-S* that was used for all coupling experiments. The red lines depict the corresponding SNR for the 500 MHz *FEMTO HBPR* which was used for the coupling experiments. (b) SNR of the detection for different ratios between LO and signal beam.
For both simulations the individual quantum efficiencies of the photodiodes $\eta_{\mathrm{HCA-S}} = 0.86$ and $\eta_{\mathrm{HBPR}} = 0.81$ as well as a load resistance of $R_{\mathrm{L}} = 50\,\Omega$ and a temperature of $T = 295\,\mathrm{K}$ were used. The simulation neglects polarization fluctuations and assumes a fixed phase relation at $\Delta\phi = \pi$ between both beams and a shot noise limited detection.

equation 2.33 and inserting them into equation 2.34 we obtain the SNR for an optical homodyne detection setup:

$$\mathrm{SNR}_{\mathrm{HD}} = \frac{1}{B_{\mathrm{e}}} \cdot \frac{R_{\mathrm{L}}}{4k_{\mathrm{B}}T} \cdot \frac{\mathcal{R}^2 P_{\mathrm{SIG}}(t) P_{\mathrm{LO}}}{2\mathrm{e}\mathcal{R}(P_{\mathrm{SIG}}/2 + P_{\mathrm{LO}})} \tag{2.36}$$

This expression allows for an estimation of the necessary detection setup parameters for the different experiments that are presented in this thesis. While the coupling experiments in Chapter 3 were conducted with a 1 MHz balanced photoreceiver[21], the pulsed experiments require for much larger bandwidths which made the use of a 500 MHz balanced photoreceiver[22] necessary. Figure 2.15 depicts an overview plot for the detection SNR for the different detector configurations. Due to the much higher bandwidth and lower quantum efficiency, the SNR of the 500 MHz detection setup is 27 dB lower that the 1 MHz setup when using the same operating parameters. Both systems benefit from a large ratio between the LO and signal beam power. For most of the configurations, the SNR is barely improving for ratios above 2000:1. While for the HCA-S

[21] *FEMTO HCA-S*
[22] *FEMTO HBPR-500-FST*

configuration, in principle every simulated combination exhibits SNR > 1, the setup using the HBPR-500 requires at least a ratio of 300:1 at 100 nW signal beam power to fulfill this requirement. The maximum possible ratio is limited by the damage threshold of the used photodetectors. Thus, the set LO:SIG ratios in the presented experiments differ between 2000:1 and 15000:1.

Balanced homodyne detection:
In the previous section we assumed the direct detection components to be negligible and the LO to be free of intensity noise. In a real experiment, this assumption does not hold. Large LO powers can be linked to intensity fluctuations that introduce noise to the system and the direct detection components can overlap and interfere with the coherent detection of the system. To overcome these limitations and reduce the noise further, the homodyne detection is balanced as depicted in Fig. 2.14. Assuming an optimal configuration with $\epsilon = 1/2$, $\omega_{\mathrm{IF}} = 0$ and equal polarization, the beams can be described by their respective field amplitudes [112]:

$$A_{\mathrm{SIG}}(t) = A_{\mathrm{SIG}} + \delta Q_{\mathrm{SIG}}(t) + \mathrm{i}\delta P_{\mathrm{SIG}}(t) \tag{2.37}$$

$$A_{\mathrm{LO}}(t) = \left[A_{\mathrm{LO}} + \delta Q_{\mathrm{LO}}(t) + \mathrm{i}\delta P_{\mathrm{LO}}(t)\right] e^{\mathrm{i}\phi_{\mathrm{LO}}} \tag{2.38}$$

where δQ and δP describe the amplitude and phase quadrature. As discussed in the previous section, the detection benefits from large power ratios. Assuming $A_{\mathrm{LO}}^2 \gg A_{\mathrm{SIG}}^2$ the intensities on both detectors can be treated as equal:

$$\begin{aligned} A_1 &= \sqrt{\frac{1}{2}} A_{\mathrm{LO}}(t) + \sqrt{\frac{1}{2}} A_{\mathrm{SIG}}(t) \\ A_2 &= \sqrt{\frac{1}{2}} A_{\mathrm{LO}}(t) - \sqrt{\frac{1}{2}} A_{\mathrm{SIG}}(t) \end{aligned} \tag{2.39}$$

From this representation we calculate the resulting photocurrents $i_1(t)$ and $i_2(t)$ on the detectors

$$i_1(t) = |A_1|^2 = \frac{1}{2}\left(|A_{\mathrm{LO}}(t)|^2 + |A_{\mathrm{SIG}}(t)|^2 + A_{\mathrm{LO}}(t)A_{\mathrm{SIG}}^*(t) + A_{\mathrm{LO}}^*(t)A_{\mathrm{SIG}}(t)\right) \tag{2.40}$$

$$i_2(t) = |A_2|^2 = \frac{1}{2}\left(|A_{\mathrm{LO}}(t)|^2 + |A_{\mathrm{SIG}}(t)|^2 - A_{\mathrm{LO}}(t)A_{\mathrm{SIG}}^*(t) - A_{\mathrm{LO}}^*(t)A_{\mathrm{SIG}}(t)\right) \tag{2.41}$$

The resulting balanced detector signal is:

$$\Delta i(t) = i_2(t) - i_1(t) = \frac{1}{2}\left(-2A_{\mathrm{LO}}(t)A_{\mathrm{SIG}}^*(t) - 2A_{\mathrm{LO}}^*(t)A_{\mathrm{SIG}}(t)\right) \tag{2.42}$$

Using the expressions 2.37, 2.38 and omitting terms similar to $A_{\mathrm{LO}}A_{\mathrm{SIG}}^*$ and $A_{\mathrm{SIG}}\delta Q^*$ these equations transform to [112]:

$$\Delta i(t) \approx 2A_{\mathrm{LO}}\left(\delta Q_{\mathrm{SIG}}(t)\cos(\phi_{\mathrm{LO}}) + \mathrm{i}\delta P_{\mathrm{SIG}}(t)\sin(\phi_{\mathrm{LO}})\right) \tag{2.43}$$

This detection scheme omits the direct detection terms since they are common mode on both photodiodes. The mixed term becomes dominant. Expression 2.43 shows the remaining contributions to the overall homodyne signal. Besides a term that originates from the mixing of signal and LO, it is mainly dependent on the strength of the LO beam A_{LO} and the amplitude or phase quadrature of the signal beam. Which of these components is measured depends on the chosen phase $\Delta\phi$. In our experiment, the resonator modulates the phase quadrature δP_{SIG}. Thus, according to equation 2.43 the phase is locked at $\Delta\phi = \pi/2$.

The measurements conducted on the resonator separate into weak, continuous and strong, projective measurements. For weak measurements the disturbance of the system due to the measurement is minimal at the cost of a lower information gain about the system state [113]. Strong projective measurements allow for an almost arbitrarily precise measurement of one system observable at the cost of the state destruction [113]. The effects of introducing back-action noise into the system by a strong measurement opposed to the increase of imprecision noise by a weak measurement form the SQL as depicted in Fig. 2.16. For continuous measurements, an optimum in detection accuracy can be reached if the combination of imprecision noise and backaction noise is minimized. The SQL is a direct consequence of the fundamental Heisenberg limit [114]. In Chapter 4 we present a back-action evading QND measurement technique [59, 72, 114] that allows to surpass the SQL by utilizing very short, intense measurement pulses on the timescale of the cavity linewidth. This technique maximizes the ratio between the information gain of a single measurement and the introduced back-action noise. For these considerations to hold the detection has to be shot-noise limited.

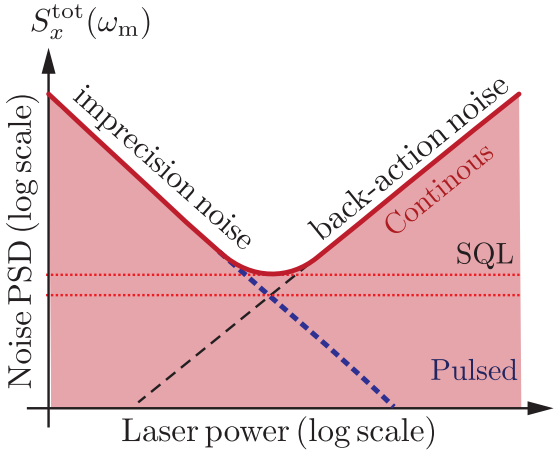

Figure 2.16: The SQL of displacement sensing:
Noise PSD $S_x^{\mathrm{tot}}(\omega_{\mathrm{m}})$ of a mechanical oscillator with eigenfrequency ω_{m}.
The standard quantum limit is defined at the point where the introduced imprecision noise at low detection powers is equal to the backaction noise that arises from the measurement itself. The backaction noise can be minimized in a pulsed measurement scheme which allows to beat the SQL.

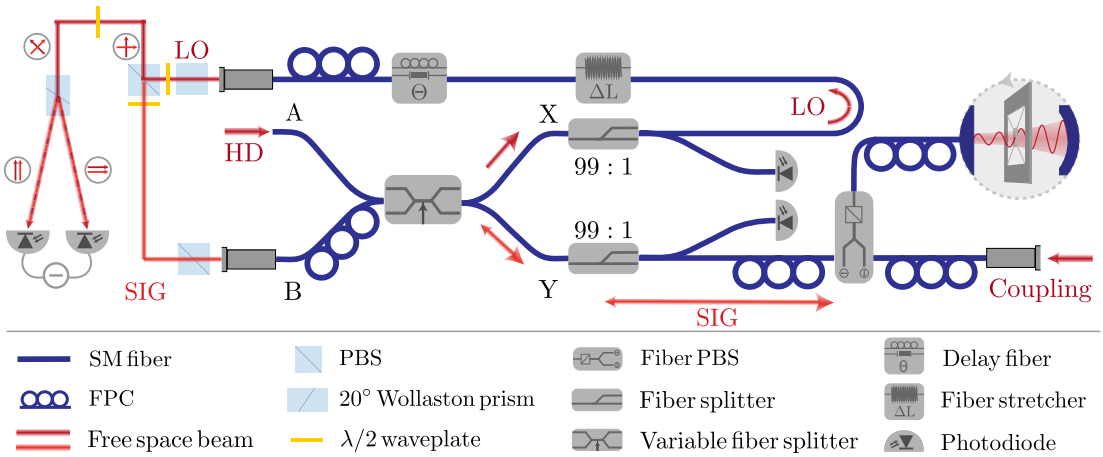

Figure 2.17: Sketch of the modified homodyne detection setup for hybrid coupling experiments: Light from the homodyne detection branch (HD) is coupled into a variable fiber beamsplitter (*Evanescent Optics Model-905-SM*) that splits the light into an LO (port X) and signal branch (port Y) at a ratio between 2000:1 and 15000:1. The power in both branches is monitored by a photodiode (*Thorlabs PD36A*) where the LO branch PD is used for intensity regulation. This allows us to set the splitting ratio independently of the set LO power. The signal beam is coupled into the cavity with perpendicular polarization to the coupling beam. It is reflected from the cavity travelling the same path backwards and is outcoupled at port B. Here the losses at the beamsplitters are small due to the large splitting ratios ($R_{\mathrm{loss}} \approx 1\%$). The LO beam is delayed by a fiber that compensates for the path length difference between the two branches and a home-built fiber stretcher that is used as a high bandwidth phase-lock. The polarization of both signal and LO beam is cleaned by a PBS. Both beams are overlapped at perpendicular polarization and directed onto a balanced photoreceiver through a $\lambda/2$ waveplate in a high precision rotation mount and a 20° Wollaston prism. The respective polarization states are shown in the sketch. To achieve excellent mode match, both outcouplers (*Schäfter & Kirchhoff FC60-4-M12-37*) are of the same production batch. FPCs are placed in front of every polarization selective element. Splices are omitted in this figure.

2.4.2 Fiber based homodyne detection setup

The considerations made above define the requirements on the detection. Particularly for the pulsed measurements it is necessary to work at high power ratios between signal and LO beam (refer to Fig. 2.15). Furthermore, an excellent mode match between both beams, spatially and in the time domain, is required. The continuous operation at higher cavity finesses requires working with much lower signal beam powers while the detection has to remain shot-noise limited. Based on these considerations and experiences in other groups [115], we set up a new detection system design using a mainly fiber components. A setup sketch for hybrid coupling experiments is depicted in Fig. 2.17[23]. The use of free space components was heavily reduced compared to the previous setup [63][24]. This comes at an advantage of a much higher passive stability once the system is set up. The use of a variable fiber splitter allows to set the ratio between the LO and signal branch arbitrarily high without requiring for any re-coupling. The pathlength compensation is seamlessly integrated in the LO branch.

[23] The version modified for pulsed experiments is introduced in Chapter 4.
[24] For details on the previous setup refer to Appendix A.1.

Detection system	η_{HD}	$\eta_{det,780}$	Total losses η_{loss}	$\mathcal{V}^2$ [%]
Free space HCA-S (old, hybrid)	0.56-0.6	0.86	0.72	95-99
Free space HBPR 500 (old, pulsed)	0.53-0.57	0.81	0.72	95-99
Fiber based HCA-S (hybrid)	>0.47	0.86	0.56	>99
Fiber based HBPR 500 (pulsed)	>0.52	0.81	0.66	>99

Table 2.2: Detection efficiency for different setups:
Comparison of the detection properties for the setups used in this thesis regarding losses, quantum efficiency and visibility. The total losses η_{tot} are the accumulated losses on the path between the cavity and the last PBS in front of the detector. $\eta_{HD,780}$ denotes the quantum efficiency of the detector at 780 nm. And $\eta_{HD} = \mathcal{V}^2\eta_{det,780}\eta_{loss}$ the detection efficiency.

It can be accurately dimensioned by choosing the according fiber length which reduces the losses in this branch over the previous setup by 25%. A home-built fiber stretcher phaselock allows for an estimated 40 times higher bandwidth than in the previous setup ($B_{FS} = 4\,\text{kHz}$, refer to Appendix B.2) and can be operated at low voltages ($U_{lock} \approx 1 V_{PP}$). Since the used outcouplers and corresponding fibers are of the same type and batch, the mode match between both branches is inherently optimized yielding a constantly high visibility of $\mathcal{V} > 99\%$[25].

The new detection setup is shot-noise limited over the full range of feasible measurement parameters. Beginning at a LO power of 20 mW (recommended maximum optical power) and a splitting ratio of 5000:1 ($P_{SIG} = 4\,\mu\text{W}$) we measure the detection noise floor in the range between 150 and 160 kHz for varying LO powers. Figure 2.18 shows the noise floor averaged over 10 traces for the respective signal and LO powers. The old setup showed classical effects to be dominant above an LO power of 11 mW [62]. The new system allows for operating the detection at higher LO powers which improves the SNR.

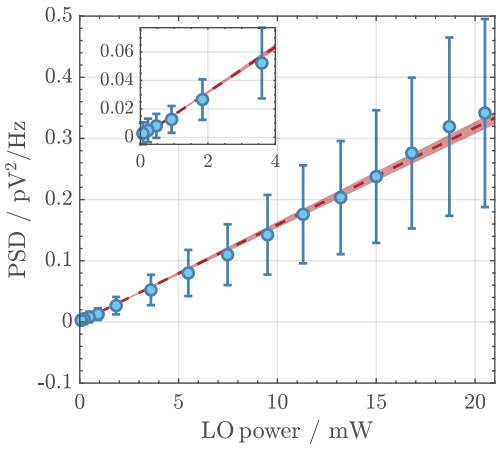

Figure 2.18: Noisefloor dependent on LO power for FEMTO HCA-S:
Noise floor power spectral density (PSD) for different LO powers at a LO:SIG beam power ratio of 5000:1. For a locked phase at $\Delta\phi = \pi/2$, the noise floor PSD between 150 kHz and 160 kHz was measured via lock-in detection. Each datapoint consists of a 10 times averaged spectrum. The optomechanical system was kept off-resonant.
The PSD is linearly dependent on the LO power over the whole range of chosen powers ($P_{LO,min} = 74\,\mu\text{W} - P_{LO,max} = 20.5\,\text{mW}$). This indicates a shot noise limited detection for all LO powers at this ratio.

[25] Here we use the definition $\mathcal{V} = \frac{VIS_{meas}}{VIS_{theo}}$ with $VIS_{meas} = \frac{I_{max}-I_{min}}{I_{max}+I_{min}}$ and $VIS_{theo} = \frac{2\sqrt{I_{SIG}I_{LO}}}{I_{SIG}+I_{LO}}$.

A comparison between the individual detection efficiencies and interference contrasts (visibilities) is presented in Table 2.2. Although we find advantages to this new setup, there are drawbacks regarding the detection efficiency. This can be accounted to losses in the splices of the fiber optical components, some of which were only available with specific fiber types, and the need of additional polarization filter optics to compensate for noise arising due to the long fiber lengths. Nonetheless, the improvements outweigh the disadvantages, particularly for the pulsed experiments[26].

2.4.3 Homodyne calibration

The homodyne detection output is a voltage signal U_{HD} that relates to the resonator displacement x_{m} via a calibration factor $c_{\mathrm{HD}} = \partial U_{\mathrm{HD}}/\partial x_{\mathrm{m}}$. This quantity is dependent on the alignment of the optomechanical system and the cavity linewidth [57]:

$$c_{\mathrm{HD}} = \frac{\partial U_{\mathrm{HD}}}{\partial x_{\mathrm{m}}} = \underbrace{\frac{\partial \omega_{\mathrm{cav}}}{\partial x_{\mathrm{m}}}\frac{\partial \phi_{\mathrm{x}}}{\partial \omega_{\mathrm{cav}}}}_{\text{(A)}}\underbrace{\frac{\partial U_{\mathrm{HD}}}{\partial \phi_{\mathrm{x}}}}_{\text{(B)}} \tag{2.44}$$

Expression (A) is determined by effectively changing the resonator position x_{m} in the intra-cavity field and recording the frequency response. Both cavity mirrors are scanned symmetrically and in phase around the resonator. The intensity of the reflection signal from the cavity is recorded and fitted with the relation for the cavity resonance with the cavity mirror reflectivities R_1 and R_2 as free fit parameters [57]:

$$I_{\mathrm{ref,norm}}(x_{\mathrm{m}}) = \left| \frac{\sqrt{R_1} - e^{4\pi \mathrm{i} x_{\mathrm{m}}}\sqrt{R_2}}{1 - e^{4\pi \mathrm{i} x_{\mathrm{m}}}\sqrt{R_1 R_2}} \right|^2 \tag{2.45}$$

The determined reflectivities are used to calculate the phase response ϕ_{x}:

$$\phi_{\mathrm{x}} = \mathrm{Im}\left(\sqrt{R_1}\frac{e^{4\pi \mathrm{i} x_{\mathrm{m}}}(1-R_1)\sqrt{R_2}}{e^{4\pi \mathrm{i} x_{\mathrm{m}}}\sqrt{R_1 R_2} - 1} \right) \tag{2.46}$$

The global maximum of the derivative of this expression yields the calibration factor $\partial\phi_{\mathrm{x}}/\partial x_{\mathrm{m}}$. Measurements of this quantity are depicted in Fig. 2.19 for all used experimental configurations in this thesis. Towards higher finesses the calibration factor increases due to the reduction of the cavity linewidth. Furthermore, the position of the resonator inside the cavity has a large impact on the calibration since it also influences the cavity linewidth.

$\mathcal{F}$	σ_{on}	$c_{\mathrm{HD},\mathcal{F}}$ / $\frac{\mathrm{rad}}{\mathrm{nm}}$
140	0.53 ± 0.01	0.56 ± 0.01
650	0.82 ± 0.02	4.4 ± 0.2
1500	0.65 ± 0.01	12.2 ± 0.5
14500	0.20 ± 0.04	170 ± 40

Table 2.3: Homodyne calibration for different fiber cavities:
Overview of the reflectivity on resonance and homodyne calibration factor. The small reflectivity on resonance of the high finesse cavity is discussed in more detail in Chapter 4.

[26] The modified setup for the pulsed measurements is discussed in Section 4.2.3.

It is worth noting that the properties of the higher finesse cavities are much more sensitive to slight deviations in alignment.
Most of the measurements in this thesis are conducted at room temperature. Thus, the quantity $\partial\phi_\mathrm{x}/\partial x_\mathrm{m}$ cannot be considered as a fixed quantity and is determined on a daily basis. Expression (B) in equation 2.44 is determined by scanning the LO phase relative to the signal beam. This creates a sinusoidal signal with a peak-to-peak voltage U_PP where the slope at the turning points of the signal is given via $\partial U_\mathrm{HD}/\partial\phi_\mathrm{x} = U_\mathrm{PP}/2$. This signal critically depends on the mode match between signal and LO beam, the general alignment and the used detector. Like the previous quantity, this signal is optimized and measured on a daily basis. Using this expression, the homodyne calibration yields:

$$\frac{\partial U_\mathrm{HD}}{\partial x_\mathrm{m}} = \frac{\partial\phi_\mathrm{x}}{\partial x_\mathrm{m}} \cdot \frac{U_\mathrm{PP}}{2} \tag{2.47}$$

Additionally, we measure the reflectivity on resonance of the system. The properties and resulting calibration factors of each system are presented in Table 2.3[27].

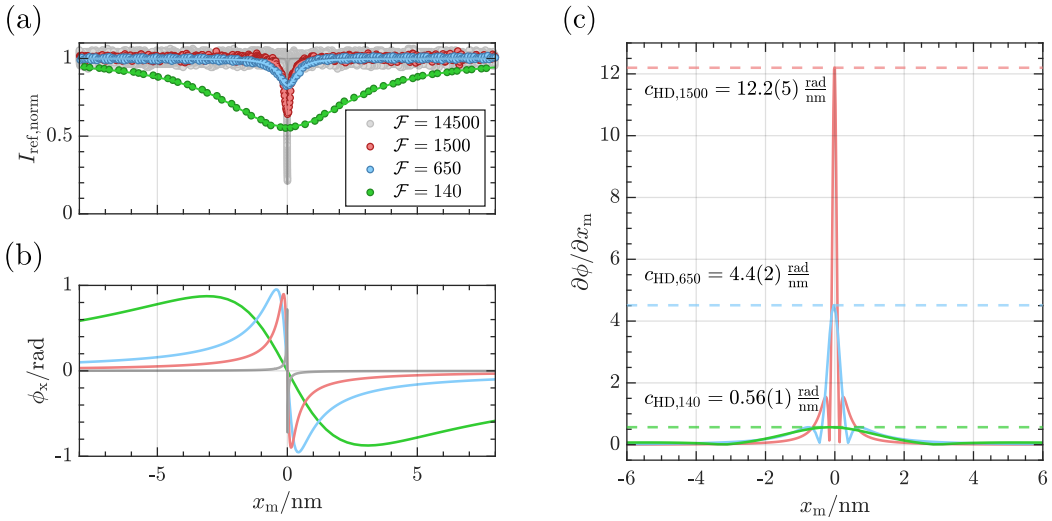

Figure 2.19: Calibration measurements for different cavity configurations: (a) Normalized reflection signal for a symmetric scan of the cavity mirrors around the membrane. The solid lines show the fit of equation 2.45 with the reflectivities R_1 and R_2 as free fit parameters. (b) Calculated phase ϕ_x from the previously acquired reflectivities according to equation 2.46. (c) Derivative $\partial\phi_\mathrm{x}/\partial x_\mathrm{m}$. The global maximum yields the phase change per membrane displacement at the turning point and determines the homodyne calibration. The red ($\mathcal{F} = 650$) and blue ($\mathcal{F} = 1500$) curves are measured for the same cavity but at different positions of the resonator in the intra-cavity field. The calibration curve of the cavity at $\mathcal{F} = 14500$ is omitted for better overview and yields $c_\mathrm{HD,15k} = (170 \pm 40)\ \frac{\mathrm{rad}}{\mathrm{nm}}$. A comparison between all systems is concluded in Table 2.3.

[27]The shown values are examples in that they have the correct order of magnitude. Due to daily drifts of the system they differ between the individual measurements presented in this thesis.

Overview over the different experimental systems

During this thesis experiments with three different cavities were conducted:

- The cavity with $\mathcal{F}_{\text{empty}} = 60$ from Ref. [57] was used for experiments on pump-asymmetry-compensation (PAC).
- The cavity with $\mathcal{F}_{\text{empty}} = 785$ was used for new hybrid coupling experiments where the positioning of the resonator in the intra-cavity field allowed for operation at two different finesses.
- The cavity with $\mathcal{F}_{\text{empty}} = 14500$ was exclusively used for pulsed measurements and operated at cryogenic temperatures.

Further optomechanical properties of the systems are concluded in Appendix B.1.

2.5 Production and characterization of high finesse fiber cavities

The cavities used in this thesis were produced at this experiment and coated externally dependent on the needed cavity properties. The cavities at $\mathcal{F}_{\text{empty}} = 785$ were produced during Ref. [67]. The pulsed measurements require for an even for higher finesse. Thus, we produced another batch of fiber cavities while aiming for the highest finesse ($\mathcal{F}_{\text{empty}} = 14500$) that is technically feasible in this configuration. The setup used for the cavity production is described in Refs. [67, 100]. When starting the production of the new cavities the previously used CO_2 laser[28] malfunctioned due to degradation of the laser-medium gas[29]. This chapter focuses on the design considerations and the characterization of the produced cavities.
We require a high finesse at a high reflectivity on resonance, to get as much information from a single measurement of the resonator as possible. Both the finesse $\mathcal{F}$ and the field reflectivity on resonance $\bar{\rho}$ of the system[30] can be defined by the total losses in the system. Assuming these losses to be only caused by the finite reflectivities of the cavity mirrors, they can be calculated to [116]:

$$\mathcal{F} = \frac{\pi (R_1 R_2)^{1/4}}{1 - \sqrt{R_1 R_2}} \tag{2.48}$$

$$\bar{\rho} = \frac{\sqrt{R_1} - \sqrt{R_2}}{1 - \sqrt{R_1 R_2}} \qquad \bar{\rho} \in [-1, 1] \tag{2.49}$$

Modern coating techniques allow for excellent reflectivities at losses below 10 ppm [117], given the right surface conditions. The most demanding task for our configuration is achieving a good mode match between the fiber guided light mode and the cavity mode [118, 119]. Since there are no additional optics available, the parameters of the

[28] *Access Laser AL30*
[29] For a characterization the replacement laser (*Coherent Diamond C20*) refer to Appendix B.5.
[30] The quantity $\bar{\rho}$ is not to be confused with the reflectivity on resonance $\rho = |\bar{\rho}|^2$.

outcoupling concave fiber mirror have to be optimized to recouple into the fiber mode with high efficiency. The influence of the mode match onto the reflectivity on resonance is critical and has been investigated thoroughly in Ref. [119]. Assume a light field ψ_i in a glass fiber. This field consists of a part that is mode matched with the cavity mode ψ_mm and a part ψ_nm that is not, according to the coefficients $\beta_{1,2}$:

$$\psi_\mathrm{i} = \beta_1\psi_\mathrm{mm} + \beta_2\psi_\mathrm{nm} \qquad \text{with} \qquad \sum\nolimits_i \beta_\mathrm{i} = 1 \tag{2.50}$$

The overlap integral yields the mode match parameter β [119]:

$$\beta = |\bar{\beta}_1| = |\bar{\beta}_2| - 1 \qquad \beta \in [0,1] \tag{2.51}$$

Perfect mode match corresponds to $\beta = |\bar{\beta}| = 1$. For a real system the mode match will always be $\beta < 1$ due to the tolerance in the production of concave profiles and in alignment. A smaller mode match leads to interference effects between the different field components in the cavity thus reducing the reflected signal of the cavity σ:

$$\sigma = |1 - \beta + \bar{\rho}\beta|^2 \tag{2.52}$$

In the other chapters the reflected signal from the cavity σ is referred to as the "reflectivity on resonance". This quantity includes the influence of the reduced mode match parameter β. The parameter ρ describes the reflectivity on resonance for an idealized system with $\beta = 1$.

Optimizing the mode match

The mode match for a plano-concave cavity with length L and a curved mirror radius of curvature r_2 is maximized, if the mode-field diameters of the fiber and the cavity mode perfectly overlap at the surface of the incoupling fiber. This condition can be expressed via [119]:

$$\beta_\mathrm{PC} = \beta(L, r_2) = \frac{4}{\mathrm{w}_0(L, r_2)/\mathrm{w_f} + \mathrm{w_f}/\mathrm{w}_0(L, r_2)} \tag{2.53}$$

where $\mathrm{w_f}$ is the mode-field radius of the fiber and $\mathrm{w}_0(L, r_2)$ the diameter of the cavity mode at the incoupling mirror. They are calculated via [119]:

$$\mathrm{w}_0(L, r_2) = \sqrt{\frac{r_2\lambda}{\pi}}\left[\frac{L}{r_2}\left(1 - \frac{L}{r_2}\right)\right]^{1/4} \tag{2.54}$$

The mode-field radius of the used fibers[31] is $\mathrm{w_f} = (2.85 \pm 5)\,\mu$m. From the condition $\mathrm{w_f} = \mathrm{w}_0$ we can deduct the optimum radius of curvature for the concave fiber mirror which is [119]:

$$r_2 = \mathrm{w_f}^2\frac{2\pi}{\lambda} \qquad \text{which yields} \qquad r_{2,\mathrm{opt}} = (65.4 \pm 1.5)\,\mu\mathrm{m} \tag{2.55}$$

[31] We use copper coated CU800 fibers from *IVG fibers*. These fibers are well suited for low loss coatings which require to use materials that do not gas out in the coating facilities.

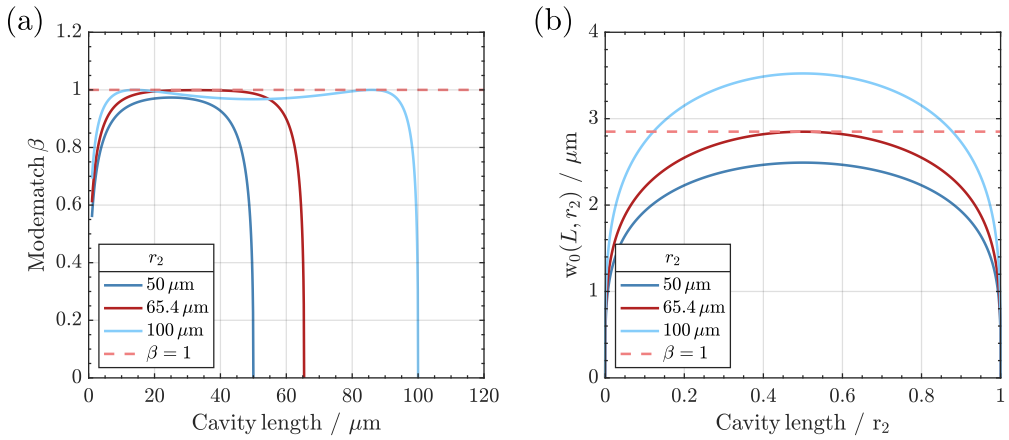

Figure 2.20: Calculations on optimal mode match:
(a) Mode match dependent on the cavity length (Eq. 2.53) for different radii of curvature r_2. (b) Mode-field radius of the cavity mode $w_0(L, r_2)$ (Eq. 2.54) for different cavity lengths in units of r_2. Optimal mode match is achieved if $w_f = w_0$. The blue lines denote radius of curvature below (dark shade) and above (light shade) the optimal value. The red curve shows the optimal ROC for this system. The dashed red line always marks the point where $\beta = 1$.

It is a property of the used fiber and can be determined by measuring the divergence of the outcoupled light in the far-field. Figure 2.20 shows the impact of the right choice of r_2 and the cavity length L on the mode match. While a too small r_2 makes it theoretically impossible to achieve $\beta = 1$, hitting the optimal ROC yields perfect mode match of the whole possible range of cavity lengths. Furthermore, Fig. 2.20(b) shows that the change of the cavity mode-field radius dependent on the length at an optimum ROC is lowest for $L = r_2/2$. Setting the cavity to this length yields the highest stability. The considerations made above assume a spherical concave cavity mirror profile.

As discussed in Refs. [91, 100], this assumption does not hold for the profiles made at this experiment. Due to the use of a CO_2 laser that is focused on the fiber end to ablate material, the shape of the profiles resembles a Gaussian curve. The Gaussian geometry influences the mode match of the system. In Refs. [91, 100] the Fourier transform code OSCAR, which allows to simulate the propagation of arbitrary light fields and effects of optical components, was used to investigate the effect of the Gaussian geometry on the mode match. It was found that deep profiles of multiple micrometer benefit a higher mode match. The geometry of the Gaussian profile in the center region is close to a spherical profile. Thus, r_2 is defined by the ratio between the profile width b and the depth a [118]:

$$r_2 = \frac{b^2}{4a} \tag{2.56}$$

For deeper profiles this region is larger. Thus, we aim for deep profiles with $a > 1.5\,\mu$m

The influence of surface roughness

Another parameter to consider when designing high finesse cavities is the surface roughness σ_{rms} of a processed fiber which limits the maximum achievable reflectivity of a coating. A high surface roughness leads to losses due to stray light at the contact region between the fiber surface and the coating. The relation between a minimum achievable transmission losses $T(\sigma_{\mathrm{rms}})$ and the surface roughness has been investigated in Ref. [120] and holds:

$$T(\sigma_{\mathrm{rms}}) = 1 - \exp\left[\frac{-4\pi\sigma_{\mathrm{rms}}^2}{\lambda^2}\right] \tag{2.57}$$

The surface roughness of a processed fiber limits the maximum achievable reflectivity and thus the maximum achievable finesse. We consistently achieve roughness values of $\sigma_{\mathrm{rms}} < 0.3\,\mathrm{nm}$. Figure 2.21 shows the requirements on the surface roughness to achieve certain reflectivities. The roughness of the processed cavities allows for for a low loss coating with $T = 30\,\mathrm{ppm}$ which corresponds to $R = 99.997\,\%$. Aiming for a reflectivity on resonance of $\rho > 0.85$ we can use equations 2.48 and 2.49 to calculate the necessary reflectivities R_1, R_2 and the resulting finesse $\mathcal{F}$ of the new cavity to:

$$R_{\mathrm{high}} = 99.997\,\% \qquad R_{\mathrm{low}} = 99.96\,\% \qquad \text{and} \qquad \mathcal{F} \approx 15000 \tag{2.58}$$

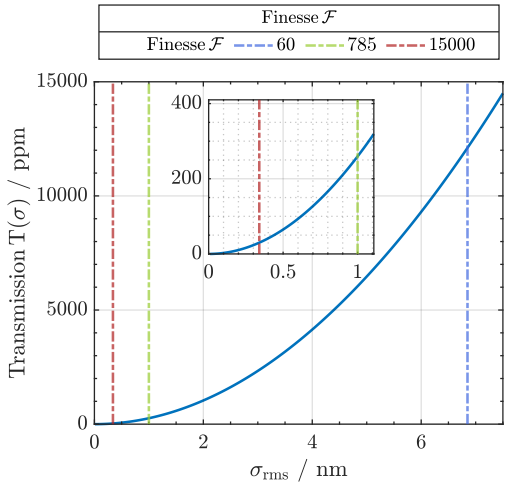

Figure 2.21: Influence of surface roughness:
Plot of the maximum achievable coating transmission in ppm dependent on the surface roughness according to equation 2.57. The dashed vertical lines show the surface roughness requirements for the high reflective coatings of the different cavities used throughout this thesis. The red dashed line corresponds to the surface roughness we measured with an AFM during Ref. [67] on a fiber that was processed by multiple laser pulses.

Characterization of the new cavities

In this thesis two newly produced fiber cavities were used. Based on the considerations made before, we aimed for deep profiles ($a > 1.5\,\mu$m) with good circular symmetry and a radius of curvature close to the theoretical optimum. In Ref. [67] 12 curved fiber mirrors and 7 plane fiber mirrors were produced and coated[32]. In this thesis we produced 18 curved fibers mirrors and 15 plane mirrors[33]. For all single mode fibers the CU800 from *IVG fibers* was used.

To achieve higher cavity transmission for the pulsed experiments we also produced 5 of the curved profiles with multi-mode fibers (*IVG fibers* CU 100/110). A complete overview of the achieved reflectivities on resonance and finesses can be seen in Appendix B.5. Within one batch the achieved cavity finesses and reflectivities on resonance (all 18 curved fibers were paired with the same plane fiber) between the individual fibers differ by up to 6 %. These differences are likely not caused by different reflection properties of the coatings but due to varying mode match of the different cavities that occurs due to the tolerances (e.g. pulse power, alignment) during the manufacturing process. We choose the combination of plane and curved fiber mirrors that exhibits the highest reflectivity on resonance for both cavities for our experiments. The measurements presented in this chapter refer to these cavities.

Figure 2.22 shows an interferogram of the fiber facet, where one fringe corresponds to a height difference of 325 nm.

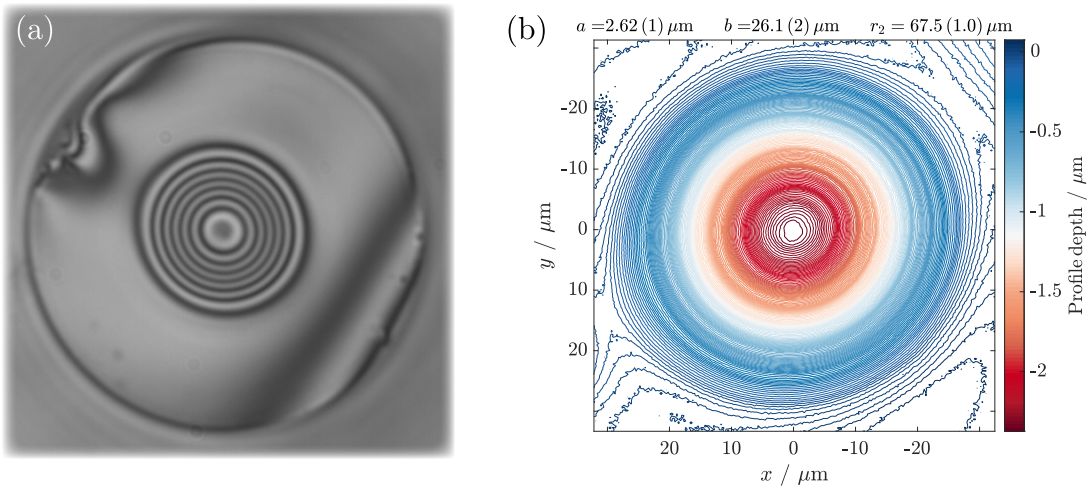

Figure 2.22: Profile analysis of a curved cavity fiber:
(a) Interferogram of a fiber facet that was prepared by multiple CO2 laser pulses. One interference fringe (black to black) corresponds to a height difference of 325 nm. (b) Profile evaluation using a phase shifting interferometry (PSI) algorithm. The plot shows a 2D Gaussian fit onto the profile depicted in (a). The image and the analysis are from the curved mirror of the $\mathcal{F}_{\mathrm{emtpy}} = 785$ cavity used for the new coupling experiments. $r_2 = 67.5\,\mu$m is close to $r_{\mathrm{opt}} = 69.5\,\mu$m. The image for the $\mathcal{F}_{\mathrm{emtpy}} = 14500$ cavity is presented in Appendix B.5.

[32] Coating by *LASEROPTIK* with $R_{\mathrm{high}} = 0.9997$ and $R_{\mathrm{low}} = 0.9925$.
[33] Coating by *LAYERTEC* with $R_{\mathrm{high}} = 0.99997$ and $R_{\mathrm{low}} = 0.9996$.

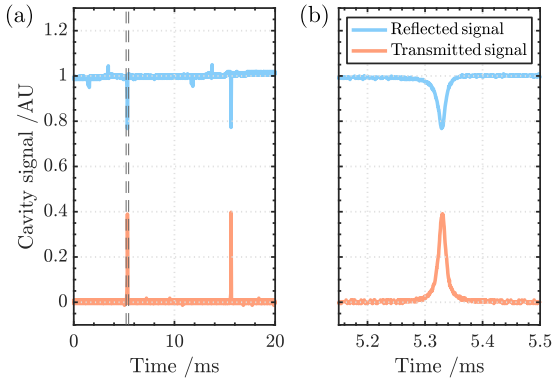

Figure 2.23: Measurement of $\mathcal{F}$ and σ: (a) Normalized cavity signal in reflection (light blue) and transmission (light red) for a triangular length scan of the plane fiber. The distance between to peaks yields the FSR. (b) Zoom into one resonance peak. The FWHM corresponds to $\delta\nu$. The minimum in reflection yields the reflectivity on resonance. To determine both parameters we average over 1000 scan ramps at a scan frequency of 20 Hz.

We measure the geometric properties of the fiber mirrors by phase shifting interferometry (PSI) of the fiber facet. The used evaluation algorithm is described in detail in Ref. [91].
The depicted fiber is part of the cavity that is used in the hybrid coupling experiments presented in Chapter 3 and has a finesse of $\mathcal{F}_{\text{emtpy}} = 785$. The profile has a depth of $a = (2.63 \pm 0.1)\,\mu$m and deviates from the optimal $r_{\text{opt}} = 69.5\,\mu$m for this fiber by 3 %. The corresponding evaluation for the finesse of $\mathcal{F}_{\text{emtpy}} = 14500$ is presented in Appendix B.5. This profile has a depth of $a = (1.57 \pm 0.1)\,\mu$m and $r_2 = (67.4 \pm 1)\,\mu$m and deviates from the optimal $r_{\text{opt}} = 65.4\,\mu$m for this fiber by 5 %.

The finesse and the reflectivity on resonance are measured by scanning the cavity over multiple resonances using the piezo tubes in the goniometer while using the definition of the finesse:

$$\mathcal{F} = \frac{FSR}{\delta\nu} = \frac{\Delta L}{\delta L} \tag{2.59}$$

Figure 2.23 shows a measurement over two resonances. Since $\mathcal{F}$ and σ are length dependent a full characterization of the cavity requires to repeat this measurement for multiple cavity lengths. Figure 2.24 shows $\mathcal{F}$ and σ dependent on the cavity length for the $\mathcal{F}_{\text{emtpy}} = 785$ cavity. While the finesse remains constant over the whole length of the cavity, σ experiences a maximum at a length of approximately 13 μm. This is likely due to improved mode match in a shorter cavity since the intra cavity light field only hits the center of the gaussian mirror profile.

The evaluation yields a finesse of $\mathcal{F}_{\text{emtpy}} = 785 \pm 15$ and a reflectivity on resonance of $\sigma = 0.82 \pm 0.01$ at this length. For the $\mathcal{F}_{\text{emtpy}} = 14500 \pm 1500$ cavity we measure a reflectivity on resonance of $\sigma = 0.62 \pm 0.02$ at a cavity length of 14 μm.

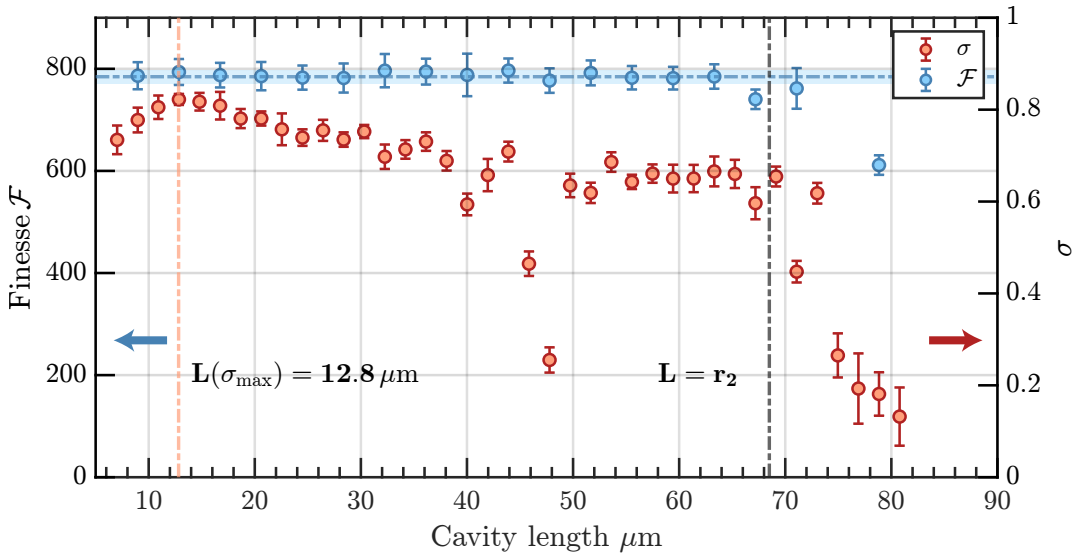

Figure 2.24: Finesse and reflectivity on resonance at different cavity lengths: Each datapoint is the result of 1000 times averaged measurements as shown in Fig. 2.23. The blue datapoints show the finesse the red data points the reflectivity on resonance. The grey dashed line indicates the point where the cavity length is equal to the radius of curvature. The averaged finesse over the whole cavity length (while excluding data points at $L > r_2$) is shown as blue dashed line with the lighter shades indicating the 1σ confidence bounds. The highest reflectivity on resonance is found at a length of 12.8 μm (red dashed line).

Chapter 3

Towards a strongly coupled atom-optomechanical hybrid system

In this chapter we report on our efforts to enter the strong coupling regime with the hybrid system. As with any other quantum system, the limiting factor in achieving "quantumness" is decoherence. In our particular case, the most impactful parameters that can be optimized are the number of atoms that participate in the coupling and the number of photons that mediate the coupling between the atoms and the MiM system. Both parameters were optimized by implementing a new pump asymmetry compensated coupling lattice and by increasing the finesse of the fiber cavity. The new lattice opened up a parameter space of operation that rendered hybrid coupling possible in the previously inaccessible, red-detuned regime. The exchange of the fiber cavity provided a significant increase in coupling strength, while showing a fundamental, back-action induced limit to this coupling scheme.

3.1 Sympathetic cooling

The first experimental realization of sympathetic cooling was published in 1986 by D.J. Larson *et al.*: "$^{198}Hg^+$ ions were confined in a Penning ion trap with laser-cooled $^9Be^+$ ions.", [121] and sympathetically cooled to temperatures below 1K [121]. From then on, sympathetic cooling has been realized with many different systems such as neutral atoms [122–125], ions [121], varieties of Bose-Fermi systems [126], hybrid systems [127] and even molecules [128, 129].
In general, it describes the cooling of one component of a mixed system by transferring its energy to another component that serves as a thermal bath [76, 101]. For our system, this is realized by the resonant coupling of the micromechanical resonator to a cloud of (ultra-) cold atoms.
The strength of the coupling is quantified via the cooperativity C_{hybrid} of the system. It can be acquired by a measurement of the sympathetic cooling rate Γ_{sym}, which is proportional to the cooperativity $C_{\mathrm{hybrid}} \propto \Gamma_{\mathrm{sym}}$.

Since this parameter is of fundamental interest to investigate the nature of the hybrid coupling and serves as a benchmark for all experiments presented in this chapter. We give a brief introduction to the underlying theory of sympathetic cooling in the following section oriented along the detailed description that has been done in previous theses [57, 63]. While a conceptual understanding can be established in the classical frame, the case of ground state cooling requires a quantized model of the process. Thus, we will introduce sympathetic cooling in a classical picture first, and use the quantized model to explain the behavior in the limiting case of the system being near its quantum ground state.

3.1.1 Sympathetic cooling in a classical picture

The coupling in our system is mediated via monochromatic, coherent light, which can be modulated regarding its amplitude, phase or polarization. Polarization modulation has been proven to be a powerful tool to mediate coupling between atomic spin states and a phononic shield resonator [38]. Here, spin state-dependent polarization rotation of the light that interacts with the atoms is translated into an intensity modulation of the light incident on the resonator. The coupling scheme to motional degrees of freedom that we use in our experiment utilizes amplitude and phase modulation of the coupling light [52]. Figure 3.1 shows a schematic of the underlying coupling mechanism.

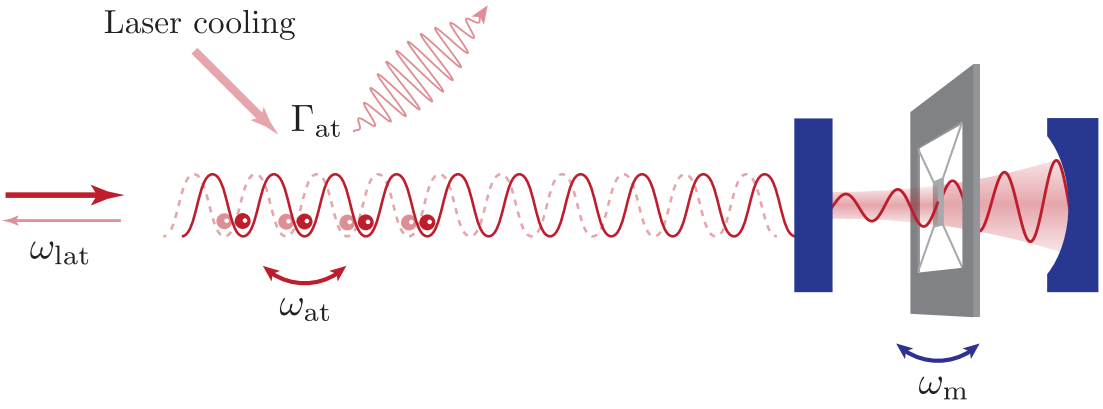

Figure 3.1: Sketch of the sympathetic cooling mechanism: The 1D coupling lattice is created from an incident lattice beam that is reflected by the fiber-Fabry-Pérot cavity (FFPC) containing the mechanical resonator. The motion of the atoms modulates the intensity of the light incident on the resonator with ω_{at}. If the resonance condition $\omega_{\mathrm{at}} = \omega_{\mathrm{m}}$ is fulfilled, the atoms couple to the resonator. The resonator motion modulates the phase of the reflected light and spatially shifts the trapping potential of the atoms. The transferred energy is dissipated via laser cooling. Sketch based on Ref. [52].

We consider an atom in a harmonic trap, formed by the coupling lattice. Any displacement from the trap equilibrium position x_{at} will result in an optical dipole force $F_{\mathrm{d}} = -m_{\mathrm{at}} x_{\mathrm{at}} \omega_{\mathrm{at}}^2$, pointing towards the trap center. Consequently, a spatial shift of the optical lattice δx_{lat} acts on an atom cloud with atom number N_{at} with $F_{\mathrm{at}} = N_{\mathrm{at}} m_{\mathrm{at}} \delta x_{\mathrm{lat}} \omega_{\mathrm{at}}^2$. This force is realized by resonant absorption and emission of photons

along the coupling lattice direction [52, 130] and a subsequent momentum transfer towards the location of the highest (red-detuned lattice) or lowest (blue-detuned lattice) field strength.
A collective spatial shift of the lattice introduces an asymmetry in the number of leftward and rightward scattered photons, which yields a modulation of the light transmitted through the atom cloud at the trapping frequency of the atoms [58]. This causes a variation of the radiation pressure force δF_{rad} on the resonator dependent on the motional state of the atoms. Assuming a momentum-kick of $\pm 2\hbar k_{\mathrm{L}}$ per absorption or emission event [58], δF_{rad} can be derived starting from the photon redistribution rate $\dot{n} = N_{\mathrm{at}} F_{\mathrm{d}}/(2\hbar k_{\mathrm{lat}})$[58]. The redistribution of photons yields a power modulation $\delta P_{\mathrm{lat}} = \dot{n}\hbar\omega_{\mathrm{lat}}$. Under the assumption that a photon has an intra-cavity lifetime of $\tau_{\mathrm{cav}} \approx 1/\kappa$, this modulation corresponds to a change of the intra-cavity photon number by $\bar{n}_{\mathrm{cav}} = 4\beta t^2 \delta P_{\mathrm{lat}}/(\hbar\omega_{\mathrm{lat}}\kappa)$, where β is the cavity incoupling efficiency and t is the one-way transmission on the path of the coupling light.
Assuming that each intra-cavity photon couples to the resonator with its optomechanical coupling strength g_{m}, this yields a force $F_{\mathrm{rad}} = \hbar g_{\mathrm{m}} \dot{n}$ on the resonator. Inserting the expressions for $\dot{n}$, δP_{lat} and F_{d} found above, it can be rewritten in the following form [58]:

$$F_{\mathrm{rad}} = \hbar g_{\mathrm{m}} \dot{n} = \beta t^2 \underbrace{\frac{2 g_{\mathrm{m}}}{k_{\mathrm{lat}} \kappa} N_{\mathrm{at}} \omega_{\mathrm{at}}^2}_{:=K} x_{\mathrm{at}} = -\beta t^2 K x_{\mathrm{at}} \tag{3.1}$$

The constant K takes the form of a spring constant [52, 53, 82]. In the case of small displacements of the atoms from their equilibrium position, a linear dependency between the restoring force and the displacement can be assumed. Within this limit, the mediated force per displacement, and thus the coupling strength itself, depends on the transmission and mode match between the two systems as well as on the atom number N_{at} and the cavity linewidth κ. As we will discuss later in this chapter, increasing N_{at} (Sec. 3.2.2) or decreasing κ (Sec. 3.3.3) is only possible up to a certain limit, beyond which the assumptions made above do not hold anymore.

The trampoline resonator is placed in a high finesse FFPC. It divides the cavity into two subcavities whose resonance conditions depend on the motional state of the resonator. This yields a motional state-dependent modulation of the cavity resonance frequency, which translates to a phase modulation of the back-reflected light at the resonator eigenfrequency [52].
The displacement dependent phase modulation $\delta\phi(x_{\mathrm{m}})$ [102] of the resonator is mainly affected by the cavity linewidth $\delta\phi_{\mathrm{m}} = (4/\kappa) g_{\mathrm{m}} x_{\mathrm{m}}$[34]. This causes a shift of the optical lattice potential by $\delta x_{\mathrm{lat}} = -\delta\phi_{\mathrm{m}}/(2k_{\mathrm{lat}}) = 2 g_{\mathrm{m}} x_{\mathrm{m}}/(\kappa k_{\mathrm{lat}})$. Inserting the expression

[34] The factor $4/\kappa$ originates from the assumption that the cavity detuning due to the membrane motion is much smaller than its linewidth $|\Delta_{\mathrm{cav}}| \ll \kappa$. For a detailed derivation, refer to [63].

found for δx_{lat} into the expression for F_{at} yields [58]:

$$F_{\mathrm{at}} = N_{\mathrm{at}} m_{\mathrm{at}} \omega_{\mathrm{at}}^2 \delta x_{\mathrm{lat}} = N_{\mathrm{at}} m_{\mathrm{at}} \omega_{\mathrm{at}}^2 \frac{2g_{\mathrm{m}}}{\kappa k_{\mathrm{lat}}} x_{\mathrm{m}} = -K x_{\mathrm{m}} \tag{3.2}$$

Note that K is the same spring constant that is derived in equation 3.1. In a classical picture, the joint system behaves like two coupled harmonic oscillators. This allows the derivation of the equations of motion from the acquired force terms [53, 58]:

$$m_{\mathrm{eff}} \ddot{x}_{\mathrm{m}} = -\Gamma_{\mathrm{m}} m_{\mathrm{eff}} \dot{x}_{\mathrm{m}} - m_{\mathrm{eff}} \omega_{\mathrm{m}}^2 x_{\mathrm{m}} - \beta t^2 K x_{\mathrm{at}} + F_{\mathrm{th}} \tag{3.3}$$

$$N_{\mathrm{at}} m_{\mathrm{at}} \ddot{x}_{\mathrm{at}} = -\Gamma_{\mathrm{at}} N_{\mathrm{at}} m_{\mathrm{at}} \dot{x}_{\mathrm{at}} - N_{\mathrm{at}} m_{\mathrm{at}} \omega_{\mathrm{at}}^2 x_{\mathrm{at}} - K x_{\mathrm{m}} \tag{3.4}$$

Both equations describe damped harmonic oscillators with the respective atomic (mechanical) damping rates Γ_{at} (Γ_{m}). The coupling is realized via the individual coupling terms $-Kx_{\mathrm{m}}$ ($-\beta t^2 K x_{\mathrm{at}}$). The thermal force noise F_{th} describes the coupling of the resonator to its thermal bath [58] via the Langevin equations and is the main contributor to decoherence.
By applying the Fourier transformation to both equations, they are translated into algebraic equations [58]:

$$-m_{\mathrm{eff}} \omega^2 X_{\mathrm{m}}(\omega) - i m_{\mathrm{eff}} \Gamma_{\mathrm{m}} \omega X_{\mathrm{m}}(\omega) + m_{\mathrm{eff}} \omega_{\mathrm{m}}^2 X_{\mathrm{m}}(\omega) = \tilde{F}_{\mathrm{th}} - \beta t^2 K X_{\mathrm{at}}(\omega) \tag{3.5}$$

$$-N_{\mathrm{at}} m_{\mathrm{at}} \omega^2 X_{\mathrm{at}}(\omega) - i N_{\mathrm{at}} m_{\mathrm{at}} \Gamma_{\mathrm{at}} \omega X_{\mathrm{at}}(\omega) + N_{\mathrm{at}} m_{\mathrm{at}} \omega_{\mathrm{at}}^2 X_{\mathrm{at}}(\omega) = -K X_{\mathrm{m}}(\omega) \tag{3.6}$$

The prefactors of $X_{\mathrm{m}}(\omega)$ and $X_{\mathrm{at}}(\omega)$[35] can be summarized in the susceptibilities $\chi_{\mathrm{m}}(\omega)$ and $\chi_{\mathrm{at}}(\omega)$. Since the relevant coupling dynamics occur near the systems resonance ($\omega \approx \omega_{\mathrm{at/m}}$), the susceptibilities can be further approximated by a Taylor expansion around $\omega_{\mathrm{at/m}}$:

$$\chi_{\mathrm{m}}(\omega) = m_{\mathrm{eff}} \left(\omega_{\mathrm{m}}^2 - \omega^2 - i\Gamma_{\mathrm{m}} \omega \right) \approx 2 m_{\mathrm{eff}} \omega_{\mathrm{m}} \left(\omega_{\mathrm{m}} - \omega - i\Gamma_{\mathrm{m}}/2 \right) \tag{3.7}$$

$$\chi_{\mathrm{at}}(\omega) = N_{\mathrm{at}} m_{\mathrm{at}} \left(\omega_{\mathrm{at}}^2 - \omega^2 - i\Gamma_{\mathrm{at}} \omega \right) \approx 2 N_{\mathrm{at}} m_{\mathrm{at}} \omega_{\mathrm{at}} \left(\omega_{\mathrm{at}} - \omega - i\Gamma_{\mathrm{at}}/2 \right) \tag{3.8}$$

This leads to the equations of motion in the frequency domain:

$$\chi_{\mathrm{m}}(\omega) X_{\mathrm{m}}(\omega) = \tilde{F}_{\mathrm{th}} - \beta t^2 K X_{\mathrm{at}}(\omega) \tag{3.9}$$

$$\chi_{\mathrm{at}}(\omega) X_{\mathrm{at}}(\omega) = -K X_{\mathrm{m}}(\omega) \tag{3.10}$$

Both equations describe the amplitude response of both constituents of the hybrid system to mutual coupling. The extent to which the subsystems respond to any force exerted by their hybrid partner is described by their individual susceptibilities. By inserting equation 3.10 into 3.9 we merge both systems and obtain a single equation to

[35] Here $X_{\mathrm{m}}(\omega)$ and $X_{\mathrm{at}}(\omega)$ denote the Fourier transformation of x_{m} and x_{at}.

describe the hybrid system [58]:

$$\left(\chi_{\mathrm{m}}(\omega) - \underbrace{\beta t^2 K^2 \chi_{\mathrm{at}}^{-1}(\omega)}_{\chi_{\mathrm{sym}}(\omega)}\right) X_{\mathrm{m}}(\omega) = \chi_{\mathrm{eff}}(\omega) X_{\mathrm{m}}(\omega) = F_{\mathrm{th}} \tag{3.11}$$

Here we introduce $\chi_{\mathrm{sym}}(\omega)$ as the sympathetic susceptibility. Expanding the expression with $(\omega_{\mathrm{at}} - \omega + i\Gamma_{\mathrm{at}}/2)$ and using the previously introduced definition of K (Eq. 3.1) yields:

$$\chi_{\mathrm{sym}}(\omega) = \frac{2\beta t^2 g_{\mathrm{m}}^2 N_{\mathrm{at}} \omega^3}{m_{\mathrm{at}} k_{\mathrm{lat}} \kappa^2} \frac{\omega_{\mathrm{at}} - \omega + i\Gamma_{\mathrm{at}}/2}{(\omega_{\mathrm{at}} - \omega)^2 + (\Gamma_{\mathrm{at}}/2)^2} \tag{3.12}$$

This description shows the dependency of the coupling on the fulfillment of the resonance condition ($\omega_{\mathrm{at}} = \omega_{\mathrm{m}}$). Furthermore, it contains an effective increase of the mechanical damping rate Γ_{m} within the imaginary part of χ_{sym}. The expression found in equation 3.12 inserted into 3.11 yields the effective susceptibility $\chi_{\mathrm{eff}}(\omega)$ of the hybrid system [53, 101], where we introduce the single-phonon coupling rate g_{N}:

$$\chi_{\mathrm{eff}}(\omega) = 2 m_{\mathrm{eff}} \omega_{\mathrm{m}} \left(\omega_{\mathrm{m}} - \omega - i\Gamma_{\mathrm{m}}/2 - \frac{2\beta t^2 g_{\mathrm{N}}^2 \left(\omega_{\mathrm{at}} - \omega + i\Gamma_{\mathrm{at}}/2\right)}{(\omega_{\mathrm{at}} - \omega)^2 + (\Gamma_{\mathrm{at}}/2)^2}\right) \tag{3.13}$$

$$g_{\mathrm{N}} = \mid r_{\mathrm{m}} \mid \omega_{\mathrm{at}} \sqrt{\frac{N_{\mathrm{at}} m_{\mathrm{at}} \omega_{\mathrm{at}}}{m_{\mathrm{eff}} \omega_{\mathrm{m}}}} \frac{2\mathcal{F}}{\pi} \frac{G}{G_{\mathrm{max}}} \tag{3.14}$$

The single-phonon coupling rate is a property of the mechanical resonator. It describes the frequency shift of the resonator upon coupling to a single phonon and has a significant influence on the coupling strength. The most influential parameter to be optimized is the finesse $\mathcal{F}$ as will be discussed in section 3.3.
Since the atomic damping rate exceeds the mechanical damping rate by orders of magnitude ($\Gamma_{\mathrm{at}} \gg \Gamma_{\mathrm{m}}, g_{\mathrm{m}}$), contributions to χ_{sym} aside from the mechanical resonator are suppressed such that we can assume $\omega \to \omega_{\mathrm{m}}$ in the following [58]. Equation 3.13 can be rewritten and the prefactors and resonance condition are summarized in the sympathetic cooling rate Γ_{sym}:

$$\chi_{\mathrm{eff}}(\omega) = 2 m_{\mathrm{eff}} \omega_{\mathrm{m}} \left(\omega_{\mathrm{m}}' - \omega - \frac{i}{2} \Gamma_{\mathrm{m}} \left(1 + \frac{\Gamma_{\mathrm{sym}}}{\Gamma_{\mathrm{at}}}\right)\right) \tag{3.15}$$

with

$$\omega_{\mathrm{m}}' = \omega_{\mathrm{m}} + (\omega_{\mathrm{m}} - \omega_{\mathrm{at}}) \frac{\Gamma_{\mathrm{sym}}}{\Gamma_{\mathrm{at}}} \tag{3.16}$$

and

$$\Gamma_{\mathrm{m}}' = \Gamma_{\mathrm{m}} \left(1 + \frac{\Gamma_{\mathrm{sym}}}{\Gamma_{\mathrm{m}}}\right) = \Gamma_{\mathrm{m}}(1 + g_{\mathrm{sym}}) \tag{3.17}$$

This leads to the expression for the sympathetic cooling rate Γ_{sym} which is a benchmark for the hybrid coupling strength in our system:

$$\Gamma_{\mathrm{sym}} = \frac{\beta t^2 g_{\mathrm{N}}^2 \Gamma_{\mathrm{at}}}{(\omega_{\mathrm{at}} - \omega_{\mathrm{m}})^2 + (\Gamma_{\mathrm{at}}/2)^2} \tag{3.18}$$

Equations 3.16 and 3.17 show two properties of sympathetic cooling. Firstly, it shifts the mechanical frequency of the resonator [36]. Since the sympathetic cooling rate is small compared to the atomic damping rate ($\Gamma_{\mathrm{at}} \gg \Gamma_{\mathrm{sym}}$), this effect is negligible. Analogously, the increase of the mechanical damping rate by the sympathetic cooling gain g_{sym} is a velocity dependent feedback effect and linked to the mode temperature of the resonator via [58]:

$$T_{\mathrm{mode}} = \frac{T_{\mathrm{bath}}}{1 + g_{\mathrm{sym}}} = T_{\mathrm{bath}} \frac{\Gamma_{\mathrm{m}}}{\Gamma_{\mathrm{m}} + \Gamma_{\mathrm{sym}}} \tag{3.19}$$

Hence, Γ_{sym} can be directly determined from the mode temperature reached by sympathetic cooling.

Ensemble-integrated sympathetic cooling rate

The description of sympathetic cooling found above holds for an idealized system of atoms and resonator in which the atom number density and the atomic trapping potential are constant throughout the coupling lattice volume. While it is feasible to assume a constant atom number density, because of the large extent of the MOT compared to the coupling lattice waist ($R_{\mathrm{at}} \gg \mathrm{w}_{\mathrm{lat}}$), the trapping potential can be considered constant only along the axial direction of the coupling lattice due to its large Rayleigh range $z_{\mathrm{r}} = \pi \mathrm{w}_{\mathrm{lat}}^2/\lambda \approx 2$ cm [63]. Radially, we have to take into account the Gaussian intensity profile of the lattice beam, which causes a reduction of the trapping frequency as $\omega_{\mathrm{at,r}}(r) = \omega_{\mathrm{at},0} e^{-r^2/\mathrm{w}_{\mathrm{lat}}^2}$. This is accounted for by integrating expression 3.18 along the radial beam profile [58] in radial coordinates:

$$\Gamma_{\mathrm{sym}}^{\mathrm{int}}(R_{\mathrm{at}}) = 2R_{\mathrm{at}} n_{\mathrm{at}} \int_0^{R_{\mathrm{at}}} 2\pi r \; \Gamma_{\mathrm{sym}}\left(N = 1, \omega_{\mathrm{at}}(r)\right) dr \tag{3.20}$$

By using the expression for the radial frequency dependency of $\omega_{\mathrm{at,r}}$, equation 3.20 is converted to an integral over the frequency with the integral prefactor $N_{\mathrm{lat}} = 2\pi R_{\mathrm{at}} \mathrm{w}_{\mathrm{at}}^2 n_{\mathrm{at}}$:

$$\begin{aligned} \Gamma_{\mathrm{sym}}^{\mathrm{int}}(\omega_{\mathrm{at},0}) &= N_{\mathrm{lat}} \int_{\omega_{\mathrm{at}}(R_{\mathrm{at}})}^{\omega_{\mathrm{at},0}} \frac{\Gamma\left[N = 1, \omega_{\mathrm{at}}\right]}{\omega_{\mathrm{at}}} d\omega_{\mathrm{at}} \\ &= |r_{\mathrm{m}}|^2 \, \beta t^2 \frac{m_{\mathrm{at}} N_{\mathrm{lat}} \Gamma_{\mathrm{at}}}{m_{\mathrm{eff}} \omega_{\mathrm{m}}} \left(\frac{2\mathcal{F}}{\pi}\right)^2 \int_{\omega_{\mathrm{at}}(R_{\mathrm{at}})}^{\omega_{at,0}} \frac{\omega_{\mathrm{at}}^2}{(\omega_{\mathrm{at}} - \omega_{\mathrm{m}})^2 + (\Gamma_{\mathrm{at}}/2)^2} \end{aligned} \tag{3.21}$$

The atom cloud is much larger than the waist of the coupling beam in our experiment $R_{\mathrm{at}} \gg \mathrm{w}_{\mathrm{lat}}$ such that the lower integration limit yields $\omega_{\mathrm{at}}(R) \to 0$. Equation 3.21

[36] This is a displacement dependent effect and similar to the displacement dependent feedback cooling presented in Appendix C.

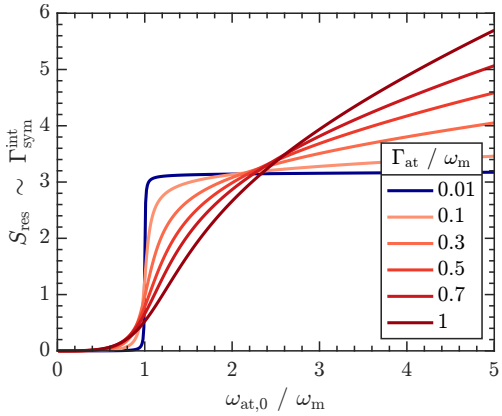

Figure 3.2: Ensemble-integrated sympathetic cooling rate $\Gamma^{\mathrm{int}}_{\mathrm{sym}}$ for varying Γ_{at}:

Plot of S_{res} (Eq. 3.23) in dependence of the coupling lattice trapping frequency. While for $\Gamma_{\mathrm{at}}/\omega_{\mathrm{m}} \ll 1$ (blue) the coupling increases rapidly at $\omega_{\mathrm{at},0}/\omega_{\mathrm{m}} \approx 1$, the diverging properties become dominant with increasing Γ_{at} (red). Here we assume a constant atom number density in the system. Figure adapted from Ref. [63].

transforms to [58]:

$$\Gamma^{\mathrm{int}}_{\mathrm{sym}}(\omega_{\mathrm{at},0}) = 2\,|r_{\mathrm{m}}|^2\,\beta t^2 \frac{m_{\mathrm{at}} N_{\mathrm{lat}} \omega_{\mathrm{m}}}{m_{\mathrm{eff}}} \left(\frac{2\mathcal{F}}{\pi}\right)^2 S_{\mathrm{res}}(\omega_{\mathrm{at},0}) \tag{3.22}$$

where $S_{\mathrm{res}}(\omega_{\mathrm{at},0})$ is defined via [58]:

$$\begin{aligned} S_{\mathrm{res}}(\omega_{\mathrm{at},0}) := &\left(1 - \frac{\Gamma_{\mathrm{at}}^2}{4\omega_{\mathrm{m}}^2}\right)\left(\mathrm{atan}\left[\frac{2\omega_{\mathrm{m}}}{\Gamma_{\mathrm{at}}}\right] + \mathrm{atan}\left[\frac{2(\omega_{\mathrm{at},0} - \omega_{\mathrm{m}})}{\Gamma_{\mathrm{at}}}\right]\right) \\ &+ \frac{\Gamma_{\mathrm{at}}}{2\omega_{\mathrm{m}}^2}\left(\omega_{\mathrm{at},0} + \omega_{\mathrm{m}} \ln\left[\frac{\Gamma_{\mathrm{at}}^2 + 4(\omega_{\mathrm{at},0} - \omega_{\mathrm{m}})^2}{\Gamma_{\mathrm{at}}^2 + \omega_{\mathrm{m}}^2}\right]\right) \end{aligned} \tag{3.23}$$

The ensemble integrated sympathetic cooling rate (Eq. 3.22) as a function of the trapping frequency is depicted in Fig. 3.2. For $\Gamma_{\mathrm{at}} \to \omega_{\mathrm{m}}$ it gradually grows and diverges. Experimentally, this growth is limited by the finite size of the MOT. In the limit of small atomic damping rates $\Gamma_{\mathrm{at}} \ll \omega_{\mathrm{m}}$, it becomes a step-like function. This behavior arises from the small linewidth of Γ_{at} which suppresses the diverging term in equation 3.23. As such, the step width is given by Γ_{at}. As we will see for the conducted coupling experiments, the effect described in this chapter is experimentally relevant.

3.1.2 Sympathetic cooling in a quantum mechanical picture

While the classical approach allows for an intuitive understanding of the sympathetic cooling mechanism, it is not sufficient to describe the system behavior in the quantum regime. This can be seen by noting that equation 3.19 allows for an arbitrarily low mode temperature if Γ_{sym} is sufficiently high. To account for quantum effects such as shot noise and photon scattering, we have to move to a quantized model of the system that was developed by B. Vogell *et al.* in Ref. [52]. In a quantized picture, the hybrid coupling yields an energy exchange between the mechanical and the atomic mode that is mediated by the creation and annihilation of the respective mode quanta. This process can be described by the interaction Hamiltonian of the system [52]:

$$\hat{H}_{\mathrm{int}} = \hbar g_{\mathrm{N}} \left(\hat{a}_{\mathrm{m}} + \hat{a}_{\mathrm{m}}^{\dagger}\right)\left(\hat{a}_{\mathrm{at}} + \hat{a}_{\mathrm{at}}^{\dagger}\right) \tag{3.24}$$

Here $\hat{a}_{\mathrm{m}}^{\dagger}/\hat{a}_{\mathrm{m}}$ ($\hat{a}_{\mathrm{at}}^{\dagger}/\hat{a}_{\mathrm{at}}$) are the creation and annihilation operators for phonons (photons) in the mechanical (atomic) mode of the system. The quantum mechanical description introduces additional decoherence effects that become relevant for low phonon occupations and near the strong coupling regime.
On the mechanical side, the quantized model leads to heating of the resonator by shot noise of the intra-cavity photons [52]. This effect is described by the mechanical momentum diffusion rate [52]:

$$\Gamma_{\mathrm{m}}^{\mathrm{diff}} = |r_{\mathrm{m}}|^2 \frac{4P_{\mathrm{in}}\omega_{\mathrm{cav}}}{m_{\mathrm{eff}}c^2\omega_{\mathrm{m}}} \left(\frac{2\mathcal{F}}{\pi}\right)^2 \tag{3.25}$$

Additionally, the coupling of the resonator to the thermal bath adds to the thermal decoherence rate $\Gamma_{\mathrm{m}}^{\mathrm{th}}$:

$$\Gamma_{\mathrm{m}}^{\mathrm{th}} = \Gamma_{\mathrm{m}} \frac{k_{\mathrm{B}}T_{\mathrm{bath}}}{\hbar\omega_{\mathrm{m}}} = \Gamma_{\mathrm{m}}\bar{n}_{\mathrm{th}} \tag{3.26}$$

The atomic component of the system experiences photon scattering effects that lead to the atomic momentum diffusion rate $\Gamma_{\mathrm{at}}^{\mathrm{diff}}$:

$$\Gamma_{\mathrm{at}}^{\mathrm{diff}} = \Gamma_{\mathrm{sc}} \left(k_{\mathrm{lat}}x_{\mathrm{lat}}^{\mathrm{at}}\right)^2 = \frac{\left(k_{\mathrm{lat}}x_{\mathrm{lat}}^{\mathrm{at}}\right)^2 \Gamma_{\mathrm{at}} V_{\mathrm{lat}}}{\hbar\Delta_{\mathrm{at,L}}} \tag{3.27}$$

The decoherence rates found in equations 3.25 - 3.27 add up to the total decoherence rate Γ in the system. To couple coherently and be described as a true hybrid quantum system, the strong coupling condition must be satisfied:

$$g_{\mathrm{N}} \gg \Gamma \;\text{ with }\; \Gamma = \Gamma_{\mathrm{m}}^{\mathrm{th}} + \Gamma_{\mathrm{m}}^{\mathrm{diff}} + \Gamma_{\mathrm{at}}^{\mathrm{diff}} \tag{3.28}$$

While the coupling conditions for the thermal decoherence rate ($\Gamma_{\mathrm{m}}^{\mathrm{th}}/g_{\mathrm{N}}$) and the atomic diffusion rate ($\Gamma_{\mathrm{at}}^{\mathrm{diff}}/g_{\mathrm{N}}$) scale with $1/\mathcal{F}$ and suggest a higher finesse to be beneficial to enter the strong coupling regime, the mechanical diffusion rate ($\Gamma_{\mathrm{m}}^{\mathrm{diff}}/g_{\mathrm{N}}$) is proportional to $\mathcal{F}^2$.
Figure 3.3 shows the contributions of the individual decoherence rates, calculated with the parameters presented in Appendix B.1. The point at which all effects are balanced leads to the optimal finesse for our system $\mathcal{F} \approx 600$ [37].

The decoherence rates allow for the calculation of the steady state phonon occupation $\bar{n}_{\mathrm{ss}}$ that can be acquired by sympathetic cooling [64].

$$\bar{n}_{\mathrm{ss}} = \frac{\Gamma_{\mathrm{m}}^{\mathrm{th}}}{\Gamma_{\mathrm{m}} + \Gamma_{\mathrm{sym}}} + \frac{\Gamma_{\mathrm{m}}^{\mathrm{diff}}}{\Gamma_{\mathrm{m}} + \Gamma_{\mathrm{sym}}} + \frac{\Gamma_{\mathrm{at}}^{\mathrm{diff}}}{\Gamma_{\mathrm{at}}} + \left(\frac{\Gamma_{\mathrm{at}}}{4\omega_{\mathrm{at}}}\right)^2 \tag{3.29}$$

[37] Assuming $T_{\mathrm{bath}} = 4\,\mathrm{K}$ and $Q = 8.9 \cdot 10^7$. The case $T_{\mathrm{bath}} = 293\,\mathrm{K}$ and $Q = 6.8 \cdot 10^6$ is also depicted in Fig. 3.3.

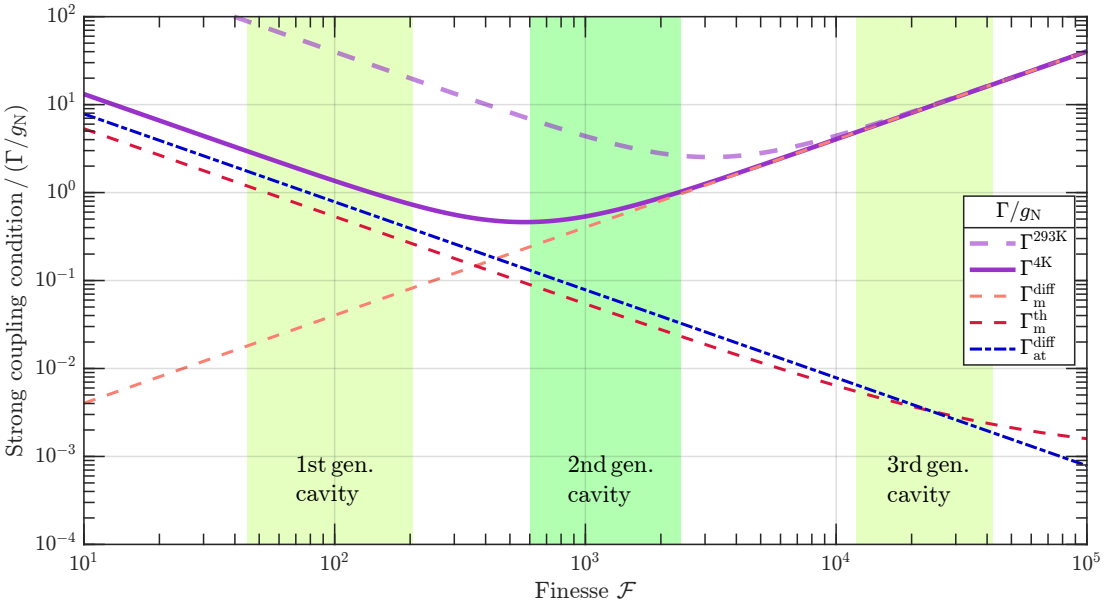

Figure 3.3: Fulfillment of the strong coupling condition dependent on the finesse: Taking the atomic and mechanical diffusion rates (Γ_{at}^{diff}, Γ_m^{diff}) as well as the resonator coupling to the thermal bath (Γ_m^{th}) into account, the strong coupling condition (Γ/g_N) exhibits a minimum at $\mathcal{F} \approx 600$. The green shaded areas show the regimes that are accessible with the fiber cavities, that were built at this experiment. While all experiments in the past (including the PAC experiments in section 3.2) were conducted with the first generation of fiber cavities, the most recent coupling experiments that are described in section 3.3, used the second generation. The third generation of fiber cavities is used for the pulsed preparation experiments that are documented in Chapter 4. The values used for calculation are listed in Appendix B.1.

For resonant coupling $\omega_m \approx \omega_{at}$, the first two terms can be simplified under the assumptions $\Gamma_{sym} \gg \Gamma_m$ and $\Gamma_m^{th} \gg \Gamma_m^{diff}$ to [53, 64]

$$\frac{\Gamma_m^{th} + \Gamma_m^{diff}}{\Gamma_m + \Gamma_{sym}} \approx \frac{\Gamma_m^{th}}{\Gamma_{sym}} = \frac{\bar{n}_{th}}{C_{hybrid}} \tag{3.30}$$

with the hybrid cooperativity

$$C_{hybrid} = \frac{4\beta t^2 g_N^2}{\Gamma_{at}\Gamma_m} = \frac{\Gamma_{sym}}{\Gamma_m} \tag{3.31}$$

Measuring the hybrid cooperativity is an important benchmark of the coupling strength. According to equation 3.30 strong coupling requires $C_{hybrid} \gg \bar{n}_{th}$.

To meet this condition, the system was optimized regarding the losses due to the intracavity mode match β and the overall losses t^2 on the path between both constituents [76]. Furthermore, C_{hybrid} benefits from a small mechanical linewidth Γ_m due to the reduced coupling to the thermal bath, and a large single-phonon coupling rate g_N.
The mechanical properties of the system were optimized by exchanging the initially used membrane design by a trampoline resonator which lead to a significantly reduced effective mass ($m_{eff,Mem}/m_{eff,Tramp} \approx 25$) and a smaller mechanical linewidth

($\Gamma_{\mathrm{m,Mem}}/\Gamma_{\mathrm{m,Tramp}} \approx 14$) [62]. Together with a cavity finesse of $\mathcal{F} \approx 140$, this system reached a hybrid cooperativity of $C_{\mathrm{hybrid}} = 151 \pm 9$. At $T_{\mathrm{bath}} = 5\,\mathrm{K}$, we miss the strong coupling condition by four orders of magnitude ($\bar{n}_{\mathrm{th}}/C_{\mathrm{hybrid}} = 3.95 \cdot 10^6/151 \approx 26000$).

In this thesis, we optimized two parameters to increase the single-phonon coupling rate further[38]:

- Since g_{N} scales with the number of atoms that participate in the coupling by $g_{\mathrm{N}} \propto \sqrt{N_{\mathrm{at}}}$, we tried to increase N_{at} by using a red-detuned coupling lattice. As discussed in more detail in Section 3.2, this regime was previously inaccessible due to a dynamic instability that arises for high atomic densities in the lattice volume.

- We exchanged the cavity of our system for a new cavity with an empty cavity finesse of $\mathcal{F}_{2,\mathrm{empty}} = 785 \pm 15$ [39] (previously $\mathcal{F}_{1,\mathrm{empty}} = 60 \pm 2$) which yields an increase in finesse by a factor of 13. This made the previously calculated regime of the highest optomechanical coupling accessible. The results are discussed in Section 3.3 of this chapter.

[38] The experimental parameters of the individual systems are summarized in Appendix B.1.
[39] This cavity was produced at the NanoBEC experiment during Ref. [67].

3.2 Pump asymmetry compensation

Increasing the number of atoms that participate in the coupling can be achieved in different ways. While the initial design of the system already allows for large atom numbers in MOT and BEC due to its two-staged MOT setup, the number of atoms in the lattice volume can be increased further by choosing an attractive (i.e., red-detuned) coupling lattice potential.
Previous experiments [64, 76, 131] that tried to operate in this regime discovered an instability in the hybrid system that emerged for small, red atom-light detunings $\Delta_{\mathrm{at,L}}$. This instability causes sympathetic cooling in the system to turn into heating [76, 131], eventually driving the resonator into limit cycle oscillations. The effect was initially discovered in the group of P. Treutlein where it was experimentally investigated by A. Vochezer [64, 131]. They found the instability to be an effect that arises in asymmetrically pumped lattices which can be explained by an asymmetry induced phase delay in the coupling. The delay is likely to originate from density waves that emerge in the coupling lattice. This creation of density waves in asymmetrically pumped optical lattices was theoretically predicted and simulated by J.K. Asboth [65, 66]. The asymmetry in the coupling lattice is an intrinsic property in atom-optomechanical hybrid systems. Due to losses in the path between the atoms and the resonator, as well as the finite reflectivity on resonance cavity, reaching a balanced coupling lattice is impossible. As such, the effect of the hybrid instability can be observed in our experiment.

Figure 3.4(a) [57] shows a hybrid coupling measurement where the resonator mode temperature T_{mode} is plotted against different coupling lattice frequencies ω_{at}. While for a blue-detuned lattice, sympathetic cooling is observed for all lattice depths, the mode temperature rapidly increases for a red-detuned coupling lattice at $\omega_{\mathrm{at}} = 1.25\omega_{\mathrm{m}}$. The heating effect due to the lattice asymmetry can also be observed in the blue-detuned lattice as depicted in Fig. 3.4(b) [62]. Here the pump asymmetry $\mathcal{A}$ (Eq. 3.32) was artificially increased by dumping part of the back-reflected coupling beam from the resonator and the mode temperature was measured as a function of pump asymmetry $\mathcal{A}$. While for $\mathcal{A} < 2.4$, sympathetic cooling could still be observed, it quickly turned into heating for higher asymmetries.
The observations made from our experiment and in Ref. [64] identify the pump asymmetry as the main cause for hybrid instability. In the following section we will describe the static and dynamic effects of the pump asymmetry in the framework of beamsplitter matrices and investigate the feasibility of compensating for the asymmetric pumping by introducing an auxiliary compensation beam. Due to the thematic similarity to Refs. [63, 66, 131], this chapter is structurally oriented along these works.

3.2.1 Theoretical description

Hybrid quantum systems as described in this thesis and in Ref. [58, 64] have experimental constraints that favor the emergence of hybrid instability. The creation of the coupling lattice by retro-reflecting the coupling beam comes with an intrinsic pump asymmetry due to losses along the optical path [76]. Furthermore, the coupling is mediated by the laser light that is used to create the coupling lattice potential. Since high

laser powers lead to heating of the resonator we are limited to use low coupling lattice powers (typically on the order of 100 μW). To fulfill the resonance condition nonetheless, the laser-atom detuning has to be small ($\Delta_{\mathrm{at,L}} < 1\,\mathrm{GHz}$). In this near detuned regime, the back-action of the atomic motion on the laser light is not negligible anymore, in contrast to far detuned lattices usually used in cold atom experiments. This requires us to treat the atoms as a dynamic system of semi-transparent beamsplitters. The idea to this description was first introduced by J.K. Asboth *et al.* in Refs. [65, 66] where they found the emergence of density waves in an asymmetric, near detuned lattice in a numerical simulation. This simulation was adapted by A. Vochezer in Ref. [64] to calculate the phase shift in the coupling between cold atoms and a mechanical resonator coupled by an asymmetric optical lattice. In Ref. [64] they could verify experimentally and via a simulation that the emergence of density waves led to a phase delay in the coupling that can be large enough to introduce positive feedback between the atoms and the resonator, leading to the hybrid instability.
To access the red-detuned coupling lattice regime nonetheless we introduce an additional auxiliary beam that is phase-locked and mode-matched with the coupling lattice back-reflex beam. We evaluated the feasibility of this approach by reproducing the simulation from Ref. [131], adding an additional pump asymmetry compensation beam and studying its effect on the phase delay in the coupling. The creation of a proper model and the results of the simulation are discussed in the following section.

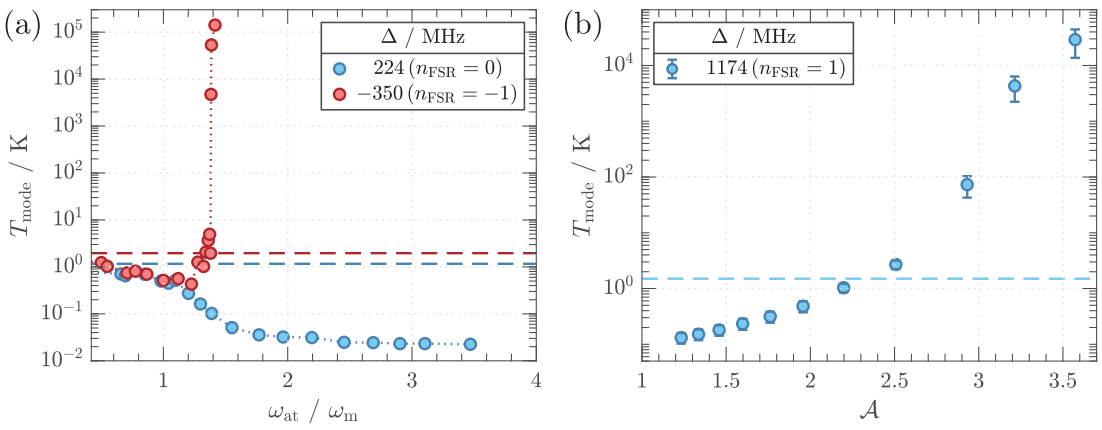

Figure 3.4: Hybrid instability in an asymmetric coupling lattice:
(a) Measurement of the mode temperature for different trapping frequencies in a blue-detuned (blue points) and red-detuned (red points) coupling lattice. For $\omega_{\mathrm{at}} < 1.25\,\omega_{\mathrm{m}}$ sympathetic cooling occurs in both configurations. For higher trapping frequencies, the hybrid instability emerges in the red-detuned lattice and the resonator is driven into limit cycles. The trapping frequency is varied by a power sweep of the coupling lattice beam. Blue detuning ($\Delta_{2,3} > 0$) refers to the $|F = 2 \rightarrow F' = 3\rangle$ transition of the Rb D_2-line. Red detuning ($\Delta_{2,1} < 0$) refers to the $|F = 2 \rightarrow F' = 1\rangle$ transition of the Rb D_2-line. Plot adapted from Ref. [76]. (b) Measurement of the mode temperature in the blue-detuned coupling lattice for different asymmetries $\mathcal{A} = (I_{\mathrm{inc}} - I_{\mathrm{back}})/\sqrt{I_{\mathrm{inc}} I_{\mathrm{back}}}$. The pump asymmetry is introduced by partially dumping the beam that is reflected from the cavity. For $\mathcal{A} > 2.5$, the pump asymmetry causes heating in the blue-detuned lattice. The dashed lines indicate the bath temperature of the system before the hybrid coupling takes place. Plot adapted from Refs. [62, 63].

3.2.1.1 Static model of the 1D coupling lattice

The coupling lattice is a standing wave that is created from a beam incident on the atoms with intensity I_{inc} and a beam back-reflected from the MiM-system with intensity I_{back}. Figure 3.5 shows an illustration of the 1D lattice model. Both beams are related by the losses R that occur on the path between the atoms and the MiM-system such that $I_{\mathrm{back}} = RI_{\mathrm{inc}}$. In the 1D lattice potential, the trapped atoms form disk-shaped clouds at the intensity maxima (red detuning) or minima (blue detuning) that are separated by the distance d_{j}. Each atom cloud experiences dipole and radiation pressure forces based on the respective in- and outgoing field amplitudes A_{j}, B_{j}, C_{j} and D_{j} [132]. The clouds themselves can be described as thin beamsplitters at position x_{j}. The two counter-propagating fields are expressed via $E_{\mathrm{left}}(x) = E_{\mathrm{inc}}e^{-ikx}$ (for the incident beam propagating to the left) and $E_{\mathrm{right}}(x) = E_{\mathrm{back}}e^{ikx}$ (for the backreflected beam propagating to the right)[40]. From the electric field amplitudes, the intensities of the beams are calculated via $I_{\mathrm{inc,ref}} = \frac{1}{2}\epsilon_0 c|E_{\mathrm{inc,ref}}|^2$.
We define the asymmetry of the system by the imbalance between I_{inc} and I_{back} to [66]:

$$\mathcal{A} = \frac{|I_{\mathrm{inc}} - I_{\mathrm{back}}|}{\sqrt{I_{\mathrm{inc}} I_{\mathrm{back}}}} \tag{3.32}$$

$\mathcal{A}$ is a dimensionless parameter. The system is balanced if $\mathcal{A} = 0$.
Based on this model we investigate the influence of an asymmetric lattice on the system. It can be divided into two effects that are described in more detail in the following section.

- A static contraction of the lattice due to a modified refractive index of the atomic cloud at small detunings.
- A dynamic emergence of collective density oscillations in the system.

Static effects of pump asymmetry

In near red-detuned lattices, the interaction between the light and the atoms leads to a static contraction of the lattice. This was observed in Refs. [133, 134] and theoretically described by Deutsch *et al.* in Ref. [132]. If the detuning is small, the atoms can be treated as a medium with a high refractive index, which alters the wavelength of the transmitted light. This effect can only occur in the red-detuned regime because here, the atoms gather at the intensity maxima of the light field. In the blue-detuned regime, most of the atoms are trapped in the dark parts of the lattice where the intensity reaches its minimum, thus leaving the light field unaffected. Introducing any asymmetry to the lattice changes these properties. Since in an asymmetric lattice the interference between the counter propagating beams cannot be fully destructive, there are no dark spots anymore. As such, the contraction effect becomes relevant in the blue-detuned lattice and is intensified even more in the red-detuned case [132].

[40] The propagation direction of the beams is chosen to be as in Fig. 3.5. The choice is arbitrary and does not have an influence on the outcome of the simulation.

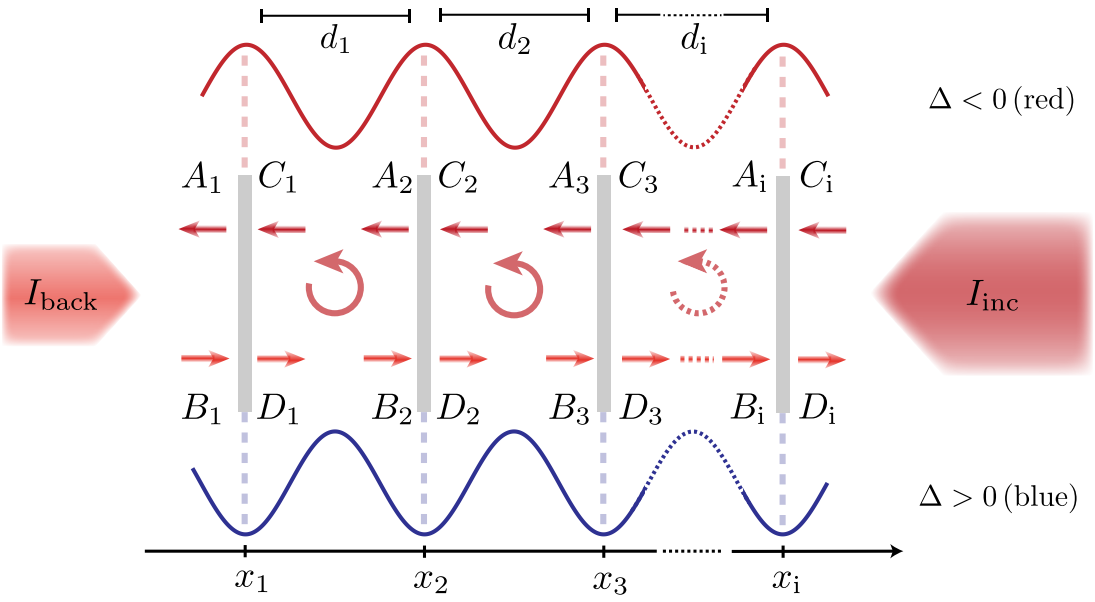

Figure 3.5: Beam splitter model of a 1D lattice for cold atoms:
The atoms in the optical 1D lattice are described by an array of N semi-transparent beamsplitters at the positions x_j, separated by the distance $d_j \approx \lambda/2$. Each beamsplitter is acted on by the fields A_j, B_j, C_j and D_j. Dependent on the chosen detuning, the atoms gather at the intensity maxima ($\Delta_{at,L} < 0$) or minima ($\Delta_{at,L} > 0$). Because the waists of the beams are much larger than the lattice constant ($w_{inc} \approx 69\,\mu m \gg d_{lat} \approx 390\,nm$) we assume planar wavefronts incident on the atoms. Figure adapted from Ref. [105].

Using the model presented in Fig. 3.5 the effect of lattice contraction can be investigated on an array of infinitely thin beamsplitters [66], each consisting of an atom cloud with N_j atoms. Since we assume planar wavefronts, we can determine the cloud area to $\sigma_L = \pi w_{lat}^2/2$. From this, the areal density of one beamsplitter can be calculated to $\eta = N_j/\sigma_L$. The interaction of each atomic beamsplitter with the light depends on the number of atoms in each beamsplitter and the detuning between the atomic resonance and the coupling lattice light. These properties are summarized in the polarizability of the cloud, which quantifies the influence of one beamsplitter on an incident light field [131]:

$$\zeta_j = \frac{N_j}{4\sigma_L} \frac{\sigma_0 \Gamma_{at}}{(\Delta_{at,L} + i\Gamma_{at}/2)} \tag{3.33}$$

Here Γ_{at} is the atomic linewidth and $\sigma_0 = 3\lambda^2/2\pi$ the scattering cross-section. The polarizability contains a real and an imaginary part. While the real part accounts for dispersive coupling between the atoms and the light field, the imaginary part describes absorption and scattering losses and becomes relevant when $\Delta_{at,L} \to \Gamma_{at}$. This scenario is not relevant for the PAC experiments since we operate at least 224 MHz away from the atomic resonance while $\Gamma_{at} \approx 6$ MHz. Referring to Ref. [132] we can use expression 3.33 to describe the interaction of the light with N atomic disks using the scalar Helmholtz

equation [132]:

$$\left(\partial_x^2 + k^2\right) E(x) = -2kE(x) \sum_{\mathrm{j}=1}^{N} \zeta \delta(x - x_{\mathrm{j}}) \tag{3.34}$$

The solution of this equation for the field between two beamsplitters at position j is a superposition of plane waves with the respective field amplitudes (A_{j}, B_{j}, $C_{\mathrm{j-1}}$, $D_{\mathrm{j-1}}$) [66, 132]:

$$\begin{aligned} E(x_{\mathrm{j-1}} < x < x_{\mathrm{j}}) &= A_{\mathrm{j}} e^{-ik(x-x_{\mathrm{j}})} + B_{\mathrm{j}} e^{ik(x-x_{\mathrm{j}})} \\ &= C_{\mathrm{j-1}} e^{-ik(x-x_{\mathrm{j-1}})} + D_{\mathrm{j-1}} e^{-ik(x-x_{\mathrm{j-1}})} \end{aligned} \tag{3.35}$$

which has to fulfill boundary conditions for the leftward $E(x_{\mathrm{j},-})$ and rightward $E(x_{i,+})$ propagating fields at position j [66]:

$$E(x_{\mathrm{j},-}) = E(x_{\mathrm{j},+}) \quad \text{and} \quad \partial_x E(x_{\mathrm{j},-}) = \partial_x E(x_{\mathrm{j},+}) + 2k\zeta E(x_{\mathrm{j}}) \tag{3.36}$$

Using the boundary conditions in equation 3.35 leads to the equations for the field amplitudes incident on an atomic cloud [66]:

$$\begin{aligned} A_{\mathrm{j}} &= \mathbf{r} B_{\mathrm{j}} + \mathbf{t} C_{\mathrm{j}} \\ D_{\mathrm{j}} &= \mathbf{t} B_{\mathrm{j}} + \mathbf{r} C_{\mathrm{j}} \end{aligned} \tag{3.37}$$

These expressions are similar to beamsplitter relations with the only difference being that the coefficients $\mathbf{r}$ and $\mathbf{t}$ are quantities that depend on the atomic beamsplitter- and lattice light properties[66]:

$$\mathbf{r} = \frac{i\zeta}{1 - i\zeta} \quad \text{and} \quad \mathbf{t} = \frac{1}{1 - i\zeta} \quad \text{with} \quad \zeta = -i\frac{\mathbf{r}}{\mathbf{t}} \tag{3.38}$$

The expressions found above allow for a description of the effects that asymmetric pumping has on the coupling lattice. The atomic beamsplitters experience an optical force by the electromagnetic field. This force can be calculated from the momentum transfer rate of the electromagnetic field by integration of the momentum flux over the Volume $V = \sigma_{\mathrm{L}} dL$ [135], which leads to the following expression for the optical force:

$$F = \frac{\epsilon_0}{2} \left(|A|^2 + |B|^2 - |C|^2 - |D|^2 \right) \tag{3.39}$$

By introducing the field amplitudes from the incident and back-reflected beam $B(x) = E_{\mathrm{back}} e^{ikx}$ and $C(x) = E_{\mathrm{inc}} e^{-ikx}$ and using equation 3.37 this expression can be transformed to [66]:

$$F(x) = \underbrace{-4\frac{\sqrt{I_{\mathrm{inc}} I_{\mathrm{back}}}}{c} \frac{\mathrm{Re}(\zeta)}{|1 - i\zeta|^2} \sin(2kx + \phi)}_{(A)} + 2\frac{I_{\mathrm{inc}} - I_{\mathrm{back}}}{c} \left(\underbrace{\frac{\mathrm{Im}(\zeta)}{|1 - i\zeta|^2}}_{(B)} + \underbrace{\frac{|\zeta|^2}{|1 - i\zeta|^2}}_{(C)} \right) \tag{3.40}$$

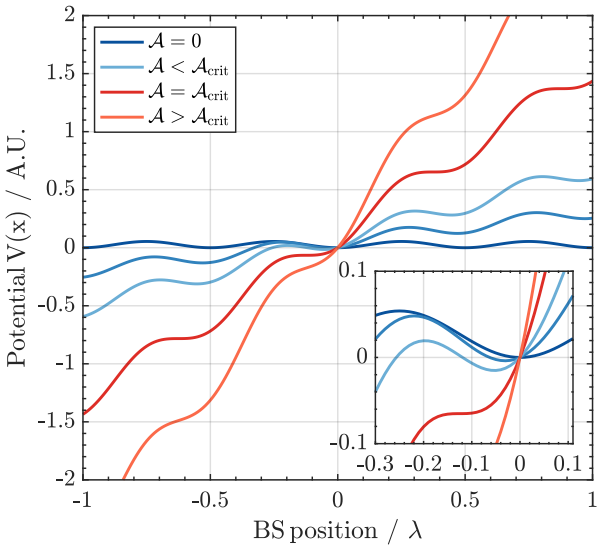

Figure 3.6: Trapping potential in an asymmetric lattice: Potential $V(x)$ calculated from equation 3.40 via $\int_0^x F(x)dx$ for different asymmetries for a single atom cloud. Blue shades indicate the fulfillment of the stability criterion while red shades indicate that the critical asymmetry is exceeded. For $\mathcal{A} = 0$, $V(x)$ resembles a symmetric, harmonic 1D-lattice potential. For $\mathcal{A} > \mathcal{A}_0$, the potential is tilted and globally translated on the x-axis due to radiation pressure imbalance. For $\mathcal{A} >= \mathcal{A}_{\mathrm{crit}}$, the system collapses since the potential has no local minima to trap the atoms.

The force on an atomic cloud can be separated into three contributions:

(A) describes the dipole force on the atom cloud that arises due to interference between the transmitted and reflected light.

(B) accounts for the radiation pressure force due to absorption and moves the system towards the beam with lower power.

(C) accounts for incoherent reflection processes. These do not interfere and are more likely for higher polarizabilities. For high atomic densities, this term can become dominant and (in combination with (A) and (B)) eventually leads to a significant "tilt" in the optical trapping potential $V(x) = \int_0^x F(x)dx$.

Figure 3.6 shows the optical trapping potential calculated from equation 3.40 for different asymmetries. It provides an intuitive understanding of the critical asymmetry upon which the lattice would collapse. This happens when there are effectively no local potential minima available in which the atoms can gather.
As such the requirement for stability is $F(x) > 0 \quad \forall x$. From this requirement a condition for the critical asymmetry in the system can be derived according to Ref. [66]:

$$\mathcal{A} < \mathcal{A}_{\mathrm{crit}} = 2 \left| \frac{\mathrm{Re}(\zeta)}{|\zeta|^2 + \mathrm{Im}(\zeta)} \right| \tag{3.41}$$

which simplifies in the purely dispersive case to:

$$\mathcal{A}_{\mathrm{crit}} = \frac{2}{\zeta} \quad \Leftrightarrow \quad \zeta_{\mathrm{crit}} = \frac{2}{\mathcal{A}} \tag{3.42}$$

As long as this condition is fulfilled, the outgoing fields are strong enough to counteract the radiation pressure force towards the weaker pumping beam. Thus, the system reaches a stable equilibrium configuration in spite of asymmetric pumping. The new steady state configuration becomes dependent on the polarizability and the asymmetry

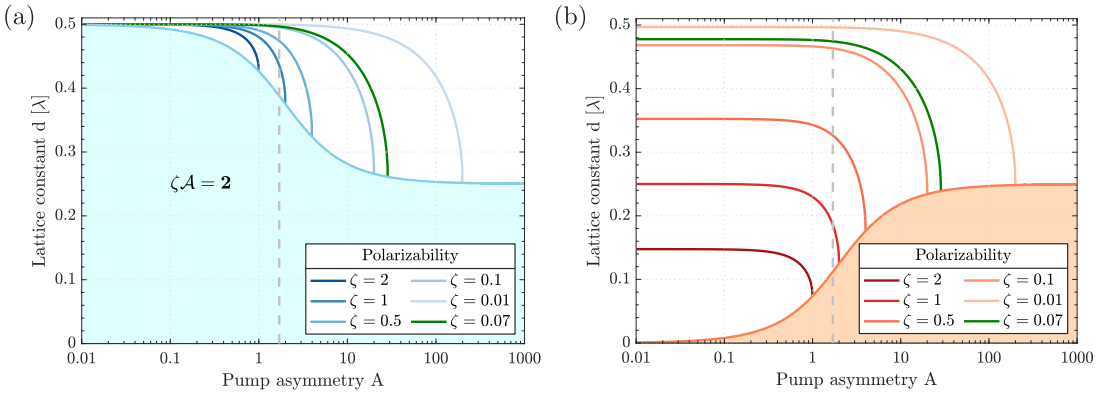

Figure 3.7: Static lattice contraction in an asymmetric coupling lattice
The lattice contraction for different polarizabilities is plotted as a function of the pump asymmetry. The shaded areas show the region of instability described by equation 3.44a. The gray dashed line denotes the asymmetry of our setup ($\mathcal{A} = 1.7$). The green line and the green circle show the parameters that we calculated for the case of $N_{\mathrm{at}} = 5.5 \cdot 10^7$. For this atom number the hybrid instability begins to emerge in the numerical simulation of the lattice dynamics (Fig. 3.8). (a) Lattice contraction for the blue-detuned lattice. (b) Lattice contraction for the red-detuned lattice. Figure based on Ref. [66].

in the system. Propagation of the lattice light through the atom clouds causes a phase delay χ with [66]:

$$\chi^{\pm} = \arcsin\left(\frac{\zeta\sqrt{4+\mathcal{A}} \pm \zeta\sqrt{4-\zeta^2\mathcal{A}^2}}{2(1+\zeta^2)}\right) \tag{3.43}$$

This yields a reduced lattice constant dependent on the detuning and the asymmetry [66]:

$$d_{\mathrm{red}}(\zeta,\mathcal{A}) = \frac{\lambda}{2}\left(1 - \frac{\chi^{+}(\zeta,\mathcal{A})}{\pi}\right) \quad \text{for} \quad \zeta > 0 \tag{3.44a}$$

$$d_{\mathrm{blue}}(\zeta,\mathcal{A}) = \frac{\lambda}{2}\left(1 - \left|\frac{\chi^{-}(\zeta,\mathcal{A})}{\pi}\right|\right) \quad \text{for} \quad \zeta < 0 \tag{3.44b}$$

Figure 3.7 depicts and overview of the lattice contraction and the stability criterion (Eq. 3.44a) dependent on the pump asymmetry for different detunings and polarizabilities and shows the placement of our system within these parameters. The static effect of lattice contraction is weak in both the red-detuned and blue-detuned regime and masked by the much more dominant effect of the dynamic instability [76, 131]. It has to be considered nonetheless in the numerical simulation that is described in the next section.

3.2.2 Model of the 1D lattice dynamics

The model introduced in Fig. 3.5, allowed for a description of the static effects asymmetric pumping has on the 1D coupling lattice. Based on these findings, we want to investigate the dynamic effects the pump asymmetry has on the lattice and, more importantly, if it is feasible to compensate for these effects by introducing a third pump asymmetry compensation beam. Based on [131] we set up a simulation to model the systems behavior, verify the dynamic instability and try to compensate for it. The results presented in this section were acquired together with J. Butlewski [63].

Modeling the system as an array of beamsplitters comes at an advantage that we can use simple matrix multiplication to describe the system in its whole complexity. Each atom cloud is modeled as a beamsplitter with the beamsplitter matrix M_{BS} [66]:

$$M_{\mathrm{BS}} = \frac{1}{\mathbf{t}} \begin{bmatrix} \mathbf{t}^2 - \mathbf{r}^2 & \mathbf{r} \\ -\mathbf{r} & 1 \end{bmatrix} \overset{(3.38)}{=} \begin{bmatrix} 1 + i\zeta & i\zeta \\ -i\zeta & 1 - i\zeta \end{bmatrix} \tag{3.45}$$

Each cloud is separated by a distance d_{j}. The propagation of the light field as well as interference effects between the individual reflected and transmitted fields are accounted for by the corresponding propagation matrices

$$M_{\mathrm{prop,i}} = \begin{bmatrix} e^{ikd_{\mathrm{j}}} & 0 \\ 0 & e^{-ikd_{\mathrm{j}}} \end{bmatrix} \tag{3.46}$$

The evolution of the light field passing through an array of beamsplitters is then described by the product of the matrices 3.45 and 3.46. Considering a system of N atomic beamsplitters, the fields A_{j} and B_{j} at any site j can be calculated from the fields C_{N} and D_{N} at the outermost lattice site N by:

$$\begin{bmatrix} A_{\mathrm{j}} \\ B_{\mathrm{j}} \end{bmatrix} = \underbrace{M_{\mathrm{BS}} \cdot \prod_{\mathrm{j}}^{\mathrm{N}} M_{\mathrm{prop,i}} \cdot M_{\mathrm{BS}}}_{M_{\mathrm{sys,i}}} \begin{bmatrix} C_{\mathrm{N}} \\ D_{\mathrm{N}} \end{bmatrix} \tag{3.47}$$

Here we introduce the system matrix $M_{\mathrm{sys,i}}$ which is the product of all beamsplitter and propagation matrices between the lattice site j and the outermost beamsplitter of the system. This representation is very powerful as we can calculate the fields at any position from only the two input field amplitudes B_1 and C_{N}. This becomes apparent when calculating equation 3.47 for the whole system:

$$\begin{bmatrix} A_1 \\ B_1 \end{bmatrix} = M_{\mathrm{sys,1}} \begin{bmatrix} C_{\mathrm{N}} \\ D_{\mathrm{N}} \end{bmatrix} = \begin{bmatrix} M_{11} & M_{12} \\ M_{21} & M_{22} \end{bmatrix} \begin{bmatrix} C_{\mathrm{N}} \\ D_{\mathrm{N}} \end{bmatrix} \Rightarrow D_{\mathrm{N}} = \frac{B_1 - M_{21} C_{\mathrm{N}}}{M_{22}} \tag{3.48}$$

Equation 3.48 shows that D_{N} can be expressed in terms of both input fields.

The mechanical resonator modulates the phase of the back-reflected light with the eigenfrequency ω_m. Thus, its influence can be included in the model by adding a phase term $\Phi(t) = \Phi_0 \cos(\omega t)$ to the back-reflected field such that $B_1 = E_\mathrm{back} e^{ikx + i\Phi(t)}$. The back-action of the atoms onto the resonator, including effects of the dynamic instability of the system, is contained in the outgoing field A_1.

The dynamic of the system is described by a set of coupled differential equations each of which describe an atomic cloud trapped in a harmonic potential. Since any motion of one atom could yields a change of the reflected and transmitted light fields, it influences the whole system. While for specific cases (e.g., small perturbations near the lattice equilibrium), a fully analytic description of the system is possible (refer to [65, 66]), describing the system in its whole complexity requires a numerical solution.

We set up the simulation at ($t = 0$). All atomic beamsplitters are located at their lattice sites j and slightly shifted from their steady state equilibrium positions x_j^ss by their initial displacement $\xi_\mathrm{j}(t = 0)$. The initial displacement is generated by a random number generator[41] between the values $[-\xi_\mathrm{ini}, \xi_\mathrm{ini}]$ with $\xi_\mathrm{ini} = 5 \times 10^{-4}\lambda$. At t=0 the system then reads [131]

$$x_\mathrm{j}(t = 0) = x_\mathrm{j}^\mathrm{ss} + \xi_\mathrm{j}(t = 0) = x_1^\mathrm{ss} + (\mathrm{j} - 1) d_\mathrm{red,blue} + \xi_\mathrm{j}(t = 0) \tag{3.49}$$

x_1^ss accounts for the spatial shift of the potential due to the asymmetric radiation pressure as depicted in Fig. 3.6 and for the relative phases between the lattice beams. In this model the detuning only has an influence via the chosen lattice constant d. The force on each beamsplitter F_j in this system can be calculated from the respective field amplitudes using equation 3.39. Starting from equation 3.49, the system evolution is calculated by numerically solving the corresponding system of coupled ordinary differential equations (ODEs) [131]:

$$m_\mathrm{BS} \ddot{x}_\mathrm{j} = -m_\mathrm{BS} \Gamma_\mathrm{at} \dot{x}_\mathrm{j} + F_\mathrm{j}(x_1, .., x_\mathrm{N}) \tag{3.50}$$

These ODEs represent a system of coupled, damped harmonic oscillators with (beamplitter) mass $m_\mathrm{BS} = N_\mathrm{at,BS} m_\mathrm{Rb}$ and (atomic) damping rate Γ_at. Note that F_j depends on the individual position of all beamplitters in the system, which is automatically accounted for by using the transfer matrix formalism introduced before.
We use the MATLAB ordinary differential equation solver `ode45` to simulate the system with the initial positions defined as in equation 3.49 and the initial velocities $\dot{x}_\mathrm{j}(t = 0) = \omega \xi_\mathrm{j}(t = 0)$[42]. We simulate over 40 oscillation periods with $\tau_\mathrm{osc} = 2\pi/\omega$.
`ode45` is a numerical ODE solver that implements a Runge-Kutta method to solve the system for each time step. After every run, the newly acquired values for x_j and $\dot{x}_\mathrm{j}$ are used as initial conditions for the next iteration. Precise knowledge about the parameters allows us to calculate the individual fields and beamsplitter dynamic in the system

[41] MATLAB function `randn()`

[42] We took this choice out of convenience as it leads to the correct order of magnitude for the velocities while being aware that this choice does not resemble the ICs in a real system. Because the dynamic is investigated for a strongly damped system after the transient time $T_\mathrm{trans} > 1/\Gamma_\mathrm{at}$, the influence on the dynamic is negligible. This was verified for other initial velocities that lead to similar results.

at any given time. Since the system requires the transient time $T_{\mathrm{trans}} = 1/\Gamma_{\mathrm{at}}$ to reach an equilibrium state, we consider only results after T_{trans}. The coupling is mediated via radiation pressure on the resonator. Thus, the quantity of interest is the leftwards outgoing power modulation of the system $P_{\mathrm{left}} = \epsilon_0 c \pi \mathrm{w}_{\mathrm{lat}}^2 |A_1|^2/4$ and the phase of this modulation relative to the ingoing phase from the resonator $\Phi(t)$ [131]. The phase difference can be assumed to be directly linked to the stability of the system since it dictates, if the resonator experiences positive or negative feedback from the atoms.

3.2.3 Simulation results

We simulate the behavior for our system parameters and asymmetry at different modulation frequencies $5\,\mathrm{kHz} < \omega < 500\,\mathrm{kHz}$ and for different atom numbers N_{at}. The lattice power P_{inc}, and detuning $\Delta_{\mathrm{at,L}}$ are chosen such that $\omega = \omega_{\mathrm{m}} = \omega_{\mathrm{at}}$ fulfills the resonance condition of the system. For each frequency step, the ODE for the whole system as described above is solved. The relative amplitude $A_{\mathrm{rel}} = (P_{\mathrm{left}} - \langle P_{\mathrm{left}}\rangle)/\langle P_{\mathrm{left}}\rangle$[43] and phase[44] of the leftward propagating field is calculated after the transient time. Figure 3.8 shows the simulation results for a symmetric ($R = I_{\mathrm{back}}/I_{\mathrm{inc}} = 1$) coupling lattice in direct comparison to our asymmetric lattice (i.e. $R = 0.22$).

Notably the simulation for the balanced lattice differs from the naive theoretical expectation in that the phase is already delayed by $\Delta\Phi = -90°$ [63] for low modulation frequencies. This effect occurs due to the high atomic damping rate $\Gamma_{\mathrm{at}} = 0.3\,\omega_{\mathrm{m}}$ that is assumed based on the findings in previous experiments [62, 76][45]. For the symmetric case the system response can be intuitively understood. The phase modulation of the back-reflected beam moves the trapping potential wells at the frequency ω. For frequencies that are low compared to the trapping frequency, the atoms adiabatically follow the motion of the potential. For higher driving frequencies the response gradually increases until it hits the maximum at the systems resonance frequency after which it decreases since the atoms cannot follow the modulation of the potential anymore and settle at the time averaged potential minimum. The phase delay in this configuration never exceeds $\Delta\Phi = -180°$. This is the condition for the hybrid system to remain stable as illustrated in Fig. 3.9. A phase delay of $\Delta\Phi = -180°$ corresponds to the case where the maximum deflection of the resonator coincides with the atomic beamsplitter located at the trapping potential minimum. Here two scenarios can be distinguished:

- $\Delta\Phi < -180°$: The atom emits photons in phase of with the resonator motion, thus driving it.
- $\Delta\Phi > -180°$: The atom emits photons out of phase with the resonator motion effectively reducing its phonon occupation and cooling it.

[43] $\langle P_{\mathrm{left}}\rangle$ describes the mean value of P_{left}.
[44] Relative to the ingoing field $\Phi(t)$.
[45] Reducing Γ_{at} yields an amplitude and phase response as depicted in the inset of Fig. 3.8 which resembles the response of a driven harmonic oscillator again.

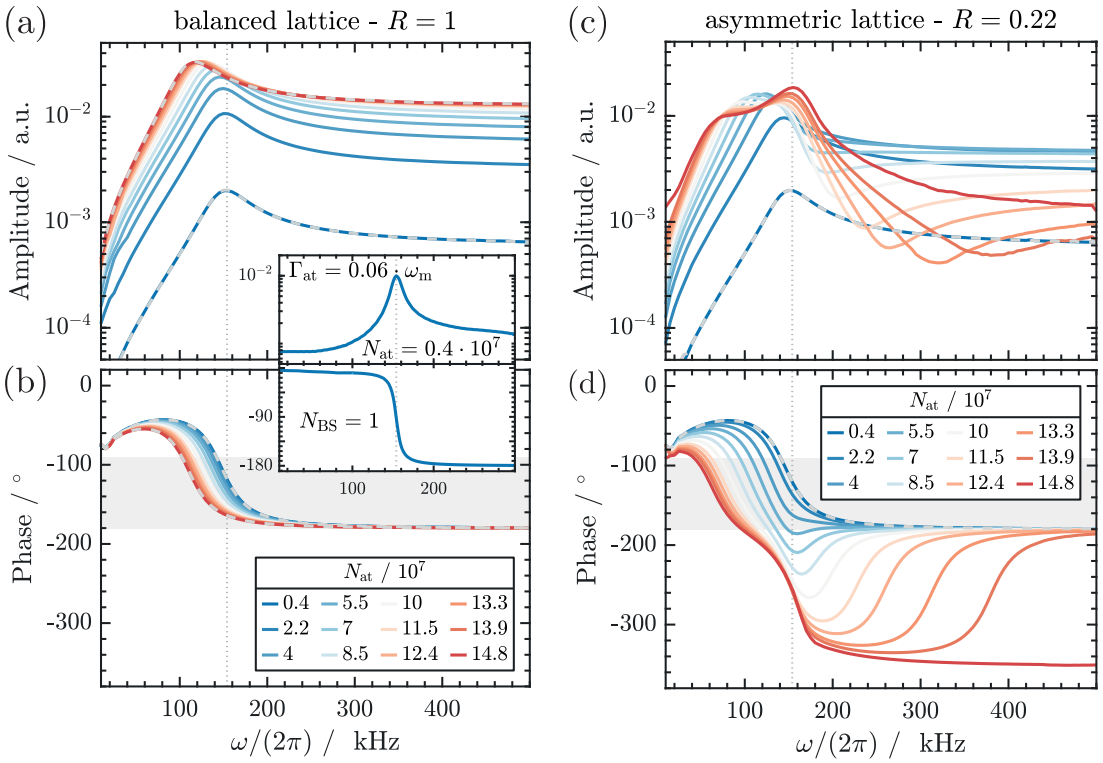

Figure 3.8: Response of the coupling lattice for different atom numbers N_{at}: Simulation of the relative amplitude A_{rel} and phase response of the outgoing modulated beam dependent on the modulation frequency ω with the phase referenced to the ingoing field modulation $\Phi(t)$. Our systems resonance frequency $\omega_m = 154\,\text{kHz}$ is marked by the vertical dotted line. The dashed lines show the response for a single beamsplitter. Sympathetic cooling occurs within the grey shaded areas. We simulate a system size of $N_{BS} = 10$ beamsplitters. (a,b): Expected response for a balanced lattice ($R = 1$). We use the parameters $P_{inc} = \pi w_{lat}^2 I_{inc}/2 = 100\,\mu\text{W}$ and $\Delta_{at,L} = -9.6\,\text{GHz}$. (c,d): Expected response for a unbalanced lattice ($R = 0.22$). We assume the same lattice incident power and $\Delta_{at,L} = -4.55\,\text{GHz}$. For both cases we use $w_{lat} = 70\,\mu\text{m}$, a driving amplitude of $\Phi_0 = 2\pi \cdot 10^{-3}$ and $\Gamma_{at} = 0.3\omega_m = 290\,\text{kHz}$. Inset: Response at a reduced atomic damping rate for a single atom beamsplitter of $\Gamma_{at} = 0.06\omega_m$ with $N_{at,BS} = 0.4 \cdot 10^7$ atoms. Figure from Ref. [63].

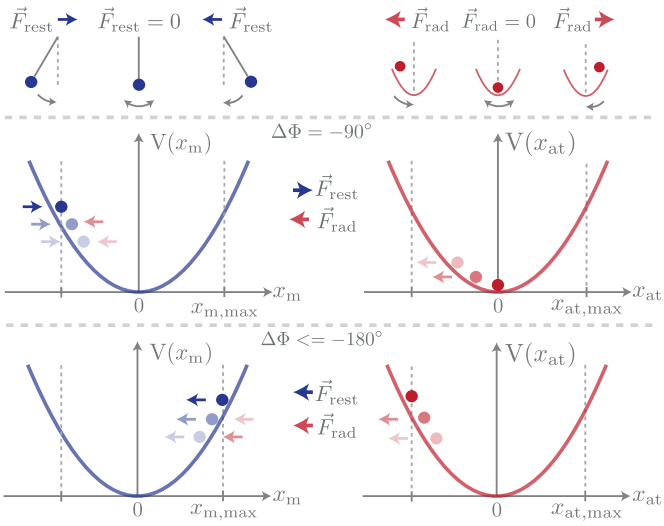

Figure 3.9: Coupling scenario for different $\Delta\Phi$
The resonator experiences a restoring force $\vec{F}_{\mathrm{rest}}$ towards the potential minimum. The atoms emit photons in either direction of the light field dependent on their displacement, resulting in a radiation pressure force $\vec{F}_{\mathrm{rad}}$. For $\Delta\Phi = -90°$, the atoms are located in the trapping potential relative to the resonator such that the resulting radiation pressure force $\vec{F}_{\mathrm{rad}}$ counteracts the restoring force $\vec{F}_{\mathrm{rest}}$. For phases $\Delta\Phi <= -180°$, the delay is so large that $\vec{F}_{\mathrm{rad}}$ and $\vec{F}_{\mathrm{rest}}$ always point in the same direction, leading to heating. The light shaded dots indicate the movement direction in the respective potentials.

The simulation verifies that for a symmetric lattice, the stability condition is fulfilled at all times for our system parameters. For the asymmetric configuration, the simulation shows a different behavior. For atom numbers $N_{\mathrm{at}} > 5.5 \cdot 10^7$ the stability condition is not fulfilled when approaching resonance ($\omega \to \omega_{\mathrm{m}}$). This effect intensifies for larger atom numbers until the phase lag approaches $\Delta\Phi \to -360°$ for $N_{\mathrm{at}} > 14.8 \cdot 10^7$. The large phase shift can be explained by density waves arising in the system that lead to accumulation of an additional phase lag between the input and output fields. As mentioned before. The simulation does not distinguish whether the lattice is in the red-detuned or blue-detuned regime, other than by the reduced lattice constant. It clearly shows a dependence on the number of atoms that are contributing to the coupling. Thus, we can conclude that the observed effect of hybrid instability in red-detuned lattices mainly arises due to the higher atomic densities.

These results raise the question whether it is feasible to compensate for the asymmetry by introducing an auxiliary beam that adds to the intensity of the back-reflected beam such that $I_{\mathrm{aux}} + I_{\mathrm{back}} = I_{\mathrm{inc}}$. This beam would have to be of the same mode as the back-reflex beam while maintaining a fixed phase relation. Assuming a relative phase of $\phi_{\mathrm{aux,back}}$ we can simply add this beam to the simulation by rewriting $B_1 = E_{\mathrm{back}} e^{ikx+i\Phi(t)} + E_{\mathrm{back}} e^{ikx+i\phi_{\mathrm{aux,back}}}$ with $E_{\mathrm{aux}} = \sqrt{(1-R)} E_{\mathrm{inc}}$. Using this expression on the simulation allows to predict the system behavior with a pump asymmetry compensated lattice. The result is presented in Fig. 3.10.

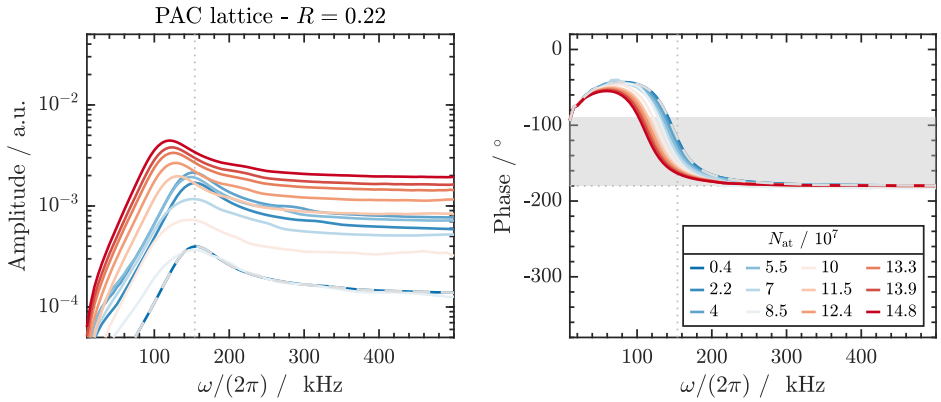

Figure 3.10: Response of the PAC lattice for different atom numbers N_{at}: Simulation of the relative amplitude A_{rel} and phase response of the outgoing modulated beam dependent on the modulation frequency ω with the phase referenced to the ingoing field modulation $\Phi(t)$ for a pump asymmetry compensated lattice. We introduce an auxiliary beam to the simulation with intensity $I_{aux} = 0.78 I_{inc}$ locked to the back-reflex beam at the phase $\phi_{aux,back} = \pi/2$. This yields a compensation of the lacking back-reflex intensity and an intensity balancing of the lattice. The dashed line is the simulated behavior for a single beamsplitter and the grey shaded area the region in which sympathetic cooling takes place. The simulation parameters are equivalent to the parameters in Fig. 3.8. The detuning is $\Delta_{at,L} = -9.6\,\text{GHz}$. Figure adapted from Ref. [63].

The simulation suggests the use of an auxiliary beam to compensate for the asymmetry to be feasible. The stability criterion is fulfilled for all configurations. The most prominent difference to the balanced case is the reduced amplitude modulation which can be explained by the much weaker modulation $\Phi(t)$ from the back-reflected beam.

Conclusion

Applying the model from Ref. [66] onto our system and numerically simulating the system dynamic based on Ref. [131] allowed for a better understanding of the coupling lattice dynamics in the red-detuned regime and the boundary at which the dynamic instability occurs. The simulation results are consistent with our own and other group's experimental observations and suggest that it is possible to overcome the detrimental effect of pump asymmetry by introducing an auxiliary beam that compensates the imbalance. The observed effects are summarized to [63]:

- Low laser atom detunings $\Delta_{at,L}$ yield higher atomic polarizabilities which benefit the emergence of collective effects.
- In an asymmetric lattice, collective effects are strongly dependent on the number of atoms participating in the coupling. The more atoms participate in the coupling, the lower the critical asymmetry upon which collective oscillations arise.
- The sign of the detuning does not have a direct effect on the dynamics. The observed instability in the red-detuned regime likely arises due to the attractive potential and the consequently higher atom numbers in the system.

3.2.4 Coupling experiments in the PAC lattice

Motivated by the findings in Chapter 3.2.2 we decided to implement a pump-asymmetry-compensation (PAC) beam to the experimental setup. The PAC beam requires to be excellently mode matched with the back-reflected beam from the cavity while also being locked to its phase. We achieve this by deriving the auxiliary beam from the coupling lattice incident beam. We adjust this beams shape to meet the geometry of the back-reflected beam and implemented a two-component phase lock with a low-bandwidth and high capture range piezo-lock and a free space EOM to account for fast frequency drifts. The results of these efforts and the influence on the hybrid coupling are presented in this chapter. The experimental setup and all measurements were done together with J. Butlewski[46] [63].

We investigate the influence of PAC on the hybrid system by measuring the sympathetic cooling rate of the oscillator Γ_{sym}. As introduced in equation 3.31, this parameter allows to directly deduct the hybrid cooperativity C_{hybrid}. As depicted in Fig. 3.2 the sympathetic cooling rate shows a specific resonance behavior dependent on the atomic trapping frequency ω_{at} relative to the resonator frequency ω_{m}. To investigate this behavior, particularly with respect to different asymmetries, we sweeped ω_{at} to obtain the lattice depth dependent sympathetic cooling rate $\Gamma_{\mathrm{sym}}(\omega_{\mathrm{at}})$. Since $V_{\mathrm{lat}} \propto I_{\mathrm{lat}}/\Delta_{\mathrm{at,L}}$ this sweep can either be achieved by changing the lattice power P_{lat} or the detuning to the atomic resonance $\Delta_{\mathrm{at,L}}$. Both methods affect the system differently. While changing the detuning mostly has an effect on the atomic part of the system, by higher scattering losses for near detunings, the change in coupling lattice power mainly effects the optomechanical part of the system by heating of the resonator and introducing thermal drifts of the cavity. For most of the experiments in this chapter we sweep the lattice detuning at a constant lattice power $P_{\mathrm{lat}} \approx 100\mu\mathrm{W}$. This comes at an advantage of high controllability. The detuning can be accurately set using the TiSa transfer-lock and the cavity length can be actively stabilized at the used lattice power using the optical spring lock [110].

The experiments presented here were conducted at room temperature, since it was not possible to cool down the cryostat (Appendix E). While this has no qualitative effect on the observed physics, it influences the system parameters. The optomechanical damping rate Γ_{m} is increased, such that the mechanical linewidth exceeds the optomechanical heating rate. Consequently, the system is more stable, less susceptible to optomechanical heating and does not require for additional radiation pressure cooling [47]. Furthermore, a higher bath temperature yields a higher acquired final mode temperature of the system. Because the system operates far from the quantum-coherent-oscillation regime, ground state cooling is not possible at room temperature.

[46] A detailed description and characterization of the setup used for PAC is presented in Ref. [63] and omitted in this thesis. A sketch of the PAC setup is depicted in Appendix A.2.

[47] This is a significant difference to the operation at base temperature where the high Q-factor and low mechanical linewidth require constant radiation pressure cooling to keep the system stable.

3.2.4.1 Experimental sequence

The coupling experiments were conducted with a compressed highly optically dense MOT (high-OD-MOT) as introduced in Ref. [76]. In previous experiments we found this configuration to yield the highest cooperativities. A sketch of the experimental sequence is presented in Fig. 3.11. The high-OD-MOT is created from the uncompressed MOT. After loading the uncompressed 3D-MOT from the 2D-MOT for 5 s with optimized loading parameters, the pushing beam is rapidly switched off and the trapping parameters are linearly ramped within 500 ms to a configuration that benefits high ODs. This yields:

- A strong increase of the magnetic field gradient
  $(5\,\mathrm{G/cm} \rightarrow 45\,\mathrm{G/cm})$
- Reducing the cooling light intensity
  $(I_0 = 31.5\,I_{\mathrm{sat}} = 52.6\,\mathrm{mW/cm^2} \rightarrow I_0 = 2.25\,I_{\mathrm{sat}} = 3.8\,\mathrm{mW/cm^2})$
- Increasing the cooling-light detuning
  $(\Delta_{\mathrm{MOT}} = 17.8\,\mathrm{MHz}\,(2.9\,\Gamma_{\mathrm{D_2}}) \rightarrow \Delta_{\mathrm{MOT}} = 37.8\,\mathrm{MHz}\,(6.2\,\Gamma_{\mathrm{D_2}}))$.

After reaching the final parameters, the coupling lattice is ramped up to its final power within 1 ms, and kept at a constant power for 3 s during which the coupling experiments take place. In case of the PAC experiments the auxiliary beam is phase stabilized within the first 50 ms after the lattice is ramped up. After the coupling experiment took place, the lattice is rapidly ramped down within 10 ms and the system re-thermalizes for 5 s after which the sequence starts over again.

The sympathetic cooling rate is derived from measurements of the mode temperature of the resonator T_{mode}. The mode temperature is acquired from the homodyne detection by measuring the power spectral density $S_{\mathrm{y}}(\omega)$ with a lock-in amplifier that

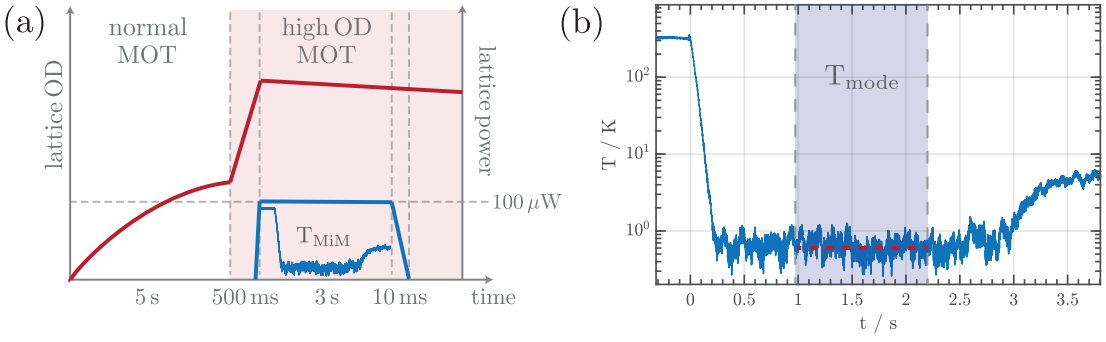

Figure 3.11: High-OD MOT sequence for sympathetic cooling:
(a): Sketch of the high OD MOT sequence. The red line denotes the OD of the MOT, the blue line the coupling lattice power. After loading the MOT for 5 seconds, the parameters are switched to high OD settings within 500 ms and the lattice power is ramped up to 100 μW within 1 ms. Coupling takes place in a 3 s time frame before the lattice power is ramped down within 10 ms. (b) Time trace of the resonator mode temperature. The mode temperature of a single cycle is acquired from the average temperature (red dashed line) of the blue shaded area. The final mode temperature is acquired from the average of 15 cycles. Figure (a) based on Ref. [76].

demodulates the signal at $\omega = \omega_\mathrm{m}$ to acquire the demodulator output $V_\mathrm{d}(t)$. For a sufficiently high SNR where the displacement PSD is higher than the detection imprecision noise $S_\mathrm{x}(\omega_\mathrm{m}) \gg S_\mathrm{x}^\mathrm{imp}$, $V_\mathrm{d}(t)$ is proportional to the integrated PSD and the mode temperature $\langle x^2(t)\rangle \propto T_\mathrm{mode}$. To avoid optomechanical heating the cavity is stabilized in the red-detuned regime where the resonator experiences moderate optomechanical cooling. The homodyne calibration for the presented PAC measurements is $|\partial\phi_\mathrm{x}/\partial x_\mathrm{m}| = (0.74 \pm 1)\,\mathrm{rad/nm}$.
Figure 3.11 shows a time trace of the resonator mode temperature during the experimental sequence. At t=0 the lattice is ramped up, followed by sympathetic cooling of the resonator. The final mode temperature, which is also used for calculation of the hybrid cooperativity is determined after 1 second in a window of 1.4 seconds (indicated as shaded area). After 3 seconds the lattice is switched off and the mode temperature rises during re-thermalization.
During the coupling, we require both the auxiliary phase lock and the active length stabilization of the cavity to hold. Due to the rapid ramp up of the coupling lattice and the sudden rise in the intra-cavity power accompanied by a fast increase of the optical spring of the resonator, we sometimes observe destabilization of either lock component. This becomes apparent in a reduced transmission of the cavity (i.e., the length stabilization lock breaks) or in a random relative phase signal between the auxiliary and back-reflected beam (i.e., the auxiliary phase lock breaks). The transmission and error signal of the phase lock are recorded for each measurement. Measurements that do not fulfill the stability requirements are omitted in the evaluation.

3.2.4.2 Pump asymmetry compensation in the red-detuned lattice

The asymmetric lattice showed the most detrimental effects on the hybrid system in the red-detuned coupling lattice regime only allowing for coupling experiments with atoms in an optical molasses at low atomic densities in comparison to a MOT [76]. We want to investigate whether alleviating the asymmetry allows to access new parameter regimes for sympathetic cooling, that were not possible before as predicted by the simulation presented in Section 3.2.2.
We determined the asymmetry with the cavity on resonance to $R = P_\mathrm{back}/P_\mathrm{inc} = 0.22 \pm 0.01$ [63]. If we lock the phase between the auxiliary and back-reflected beam at $\phi_\mathrm{aux,back} = \pi/2$, the lattice is balanced if $P_\mathrm{aux} = P_\mathrm{inc} - P_\mathrm{back}$ and the error signal of the lock exhibits a large slope. To determine the needed auxiliary power accurately we measure the incident and back-reflected beam powers and derive the respective light power incident on the atoms by taking into account all losses in the optical setup. The powers that are mentioned in the presented measurements already take losses in the system into account and refer to the powers at the site of the atoms.
To investigate the sympathetic cooling performance in a balanced red-detuned lattice we set the incident beam power to $P_\mathrm{inc} = (103 \pm 1)\,\mu\mathrm{W}$ and the auxiliary beam power is set to $P_\mathrm{aux} = 0.78 P_\mathrm{inc} = (81 \pm 1)\,\mu\mathrm{W}$. To investigate the resonance behavior, the lattice detuning is swept between $\Delta_{2,1} = -2.5\,\mathrm{GHz}$ and $\Delta_{2,1} = -184\,\mathrm{MHz}$[48].

[48] We refer to blue-detuning by $\Delta_{2,3}$ which describes the detuning relative to the $|F = 2 \rightarrow F' = 3\rangle$ transition and to red-detuning by $\Delta_{2,1}$ which describes the detuning relative to the $|F = 2 \rightarrow F' = 1\rangle$ transition.

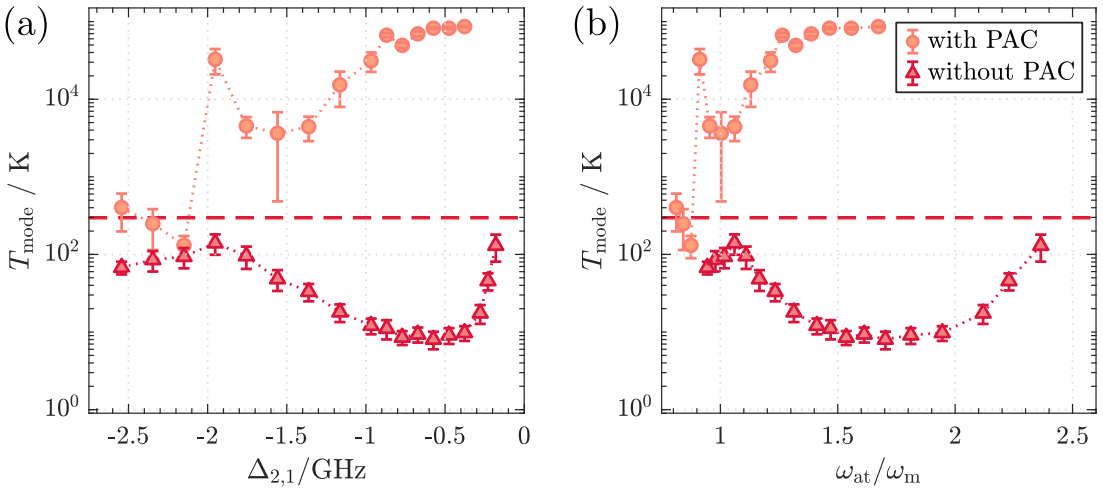

Figure 3.12: Hybrid coupling in the red-detuned PAC lattice:
Hybrid coupling experiments in a high-OD MOT for an uncompensated red-detuned lattice (light red) and a pump asymmetry compensated lattice (dark red). The lattice depth is varied by a detuning sweep of $\Delta_{2,1}$. (a) Resonator mode temperature measured for different detunings $\Delta_{2,1}$. (b) Resonator mode temperature dependent on the trapping frequency ω_{at}. The dashed line denotes the bath temperature of 293 K. All measurements were conducted at an incident coupling lattice beam power of $P_{\mathrm{inc}} = 103\,\mu\mathrm{W}$ with $P_{\mathrm{aux}} = 81\,\mu\mathrm{W}$, $P_{\mathrm{back}} = 21\,\mu\mathrm{W}$ and at a relative phase of $\phi_{\mathrm{auc,back}} = 0.78\pi$. Figure from Ref. [63].

Figure 3.12 shows the mode temperature of the resonator in this configuration for different detunings and lattice depths in comparison to the case where the lattice is not pump asymmetry compensated. While the system with the unbalanced lattice shows the same behavior as in previous experiments (i.e., the resonator is driven into limit cycles if the resonance condition is fulfilled), the compensated lattice actually shows significant, sympathetic cooling in the previously inaccessible, red-detuned regime with a final mode temperature of $T_{\mathrm{mode}} = (8 \pm 2)\,\mathrm{K}$.

This observation further supports the theory, that pump asymmetry is the main cause for the hybrid instability and shows, that its effects can be compensated. Interestingly, we observed sympathetic cooling to occur not in the balanced case at a relative auxiliary, back-reflex phase of $\phi_{\mathrm{aux,back}} = \pi/2$ but at a relative phase of $\phi_{\mathrm{aux,back}} = 0.78\pi$. At this phase both beams destructively interfere which yields a reduced power of the compensated back-reflex beam of $P_{\mathrm{ref,tot}} = 38.5\,\mu\mathrm{W}$. This is an unexpected result. Although, PAC makes it possible to work in the red-detuned regime, it requires the relative phases between auxiliary and back-reflex beam to be set such that the new lattice is still imbalanced. At the same time a configuration in which the lattice is theoretically balanced still shows hybrid instability. This result motivated us to investigate the parameters, for which PAC works, more closely.

3.2.4.3 Optimization of PAC parameters

The findings of the previous section require to further investigate the parameter regime in which PAC works. A balanced lattice can be acquired from different combinations of auxiliary beam powers P_{aux} and relative phases $\phi_{\mathrm{aux,back}}$. To find the best parameters of the compensated lattice we tuned both parameters and swept the relative phase $\phi_{\mathrm{aux,back}}$ for different ratios $P_{\mathrm{aux}}/P_{\mathrm{inc}}$. The results are depicted in Fig. 3.13.

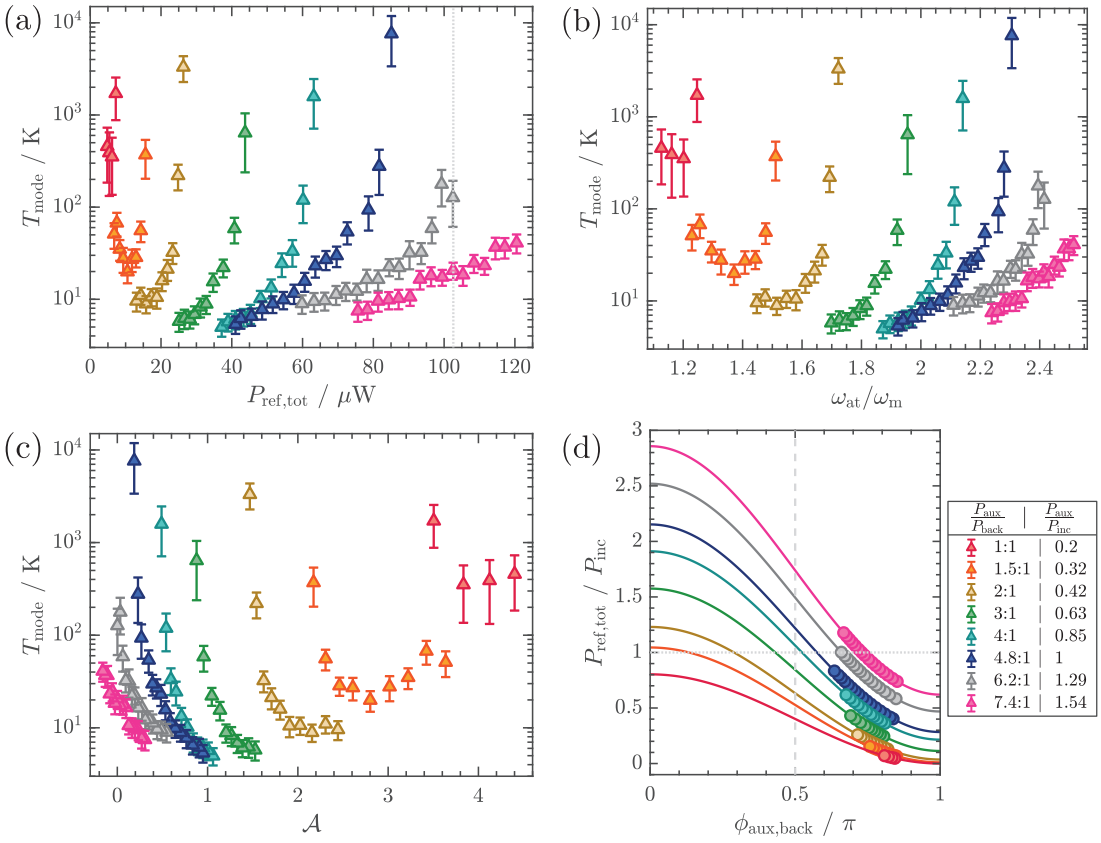

Figure 3.13: Hybrid coupling in the red-detuned PAC lattice at different auxiliary beam settings:
To identify the parameters in the compensated lattice that yield the highest cooperativities, we investigate the sympathetic cooling for different power ratios $P_{\mathrm{aux}}/P_{\mathrm{inc}}$. Each color yields a different power ratio. For each ratio the compensated back-reflex beam power $P_{\mathrm{ref,tot}}$ is varied by changing the relative phase $\phi_{\mathrm{aux,back}}$. For each power ratio, $\phi_{\mathrm{aux,back}}$ is varied until sympathetic cooling is not possible anymore to cover the whole parameter space in which cooling occurs. (a) Mode temperature dependent on the compensated back-reflex beam power $P_{\mathrm{ref,tot}}$. The grey dashed line shows the power at which the lattice would be balanced. (b) Mode temperature over the corresponding trapping frequency in units of the resonance frequency ω_{m}. (c) Mode temperature dependent on the systems asymmetry (equation 3.32). The lowest temperature is achieved at $\mathcal{A} = 1$ and rises towards $\mathcal{A} \to 0$. (d) Total power of back-reflex and auxiliary beam dependent on their relative phase. The lines resemble the two-beam interference signal for the phase $\phi_{\mathrm{aux,back}}$. The colored dots indicate the lock points on the slopes at which the individual measurements from (a-c) were conducted. Note that except for the traces with $P_{\mathrm{aux}}/P_{\mathrm{inc}} <= 0.42$ the lowest mode temperatures were acquired at the highest $\phi_{\mathrm{aux,back}}$ at the bottom of the interference signal. Experimental parameters: $P_{\mathrm{inc}} = (103 \pm 1)\,\mu$W, $P_{\mathrm{back}} = (21.4 \pm 0.5)\,\mu$W and $\Delta_{2,1} = -475\,$MHz. Figure from Ref. [63].

All measurements were done at an incident power of $P_{\mathrm{inc}} = (103 \pm 1)\,\mu\mathrm{W}$. Each color corresponds to one power ratio between auxiliary and incident beam. The compensated back-reflected beam power is adjusted $P_{\mathrm{ref,tot}}$ via the relative phase $\phi_{\mathrm{aux,back}}$ which is depicted in Fig. 3.13(c). Notably, cooling only occurs for phase settings $\phi_{\mathrm{aux,back}} > 0.6\pi$ which corresponds to a lock point at the bottom of the interference signal. For low auxiliary powers ($P_{\mathrm{aux}} < 0.42\,P_{\mathrm{inc}}$), the mode temperature dependent on $P_{\mathrm{ref,tot}}$ exhibits local minima which suggests, that an optimal phase setting exists for these configurations. For higher auxiliary lattice powers such a minimum is not observable and the point of strongest sympathetic cooling corresponds to the maximum possible value of $\phi_{\mathrm{aux,back}}$ (which is limited by the stability of the lock near the anti-node of the interference signal.). This point also corresponds to the point of maximum destructive interference between both beams and thus still yields an asymmetric lattice configuration for most beam settings.

More surprisingly the measurements suggest, that the lowest mode temperature is achieved for a ratio $P_{\mathrm{aux}} : P_{\mathrm{inc}} = (0.85 : 1)$ and $(1 : 1)$ at a configuration where the asymmetry is $\mathcal{A} = 1$. For $\mathcal{A} \to 0$ the cooling performance even slightly decreases. Also, this balanced configuration can be achieved only for power ratios $P_{\mathrm{aux}} : P_{\mathrm{inc}} > (1.5 : 1)$. To further investigate the previously found optimal PAC-lattice configurations, we measure the resonance behavior of the system for the cases of strongest sympathetic cooling and for the balanced lattice. We set the power ratios and the rel-

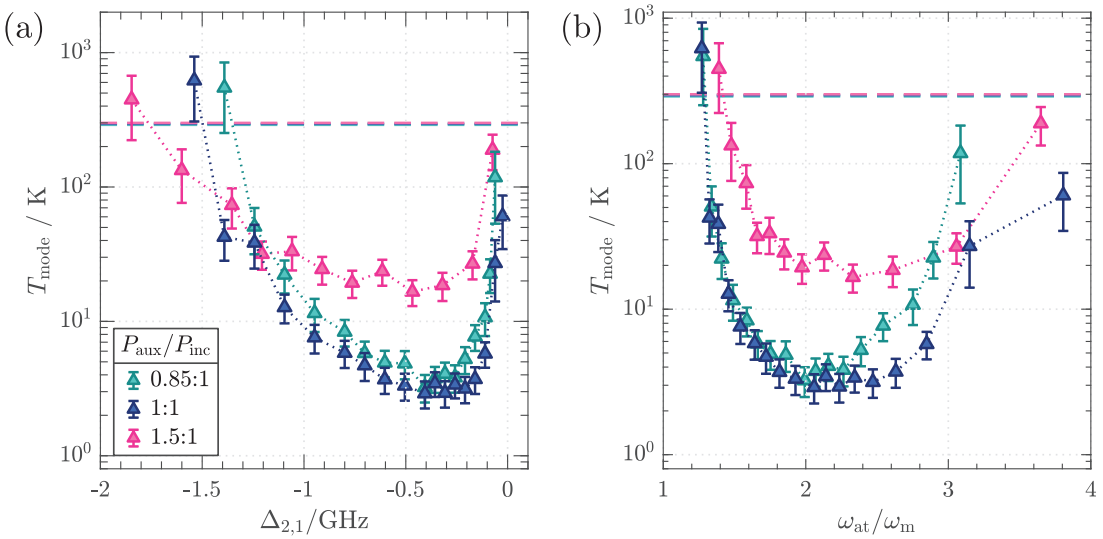

Figure 3.14: Hybrid coupling in the red-detuned PAC for optimized settings: Hybrid coupling experiments in a high-OD MOT for a PAC compensated red-detuned lattice dependent on the resonant lattice depth for the parameters with the lowest mode temperature (blue shades) and a compensated lattice (magenta). The lattice depth is varied by a detuning sweep of $\Delta_{2,3}$. (a): Resonator mode temperature measured for different detunings $\Delta_{2,1}$. (b): Resonator mode temperature dependent on the trapping frequency ω_{at}. The dashed line denotes the bath temperature of 293 K. All measurements were conducted at a incident coupling lattice beam power of $P_{\mathrm{inc}} = (103 \pm 1)\,\mu\mathrm{W}$ and $P_{\mathrm{back}} = (21 \pm 0.5)\,\mu\mathrm{W}$. The relative phases are $\phi_{\mathrm{aux,back,0.85:1}} = 0.76\pi$, $\phi_{\mathrm{aux,back,1:1}} = 0.81\pi$ and $\phi_{\mathrm{aux,back,1.5:1}} = 0.57\pi$. At these settings we acquire the mode temperatures: $T_{\mathrm{min,0.85:1}} = (3.2 \pm 0.8)\,\mathrm{K}$, $T_{\mathrm{min,1:1}} = (2.9 \pm 0.7)\,\mathrm{K}$ and $T_{\mathrm{min,0.1.5:1}} = (17 \pm 4)\,\mathrm{K}$. Figure from Ref. [63].

ative phase to the optimal values found in the previous measurement and sweep the lattice detuning $\Delta_{2,3}$. The acquired mode temperatures dependent on the detuning and the derived trapping frequencies are depicted in Fig. 3.14. The cooling curve for $P_{\mathrm{aux}} : P_{\mathrm{inc}} = (0.85 : 1)$ and $(1 : 1)$ $(\mathcal{A} \approx 1)$ qualitatively resembles the same behavior as for an unbalanced, blue-detuned lattice (Fig. 3.16) with the minimal mode temperatures ($T_{\mathrm{min,0:85:1}} = (3.2 \pm 0.8)\,\mathrm{K}$, $T_{\mathrm{min,1:1}} = (2.9 \pm 0.7)\,\mathrm{K}$) acquired at $\omega_{\mathrm{at}} \approx 2\,\omega_{\mathrm{m}}$[49]. For the configuration with $P_{\mathrm{aux}} : P_{\mathrm{inc}} = (1.5 : 1)$ $(\mathcal{A} \approx 0)$ this minimum is slightly shifted and the region in which cooling is observed is broader. There is a significant difference in the final mode temperature since the balanced configuration only reaches $T_{\mathrm{min,1:1}} = (17 \pm 4)\,\mathrm{K}$. The measurements of the trapping frequency dependent final mode temperature allow to determine the sympathetic cooling rate and the hybrid cooperativity of the balanced system. Using equation 3.23 we calculate the sympathetic cooling rate Γ_{sym} at the respective trapping frequencies ω_{at}. We can expect a resonance behavior according to the model of the ensemble integrated sympathetic cooling rate presented in Section 3.1.1 and deduct $\Gamma_{\mathrm{sym,max}}$ and the hybrid cooperativity. The results are presented in Fig. 3.15. The hybrid cooperativities for the individual PAC lattice configurations are:

$$C^{\mathrm{noPAC}}_{\mathrm{hybrid,0.85:1}} = 90 \pm 20 \quad C^{\mathrm{PAC}}_{\mathrm{hybrid,1:1}} = 100 \pm 20 \quad \text{and} \quad C^{\mathrm{PAC}}_{\mathrm{hybrid,1.5:1}} = 17 \pm 4 \tag{3.51}$$

The resulting cooperativities are lower than in the unbalanced blue-detuned case that is presented in the next Section 3.2.4.4[50].

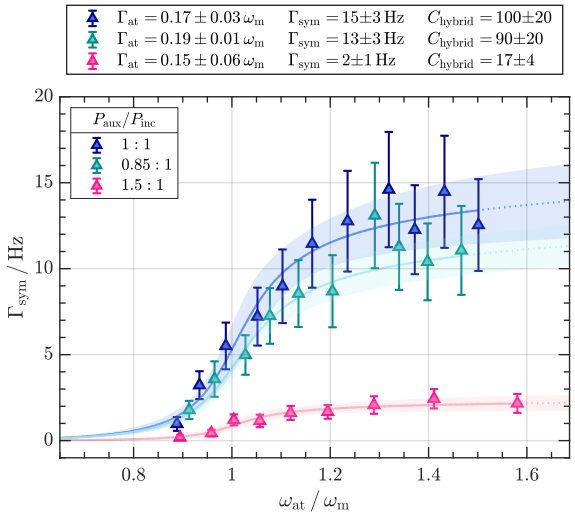

Figure 3.15: Sympathetic cooling rates in the red-detuned PAC lattice
Γ_{sym} calculated from equation 3.19 using the in Fig. 3.14 acquired mode and bath temperatures. The data are fitted with expression 3.23. The x-axis is rescaled to fulfill the resonance condition. The light shaded areas denote the 2σ confidence bounds of the fits. Data points that show a decreasing Γ_{sym} for higher lattice depths are omitted. Figure adapted from Ref. [63].

[49] The observed cooling at multiple ω_{m} comes from the Gaussian intensity profile of the beam that is not accounted for in the lattice depth calibration. It is accounted for in the calculation of the ensemble integrated sympathetic cooling rate that is used to determine C_{hybrid}.

[50] A parameter that remained undiscussed in this section is the incident beam power. Measurements where P_{inc} was swept at the optimized PAC settings, suggest a optimal beam power at $P_{\mathrm{inc}} = 65\,\mu\mathrm{W}$ [63]. However, the improvement turned out to be insignificant compared to the performance in the blue-detuned lattice.

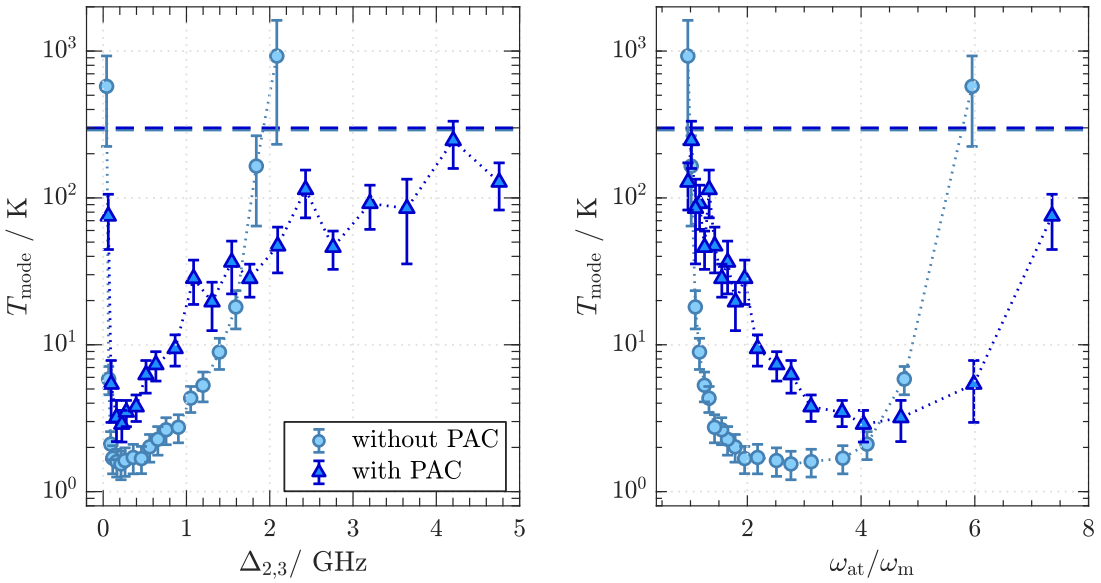

Figure 3.16: Hybrid coupling in the blue-detuned lattice without PAC and for optimized PAC settings:
Hybrid coupling experiments in a high-OD MOT for an uncompensated blue-detuned lattice and a PAC lattice with optimized parameters found in Section 3.2.4.3. The lattice depth is varied by a detuning sweep of $\Delta_{2,3}$. (a) Resonator mode temperature measured for different detunings $\Delta_{2,3}$. (b) Resonator mode temperature dependent on the trapping frequency ω_{at}. The dashed line denotes the bath temperature of 293 K. All measurements were conducted at a incident coupling lattice beam power of $P_{\mathrm{inc}} = 103\,\mu\mathrm{W}$ and $P_{\mathrm{back}} = 21\,\mu\mathrm{W}$. The relative phases for the PAC case is $\phi_{\mathrm{aux,back,1.5:1}} = 0.57\pi$. At these settings we acquire the mode temperatures: $T_{\mathrm{min,noPAC}} = (1.5 \pm 0.3)\,\mathrm{K}$ and $T_{\mathrm{min,PAC}} = (2.9 \pm 0.7)\,\mathrm{K}$. Figure from Ref. [63].

3.2.4.4 Pump asymmetry compensation in the blue-detuned lattice

Previous experiments showed the highest cooperativities to occur in the blue-detuned regime [62, 63] where no hybrid instability was observed. Thus, we investigate the impact of a PAC lattice in this regime at the previously found optimal parameter sets.
We set the incident beam power to $P_{\mathrm{inc}} = (103 \pm 1)\,\mu\mathrm{W}$ and the auxiliary beam power to $P_{\mathrm{aux}} = 0.78 P_{\mathrm{inc}} = (81 \pm 1)\,\mu\mathrm{W}$. The lattice detuning is swept between $\Delta_{2,3} = 5\,\mathrm{GHz}$ and $\Delta_{2,3} = 50\,\mathrm{MHz}$.
Figure 3.16 shows the resonance behavior of the mode temperature for different detunings and lattice depths comparing the PAC case with the uncompensated lattice. Clearly it is possible to sympathetically cool in the blue-detuned regime in a compensated lattice and it is possible to cool the resonator from room temperature to a final mode temperature of $T_{\mathrm{mode}} = 3\,\mathrm{K}$. The region, in which the PAC lattice can be operated is very narrow and the relative phase has to be set around $\phi_{\mathrm{aux,back}} = 0.5\pi$ to observe sympathetic cooling in contrast to the red-detuned case. In the uncompensated lattice the minimal mode temperature achieved is $T_{\mathrm{min,mode}} = (1.5 \pm 0.3)\,\mathrm{K}$. For the PAC lattice the temperature is higher ($T_{\mathrm{min,mode}} = (2.9 \pm 0.7)\,\mathrm{K}$) and shifted with respect to the resonance condition as it is acquired at $\omega_{\mathrm{at}} \approx 4\omega_{\mathrm{m}}$. Determining the sympathetic

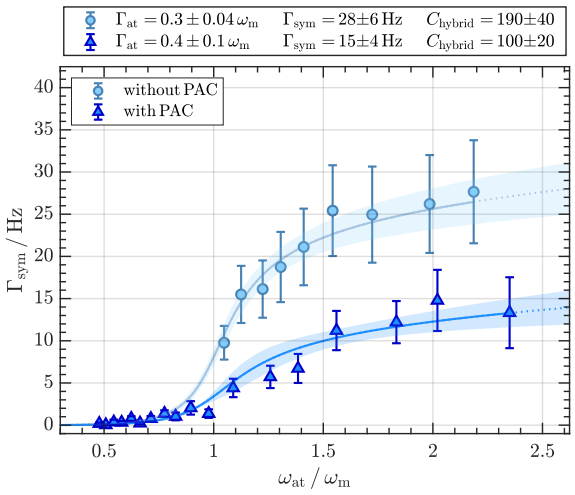

Figure 3.17: Sympathetic cooling rates in the blue-detuned lattice
Γ_{sym} calculated from equation 3.19 using the in Fig. 3.16 acquired mode and bath temperatures. Expression 3.23 is fitted onto the data. The x axis is rescaled to fulfill the resonance condition. The light shaded areas denote the 2σ confidence bounds of the fits. Data points that show a decreasing Γ_{sym} for higher lattice depths are omitted. Notably the PAC lattice yields much lower cooperativities than the lattice without PAC. Figure adapted from Ref. [63].

cooling rates (Fig. 3.17) and the hybrid cooperativities leads to the following results:

$$C_{\text{hybrid}}^{\text{noPAC}} = 190 \pm 40 \qquad \text{and} \qquad C_{\text{hybrid}}^{\text{PAC}} = 100 \pm 20 \tag{3.52}$$

While PAC works in the blue-detuned regime the resulting cooperativities are significantly inferior to the uncompensated blue-detuned case. The worse cooling performance in the compensated blue-detuned lattice might be explained by increased scattering losses. Previous experiments on the system in the blue-detuned regime showed similar behavior when increasing the lattice power. P. Christoph observed in Ref. [76] that the minimal achieved mode temperature increased by a factor of 1.6 (in our case a factor of 1.9) for a lattice power increase by a factor of 4. Another possible explanation, although not experimentally verified, would be additional noise introduced to to the system by the auxiliary beam such as residual phase noise or small local disturbances in the combined mode profile of the compensated beam.

3.2.4.5 Conclusion

Performing coupling experiments with a red-detuned coupling lattice was a promising idea but did not show the anticipated improvements. To understand the underlying mechanisms of the hybrid instability, that is an intrinsic property of systems like ours, we took a close look on the effects pump asymmetry has on a 1D coupling lattice and discussed the emerging static and dynamic effects. We simulated the dynamics of our system with a numerical simulation based on Ref. [131] and could not only verify the emergence of the hybrid instability in our system, but also extend the model to predict the effects of introducing an auxiliary compensation beam to alleviate the asymmetry. Based on this finding we implemented a pump-asymmetry-compensation lattice and investigated the performance in both the blue and red-detuned regime and for different power ratios. The measurements in the PAC lattice showed, that the destabilizing effect of pump asymmetry can be alleviated which allows to operate the hybrid system in new parameter spaces. We observe sympathetic cooling in the previously inaccessible, red-detuned regime. Surprisingly, the highest cooperativities are not achieved for the

balanced configuration but for an asymmetry of $\mathcal{A} = 1$ at $P_{\mathrm{aux}} = P_{\mathrm{inc}}$. Overall, the highest achieved cooperativity in the red-detuned regime is by a factor 2 smaller than for the unbalanced blue-detuned coupling lattice.
While the experiments showed PAC to also work in the blue-detuned regime, the requirements for it to work differ from the red-detuned regime. Cooling the blue lattice could only be observed for a balanced configuration ($\mathcal{A} \approx 0$). Other configurations exhibited heating of the resonator. The maximum cooperativities in the PAC lattice were inferior to the uncompensated configuration. An overview of the highest achieved cooperativities in the respective configurations shows:

Blue lattice	$T_{\mathrm{min}}^{\mathrm{mode}}$	$\Gamma_{\mathrm{sym}}^{\mathrm{max}}$	C_{hybrid}
without PAC	$1.5 \pm 0.3\,\mathrm{K}$	$28 \pm 6\,\mathrm{Hz}$	190 ± 40
with PAC	$2.9 \pm 0.7\,\mathrm{K}$	$15 \pm 4\,\mathrm{Hz}$	100 ± 25
Red lattice			
with PAC	$2.9 \pm 0.7\,\mathrm{K}$	$14.5 \pm 3.5\,\mathrm{Hz}$	100 ± 25

Here it becomes apparent, that the highest cooperativities for the PAC experiments in the red and blue-detuned regime are similar. This observation suggests that the use of PAC cannot increase the coupling strength, although it makes sympathetic cooling possible in both red- and blue- detuned lattices.
We conclude that PAC is not a viable option to increase the system cooperativity and that other approaches have to be pursed. Another parameter that significantly can improve the cooperativity is the cavity finesse. In Section 3.1.1 we found a finesse of $\mathcal{F} = 600$ to yield the highest improvement in cooperativity. In the next chapter we will enter this regime with the new cavities from Ref. [67] and investigate their influence on the hybrid coupling.

3.3 High finesse cavities for enhanced coupling strength

In Section 3.1.2 we derived the impact of the cavity finesse on the optomechanical coupling and determined the optimal finesse for the system to $\mathcal{F}_{4K} = 600$ and $\mathcal{F}_{293K} = 3300$. The new cavities from [67] allow to be adjusted to values of $\mathcal{F}_{low} = (650 \pm 50)$ and $\mathcal{F}_{high} = (1500 \pm 100)$. In contrast to the experiments that were conducted at lower finesses, the new system exhibits a much higher optical spring effect and thus significant optomechanical cooling rates. Figure 3.18 shows the optomechanical damping rates at a lattice power P_{lat}[51] acquired from the optical spring measurements in Section 2.3.3. Fitting a linear function allows to calculate the power dependence of the optomechanical damping rate $\partial\Gamma_{opt}/\partial P_{lat}$ if the system is aligned to experience maximum optical spring:

$$\frac{\partial\Gamma_{opt,\mathcal{F}=650}}{\partial P_{lat}} = 18.1 \pm 0.4\,\frac{\text{mHz}}{\mu\text{W}} \quad \text{and} \quad \frac{\partial\Gamma_{opt,\mathcal{F}=1500}}{\partial P_{lat}} = 174 \pm 12\,\frac{\text{mHz}}{\mu\text{W}} \tag{3.53}$$

The high damping rates have implications for the measurements conducted in this system. Already at lattice powers of $1\,\mu$W the optomechanical cooling is similar to the mechanical damping rate of the system (Tbl. 2.1). This makes the system very sensitive and unstable when switching on the coupling lattice coupling lattice which is usually operated in the range of $10 - 100\,\mu$W. If the system is not continuously cooled (e.g., by sympathetic or radiation pressure cooling) and brought on resonance such that $\Delta = \omega_{cav} - \omega_{TiSa} = 0$, even small drifts of the resonator towards the side of optomechanical heating, drive the system into limit cycles.
For experiments that require cycled runs, e.g., coupling experiments with the compressed MOT, this unstable behavior renders it impossible to operate the system at a detuning of $\Delta \to 0$. One option to counteract this behavior would be continuous radiation pressure cooling [62, 136, 137]. Although the feedback cooling scheme was implemented in the new system, and allowed cooling to similar final mode temperatures (Appendix C) as in Ref. [62], it is not fully applicable to cycled experiments as it requires for continuous measurement of the resonator state.

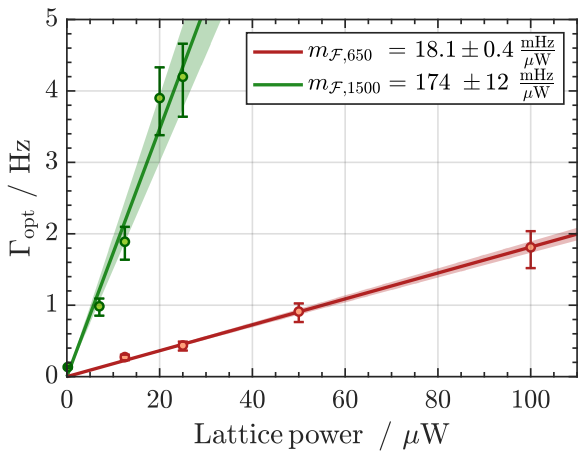

Figure 3.18: Optomechanical cooling dependent on finesse and lattice power: Γ_{opt} determined from the optical spring measurements in Fig. 2.13 for different coupling lattice powers P_{lat}. For a set lattice power, the maximum optical spring was determined to calculate Γ_{opt} using equation 2.21. Green data points denote measurements at $\mathcal{F} = 1500$, red data points measurements at $\mathcal{F} = 650$. The dark lines are linear fits $f(x) = m \cdot x$. The lighter shades denote the 2σ confidence bounds of the fits.

[51] Measured in front of the glass cell.

Due to the 30 times larger optical spring[52] that the resonator experiences when the coupling lattice is ramped up, the change in ω_m in combination with slight drifts of the cavity on the optomechanical heating side regularly lead to limit cycle oscillations despite active radiation pressure cooling.

Another option is choosing the detuning of the optomechanical system such that the resonator always experiences optomechanical cooling (i.e., at the point of maximum optical spring). Here we can calculate the optomechanical cooling rate according to equation 3.53. During the experiments we found this option to be favorable as it yielded the highest stability and showed reproducible results.
We conducted hybrid coupling experiments both with a continuously loaded, uncompressed MOT and a high OD MOT in a cycled experiment. Based on the findings in the previous section we decided to only work with the blue-detuned coupling lattice. Because of persisting issues with the cryostat, the measurements presented here were conducted at room temperature. Since the optomechanical properties of the new system are more sensitive to slight misalignment, the system has to be characterized on a daily basis when operated at room temperature. Thus, the homodyne calibration and the reflectivity on resonance vary slightly between the measurements. The averaged value of both quantities for the individual measurements is denoted by subscripts in the respective figures.

3.3.1 Coupling experiments with a MOT

The uncompressed MOT is continuously loaded from the 2D-MOT with the settings described in section 3.2.4.1. During the experiments, the coupling lattice is constantly switched on. This allows to align the system close to $\Delta = 0 \pm 1\,\mathrm{GHz}$ without the system getting unstable as long as the sympathetic cooling rate is large enough. Thus, we assume the bath temperature to be equal to room temperature $T_\mathrm{bath} = 293\,\mathrm{K}$ and that there is no reduction in the initial phonon occupation of the resonator by additional optomechanical cooling. By choosing the proper alignment we adjust the system to operate in the high and low finesse configuration to investigate the influence of the finesse on the hybrid cooperativity.

Low finesse configuration

The low finesse configuration of $\mathcal{F}_\mathrm{low} = (650 \pm 50)$ with a continuously loaded MOT exhibits strong sympathetic cooling. Figure 3.19 shows the acquired minimal mode temperature for different coupling lattice incident beam powers P_inc.
Fig. 3.19(a) shows the resonance behavior of the system and the acquired mode temperature dependent on the atomic trapping frequency ω_at. Fig. 3.19(b) depicts the mode temperature dependent on the laser-atom detuning $\Delta_{2,3}$. Qualitatively we observe a similar behavior as already observed in Ref. [76]. The minimal acquired mode temperature decreases for lower coupling lattice powers. For higher lattice powers ($P_\mathrm{lat} > 50\,\mu\mathrm{W}$) the resonance behavior shows a minimum in mode temperature around $\omega_\mathrm{at} = 3\,\omega_\mathrm{m}$.

[52] That is for the $\mathcal{F} = 1500$ configuration.

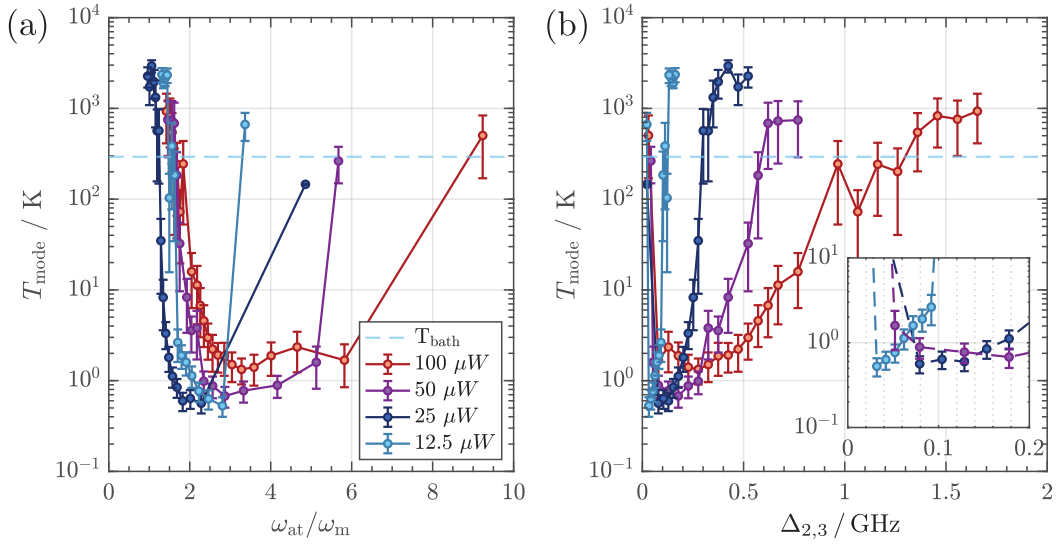

Figure 3.19: Hybrid coupling with an uncompressed MOT for $\mathcal{F} = 650$:
Hybrid coupling experiments at the low finesse configuration in a blue-detuned coupling lattice for different coupling lattice powers P_{lat}. (a) Resonance behavior of the mode temperature T_{mode} dependent on the trapping frequency in units of ω_{m}. The lattice depth is varied by sweeping the detuning $\Delta_{2,3}$. (b) Acquired mode temperature dependent on the detuning $\Delta_{2,3}$. Inset: Zoom into the resonance behavior for small detunings ($0 - 200\,\mathrm{MHz}$). The detuning of the $12.5\,\mu\mathrm{W}$ lattice is varied from 22 MHz to 162 MHz in steps of 10 MHz using the improved transfer lock. The dashed line denotes the bath temperature $T_{\mathrm{bath}} = 293\,\mathrm{K}$. The mode temperature is determined by averaging over five 10 s time traces of the of the integrated PSD. The homodyne calibration for these measurements is $|\frac{\partial\Phi}{\partial x_{\mathrm{m}}}| = (4.0 \pm 0.3)\frac{\mathrm{rad}}{\mathrm{nm}}$. The reflectivity on resonance was $\sigma = (0.8 \pm 0.02)$

The mode temperature shows a constant decrease for $\Delta_{2,3} \to 0$ and higher lattice depths until it suddenly rises when hitting the atomic resonance. This behavior can be interpreted as the vanishing of the optical lattice due to the high OD of the atomic cloud near resonance and for low lattice powers[53]. Conducting coupling experiments at $12.5\,\mu\mathrm{W}$ power requires very accurate control of the lattice detuning to get meaningful results. The resonance condition is only fulfilled for detunings $\Delta_{2,3} < 100\,\mathrm{MHz}$. The newly tunable transfer lock allows for accurate[54] measurements in the very near detuned regime. We reach a minimal mode temperatures of $T_{\mathrm{mode},100} = (1.3 \pm 0.4)\,\mathrm{K}$, $T_{\mathrm{mode},50} = (0.7 \pm 0.2)\,\mathrm{K}$, $T_{\mathrm{mode},25} = (0.6 \pm 0.1)\,\mathrm{K}$ and $T_{\mathrm{mode},12.5} = (0.5 \pm 0.1)\,\mathrm{K}$. Here we see an improvement over the old system. As presented in Fig. 3.16, the minimal mode temperature with a blue-detuned lattice for $T_{\mathrm{bath}} = 293\,\mathrm{K}$ was $T_{\mathrm{min}}^{\mathrm{mode}} = (1.5 \pm 0.3)\,\mathrm{K}$. This yields a factor of three lower mode temperature and indicates the stronger coupling that can be achieved with the higher finesse.

We use the acquired mode temperatures to determine the sympathetic cooling rate and thus, the hybrid cooperativity of the system. The results are presented in Fig. 3.20. While there is a significant improvement in cooperativity between the 100 μW and 50 μW coupling lattice, the highest reached cooperativities for the lattice settings

[53] This phenomenon is investigated in detail in Section 3.3.3 and shows to pose a limit on the cooperativity the system can reach.

[54] We tune the coupling lattice in steps of 10 MHz.

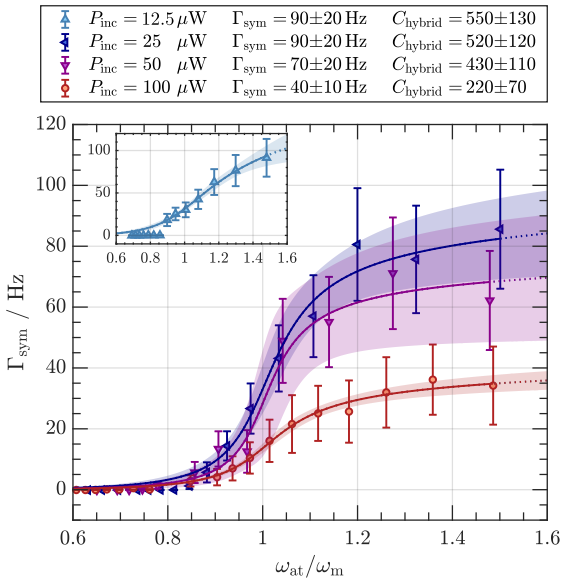

Figure 3.20: Sympathetic cooling rates for an uncompressed MOT at $\mathcal{F} = 650$: Γ_{sym} calculated from equation 3.19 using the mode and bath temperatures from Fig. 3.19. Expression 3.23 is fitted onto the data. The x axis is rescaled to fulfill the resonance condition. The light shaded areas denote the 2σ confidence bounds of the fits. Data points that show a decreasing Γ_{sym} for higher lattice depths are omitted. Inset: Γ_{sym} with the according fits for $P_{lat} = 12.5\,\mu W$. Since this plot intersects with the others it was plotted separately for a better overview.

$P_{lat} < 100\,\mu W$ are roughly similar within the determined error margins. Notably, the shape of the $12.5\,\mu W$ curve differs from the curves of higher lattice powers, indicating a higher atomic damping rate Γ_{at}. In this configuration the system reaches the following cooperativities:

$P_{lat,inc}$	$100\,\mu W$	$50\,\mu W$	$25\,\mu W$	$12.5\,\mu W$
C_{hybrid}	220 ± 70	430 ± 110	520 ± 120	550 ± 130

The highest cooperativity is a factor 2.5 higher than the previously acquired cooperativity in the uncompensated blue-detuned lattice ($C_{hybrid} = 190\pm20$) at room temperature and even a factor 1.5 higher than in the cooperativity we reached in an uncompensated, blue-detuned lattice at base temperature ($C_{hybrid} = 350 \pm 70$).

High finesse configuration

When aligned to the high finesse configuration, the parameter space in which the system can operate becomes narrower. At lattice powers of $25\,\mu W$ the system behaves very unstable and spontaneous heating of the resonator can occur for any alignment as far as no additional cooling is introduced. This behavior was previously not observed in our system because it was operated in a semi-stable regime where the cavity linewidth exceeded the frequency shift $\omega_{cav}(x_m)$ introduced by the resonator by orders of magnitude. For the high finesse configuration we enter a new regime of operation. Here the cavity linewidth is only $\kappa_{high} = (7.6 \pm 0.2)$ GHz and comparable with the frequency shift the resonator can cause. The expected frequency shift at a given lattice power can be calculated. Assuming a intra-cavity photon lifetime of $\tau_{cav} = 1/\kappa \approx 130\,ps$ we can calculate the number of intra-cavity photons for a lattice power of 25 μW and the cavity

frequency shift it causes at a given single photon coupling rate $g_{0,\mathrm{high}} = 2\pi \cdot 204\,\mathrm{kHz}$:

$$N_{\mathcal{F}=1500,25} = \frac{25\mu\mathrm{W} \cdot \tau_{\mathrm{cav}}}{\hbar\omega_{\mathrm{TiSa}}} \approx 13000 \quad \Rightarrow \quad \Delta\omega_{\mathrm{cav}} = g_{0,\mathrm{high}} \cdot N_{\mathcal{F}=1500,25} \approx 2.7\,\mathrm{GHz} \tag{3.54}$$

Comparing this to the system at $\mathcal{F} = 650$ with 25 μW, $\kappa_{\mathrm{low}} = (17.5 \pm 0.7)$ GHz and $\tau_{\mathrm{cav}} = 1/\kappa \approx 60\,\mathrm{ps}$ the cavity frequency shift at a given single photon coupling rate $g_{0,\mathrm{low}} = 2\pi \cdot 72\,\mathrm{kHz}$ yields:

$$N_{\mathcal{F}=650,25} = \frac{25\mu\mathrm{W} \cdot \tau_{\mathrm{cav}}}{\hbar\omega_{\mathrm{TiSa}}} \approx 5600 \quad \Rightarrow \quad \Delta\omega_{\mathrm{cav}} = g_{0,\mathrm{low}} \cdot N_{\mathcal{F}=650,25} \approx 0.4\,\mathrm{GHz} \tag{3.55}$$

If the finesse is sufficiently high, the resonator can shift the cavity resonance frequency on the order of the cavity linewidth. This leads to an unpredictable behavior on resonance, as large amplitudes can arbitrarily shift the system from the side of optomechanical cooling to the side of optomechanical heating. At high lattice powers these spontaneous heating events are regularly observed, even at high sympathetic cooling rates[55]. They manifest as short spikes in the time-dependent, integrated PSD signal. We omit regions in the PSD traces that show these features, as they do not resemble the resonant hybrid system.

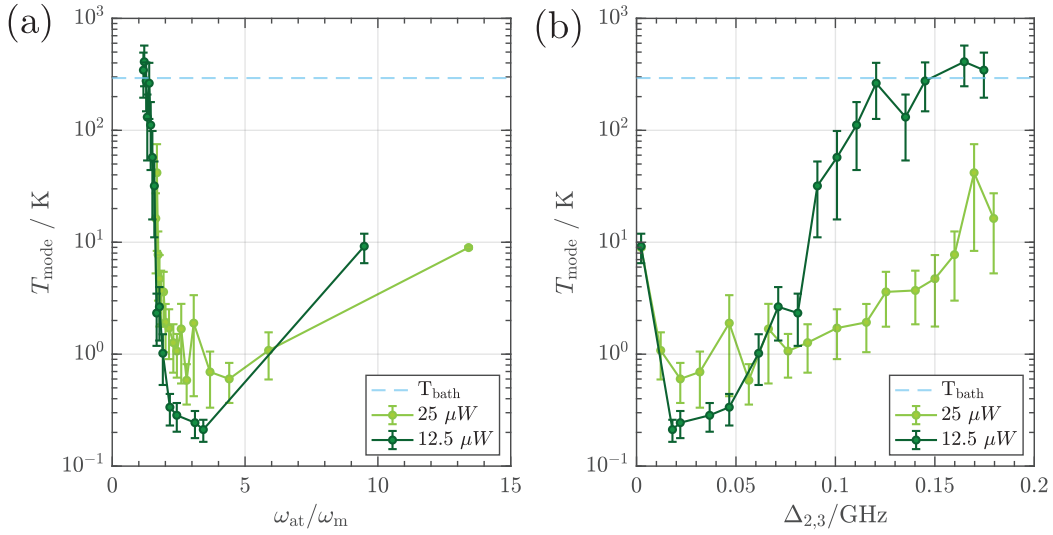

Figure 3.21: Hybrid coupling with an uncompressed MOT for $\mathcal{F} = 1500$:
Hybrid coupling experiments at the high finesse configuration in a blue-detuned coupling lattice for different coupling lattice powers P_{lat}. (a) Resonance behavior of the mode temperature T_{mode} dependent on the trapping frequency in units of ω_{m}. The lattice depth is varied by sweeping the detuning $\Delta_{2,3}$. (b) Mode temperature dependent on the detuning $\Delta_{2,3}$. The dashed line denotes the bath temperature $T_{\mathrm{bath}} = 293\,\mathrm{K}$. The mode temperature is determined by averaging over five 10 s time traces of the integrated PSD. The homodyne calibration for these measurements is $|\frac{\partial\Phi}{\partial x_{\mathrm{m}}}| = (10 \pm 1)\frac{\mathrm{rad}}{\mathrm{nm}}$. The reflectivity on resonance was $(\sigma = 0.60 \pm 0.02)$.

[55] This can happen due to fluctuations of the laser frequency, optical density fluctuations in the MOT or power fluctuations.

Figure 3.21 shows the resonance behavior of the resonator mode temperature for $P_{\mathrm{inc}} = 25\,\mu\mathrm{W}$ and $12.5\,\mu\mathrm{W}$. As in the previous measurement, the minimal mode temperature decreases with lower coupling lattice powers. A key difference is that the region, in which cooling can be observed, is much smaller and meaningful results are only obtained for detunings from $10 - 200$ MHz. Like in the previous measurement, the lowest mode temperatures are acquired at low detunings (as depicted in Fig. 3.21(b)) with the minimal mode temperatures being $T_{\mathrm{mode},25} = (0.5 \pm 0.2)\,\mathrm{K}$ for the $25\,\mu\mathrm{W}$ lattice and $T_{\mathrm{mode},12.5} = (0.20 \pm 0.05)\,\mathrm{K}$ for the $12.5\,\mu\mathrm{W}$ lattice.

This mode temperature is equal to the minimal mode temperature acquired at base temperature in Ref. [63][56]. This is a significant improvement over the old setup and yields a higher cooperativity than in the previous measurement. The analysis of the sympathetic cooling rate is presented in Fig. 3.22. We reach the highest cooperativity measured at this experiment yet at a lattice power of 12.5 μW[57]:

$P_{\mathrm{lat,inc}}$	$25\,\mu\mathrm{W}$	$12.5\,\mu\mathrm{W}$
C_{hybrid}	500 ± 200	1400 ± 300

The coupling experiments at room temperature with an uncompressed MOT support the model by Ref. [52] presented in Fig. 3.3. We observe an increased coupling strength for higher finesses. Yet we also see hints of a fundamental limit in cooperativity arising due to instability of the system when the optomechanical coupling is strong enough to modulate the cavity frequency on the order of κ.

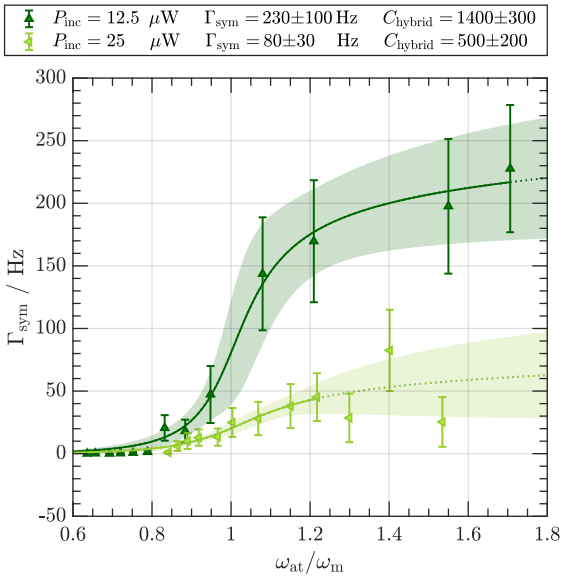

Figure 3.22: Sympathetic cooling rates for an uncompressed MOT at $\mathcal{F} = 1500$: Γ_{sym} calculated from equation 3.19 using the in Fig. 3.21 acquired mode and bath temperatures. Data are fitted using expression 3.23. The x-axis is rescaled to fulfill the resonance condition. The light shaded areas denote the 2σ confidence bounds of the fits. Data points that show a decreasing Γ_{sym} for higher lattice depths are omitted.

[56] Here a compressed MOT at a coupling lattice power of $100\,\mu\mathrm{W}$ was used to acquire $T_{\mathrm{min}} = (0.21 \pm 0.04)\,\mathrm{K}$ at base temperature.

[57] We acknowledge that in Ref. [62] a cooperativity of 3800 was reported. This value was reached by feedback assisted cooling, thus not resembling the definition in equation 3.31 or 3.56.

3.3.2 Coupling experiments with a high-OD MOT

Since the hybrid cooperativity scales with the number of atoms that participate in the coupling (Eq. 3.31) we conducted coupling experiments also with the high-OD MOT that has been introduced in Section 3.2.4.1. As the compressed MOT requires a cycled experiment sequence, we need to operate the system at the point of maximum optomechanical cooling (i.e. maximum optical spring) at all time[58] to prevent optomechanical heating due to random drifts on resonance. Working in a regime with strong optomechanical cooling was investigated in Ref. [58]. We account for the additional optomechanical damping of the resonator $\Gamma_{\mathrm{tot}} = \Gamma_{\mathrm{m}} + \Gamma_{\mathrm{sym}} + \Gamma_{\mathrm{opt}}$ by calculating Γ_{sym} via [58]:

$$\Gamma_{\mathrm{sym}} = \Gamma_{\mathrm{m}} \left(\frac{T_{\mathrm{bath}}}{T_{\mathrm{sym}}} - \frac{T_{\mathrm{bath}}}{T_{\mathrm{opt}}} \right) \quad \text{with} \quad T_{\mathrm{opt}} = T_{\mathrm{bath}} \frac{\Gamma_{\mathrm{m}}}{\Gamma_{\mathrm{m}} + \Gamma_{\mathrm{opt}}} \tag{3.56}$$

We calculate T_{opt} from the optical spring measurements and the derived optomechanical damping rates Γ_{opt} presented in Fig. 3.18. For the calculation of the hybrid cooperativity $C_{\mathrm{hybrid}} = \Gamma_{\mathrm{sym}}/\Gamma_{\mathrm{m}}$ use the definition of Γ_{sym} that is introduced in equation 3.56.

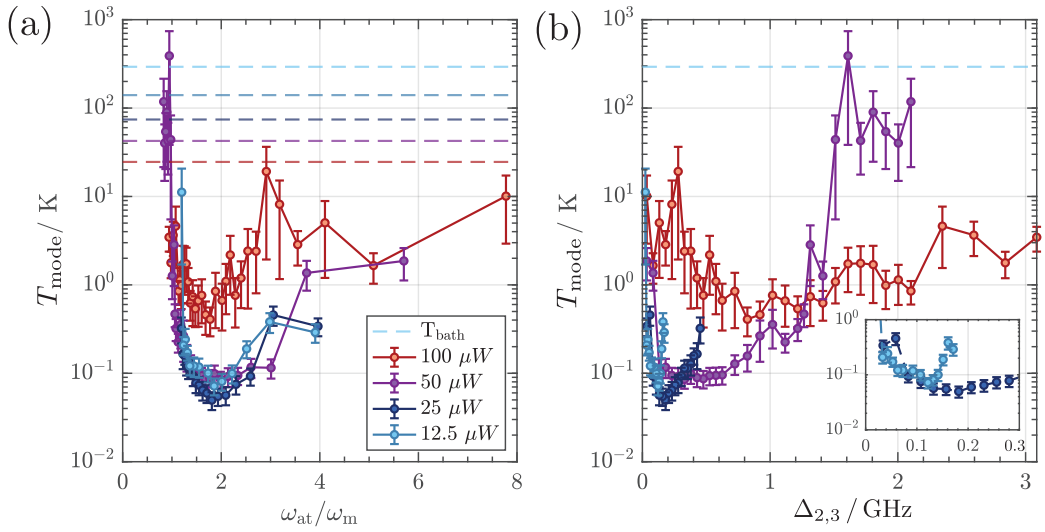

Figure 3.23: Hybrid coupling with a compressed MOT for $\mathcal{F} = 650$:
Hybrid coupling experiments at the low finesse configuration in a blue-detuned coupling lattice for different coupling lattice powers P_{lat}. (a) Resonance behavior of the mode temperature T_{mode} dependent on the trapping frequency in units of ω_{m}. The lattice depth is varied by sweeping the detuning $\Delta_{2,3}$. The dashed lines denote the respective mode temperatures T_{opt} achieved by optomechanical cooling (b) Acquired mode temperature dependent on the detuning $\Delta_{2,3}$. The light blue dashed line denotes the bath temperature $T_{\mathrm{bath}} = 293\,\mathrm{K}$. The mode temperature is determined by averaging over 10 traces of the of the integrated PSD as shown in Fig. 3.11. The homodyne calibration for these measurements yields $|\frac{\partial \Phi}{\partial x_{\mathrm{m}}}| = (4.0 \pm 0.2)\frac{\mathrm{rad}}{\mathrm{nm}}$. The reflectivity on resonance is $\sigma = (0.80 \pm 0.02)$.

[58] The optical-spring-lock [110] cannot be used in this regime, thus the cavity is tuned to this setting manually using the offset output of the lock-in amplifier.

Low finesse configuration

Figure 3.23 shows the resonant behavior of the mode temperature for different lattice powers with a compressed MOT. It becomes apparent, that the minimal temperature is consistently reached for $\omega_{at} \approx 2\omega_m$ (Fig. 3.23(a)). This can be accounted to the much higher atomic densities and a roughly similar number of coupling atoms for all lattice power settings. Except for the lattice power $P_{lat} = 100\,\mu W$ the reached mode temperature is one order of magnitude smaller than for the uncompressed MOT with $T_{mode,100} = (0.40 \pm 0.15)\,K$, $T_{mode,50} = (0.09 \pm 0.02)\,K$, $T_{mode,25} = (0.05 \pm 0.01)\,K$ and $T_{mode,12.5} = (0.07 \pm 0.02)\,K$.
The mode temperatures T_{opt} reached due to optomechanical cooling are denoted by the dashed lines in the respective colors[59]. The assumed bath temperature is $T_{bath} = 293\,K$.
Figure 3.24 shows the calculated sympathetic cooling rates and hybrid cooperativities. The cooperativities are further increased compared to both measurements with the uncompressed MOT reaching a maximum of $C_{hybrid} = (5900 \pm 1300)$ at a lattice power of $P_{lat} = 25\,\mu W$. Overall, we reach the following cooperativities:

$P_{lat,inc}$	$100\,\mu W$	$50\,\mu W$	$25\,\mu W$	$12.5\,\mu W$
C_{hybrid}	710 ± 260	3400 ± 750	5900 ± 1300	4100 ± 900

Although very large, the increase in cooperativity by a factor of roughly (30 ± 5) is reasonable considering that the finesse was increased by a factor of $\mathcal{F}_{new}/\mathcal{F}_{old} = 650/140 \approx 4.6$ and that Γ_{sym} scales with $\mathcal{F}^2$ according to equation 3.22 [60].

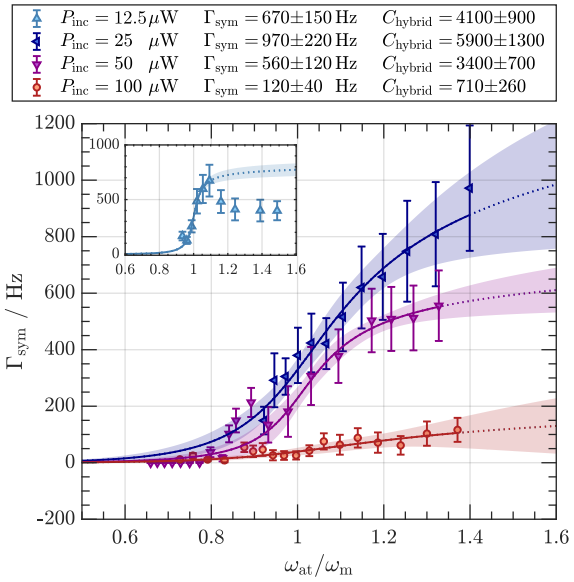

Figure 3.24: Sympathetic cooling rates for a compressed MOT at $\mathcal{F} = 650$: Γ_{sym} calculated from equation 3.56 using the in Fig. 3.23 acquired mode and bath temperatures. Data are fitted with expression 3.23. The x-axis is rescaled to fulfill the resonance condition. The light shaded areas denote the 2σ confidence bounds of the fits. Data points that show a decreasing Γ_{sym} for higher lattice depths are omitted. Inset: Γ_{sym} with the according fits for $P_{lat} = 12.5\,\mu W$. Since this plot intersects with the others it was plotted separately for a better overview.

[59] Except for $P_{lat} = 50\,\mu W$ the theoretical temperature T_{opt} is not reached because the optomechanical cooling was the dominant effect in the depicted measurements.
[60] That is, until the optimal finesse according to Fig. 3.3 is reached.

High finesse configuration

For the coupling experiments with the compressed MOT at $\mathcal{F} = 1500$ the same challenges arise as for the experiments at this finesse with the uncompressed MOT. Furthermore, the rapid ramping of the lattice introduces undesired excitation to the system and as in the case with the uncompressed MOT short events of spontaneous heating can occur, even while cooling in the system takes place. Thus, the quality of the data is worse compared to the measurements that were conducted before.

Figure 3.25 shows the resonance behavior of the mode temperature dependent on the lattice depth (Fig. 3.25(a)) and the laser-atom detuning (Fig. 3.25(b)).
The strong optomechanical cooling in this configuration leads to lower initial temperatures T_{opt} that are denoted by the dashed green lines for the respective lattice powers. Here, the measured and theoretically calculated values match within one standard deviation. For a lattice power of $12.5\,\mu$W the resonance behavior is similar to measurements at the lower finesse configuration and the minimal mode temperature of $T_{\mathrm{mode},12.5} = (0.15 \pm 0.05)\,\mathrm{K}$. At $25\,\mu$W lattice power the system behaves much more unstable and getting reproducible results, even for the same measurement parameters, is challenging. We observe significant cooling effect, reaching the same minimal mode temperature of $T_{\mathrm{mode},25} = (0.15 \pm 0.05)\,\mathrm{K}$ as in the weaker lattice.

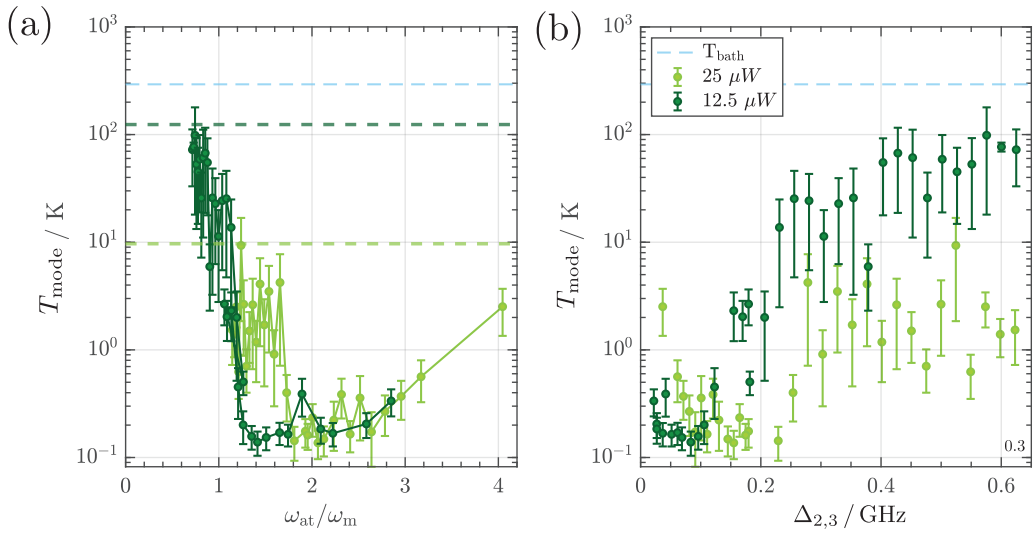

Figure 3.25: Hybrid coupling with a compressed MOT for $\mathcal{F} = 1500$:
Hybrid coupling experiments at the low finesse configuration in a blue-detuned coupling lattice for different coupling lattice powers P_{lat}. (a) Resonance behavior of the mode temperature T_{mode} dependent on the trapping frequency in units of ω_{m}. The lattice depth is varied by sweeping the detuning $\Delta_{2,3}$. (b) Acquired mode temperature dependent on the detuning $\Delta_{2,3}$. The dashed lines denote mode temperatures T_{opt} achieved by optomechanical cooling (b) Acquired mode temperature dependent on the detuning $\Delta_{2,3}$. The light blue dashed line denotes the bath temperature $T_{\mathrm{bath}} = 293\,\mathrm{K}$. The mode temperature is determined by averaging over 10 traces of the of the integrated PSD as shown in Fig. 3.11. The homodyne calibration for these measurements yields $|\frac{\partial\Phi}{\partial x_{\mathrm{m}}}| = (11 \pm 1)\frac{\mathrm{rad}}{\mathrm{nm}}$. The reflectivity on resonance is $\sigma = (0.60 \pm 0.02)$.

The data for this configuration does not allow for a meaningful analysis of the ensemble integrated sympathetic cooling rate as is does not follow the characteristic resonance behavior described by equation 3.20.
The calculated sympathetic cooling rates for the 12.5 μW lattice are depicted in Fig. 3.26. We observe a characteristic resonance behavior and reach a maximum sympathetic cooling rate of $\Gamma_{\mathrm{sym}} = (330 \pm 100)\,\mathrm{Hz}$. Although not depicted in this figure, we can calculate the maximum achieved cooperativity for the 25 μW lattice from the minimal mode temperature. This results in the cooperativities of the high finesse system with a compressed MOT:

$P_{\mathrm{lat,inc}}$	25 μW	12.5 μW
C_{hybrid}	2100 ± 600	2100 ± 500

Both configurations yield the same cooperativity within the error margins. Based on the findings in the previous measurements we can assume that higher cooperativities are to be expected for lower lattice powers and that the found cooperativities might be limited by heating effects and back-action (Eqs. 3.55, 4.33), the resonator experiences in this configuration.

A further reduction of the lattice power might increase the cooperativity but requires for smaller laser-atom detunings to fulfill the resonance condition. Close to resonance new effects in the atom-light interaction become relevant. Thus, we decided to investigate this regime of very low lattice powers and small detunings in more detail.

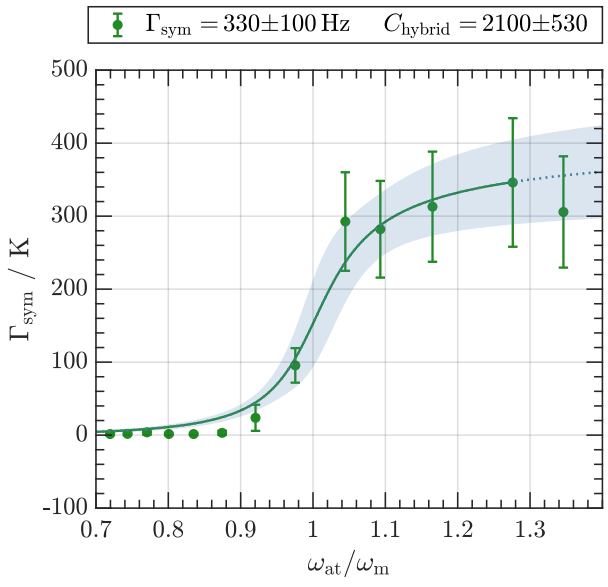

Figure 3.26: Sympathetic cooling rates for a compressed MOT at $\mathcal{F} = 1500$ and $P_{\mathrm{lat}} = 12.5\,\mu$W:
Γ_{sym} calculated from equation 3.56 using the in Fig. 3.25 acquired mode and bath temperatures. Data are fitted using expression 3.23. The x-axis is rescaled to fulfill the resonance condition. The light shaded areas denote the 2σ confidence bounds of the fits. Data points that show a decreasing Γ_{sym} for higher lattice depths are omitted.

3.3.3 Destructive effects in the limit of near detunings

The findings in Section 3.3.1 and 3.3.2 motivate us to investigate the regime of low lattice powers and near detunings more closely. The highest cooperativities in the uncompressed MOT measurements were achieved at the lowest lattice powers. For the compressed MOT we observe the highest cooperativities at a lattice power of 25 μW at a finesse of $\mathcal{F} = 650$. Figure 3.27 shows a sweep of the lattice power at a constant lattice depth of $\omega_{\mathrm{at}} = 2\omega_{\mathrm{m}}$. It becomes apparent, that the cooperativity rapidly decreases for lattice powers below 15 μW. Because of the small detunings used to fulfill the resonance condition and the high atomic densities, it is possible that this decrease in cooperativity is caused by absorption effects in the lattice due to a high optical density (OD) of the MOT. The optical density can be expressed via [76]:

$$\mathrm{OD} = \frac{\mathrm{OD}_{\mathrm{res}}}{1 + (2\Delta_{2,3}/\Gamma_{\mathrm{at}})^2} \quad \text{with} \quad \mathrm{OD}_{\mathrm{res}} = \sigma_0 \int \rho_{\mathrm{x}} \mathrm{dx} \tag{3.57}$$

Here $\mathrm{OD}_{\mathrm{res}}$ is the resonant optical depth at zero detuning that is calculated by integrating the atomic density ρ_{x} along the lattice axis and multiplying it with the scattering cross section σ_0. For small detunings the OD can reach high values that lead to a significant amount of light being absorbed according to [76]:

$$I_{\mathrm{abs}} = I_{\mathrm{lat}} e^{-\mathrm{OD}} \tag{3.58}$$

OD measurements of the MOT have been conducted previously at our experiment [76] using a detection beam that was separately set up to transmit through the MOT. Since we are only interested in the effect a high OD might have on the coupling to the resonator, we utilize the resonator itself to qualitatively assess when a high OD becomes relevant to the coupling.
This is done by recording the optical spring which is proportional to the light intensity entering the cavity. We expect the optical spring effect at a given lattice power to be

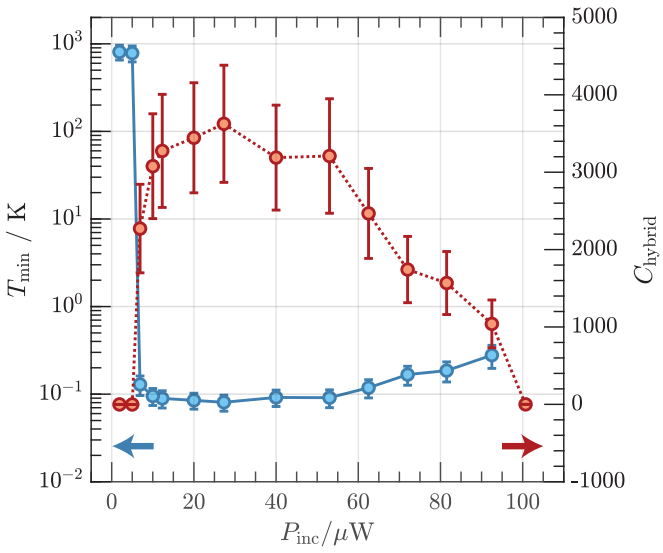

Figure 3.27: Mode temperature and cooperativity for different lattice powers: Sweep of the lattice power from 2 μW to 100 μW and the detuning to obtain a constant lattice depth of $\omega_{\mathrm{at}} = 2\omega_{\mathrm{m}}$ (where the strongest cooling was observed) with a compressed MOT. The blue data points show the measured mode temperature (left axis) and the red data points the calculated cooperativity (right axis) The system is aligned to $\mathcal{F} = 650$. We measured a homodyne calibration of $|\frac{\partial\Phi}{\partial x_{\mathrm{m}}}| = (4.0 \pm 0.1)\frac{\mathrm{rad}}{\mathrm{nm}}$ and a reflectivity on resonance of $\sigma = (0.80 \pm 0.02)$.

reduced close to resonance as less photons transmit through the MOT. Because the system behaves most stable at $\mathcal{F} = 650$ we conduct the measurement at this setting at a lattice power of 12.5 μW where we sweep the detuning and measure the maximum optical spring effect the resonator experiences. We use the data acquisition unit of the lock-in amplifier to get a time resolved 2D image of the mechanical spectrum to determine the time dependent optical spring.

Figure 3.28(a,b) shows images of the time resolved spectrum at a detuning of $\Delta_{2,3} = 130\,\mathrm{MHz}$ (a) and $\Delta_{2,3} = 20\,\mathrm{MHz}$ (b). The y-axis shows the resonator frequency and the colorbar indicates the displacement spectral density of the resonator. The resonator eigenfrequency is denoted by the orange dashed line[61]. The coupling lattice is ramped up and the coupling takes place in the red shaded area.

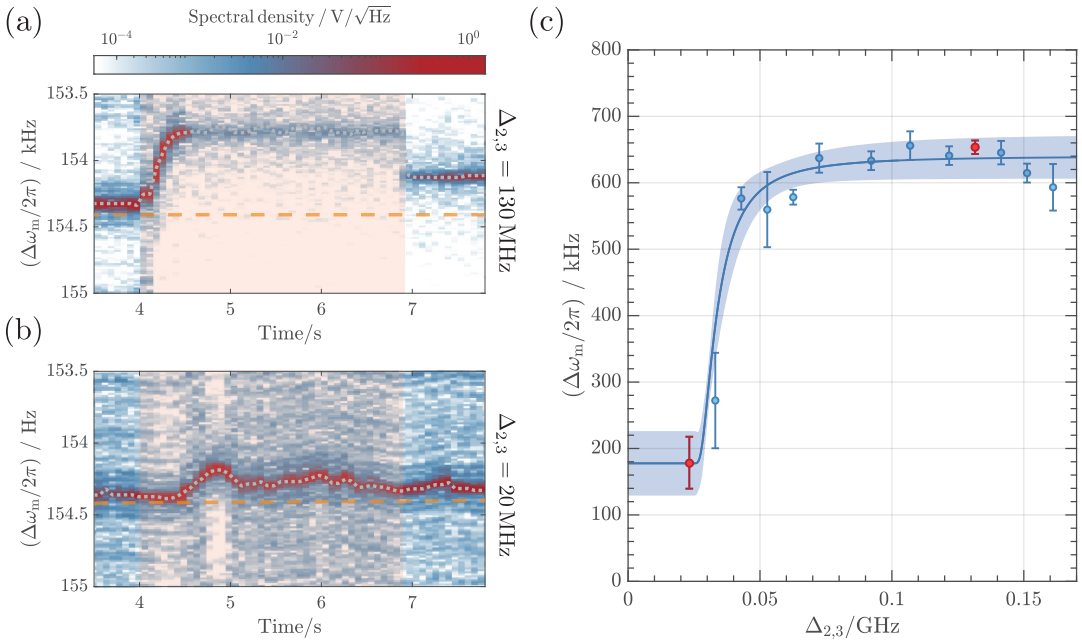

Figure 3.28: OD measurement of the compressed MOT at $\mathbf{P}_{\mathrm{lat}} = 12.5\,\mu$W:
(a,b) Time trace of the resonator displacement spectral density (SD) for different detunings $\Delta_{2,3} = 130\,\mathrm{MHz}$ (a) and $\Delta_{2,3} = 20\,\mathrm{MHz}$ (b). Dark red shades correspond to a high mode temperature. The unshifted eigenfrequency ω_{m} is denoted by the dashed orange line. The dotted grey lines denote the position of the SD peak. The coupling lattice is switched on at 4 s and coupling takes place over a 3 s interval (red shaded area). After the lattice is switched off, the system re-thermalizes. (c) Averaged frequency shift $\Delta\omega_{\mathrm{m}}$ acquired by averaging 10 SD time traces (as depicted in (a,b)) and determining the maximum optical spring while the coupling takes place. The red data points correspond to the detunings at which the measurements of (a) and (b) were conducted. The blue line fits equation 3.58 on the data points with the OD as free fit parameter. The light shades denote the 2σ confidence bounds of the fit.

[61] The initial offset in ω_{m} can be accounted to the optical spring shift caused by the homodyne detection light that is permanently switched on.

In case (a) we observe a significant shift in the resonator frequency by $\Delta\omega_{\mathrm{m}} \approx 500\,\mathrm{Hz}$ as soon as the lattice is switched on (at 4 s), followed by a decrease in the displacement spectral density indicating sympathetic cooling. For small detunings this behavior changes as depicted in (b). Here the optical spring effect is much smaller, and the displacement spectral density remains constant, indicating that no cooling takes place. In Fig. 3.28(c) we measured the optical spring over the detuning $\Delta_{2,3}$.

For the $12.5\,\mu$W lattice we observe a rapid increase in the OD at detunings $\Delta_{2,3} < 50\,\mathrm{MHz}$. The measurements clearly show a decrease in the optical spring and sympathetic cooling, indicating that the coupling lattice vanishes due to the high OD of the MOT. Since the lattice depth scales with $V_0 \propto I_{\mathrm{inc}}/\Delta_{2,3}$, reducing the power would require to reduce the detuning by the same amount to stay resonant. Since the maximum cooperativity with the $12.5\,\mu$W coupling lattice was achieved for $\Delta_{2,3} \approx 120\,\mathrm{MHz}$ a further reduction of the lattice power (e.g., to $6\,\mu$W) is not feasible. This also applies to the experiments with the compressed MOT at $\mathcal{F} = 1500$.

The OD measurements described above show, that there is a fundamental limit to the achievable cooperativity with this system. While for the $\mathcal{F} = 650$ configuration, the optimal cooperativity can be reached at 25μW lattice power, the higher finesse configuration would require lower coupling lattice powers, to improve the cooperativity further. This requires low detunings, such that we enter a regime where the OD of the MOT is so high that no coupling lattice is created.

3.4 Conclusion

Reaching the strong coupling regime has been a primary goal of this experiment since its beginning. In this chapter, we have investigated the influence of previously unchanged parameters by implementing a PAC lattice to operate in the red-detuned lattice regime as well as by exchanging the fiber cavity and operating the system at the theoretically proposed [52] optimal finesses.

We created a model of the asymmetrically pumped coupling lattice to investigate the lattice dynamics and gain a better understanding of the hybrid instability in our system. Based on the finding we implemented a PAC lattice to compensate for the asymmetry which enabled us to operate in the red-detuned coupling lattice regime. Here we found the PAC lattice to bring no improvement in the overall cooperativity of the system, even though it suppressed the emergence of a hybrid instability.

The exchange of the fiber cavity showed a significant improvement in cooperativity over the old system for every configuration that was investigated. The highest cooperativities we reached in the respective configurations are listed in the table below:

Uncompressed MOT	$\mathcal{F} = 650 \,/\, P_{\mathrm{lat}} = 12.5\,\mu\mathrm{W}$	$\mathcal{F} = 1500 \,/\, P_{\mathrm{lat}} = 12.5\,\mu\mathrm{W}$
$C_{\mathrm{hyb,max}}$	550 ± 130	1400 ± 300
Compressed MOT	$\mathcal{F} = 650 \,/\, P_{\mathrm{lat}} = 25\,\mu\mathrm{W}$	$\mathcal{F} = 1500 \,/\, P_{\mathrm{lat}} = 25\,\mu\mathrm{W}$
$C_{\mathrm{hyb,max}}$	5900 ± 1300	2100 ± 500

Coupling experiments with an uncompressed MOT showed the highest cooperativities at the high finesse configuration $\mathcal{F} = 1500$ at the lowest possible lattice powers. This is consistent with the theoretical prediction presented in Fig. 3.3.

With a compressed MOT we reached the highest cooperativity at a finesse of $\mathcal{F} = 650$ and 25 μW lattice power. We found the system to behave very unstable at $\mathcal{F} = 1500$ which we account to the strong optomechanical coupling that can lead to a modulation of ω_{cav} on the order of the cavity linewidth. We investigated the feasibility of working at even lower coupling lattice powers in this regime to improve the cooperativity. Here we found in an OD measurement, where we used the optical spring effect as indicator for the OD of the MOT, that the coupling lattice vanishes for powers of $P_{\mathrm{lat}} < 12.5\,\mu\mathrm{W}$ and detunings $\Delta_{2,3} < 50\,\mathrm{MHz}$.
The vanishing of the lattice at low lattice powers poses a fundamental limit on the achievable cooperativity of the system and indicates that the best overall achievable cooperativity of the system has been reached at:

$$\mathcal{F} = 650 \pm 50, \quad P_{\mathrm{lat}} = 25 \pm 1\,\mu\mathrm{W} \quad \text{and} \quad C_{\mathrm{hyb,max}} = 5900 \pm 1300 \tag{3.59}$$

Here, we have to consider that the experiments were conducted at room temperature. If we assume operation at the cryostat base temperature resulting in $T_{\mathrm{bath}} = 4\,\mathrm{K}$[62] the quality factor of the resonator would increase by a factor of ~ 10 and thus its mechanical linewidth would decrease to $\Gamma_{\mathrm{m}} \approx 2\,\mathrm{mHz}$. In this case the expected cooperativity would yield $C_{\mathrm{max,base}} \approx 59000$. At 4 K bath temperature the resonator is occupied with $\bar{n}_{\mathrm{th,4K}} = 5.4 \cdot 10^5$ phonons. In this case we miss the strong coupling condition only by a factor of 9.

Even though the cooperativity is much higher than in any setup used before, reaching the strong coupling regime without intense modifications is likely still not possible in this configuration. Due to the higher intra-cavity photon number and the stronger optomechanical coupling it is likely, that the bath temperature is further increased in comparison to the measurements in Ref. [76] as the system is more sensitive to radiation pressure noise. To reach the strong coupling regime we would need a bath temperature of $T_{\mathrm{bath}} \approx 500\,\mathrm{mK}$. While the cryostat is technically capable of reaching this temperature[63], it would require additional thermal shielding (e.g., the implementation of a mixing chamber shield) which would involve a redesign of the goniometer.

[62] This is the measured bath temperature for $T_{\mathrm{cryo}} = 500\,\mathrm{mK}$, discussed in Ref. [76].

[63] Oxford Instruments specifies the base temperature of the dilution unit to $T_{\mathrm{base}} = 30\,\mathrm{mK}$. We do not reach this temperature due to a missing mixing chamber shield. This decision was made to allow for better optical access.

Chapter 4

Rapid state preparation using QND measurement techniques

In the previous chapter we introduced different experimental modifications to enter the strong coupling regime and prepare the resonator in its quantum-mechanical ground state. We found a significant increase in cooperativity but had to acknowledge that it is not possible to reach the strong coupling regime without major modifications to the experimental hardware. Nevertheless we found a new semi-stable regime of optomechanical coupling in which the resonator can modulate the cavity frequency on the order of its linewidth. This comes with a high information gain for any measurements conducted on the system at the cost of its stability. The observed regime represents a limit beyond which a careful balancing between the information gain per measurement and the introduced back-action is necessary to gather meaningful results. This allows to enter the field of quantum-non-demolition (QND) measurements. In this chapter we use the versatility of our experimental platform and implement a QND measurement technique to rapidly prepare the resonator close to its quantum ground state. Specifically for this task, we implemented a high finesse cavity $\mathcal{F} = 14500$ to our system and modified the detection setup further which enabled us to resolve the resonator motion with a precision of $(16 \pm 1)\, x_{zpm}$.

The most fundamental property of quantum objects is described by the Heisenberg uncertainty principle $\Delta x \Delta p > \hbar/2$. The uncertainty principle expresses the link between gained knowledge over a quantum system and the destructive nature of acquiring this knowledge. It rises from the fact that any kind of measurement requires some kind of interaction between the probe and the measured quantum object thus leading to a collapse of its initial wave function. At the same time, the uncertainty principle does not prohibit the measurement of one of its relevant quantities with arbitrary accuracy (e.g. Δx) as long as there is no information gained about its complementary part (Δp)[114]. This consideration introduced the idea of quantum non-demolition (QND) measurements which was first proposed in a theory paper by Braginsky and Vorontsov in Ref. [138]. Based on their findings the idea was further developed[64] [114, 139, 140] and

[64] Back then with a strong focus on mechanical resonators which were used for gravity wave detection.

implemented for precise detection of e.g., optical quadratures [141–143], atomic spin measurements [144–148] and mechanical motion [149–155].
With the creation of micromechanical resonators and the prospect to measure non-classical states of these devices [77, 156] the field of QND measurements gained further importance. Since most optomechanical experiments utilize the coupling of the resonator to an electromagnetic field, they often make use of optical cavities to enhance the coupling strength [157] and use highly sensitive continuous measurement schemes to detect the mechanical motion [158, 159]. All these methods have in common that the back-action imparted on the system [72] prohibits achieving a measurement precision any higher than defined by the standard-quantum-limit (SQL) [160, 161] thus defying any measurements of non-classical features below the zero-point motion of the resonator. QND measurements pose a possible solution, to enter this regime by accurately observing one QND observable of the system, while transferring the induced uncertainty to the other. Yet there are constraints on the observables and systems, this method can be applied to. Not all observables allow for QND measurements and not all QND observables, allow for back-action evading measurements. A very thorough introduction can be found in Ref. [162]. To provide the basic understanding, the most relevant contents will be presented in the following section.

4.1 QND measurements of mechanical resonators

To understand the idea behind QND techniques and how they work, it is helpful to recall the motivation that led to their development. QND techniques were introduced to measure the influence of very weak forces onto an otherwise well defined physical system. One of the original motives was the detection of gravitational waves. A popular approach[65] was the use of resonant detectors. Heavy aluminum cylinders were suspended in a vacuum and dimensioned to fulfill the resonance condition of an incident gravitational wave. Gravitational waves were supposed to excite the normal oscillation modes of the cylinder above the thermal noise level upon arrival [163]. These setups required accurate length measurements of the masses below the SQL. A QND measurement requires knowledge about the system such that it is possible to predict the outcome of system observable at some time t_2 after the initial measurement at t_1 was made. If a second measurement is made at t_2, with the exact outcome as the first measurement, the system remained undisturbed but if the outcome changed, this would indicate the action of an external force. If the observables of the system are chosen accordingly (i.e., such that the measurement induced uncertainty has no back-action on the observable of interest), this type of back-action evading measurement can have sub-SQL precision.

[65] Before the use of interferometric detectors.

We introduce the idea of QND measurements using the quantum mechanical oscillator as example which is described by the Hamiltonian:

$$\hat{H}_{\mathrm{osc}} = \frac{\hat{p}^2}{2m} + \frac{1}{2}m\omega^2\hat{x}^2 \tag{4.1}$$

Investigating the time evolution of the system upon a measurement can be done most conveniently by describing the system via the complex amplitude $\hat{X}_{\mathrm{M}}+i\hat{P}_{\mathrm{M}}$ in a rotating frame [56, 162]:

$$\hat{x} + \frac{i\hat{p}}{m\omega_{\mathrm{m}}} = \left(\hat{X}_{\mathrm{M}} + i\hat{P}_{\mathrm{M}}\right) e^{-i\omega_{\mathrm{m}}t} \quad \text{with the commutator} \quad \left[\hat{X}_{\mathrm{M}}, \hat{P}_{\mathrm{M}}\right] = \frac{i\hbar}{m\omega_{\mathrm{m}}} \tag{4.2}$$

This allows to write $\hat{x}$ and $\hat{p}$ via the quadrature components of the complex amplitude:

$$\hat{x} = \hat{X}_{\mathrm{M}}\cos(\omega_{\mathrm{m}}t) + \hat{P}_{\mathrm{M}}\sin(\omega_{\mathrm{m}}t) \tag{4.3}$$

$$\frac{\hat{p}}{m\omega_{\mathrm{m}}} = -\hat{X}_{\mathrm{M}}\sin(\omega_{\mathrm{m}}t) + \hat{P}_{\mathrm{M}}\cos(\omega_{\mathrm{m}}t) \tag{4.4}$$

Equation 4.3 can be rewritten to express $\hat{X}_{\mathrm{M}}$ and $\hat{P}_{\mathrm{M}}$ in terms of $\hat{x}$ and $\hat{p}$:

$$\hat{X}_{\mathrm{M}} = \hat{x}\cos(\omega_{\mathrm{m}}t) - \frac{\hat{p}}{m\omega}\sin(\omega_{\mathrm{m}}t) \tag{4.5}$$

$$\hat{P}_{\mathrm{M}} = \hat{x}\sin(\omega_{\mathrm{m}}t) + \frac{\hat{p}}{m\omega}\cos(\omega_{\mathrm{m}}t) \tag{4.6}$$

$\hat{X}_{\mathrm{M}}$ and $\hat{P}_{\mathrm{M}}$ differ from $\hat{x}$ and $\hat{p}$ in that they are time independent constants of motion. Using the commutator relation $[\hat{x}, \hat{p}] = i\hbar$ they fulfill the uncertainty principle via:

$$\Delta X_{\mathrm{M}}\Delta P_{\mathrm{M}} \geq \frac{1}{2}|\langle[\hat{X}_{\mathrm{M}}, \hat{P}_{\mathrm{M}}]\rangle| = \frac{\hbar}{2m\omega_{\mathrm{m}}} = x_{\mathrm{zpm}}^2 \tag{4.7}$$

where x_{zpm} denotes the zero-point motion of the system. This expression resembles the SQL of measurement accuracy and is a direct consequence of the Heisenberg uncertainty principle.

Back-action evasion

Despite its fundamental nature, the SQL does not pose a limit to the maximum achievable measurement resolution given the measurement technique is chosen accordingly. Surpassing the SQL requires to measure one component of the complex amplitude with an accuracy $\Delta X_{\mathrm{M}} \ll \sqrt{\hbar/(2m\omega_{\mathrm{m}})}$, at the cost of an increased uncertainty in $\Delta P_{\mathrm{M}} = \hbar/(m\omega_{\mathrm{m}}\Delta X_{\mathrm{M}})$.

The concept of back-action evasion poses special requirements on the systems observables and the measurement interaction Hamiltonian. In this context, the complex-amplitude quadratures $\hat{X}_{\mathrm{M}}$ and $\hat{P}_{\mathrm{M}}$ play a special role as they exhibit no mutual back-action dependence provided the measurement technique is chosen appropriately[66]. This

[66] In that they differ from $\hat{x}$ and $\hat{p}$

can be understood, if we look at the influence of a measurement on these observables. An illustration of the described scenarios is depicted in Fig. 4.1.
In the following considerations the description of the system benefits from the use of the Heisenberg picture. This implies that, given a system Hamiltonian $\hat{H}$, the operators fulfill the Heisenberg equation of motion [164]:

$$\frac{\mathrm{d}\hat{O}}{\mathrm{d}t} = -\frac{i}{\hbar}\left[\hat{O}, \hat{H}\right] + \frac{\partial \hat{O}}{\partial t} \tag{4.8}$$

We assume a harmonic oscillator with Hamiltonian $\hat{H}_{\mathrm{osc}}$ that is exposed to an external, classical force $F(t)$. When performing an accurate measurement of $\hat{x}$ by linearly coupling to this observable the action of the measurement can be described by an interaction Hamiltonian $\hat{H}_{\mathrm{int}} = K\hat{x}\hat{Q}$. Here we define $\hat{Q}$ as the introduced quantum-mechanical uncertainty from the measurement apparatus that couples to the system via the coupling strength K. The measurement apparatus itself is described by a Hamiltonian $\hat{H}_{\mathrm{M}}$ and is important with respect to the readout observable $\hat{R}$ which describes the outcome of the measurement. The resulting total Hamiltonian reads [162]:

$$\hat{H} = \hat{H}_{\mathrm{osc}} - \hat{x}F(t) + \underbrace{K\hat{x}\hat{Q}}_{\hat{H}_{\mathrm{int}}} + \hat{H}_{\mathrm{M}} \tag{4.9}$$

If a measurement of $\hat{x}$ is conducted and we assume that the readout observable $\hat{R}$ is only affects the measurement interaction $\hat{H}_{\mathrm{int}}$ and the detection apparatus $\hat{H}_{\mathrm{M}}$ it changes according to:

$$\frac{d\hat{R}}{dt} = -\frac{i}{\hbar}\left[\hat{R}, \hat{H}_{\mathrm{M}}\right] - \frac{i}{\hbar}K\hat{x}\left[\hat{R}, \hat{Q}\right] \tag{4.10}$$

Information about $\hat{x}$ can only be acquired if $\hat{R}$ does not commute with the quantum noise introduced by the measurement $[\hat{R}, \hat{Q}] \neq 0$. This implies a gain of information about $\hat{X}_{\mathrm{M}}$ and $\hat{P}_{\mathrm{M}}$ but also an increase of uncertainty for both quadratures. If we recall equations 4.2 and 4.8 the evolution of the complex amplitude for the new system yields [162]:

$$\frac{d(\hat{X}_{\mathrm{M}} + i\hat{P}_{\mathrm{M}})}{dt} = -\frac{i}{\hbar}\left[(\hat{X}_{\mathrm{M}} + i\hat{P}_{\mathrm{M}}), \hat{H}\right] = i\left(F(t) - K\hat{Q}\right)\frac{e^{i\omega_{\mathrm{m}}t}}{m\omega_{\mathrm{m}}} \tag{4.11}$$

The measurement of $\hat{x}$ mediated by $\hat{H}_{\mathrm{int}}$ disturbs both the $\hat{X}_{\mathrm{M}}$ and $\hat{P}_{\mathrm{M}}$ quadrature via the measurement induced uncertainty $\hat{Q}$. According to equation 4.3 this uncertainty feeds back into $\hat{x}$ and $\hat{p}$ during the free evolution of the oscillator. $\hat{x}$ is not a back-action evading observable. Thus, the accuracy of this measurement is limited by the SQL described by equation 4.7.

A backaction-evading measurement becomes possible, if the measurement apparatus is capable of coupling linearly to the system constants of motion $\hat{X}_{\mathrm{M}}$ or $\hat{P}_{\mathrm{M}}$. Considering the interaction Hamiltonian $\hat{H}_{\mathrm{int}} = K\hat{X}_{\mathrm{M}}\hat{Q} = K[\hat{x}\cos(\omega_{\mathrm{m}}t) - (\hat{p}/m\omega_{\mathrm{m}})\sin(\omega_{\mathrm{m}}t)]\hat{Q}$

we can write the Hamiltonian of the measured system as [162]

$$\hat{H} = \hat{H}_{\mathrm{osc}} - \hat{x}F(t) + \underbrace{K\hat{X}_{\mathrm{M}}\hat{Q}}_{\hat{H}_{\mathrm{int}}} + \hat{H}_{\mathrm{M}} \tag{4.12}$$

The measurement operator commutes with the measured observable $[\hat{H}_{\mathrm{int}}, \hat{X}_{\mathrm{M}}] = 0$. Thus, the contribution due to the measurement interaction vanishes and the equation of motion yields [162]:

$$\frac{d\hat{X}_{\mathrm{M}}}{dt} = -\frac{i}{\hbar}\left[\hat{X}_{\mathrm{M}}, \hat{H}\right] = -\frac{F(t)}{m\omega_{\mathrm{m}}}\sin(\omega_{\mathrm{m}}t) \tag{4.13}$$

By writing down the corresponding equations of motion, the property of back-action evasion becomes visible. The time-evolution of $\hat{X}_{\mathrm{M}}$ is solely governed by the classical external force we introduced in the beginning and not by the measurement itself. The uncertainty due to the measurement is completely fed into $\hat{P}_{\mathrm{M}}$ according to the commutator $[\hat{X}_{\mathrm{M}}, \hat{P}_{\mathrm{M}}] = i\hbar/m\omega_{\mathrm{m}}$ (Eq. 4.2):

$$\frac{d\hat{P}_{\mathrm{M}}}{dt} = -\frac{i}{\hbar}\left[\hat{P}_{\mathrm{M}}, \hat{H}\right] = -\frac{F(t)}{m\omega_{\mathrm{m}}}\cos(\omega_{\mathrm{m}}t) - \frac{K}{m\omega_{\mathrm{m}}}\hat{Q} \tag{4.14}$$

We can write down the time evolution of the measurement readout $\hat{R}$ to be:

$$\frac{d\hat{R}}{dt} = -\frac{i}{\hbar}\left[\hat{R}, \hat{H}_{\mathrm{M}}\right] - \frac{i}{\hbar}\hat{K}\hat{X}_{\mathrm{M}}\left[\hat{R}, \hat{Q}\right] \tag{4.15}$$

Equations 4.13 and 4.14 show the core characteristics of back-action evading QND observables. Despite the fact that we conducted a measurement of $\hat{X}_{\mathrm{M}}$, the back-action related uncertainty is completely transferred into $\hat{P}_{\mathrm{M}}$. Furthermore, $\hat{P}_{\mathrm{M}}$ leaves $\hat{X}_{\mathrm{M}}$ undisturbed even after an in principle arbitrarily long time evolution. This allows for arbitrarily accurate measurements of $\hat{X}_{\mathrm{M}}$ as long as no information about $\hat{P}_{\mathrm{M}}$ is gained by the measurement which poses the main advantage of backaction-evading QND measurements. Thus, $\hat{X}_{\mathrm{M}}$ and $\hat{P}_{\mathrm{M}}$ are referred to as back-action evading QND observables. The $\hat{X}_{\mathrm{M}}$ signal in $\hat{R}$ has contributions from two noise sources: A contribution ΔR due to the uncertainty in $\hat{X}_{\mathrm{M}}$ and a contribution ΔR from the free evolution of $\hat{R}$ [162].

To transfer the findings above into an experimental context, we find the following requirements that have to be fulfilled to realize a back-action evading QND measurement on a mechanical resonator:

- The interaction Hamiltonian of the measurement device has to couple linearly to the $\hat{X}_{\mathrm{M}}$ quadrature of the mechanical motion.
- The measurement device has to solely measure the $\hat{X}_{\mathrm{M}}$ quadrature to maintain the back-action evading character of the measurement.
- The noise contributions from ΔX_{M} and from the free evolution of $\hat{R}$ to the measurement uncertainty ΔR should be minimized.

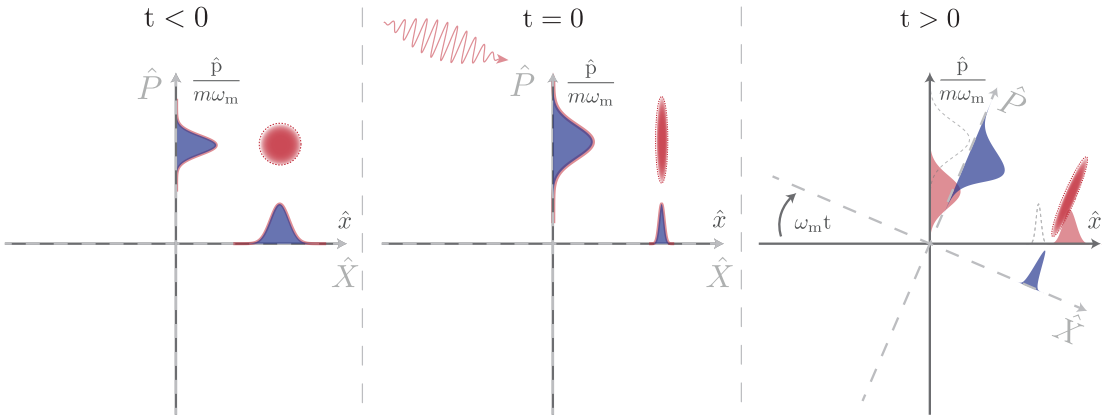

Figure 4.1: Back-action evading measurement:
Illustration of the evolution of a back-action evading QND observable in time. The red circle indicates a coherent state. The distributions on the axes show the projection of the state to the respective phase space quadratures. A coherent state before being measured (t<0) resembles a gaussian distribution in phase space at the coordinate $(\hat{x}, \hat{p}/m\omega_m)$ with a radius $\Delta x = \Delta p/m\omega_m = \sqrt{\hbar/2m\omega_m}$. If a precise measurement in $\hat{X}$ is conducted at t=0, the state is squeezed in $\hat{X}$ while experiencing anti-squeezing in $\hat{P}$. After the measurement, the state evolves in time yielding a rotation in phase space of $\omega_m t$. While the ellipse rotates relative to the $\hat{x}$ / $(\hat{p}/m\omega_m)$ axes, it remains stationary in the $\hat{X}$ / $\hat{P}$ frame. $\hat{X}$ acts on $\hat{P}$ but evades any back-action from $\hat{P}$. This is not the case for $\hat{x}$ and $\hat{p}$ where the increased uncertainty in $\hat{p}$ feeds back into $\hat{x}$ due to the rotation of the ellipse in phase space. Figure adapted from Ref. [162].

A measurement technique particularly suited for this task is balanced homodyne detection. This detection scheme allows to access only one complex amplitude quadrature by choosing the relative phase between the signal and LO beam accordingly. In our case we operate at $\phi_{LO} = \pi/2$ to couple linearly to the X_M quadrature of the resonator.
Preventing the detection from measuring contributions of $\hat{P}_M$ can be realized by the application of very short pulses at well defined homodyne phase angles ϕ_{LO}.
Lastly the minimization of measurement noise ΔR requires us to have a measurement system in which the $\hat{X}_M$ signal is large compared to ΔR. This requires high intensity measurement pulses and a large coupling constant K, which is experimentally resembled by the cavities finesse. ΔR can be further reduced by maximizing the common-mode-rejection of the detection and working with high signal to LO beam power ratios.

4.1.1 Back-action evading measurements with fast light pulses

If we want to apply a QND measurement on an optomechanical system the quadrature information is acquired via interaction of the system with a light field. This additional step in information transfer has to be taken into account when describing QND measurements in these systems.
Suppose we find the system in an unknown state and apply a single light pulse. Due to the optomechanical coupling the information from the mechanical quadrature X_M is imprinted on the measured phase quadrature of the light field P_L[67]. For Gaussian optical states it can be assigned the mean and variance [59]:

$$\langle P_\mathrm{L}\rangle = \chi\langle X_\mathrm{M}^\mathrm{in}\rangle \qquad \sigma_{P_\mathrm{L}}^2 = \sigma_{P_\mathrm{L}^\mathrm{in}}^2 + \chi^2\sigma_{X_\mathrm{M}^\mathrm{in}}^2 \tag{4.16}$$

The quantity X_M^in describes the mechanical position quadrature before the interaction with the light field and P_L^in denotes the input phase quadrature of the light. Also, we introduce the measurement strength parameter χ that quantifies the information transfer from the mechanical position quadrature onto the light field. For $\chi = 1$ the measurement outcome P_L would be equivalent to the mechanical quadrature X_M^in, resembling a "perfect" measurement of X_M. Since this parameter is of experimental importance, we discuss it in very detail in Section 4.1.3.
Describing the interaction of the pulses with the system requires to introduce a nonunitary measurement operator Υ that allows to calculate the mechanical state of the system after the pulse interaction via $\rho_\mathrm{M}^\mathrm{out} \propto \Upsilon^\dagger\rho_\mathrm{M}^\mathrm{in}\Upsilon$[59]. In the context of QND measurements the operator Υ is required to be similar to the interaction operator $\hat{H}_\mathrm{int}$ in that it is mechanical state independent and commutes with the mechanical position quadrature $[X_\mathrm{M}, \Upsilon] = 0$. In previous works in this field, it was found to be of the following form [59]:

$$\Upsilon = \frac{1}{\sqrt[4]{2\pi\sigma_{P_\mathrm{L}^\mathrm{in}}^2}}\exp\left[i\Omega X_\mathrm{M} - \frac{(P_\mathrm{L} - \chi X_\mathrm{M})^2}{4\sigma_{P_\mathrm{L}^\mathrm{in}}^2}\right] \tag{4.17}$$

If we assume a coherent probing field (i.e., $\sigma_{P_\mathrm{L}^\mathrm{in}} = 1/2$) it can be further simplified to

$$\Upsilon = \frac{1}{\sqrt[4]{\pi}}\exp\left[i\Omega X_\mathrm{M} - \frac{(P_\mathrm{L} - \chi X_\mathrm{M})^2}{2}\right] \tag{4.18}$$

The action of this operator onto a mechanical state can be dissected into two components. The first term of the exponent denotes a momentum transfer Ω which is proportional to the pulse photon number N_P. It yields a displacement of the mechanical state in phase space. The second term yields a narrowing of the mechanical position wave function proportional to χ^{-2} located around the measurement outcome P_L[68]. Thus, Υ can be understood as a combination of a displacement and a squeezing operator acting onto the system.

[67] In our case, P_L resembles a resonator displacement dependent voltage.
[68] Recalling the consideration in the previous section points out the similarity between χ and the previously used coupling constant K.

The fact the $[P_{\mathrm{M}}, \Upsilon] \neq 0$ further implies that the measurement induced uncertainty is transferred solely into the P_{M} quadrature of the system.
The influence of Υ on the measurement outcome requires to calculate the trace [59]:

$$\Pr(P_{\mathrm{L}}) = \mathrm{Tr}_{\mathrm{M}}(\Upsilon^{\dagger}\Upsilon\rho_{\mathrm{M}}^{\mathrm{in}}) = \int \frac{dX_{\mathrm{M}}}{\sqrt{\pi}} \underbrace{e^{-(P_{\mathrm{L}}-\chi X_{\mathrm{M}})^2}}_{\text{conv. kernel}} \underbrace{\langle X_{\mathrm{M}}|\rho_{\mathrm{M}}^{\mathrm{in}}|X_{\mathrm{M}}\rangle}_{\text{mech. state}} \tag{4.19}$$

where $\Pr(P_{\mathrm{L}})$ denotes the distribution expected for multiple measurements P_{L}. We see that the momentum dependent term vanishes such that the measured state solely depends on the measurement strength parameter χ. Mathematically Υ now acquires the role of a convolution kernel with width χ^{-2}. Expression 4.19 resembles the convolution between the mechanical state quadrature X_{M} and the measurement operator. For small $\chi \ll 1$ the kernel yields a large width, thus a convolution with a mechanical (ground-) state yields a broadened measurement outcome of the state. For a measurement strength $\chi = 1$ the kernel becomes narrow enough to resolve the mechanical ground state of the system. If $\chi > 1$ the convolution kernel is smaller than the mechanical ground state width. In this regime the measurement strength is strong enough to resolve non-classical features below the SQL. In this picture the measurement strength can also be regarded as a measure of the achievable resolution in the system.

In the experimental realization the only quantity which is accessible by measurement is P_{L}. Thus, the right side of equation 4.19 is implicitly measured if enough statistics about P_{L} are acquired. The width of $\Pr(P_{\mathrm{L}})$ gives a direct insight about the parameter χ in that [59] [69]:

$$\langle X_{\mathrm{M}}^{\mathrm{out}}\rangle \approx \frac{P_{\mathrm{L}}}{\chi} \qquad \text{and} \qquad \sigma^2_{X_{\mathrm{M}}^{\mathrm{out}}} \approx \frac{1}{2\chi^2} \tag{4.20}$$

4.1.2 Pulsed back-action evading state tomography

In the previous sections we introduced the idea of back-action evading QND measurement techniques to measure the resonators mechanical state with sub-SQL precision and defined the requirements to perform such measurements in our system. One topic that we left unaddressed until now is the full reconstruction of the resonator state in phase space while only having access to one QND observable. This limitation can be overcome by an appropriate timing of the individual measurements which becomes apparent when remembering equations 4.3 and 4.5 [56, 162]:

$$\hat{x}(t) = \hat{X}_{\mathrm{M}}\cos(\omega_m t) + \hat{P}_{\mathrm{M}}\sin(\omega_m t) \tag{4.21}$$

$$\frac{\hat{p}(t)}{m\omega_{\mathrm{m}}} = \hat{X}_{\mathrm{M}}\sin(\omega_m t) + \hat{P}_{\mathrm{M}}\cos(\omega_m t) \tag{4.22}$$

From equation 4.21 and 4.22 we derive the times at which a back-action evading measurement of $\hat{x}$ and $\hat{p}$ can be conducted. This is the case when the contribution of the

[69] This relation can be deducted from the action of equation 4.19 onto a mechanical state. A brief outline of this calculation is presented in Appendix D.3.

disturbed quadrature $\hat{P}_{\mathrm{M}}$, after an initial measurement at $t = 0$, vanishes which happens at $t = n\pi/\omega$ for $\hat{x}$ and at $t = (n + 1/2)\pi/\omega$ for $\hat{p}$.
Like in the theoretical description in Section 4.1 we assume X_{M} and P_{M} to be constants of motion. Experimentally, both quadratures vary in time dependent on the Brownian motion of the resonator. For the concept of back-action evasion to work, we require the system to operate in the QCO regime such that both quadratures remain unchanged within one oscillation period. This requires the Brownian motion of the resonator to be negligible during one oscillation period which is equivalent to the thermal coherence time fulfilling $\tau_{\mathrm{coh}} = 1/(\Gamma_{\mathrm{m}} n_{\mathrm{th}}) \geq 2\pi/\omega_m$.
If this condition is fulfilled, we can use a QND measurement to determine the motional state of the resonator with an accuracy better than the zero-point motion. An applicable pulsed protocol using back-action evading techniques was introduced by M. Vanner [59, 72] and shall be outlined in the following.

Suppose we find the resonator in an unknown thermal state such that it operates in the QCO regime. An initial measurement $P_{\mathrm{L}}^{(1)}$ of $\hat{X}_{\mathrm{M},1}$[70] at t=0 in principle allows for an arbitrarily precise measurement of $\hat{x}(t = 0)$. According to equation 4.22, we can gather the information about $\hat{p}$ without back-action from the initial measurement for $t = \pi/2\omega_{\mathrm{m}}$[71]. A measurement $P_{\mathrm{L}}^{(2)}$ of $\hat{X}_{\mathrm{M},2}$ at that time yields an accurate value for $\hat{p}(t = \pi/2\omega_{\mathrm{m}})$.
This technique allows us to measure two non-commuting observables with sub-SQL precision by only acquiring one back-action evading QND observable.
Although these two measurements in principle allow for a full description of the mechanical state, there is no measure to determine their absolute accuracy. For this, a third "readout" measurement $P_{\mathrm{L}}^{(r)}$ has to be conducted that is compared to the predicted system evolution based on the first two measurements. From the measurements $P_{\mathrm{L}}^{(1)}$ and $P_{\mathrm{L}}^{(2)}$ we can anticipate the resonator motion at any given time t since $\hat{X}_{\mathrm{M,r}}$ is determined through:

$$\hat{X}_{\mathrm{M,r}} = \hat{x}(0)\cos(\omega t) - \frac{\hat{p}(\pi/2\omega_{\mathrm{m}})}{m\omega}\sin(\omega t) \Leftrightarrow \hat{X}_{\mathrm{M,r}} = \hat{X}_{\mathrm{M},1}\cos(\omega t) - \hat{X}_{\mathrm{M},2}\sin(\omega t) \quad (4.23)$$

In a perfect QND measurement, the measurement $P_{\mathrm{L}}^{(r)}$ of $\hat{X}_{\mathrm{M,r}}$ would remain constant the whole time such that:

$$P_{\mathrm{L}}^{(r)} - \left(P_{\mathrm{L}}^{(1)}\cos(\omega t) + P_{\mathrm{L}}^{(2)}\sin(\omega t)\right) = 0 \quad \forall t < \tau_{\mathrm{coh}} \quad (4.24)$$

Since we have real world conditions, equation 4.24 is not entirely fulfilled. Ever so slight disturbances of the system yield different results between the measurements of $P_{\mathrm{L}}^{(1)}$, $P_{\mathrm{L}}^{(2)}$ and $P_{\mathrm{L}}^{(r)}$. These differences define the overall accuracy of the measurement. The system has to be prepared in a well defined state by the measurements $P_{\mathrm{L}}^{(1)}$ and $P_{\mathrm{L}}^{(2)}$.

[70] We use the definitions from Eq. 4.5. We refer to the mechanical position quadrature by X_{M} and to the measured quadrature by P_{L}. P_{L} couples to X_{M} via the measurement strength χ.

[71] Here it is important to once more point out the difference between $\hat{x}$ and $\hat{X}_{\mathrm{M}}$. $\hat{X}_{\mathrm{M}}$ can be measured with arbitrary precision at any time due to the back-action evading nature. $\hat{x}$, $\hat{p}$ only share this property at specific times where the contribution from $\hat{P}_{\mathrm{M}}$ vanishes.

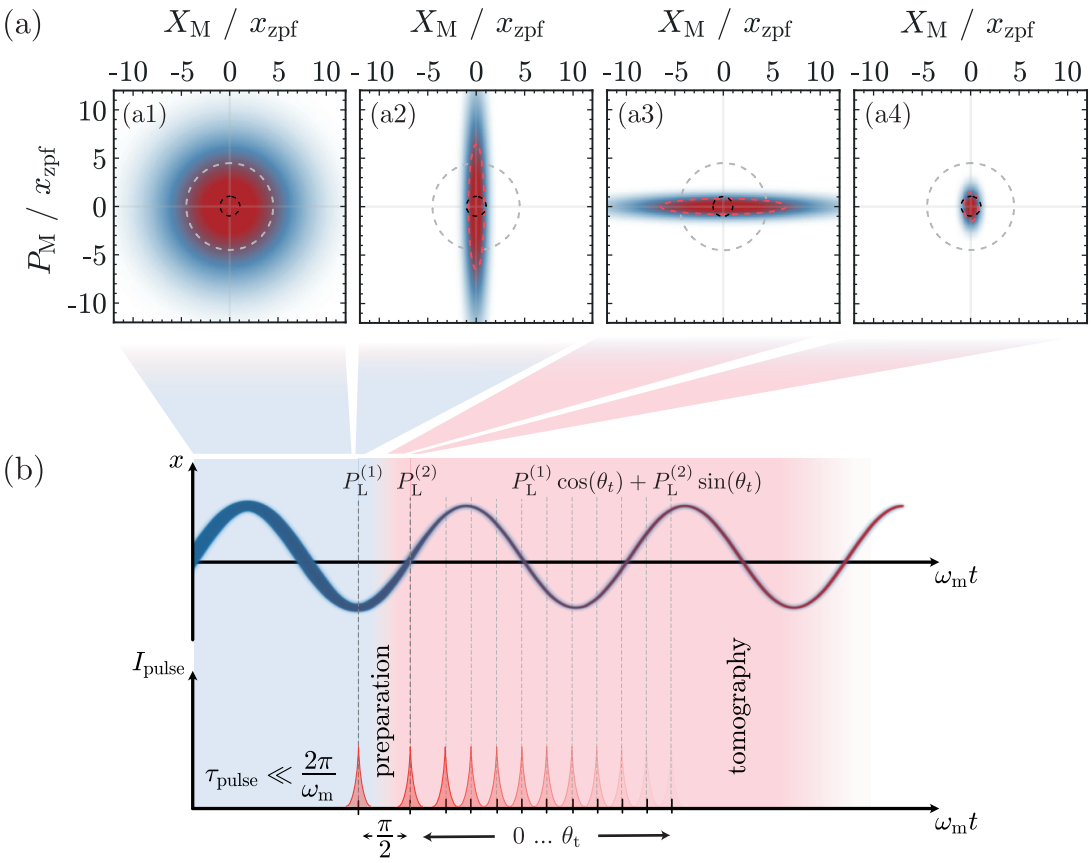

Figure 4.2: Pulsed QND state preparation and tomography:
(a) Phase space distributions during application of a pulsed QND protocol. The grey dashed circle indicates the width of the initial thermal state (a1) with a phonon occupation of $n_{th} = 40$, the black dashed circle denotes the ground state width and the red dashed lines denote squeezed states. The first measurement $P_L^{(1)}$ (a2) yields strong squeezing in the X_M quadrature and accurate knowledge $\hat{x} = \hat{X}_{M,1}$ is acquired. The system now evolves freely which yields a rotation of the state in phase space. After $t = \pi/2\omega$ (a3) the system evolves to a state of maximum uncertainty in $\hat{x}$ and a second measurement $P_L^{(2)}$ is applied. The second measurement again yields strong squeezing in the $\hat{X}_M$ quadrature this time providing accurate knowledge about $\hat{p}/m\omega = \hat{X}_{M,2}$. We obtain a highly purified state (a4). The degree of squeezing depends on the measurement strength χ. For $\chi > 1$ the state width can be reduced below the zero-point motion x_{zpm}. Note that we omitted the influence of the coherent momentum transfer Ω_L, since it has no direct effect on the squeezing. (b) Sketch of the pulsed measurement sequence with two preparation pulses and multiple tomography pulses at varying angles θ_t and the subsequently reduced uncertainty of the mechanical state that evolves according to equation 4.3. Figure adapted from Ref. [63].

The outcome of these measurements is compared with the results after a third measurement ($P_L^{(r)}$) via equation 4.24 (left side) to determine the accuracy with which the mechanical state can be measured. This is the reason for the regularly used term "conditional" state preparation [165, 166]. While the measurements on their own do not allow for a full state description, their relation via the equations of motion does. As such the measurement outcome is conditioned on the results of previous measurements. One has to be aware that being able to conduct a back-action evading measurement with

sub-SQL precision is a property of the observable. But gaining the knowledge about the precision comes from the application of a QND measurement technique.
The reduction of the state entropy can be treated like an effective reduction of the resonators phonon occupation which motivates the term "cooling by measurement" [72]. Since this measurement takes place within one oscillation period it is insensitive to external influences that act on larger timescales as long as the system is in the QCO regime. However, it is notable that the real thermal phonon occupation is not reduced and the term "cooling" solely refers to the state width reduction in phase space.
The acquired conditional state can be mapped out in phase space by a tomographic measurement. By varying the time between the third measurement pulse, and the initial two preparation pulses, the conditional state undergoes a rotation in phase space according to $\theta_\mathrm{t} = \omega_\mathrm{m} t$. When conducting multiple measurements P_L at one tomography angle θ the phase space probability distribution of the quadrature contributions $\hat{x}$ and $\hat{p}$ is projected onto P_L. Conducting multiple measurements of equally prepared conditional states gathers the necessary statistics that eventually resemble the probability distribution $\Pr(P_\mathrm{L})$[59] at a given tomography angle. The probability distribution $\Pr(P_\mathrm{L})$ is also referred to as marginal of the mechanical state. If the marginals are acquired for sufficiently many tomography angles (i.e., $\theta_\mathrm{t} = 0° \ldots 90°$ for a squeezed, but axes-symmetric state) they allow for full state reconstruction in phase space by applying the inverse radon transformation [72, 167, 168]. This method of state reconstruction is experimentally realized and presented in Section 4.3.

4.1.3 Achieving sub-SQL resolution

Until now, we omitted detailed discussions on the measurement strength and the experimental requirements to achieve $\chi > 1$. In the context of cavity optomechanical systems the measurement strength relates the information gained by the coupling of $\bar{N}$ photons to the resonator with the single photon coupling rate g_0, to the shot noise $\sqrt{\bar{N}}$. It also takes into account optical losses in the system via the factor η. For pulse lengths that exceed the intra-cavity photon lifetime this results in the expression [72, 166] [72]:

$$\chi = \frac{8 g_0 \sqrt{\eta \bar{N}}}{\kappa} \tag{4.25}$$

To observe the systems zero-point motion, the system needs to resolve the phase shift $\delta\phi_\mathrm{r} = 4 g_\mathrm{m} \delta X_\mathrm{M} / \kappa$ that is caused by one zero-point motion of the resonator. Using the number-phase uncertainty relationship $\delta\phi\delta N \geq 1/2$ [169] where δN is given via the shot noise $\propto \sqrt{\bar{N}}$ and assuming $\delta X_\mathrm{M} = x_\mathrm{zpm}$ we arrive at the requirement [59]:

$$\sqrt{\bar{N}} \geq \frac{\kappa}{8 g_0} \quad \Rightarrow \quad \underline{\underline{\chi \geq 1}} \tag{4.26}$$

Previous experiments that implemented the aforementioned measurement scheme reached measurement strengths of $\chi_\mathrm{Vanner} = 2.1 \cdot 10^{-4}$ [72] and $\chi_\mathrm{Muhonen} = 0.079$ [73]. During the first implementation of pulsed measurements in our experiment presented in Ref.

[72] We present a detailed derivation of this expression in Appendix D.4.

[63], we reached a measurement strength of $\chi \approx 0.002$[73].

The measurement strength crucially depends on the number of intra-cavity photons $\bar{N}$ that couple to the resonator. This number is proportional on the signal light power P_{SIG} and the lifetime of the photons in the cavity $\tau_{\mathrm{cav}} \approx 1/\kappa$. The intra-cavity photon number can be calculated to:

$$\bar{N} = \frac{P_{\mathrm{SIG}} \cdot \tau_{\mathrm{cav}}}{\hbar\omega_{\mathrm{TiSa}}} = \frac{P_{\mathrm{SIG}}}{\hbar\omega_{\mathrm{TiSa}}\kappa} \tag{4.27}$$

Here it becomes apparent that any pulse, that lasts longer than τ_{cav}, does not yield any gain in information, yet it transfers a way larger momentum to the resonator than a pulse of optimal duration would. the full momentum $\propto \bar{N}$ to the resonator. Thus, we aim for the pulses to be as short as technically possible due to the very small τ_{cav} of our system. Using expression 4.27 together with equation 4.25, we can calculate the necessary signal beam powers to reach $\chi > 1$ for different κ[74]:

$$\chi = \frac{8g_0}{\kappa}\sqrt{\eta\bar{N}} = \frac{8g_0}{\kappa^{\frac{3}{2}}}\sqrt{\frac{\eta P_{\mathrm{SIG}}}{\hbar\omega}} \tag{4.28}$$

An overview of χ for different finesses and signal beam powers is depicted in Fig. 4.3. It is notable that the cavity finesse is the most influential parameter on the measurement strength since $\chi \propto 1/\kappa^{3/2} \propto \mathcal{F}^{3/2}$. An increase in finesse by a factor of 10 yields an increase in χ by a factor of 30. To achieve a measurement strength at reasonable signal beam powers[75] we calculate the necessary finesse to $\mathcal{F} \approx 15000$.

For high finesse systems where pulse lengths can be on the on the order of the intra cavity photon lifetime, the measurement strength can be further increased by optimizing the shape of the measurement pulse. This only becomes relevant if the pulse width is of the same order of magnitude as the cavity ringdown time $t_{\mathrm{pulse}} \to \tau_{\mathrm{cav}}$. In this case, the cavity response has a significant effect on the signal $P_{\mathrm{L}}^{\mathrm{out}}$. Because this scenario is relevant for the newly built high finesse cavities, a detailed derivation of the optimal pulse shape is presented in Appendix D.4 where we find the optimal pulse envelope to fulfill:

$$\alpha_{\mathrm{in}}(t) = \sqrt{\kappa}e^{-\kappa|t|} \quad \text{which yields} \quad \chi_{\mathrm{opt}} = 4\sqrt{5}\frac{g_0}{\kappa}\sqrt{\bar{N}} \tag{4.29}$$

[73] That is the value acquired from the conditional state widths found in Ref. [63]. It differs from the stated value of $\chi = 0.011$ in Ref. [63] which refers to the measurement resolution for the off-resonant system. We abide by the definition of other publications in this field and define χ for the on-resonant conditional state width in this thesis.

[74] Note that $1/\kappa \propto \mathcal{F}$ via equation 2.23.

[75] Resonable in the sense that we still can assume the system to couple linearly to the light field at all times. For lattice powers of $P_{\mathrm{lat}} > 25\,\mu\mathrm{W}$ at $\mathcal{F} = 1500$, this already turned out to not be the case as described in Section 3.3.1.

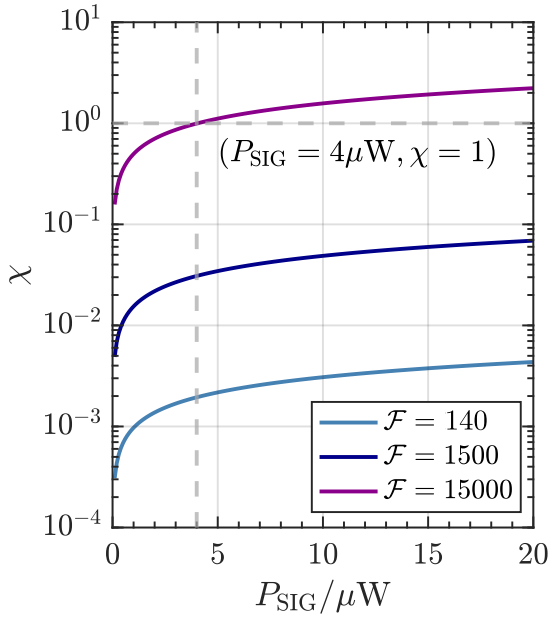

Figure 4.3: Measurement strength for different finesses: Achievable measurement strength χ according to equation 4.28 as a function of the signal beam power. The calculations show a finesse of $\mathcal{F} = 15000$ to be necessary to acquire $\chi > 1$. For $\mathcal{F} = 140$ and $\mathcal{F} = 1500$, the linewidths $\kappa_{140} = 48\,\mathrm{GHz}$ and $\kappa_{1500} = 7.6\,\mathrm{GHz}$ were obtained from optical spring measurements (Sec. 2.3.3). For $\mathcal{F} = 15000$ we calculated $\kappa \approx 750\,\mathrm{MHz}$ assuming the same cavity alignment as for the other configurations. We only calculate χ for $P_{\mathrm{SIG}} < 20\,\mu\mathrm{W}$ where the system couples linearly to the light.

4.2 Pulsed state preparation in a high finesse optomechanical system

Based on the previous considerations we can deduce the requirements that an experimental platform would need to resolve the ground state of the resonator in a pulsed QND measurement. Extracting only one quadrature with sub-SQL precision requires a very short and intense interaction between the probing field and the resonator such that $\tau_{\mathrm{pulse}} \ll T_{\mathrm{m}}$ (with $T_{\mathrm{m}} = 6.5\,\mu\mathrm{s}$) and $P_{\mathrm{SIG}} > 4\,\mu\mathrm{W}$ ($\bar{N} > 21000$) where T_{m} is the oscillation period of the resonator. Furthermore, we want to disturb the system as little as possible while gaining maximal information about the state. The acquired information at a given probing beam power is limited by the lifetime of the photons in the cavity $\tau_{\mathrm{cav}} = 1/\kappa$. Any pulses that exceed the intra-cavity lifetime more than necessary transfer momentum to the system, thus broadening the orthogonal QND quadrature[76]. For ideal measurement conditions we generate high intensity pulses with $2\pi/\omega \gg \tau_{\mathrm{pulse}} \approx \tau_{\mathrm{cav}}$. In the previous experimental setup, fulfilling both requirements was not possible due to the large cavity linewidth of $48\,\mathrm{GHz} \Rightarrow \tau_{\mathrm{cav}} \approx 20\,\mathrm{ps}$. The new system yields an optical finesse of $\mathcal{F} = 14500$. Considering a cavity length of $L_{\mathrm{cav}} = 14.0\,(5)\,\mu\mathrm{m}$ and using equation 2.23 this yields a lifetime of $\tau_{\mathrm{cav}} = 1.3\,(2)\,\mathrm{ns}$. Here, it is possible to apply pulses with lengths on the same order of magnitude as the inverse linewidth which allows to further increase the measurement strength by choosing a pulse shape presented in equation 4.29.

We require the detection to be quantum noise limited at all times and capable of re-

[76] While this has no impact on the observed quadrature in theory, in reality it can excite higher vibrational modes of the resonator. These feed back into both observable, destroying the QND property of the system.

solving pulses with a length of a few nanoseconds. Furthermore, it has to exclusively detect the X_{M} quadrature of the resonator to allow for a true back-action evading QND measurement.
While the experimental setup and measurements presented here are new to this experiment, the presented evaluation methods as well as the programming of the devices have been carried out together with J. Butlewski. The first implementation of pulsed measurements in the old setup at $\mathcal{F} = 140$ are presented in his thesis [63]. The measurements presented here were conducted at a finesse of $\mathcal{F} = 1500$ and $\mathcal{F} = 14500$. The details regarding the experimental setup, outlined in the following section, will focus to the experiment configuration at $\mathcal{F} = 14500$. Measurements at $\mathcal{F} = 1500$ differ in the choosen pulselengths and beam powers but were conducted with a same experimental setup.

4.2.1 Generating short pulses

Our measurement scheme requires the fast generation and measurement of multiple pulse trains with nanosecond pulses of arbitrary shape. Both the pulse signal generator and the optical actuator have to be capable to operate at these timescales. Since the necessary statistics emerge from multiple repetitions of a pulsed sequence, a high measurement bandwidth and sufficient memory to maximize the possible measurement repetition rate are required.
For the driving signal generation and the data acquisition we use the UHF-AWG with integrated digitizer from *Zurich Instruments*. It allows for arbitrary pulse generation at 14-bit vertical resolution at a maximum sampling rate of 1.8 GSa/s with a specified rise-time (10%-90%) of only 700 ps. Thus, the device is capable of producing sufficiently resolved pulses of arbitrary shape on the order of the cavity linewidth. The same device allows for lock-in detection of frequencies up to 600 MHz and rapid data acquisition using a 1.8 GSa/s digitizer with an internal memory of 125 MSa and 12-bit vertical resolution[77]. Figure 4.4(a) shows an exemplary pulse train for the conditional preparation of the resonator after two pulses at a distance of $\pi/2 = 90°$, the third pulse can be applied at distances from $\theta_{\mathrm{t}} = 3° - 90°$. Each of these trains were repeated 20000 times per angle θ_t at a repetition rate of 50 Hz. The high bandwidth and fast switching times of the AWG come at the cost of relatively low output amplitudes ($V_{\mathrm{AWG,max}} = \pm 1.5V$). This introduces further constraints on the optical modulator.
We found a fiber based amplitude modulating EOM (*Jenoptik AM785b*) to be the best option to exploit the full capability of the pulse generator. Its small dimensions and electrode distances render it capable of reaching modulation bandwidths in the GHz range with the half-wave-voltage $V_{\lambda/2}$ being in the range of a few volts. The performance is highly wavelength dependent and while modulators designed for the infrared (e.g. $\lambda = 1064\,\mathrm{nm}$) can be operated at $P_{\mathrm{in}} = 300\,\mathrm{mW}$ input power, current designs that operate at $\lambda = 780\,\mathrm{nm}$ yield high insertion losses of $(5 - 6)\,\mathrm{dB}$ and only allow for operation up to $P_{\mathrm{in}} = 30\,\mathrm{mW}$ input power.
Our fiber EOM has a half wave voltage of $V_{\lambda/2} = 2.02\,\mathrm{V}$ and an insertion loss of 4.9 dB

[77] Assuming one measurement acquires half an oscillation period. The corresponding trace would yields a sample length of $T_{\mathrm{acq}} \cdot 1.8\,\mathrm{GSa/s} = 8192\,\mathrm{Sa}$. The internal memory would then allow to measure $N \approx 150000$ traces within one run.

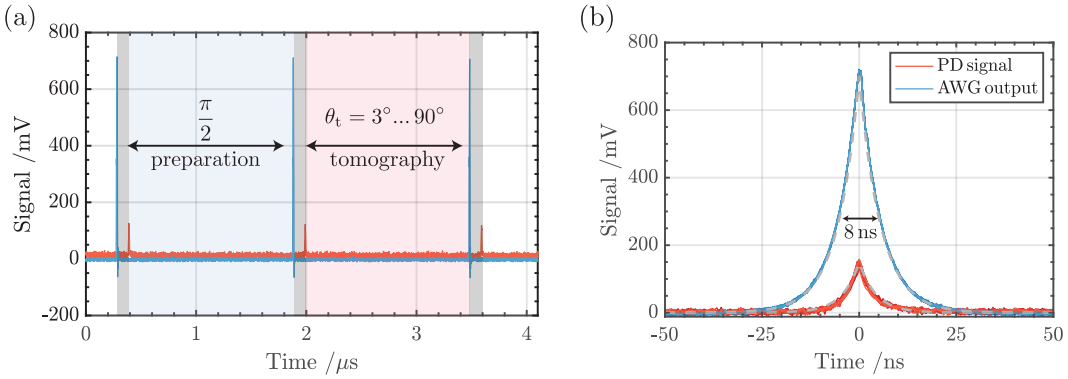

Figure 4.4: Pulse train for conditional state preparation:
(a) Time trace of a pulse train for state preparation. Two pulses separated by $\pi/2$ prepare the resonator in a squeezed state. A third pulse after a variable separation time is applied to map out the state at different tomography angles θ_t. For each angle 20000 traces are recorded to acquire sufficient statistics. The grey shades denote the delay between pulse generation and detection. (b) Optimized pulse shape according to equation 4.29. The minimal properly resolvable width (FHWM) is $\tau_{\text{pulse}} = 8\,\text{ns}$. The blue lines denote the AWG output signal, the red lines the signal measured with the PD. Dashed lines denote fits of equation 4.29 to the data. Figure (b) depicts 19 overlapped traces.

(specified by the manufacturer). Its optical rise time is 200 ps. To optimize the compatibility of our EOM with the detection system, it was custom made with an HP780PM fiber at the input and a HP780SM fiber at the output to allow for optimal mode match when spliced to the rest of the setup. To circumvent limitations due to the low power transmission and to prevent being limited by the usable LO power, the fiber EOM was installed solely in the signal branch as discussed later in Section 4.6. Figure 4.4(b) shows 19 time traces of the generation (blue) and detection (red) of 8 ns short light pulses with an optimized pulse shape described by equation 4.29 using the AWG and the fiber EOM. The dashed grey lines show a theoretical fit of equation 4.29 to the data. We found a pulse length of 8 ns to be the shortest time at which the pulse features were still sufficiently resolved.

4.2.2 Pulse detection

We conduct a phase sensitive measurement of the mechanical quadrature by employing a balanced homodyne detection scheme. The detection has to be shot noise limited over the whole range of operating powers while being fast and offering an excellent signal-to-noise ratio. For sufficiently fast detection we use the balanced detector HBPR-500M-FST[78] from *FEMTO* which is capable of operating in a frequency range up 500 MHz. This high bandwidth naturally comes at the cost of lower gain and worse signal-to-noise ratios [94] requiring for overall larger signal powers or a higher SIG:LO power ratio. In Section 2.4.1 we calculated the power dependent SNR and found the SNR to saturate for most operation scenarios at a ratio of SIG:LO=1:2000. The new detection system is optimized to achieve almost arbitrary power ratios, much higher than theoretically required.

[78] HBPR-500M-FST: DC...500 MHz, gain: 2.55-5.1 kV/W, $\text{NEP}_{\text{max}} = 60\,\text{pW}/\sqrt{\text{Hz}}$

A big advantage in the applied detection scheme arises from the common-mode rejection of the detector which is specified by the manufacturer to CMRR = 45 dB. In Ref. [63] the electronic properties and the CMRR were investigated and the shot noise limitation was verified for the new setup. The results are presented in Appendix D.1. Besides the necessary electronic capabilities, achieving a high CMRR requires spatial and temporal overlap between the signal and LO beam. While the spatial mode-match is optimized due to the use of similar glasfibers and identical fiber couplers, the increased refractive index (n ≈ 2) of the fibers yields a stronger influence of path-length differences between the signal and LO branch on the temporal mode-match. A length difference of 1 m yields a time difference of 5 ns between the signal and LO branch which can be detected by the photodiode and diminishes the CMRR capability of the setup. Thus, the path length between both branches is carefully matched. We set both signal and LO beam to be equally strong and adjust the respective polarization such that each beam hits one of the photodiode detection ports.
We use an AOM connected to an RF-switch to generate a 5 μs rectangular pulse and measure the differential photodiode signal during the pulse. The result is depicted in Fig. 4.5. Due to the mismatched path lengths, one beam arrives on the photodiode earlier leading to a spike in the differential signal (dark blue) with a width proportional to the path length difference. By splicing additional fiber into the LO branch, the width of the spike is reduced (light blue) until it is not noticeable anymore for a balanced setup (red).

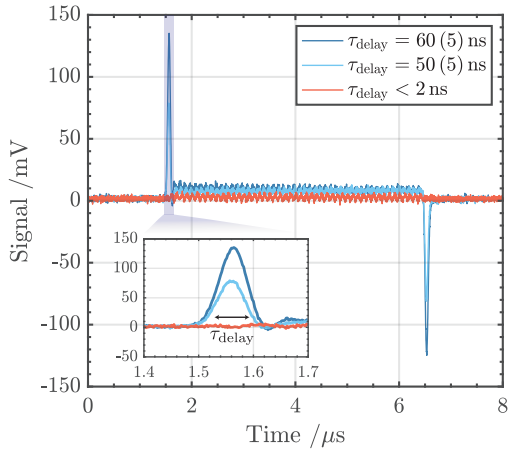

Figure 4.5: Time delay due to different branch lengths:
Signal of a 5 μs rectangular pulse light pulse for different stages of path length compensation. The signal and LO beam are equally strong and each beam is incident on one PD port. The delay causes an imbalance in power between both ports at the beginning and end of the pulse (blue shaded area) yielding a spike in the signal. Upon reduction of the path length difference (blue curves) the width of this spike decreases until it is not noticeable anymore (red curve). The modulation on the pulse was found to be caused by slight misalignment of the AOM. Realignment of the respective branch made the modulation go away.

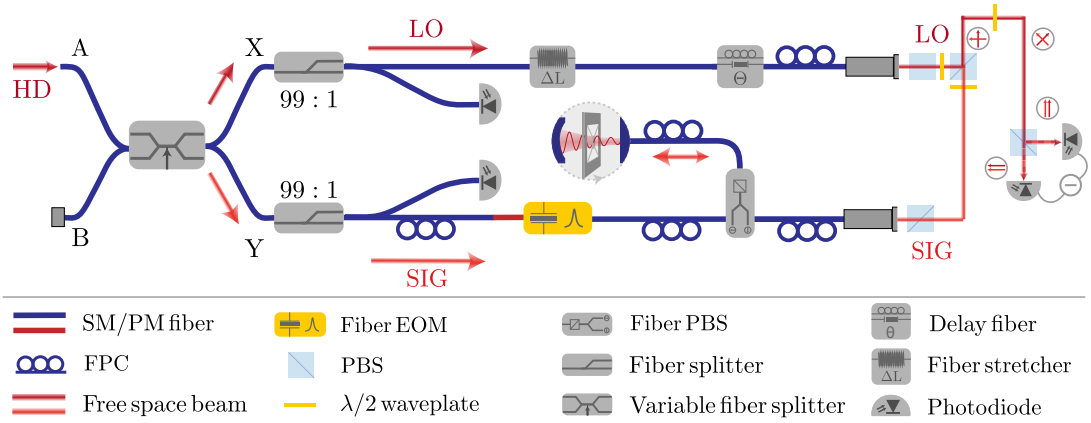

Figure 4.6: Experimental setup for pulsed optomechanics:
Sketch of the fiber based experimental setup. Light is split up by a variable fiber splitter into the signal and LO beam branch. The power at the beamsplitter outputs, is monitored by two photodiodes that are connected via a 99:1 beamsplitter. The photodiode in the LO branch is used for intensity regulation. To compensate for path length differences between both branches an additional delay fiber is spliced into the LO path. A fiber stretcher allows for phase locking between the LO and signal beam for continuous measurements. The signal beam branch contains the fiber EOM for generation of arbitrary shaped pulses. It is connected directly to the cavity via a fiber PBS. The polarization of the light reflected from the cavity is rotated such that it is transmitted through the PBS port orthogonal to the EOM port. Both beams are overlapped in a free space homodyne detection setup and detected via a balanced PD. The little red arrows indicate the polarization state of both beams in the detection.

4.2.3 Fiber based setup for pulsed state preparation

The first proof of principle experiments towards pulsed state preparation at our experiment [63] were mainly limited by the cavity finesse and by the maximum applicable pulse power. This was due to the fact that LO and signal beam were transmitted through the same fiber EOM which limited the overall power in the setup to the maximum transmission of the EOM within its damage threshold $P_{\text{in,max}} = 30\,\text{mW} \Rightarrow P_{\text{trans,max}} \approx 5.5\,\text{mW}$. In Fig. 4.3 we calculated the necessary signal power to resolve the zero-point motion at a finesse $\mathcal{F} = 15000$ to $P_{\text{SIG}} = 4\,\mu\text{W}$. At the same time, we want to maximize the SIG:LO ratio to achieve the highest optical gain and best possible SNR. This requires us to operate at LO powers of 20 mW[79].
Taking these requirements into account we rebuilt the homodyne detection using mostly fiber optical components and separated the signal path including pulse generation from the LO branch. This allowed for a seamless integration of the fiber cavity and the EOM into the setup.
In contrast to the previous setup, the EOM is implemented directly into the signal beam branch. This allows to independently set the power of the LO and signal beam and enables higher signal beam powers[80]. The EOM is connected to the fiber cavity via a fiber PBS. Differently to previous setups, the cavity features an HR coated multi-

[79] At this power 10 mW LO light are incident on each photodetector. This is slightly below the damage threshold of the photodiode.
[80] In principle up to $P_{\text{trans,max}} \approx 7.5\,\text{mW}$ at an LO power of 13.5 mW. Limited by the damage threshold of the PD.

mode fiber on the higher reflective, curved side[81]. Upon reflection from the cavity the polarization of the light is turned such that it transmits through the PBS port orthogonal to the EOM input port. Both signal and LO beam are then superimposed and directed onto the 500 MHz balanced photo-receiver in a free space setup. In front of every polarization sensitive optical element, fiber based polarization controllers are implemented. Taking all losses due to splices and transmission through optical elements into account, the overall detection efficiency of the system of a pulse that leaves the cavity and is incident on the detector is $\eta_{\mathrm{det}} = (0.52 \pm 0.02)$ at a visibility of $\mathcal{V}^2 > 99\%$. While η_{det} remains comparable to the old setup, the much higher pulse powers, the flexible adjustment of high signal to LO power ratios and the superior stability yield a significant improvement over the old system.

[81] This was done to achieve higher transmission and gain more information about the system from a single measurement.

4.3 Experimental results

Experiments were conducted at two cavity configurations at a finesse of $\mathcal{F} = 1500$ and $\mathcal{F} = 14500$. While we optimized the pulse envelope and experimental setup particularly for the high finesse configuration, because this configuration is capable of reaching the measurement strength $\chi > 1$, measurements at $\mathcal{F} = 1500$ were performed to determine the scaling of the measurement strength with the finesse. Thus, the latter measurements were conducted at room temperature. Since the system at $\mathcal{F} = 1500$ allows for continuous displacement measurements, it exhibits a much higher degree of control and can be characterized accurately as done in Section 2.3.2 whereas the system at $\mathcal{F} = 14500$ behaves fundamentally different. Here, new measurement strategies had to be developed to gather meaningful results. The largest uncertainty in the determined state widths and effective temperature comes from the uncertainty of the homodyne calibration ($c_{\mathrm{HD},1500} = (8.9\pm0.8)\frac{\mathrm{rad}}{\mathrm{nm}}$ and $c_{\mathrm{HD},15000} = (170\pm40)\frac{\mathrm{rad}}{\mathrm{nm}}$). For better readability of the plots, we decide to plot the data only using the mean value of the calibration. Yet when calculating the state widths and mode temperature errors, we take the error due to the calibration explicitly into account.

4.3.1 Pulsed state preparation at $\mathcal{F} = 1500$

For $\mathcal{F} = 1500$ the increased stability of the system compared to the high finesse configuration allows for a careful adjustment on resonance without driving it into limit cycles[82]. Due to the high initial phonon occupation, we can neglect the influence by the probe pulse momentum transfer Ω and do not need additional cooling techniques in between the measurements. The possibility to trigger the AWG dependent on the input signal level, allows to apply pulse-trains at the zero crossing of the homodyne signal. Thus, we omit a phase-lock which renders the experimental sequence very simple.

For the experiments presented here we used an LO power of 4 mW and adjusted the system such that we measure a signal power of $4\,\mu$W at the outcoupling fiber of the signal branch, if the AWG applies the maximum possible output signal to the EOM.
At the beginning of each sequence, the EOM is in a state of minimal transmission. Nonetheless, residual light that transmits though the EOM is sufficient to provide a small phase dependent homodyne signal on the order of (100 mV). Upon receiving a high TTL input, the AWG initializes the pulse sequence and waits for a zero crossing of the differential homodyne signal to occur which indicates $\phi_{\mathrm{LO}} = \pi/2$[83]. If this condition is fulfilled, the AWG applies a pulse train of three pulses with two preparation pulses $P_{\mathrm{L}}^{(1)}$, $P_{\mathrm{L}}^{(2)}$ and one tomography pulse $P_{\mathrm{L}}^{(3)}$ that is varied for multiple tomography angles. Here, $P_{\mathrm{L}}^{(1,2,3)}$ denotes the averaged amplitude of each pulse. The conditional state is calculated as derived in equation 4.24:

$$C(\theta_{\mathrm{t}}) = P_{\mathrm{L}}^{(3)} - \left(P_{\mathrm{L}}^{(2)}\cos(\theta_{\mathrm{t}}) + P_{\mathrm{L}}^{(1)}\sin(\theta_{\mathrm{t}})\right) \tag{4.30}$$

[82] That is, if its adjusted to the side of optomechanical cooling.

[83] We note that there is also a modulation from the resonator that can cause a zero crossing. This is accounted for in the later evaluation by correction of the determined phase offset.

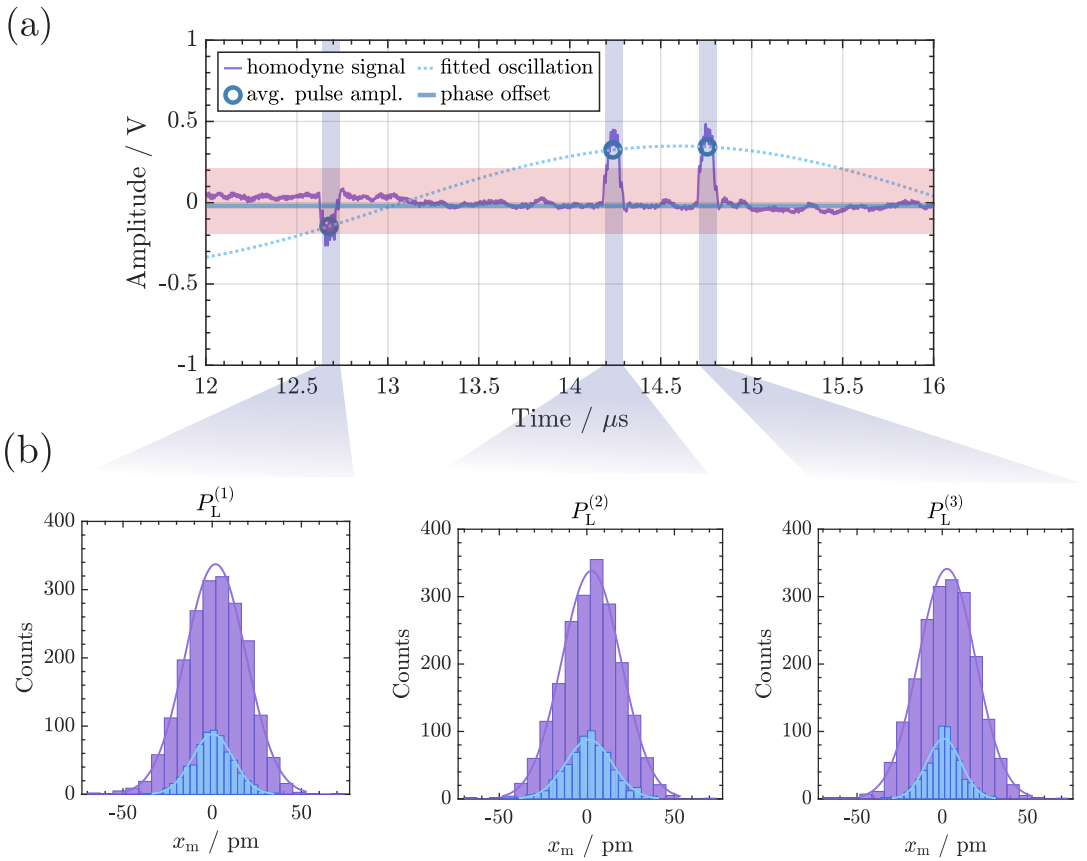

Figure 4.7: Measured pulse train and phase offset correction:
(a) Homodyne signal of a pulse train at $\theta_t = 30°$ with the cavity tuned on resonance with $t_{pulse} = 90\,ns$. The measurement outcome P_L is determined via the averaged pulse amplitudes (blue points). We fit a sinusoidal oscillation (dashed blue line) with the resonators eigenfrequency to the pulse amplitude to determine the homodyne phase offset (blue line). (b) Histograms of the measurement outcomes for each pulse at $\theta_t = 30°$ with fitted Gaussian distributions prior (violet) and after (blue) postselection. The red shaded area shows the region of acceptance for homodyne phase offset values. The homodyne signal is converted to the displacement via the homodyne calibration which is $c_{HD,1500} = (8.9 \pm 0.8)\frac{rad}{nm}$ in this configuration.

We measured five tomography angles (θ_t = 10°, 30°, 50°, 70°, 90°) with 2000 pulse trains per measurement sequence at a measurement rate of 10 Hz. The pulses are of rectangular shape and have a length of 90 ns. The AWG and the digitizer operate at a resolution of 450 MSa/s. Figure 4.7(a) shows an example measurement of such a pulse train for a tomography angle of $\theta_t = 30°$.
We only take data into account that was recorded in the linear region of the homodyne signal and that predominately measures the X_M quadrature of the system. This is crucial to maintain the QND-property of the measurement. Since the homodyne phase is freely drifting we have to post-select the data that can be used for state tomography in two steps. The first step is visualized in Fig. 4.8. From the off-resonant peak-to-peak signal $V_{PP,offres}$ of the homodyne detection, obtained by scanning the phase ϕ_{LO}, we can derive the signal $V_{PP,onres}$ from the reflectivity on resonance σ. We define the range of usable data as the range where the homodyne scan signal does not differ from a linear

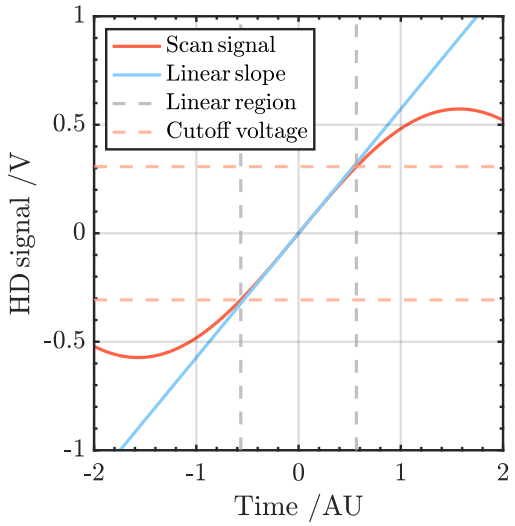

Figure 4.8: Postselection of acquired traces:
Visualization of the postselection criterium for pulsed measurements. We determine the expected homodyne peak-to-peak voltage (red line) and determine the slope of the signal at its turning point (blue line). The range within which the signal does differ by less than 5% from the linear slope (grey dashed line), is considered to be usable for evaluation. From this region a cutoff voltage (red dashed line) is derived. If any pulse in a pulse train exceeds the cutoff voltage, the whole pulse-train is excluded from further evaluation.

fit through turning point of the signal by more than 5 percent.
From this condition we can derive a cutoff voltage range $V_{\mathrm{PP,cutoff}}$. For the conditional state preparation we only take data into account for which all three measurements of one pulse train $P_{\mathrm{L}}^{(1,2,3)}$ are within the cutoff voltage range. The second criterium is applied after the initial postselection took place. Even though we trigger onto a zero crossing before the pulses are applied, this condition is not very accurate due to the small signal beam power prior to the pulses. To determine the phase offset more accurately we fit a sinusoidal function at the resonators eigenfrequency ω_{m} through the pulses as depicted in Fig. 4.7(a). From the fit we define the actual phase offset which is subtracted for further evaluation. In addition, we exclude pulse trains for which the calculated offsets are greater than $|V_{\mathrm{offset}}| > 0.2\,\mathrm{V}$. This condition enforces only measurements with large X_{M} contributions to be considered. While theoretically the exclusion boundary should be set as narrow as possible to minimize influences from P_{M}, it still has to yield sufficient amounts of data for the statistical evaluation. Figure 4.7(b) shows the data set before (violet) and after (blue) all post-selection criteria described above are applied. The blue histograms depict the data that is used for further evaluation.

The post-processed data allows for reconstruction of the conditional mechanical state by applying equation 4.30 to the measurement outcomes of each pulse train. The results are depicted in Fig. 4.9. By mapping out the measurement outcomes of the first pulse $P_{\mathrm{L}}^{(1)}$ we acquire the initial state width of the resonator with $\sigma_{\mathrm{ini}} = (11 \pm 4)\,\mathrm{pm} = (2600 \pm 1000)\,x_{\mathrm{zpm}}$. By calculating the conditional variance, we achieve strong squeezing of the state and acquire a state width of $\sigma_{\mathrm{cond}}^{\theta_{\mathrm{t}}=0^\circ} = (70 \pm 4)\,\mathrm{fm} = (16 \pm 1)\,x_{\mathrm{zpm}}$ and $\sigma_{\mathrm{cond}}^{\theta_{\mathrm{t}}=90^\circ} = (225 \pm 20)\,\mathrm{fm} = (53 \pm 5)\,x_{\mathrm{zpm}}$. The corresponding conditional state variances are denoted by the dark red histograms. The histograms represent the projection of the mechanical sate onto the X_{M} axis in phase space. They are equivalent to the mechanical marginals introduced in Section 4.1.2. We determine the width of the state by applying a Gaussian fit to the histograms. From the theory discussed in Section 4.1 we expect a constant width of the thermal state for all tomography angles and a broader distribution of the conditional state in the P_{M} quadrature due to the back-action from

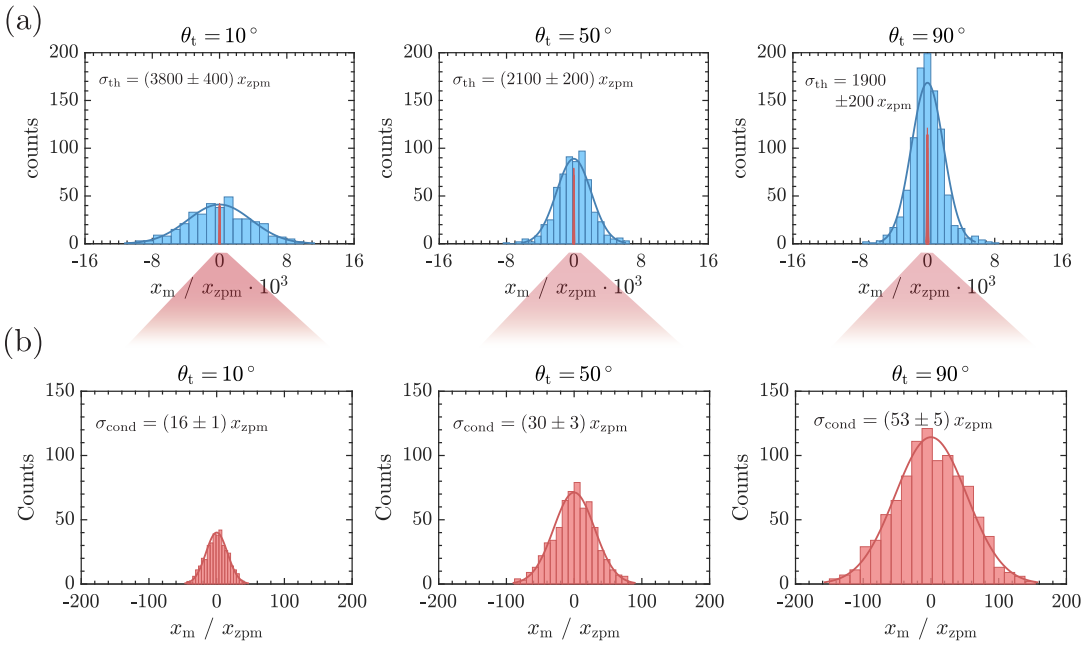

Figure 4.9: Marginal distributions at different tomography angles:
(a) Mechanical marginals at different tomography angles as determined in Fig. 4.7 (blue histograms) with a gaussian fit to determine the state width. The conditional state (red histograms) calculated by equation 4.30 is strongly squeezed in comparison to the initial distribution. (b) Zoom into the conditional state histogram. The minimal acquired state width is $\sigma_{cond} = (16 \pm 1)\, x_{zpm}$. Towards higher tomography angles the state width increases.

X_M onto P_M. This holds true for the conditional state which shows a slight increase in width towards higher tomography angles. Due to the high phonon occupation at room temperature we can assume the pollution of P_M due to the measurement to be small, thus not changing significantly for different tomography angles. The large error of the initial state σ_{ini} can be accounted to the Brownian motion of the resonator by coupling to the thermal bath which, due to the small mechanical linewidth, varies the oscillation amplitudes on the order of minutes [101]. Furthermore, the alignment of the cavity to the side of optomechanical cooling reduces the mode temperature. An additional systematic error originates from the postselection of the data combined with the large phase shift the resonator generates. In our particular case a state width of a 293 K warm thermal state ($\sigma_{th} \approx 9000\, x_{zpm}$) produces a signal amplitude outside the linear region of the homodyne signal which leads to the data set being rejected during post-selection. Although we lose information about the initial state, this is necessary to ensure to QND properties of the measurements. Thus, we refer to the measurement outcome of the first pulse as “initial” and not as “thermal” state.
From the acquired state widths, we can calculate the effective state temperatures to [72]

$$T_{eff}^{ini} = \frac{m_{eff}\omega_m^2 \bar{\sigma}_{ini}^2}{k_B} \quad \text{and} \quad T_{eff}^{cond} = \frac{m_{eff}\omega_m^2 \sigma_{cond}^{\theta_t=10°} \sigma_{cond}^{\theta_t=90°}}{k_B} \tag{4.31}$$

The representation of the thermal and conditional states in phase space is acquired by

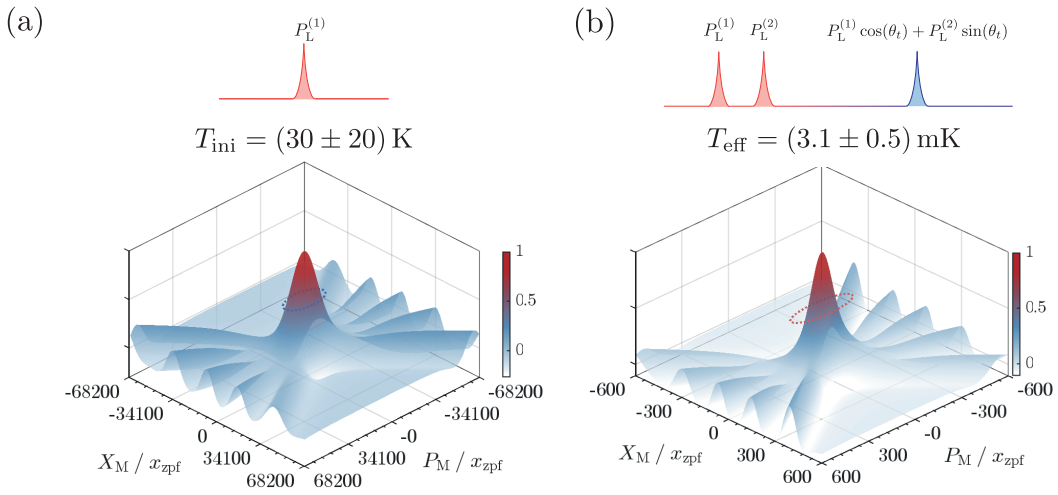

Figure 4.10: State reconstruction in phase space:
(a) Reconstruction of the initial state by evaluation of the first pulse of each pulse train. We apply the inverse radon transform on the acquired marginals. The blue circle denotes the 2σ radius of the respective initial distributions at the different tomography angles. The squeezing is attributed to long term amplitude fluctuations of the system and the possibility of optomechanical cooling. (b) Reconstruction of the conditional state in phase space. The state exhibits only a slight asymmetry, indicating the back-action from the measurement on the system to be negligible against the large thermal phonon occupation. We calculate the effective temperatures according to equation 4.31. The pulsed measurement sequences to acquire the data are illustrated above the plots. Note that the axis scaling in (a) is by a factor 100 larger than in (b).

applying the inverse radon transformation to the mechanical marginals. The results are depicted in Fig. 4.10. Based on equation 4.31 we calculate the effective mode temperature of the resonator to $T_{\mathrm{eff}}^{\mathrm{cond}} = (3.1 \pm 0.5)\,\mathrm{mK}$. From the mean squeezed state width $\bar{\sigma}_{\mathrm{cond,1500}}^{\mathrm{mean}} = (33 \pm 12)\,x_{\mathrm{zpm}}$ we can calculate the measurement strength of the system in this configuration by using equation 4.20 [59]:

$$\chi_{1500} \approx \frac{1}{\sqrt{2}\sigma_{\mathrm{cond}}} = 0.021\,(+0.012\,/\,-0.005) \tag{4.32}$$

This result aligns with the theoretical prediction presented in Fig. 4.3. Furthermore, the state width of $16\,x_{\mathrm{zpm}}$ is close to a fundamental limit arising from amplitude fluctuations due to the Brownian motion of the resonator at room temperature. If we compare this result with the mean conditional variance of the system at $\mathcal{F} = 140$ we find $\bar{\sigma}_{\mathrm{cond,140}}^{\mathrm{mean}} = (400 \pm 200)\,x_{\mathrm{zpf}}$ and $\chi_{140} = 0.002\,(+0.002\,/\,-0.001)$. Thus, we can conclude, that the increase of the finesse by a factor of 10 yields an increase of a measurement strength by a factor of $10\,(+20\,/\,-6)$. The increase in measurement strength aligns with the theoretically expected value of 30 within the error margins. This further motivates the implementation of a high finesse cavity to beat the condition $\chi > 1$.

4.3.2 Pulsed state preparation at $\mathcal{F} = 14500$

The operation of the experiment at $\mathcal{F} = 14500$ is incomparable with previous setups. Experiments in this regime have been conducted by Leijssen *et al.* [170]. They found a regime where the optomechanical coupling between the cavity photons and the Brownian motion of the mechanical resonator "induces optical frequency fluctuations larger than the intrinsic optical linewidth" [170]. This leads to non-linear effects in the system which disallows continuous optical access without putting the system into a highly non-linear state. The results in this section are the first results measured with the new cavity and can be regarded as a preliminary assessment of the experimental parameters that need further improvement to use the system to its full capability.

The emergence of non-linear dynamics implies, that we cannot apply continuous measurement schemes to characterize the system (as done in the previous chapters) and that active cooling techniques (e.g., radiation pressure cooling) are not applicable. First hints of this phenomenon were already observed during the sympathetic cooling measurements presented in Section 3.3.2. For the current system, this property does not allow any kind of continuous measurement, even if the beam exhibits only a few 100 nW of power. For a single photon coupling rate of $g_0 = 2\pi \cdot 204\,\mathrm{kHz}$ we find:

$$N_{25\,\mu\mathrm{W}} = \frac{100\mathrm{nW} \cdot \tau_{\mathrm{cav}}}{\hbar\omega_{\mathrm{TiSa}}} \approx 510 \quad \Rightarrow \quad \Delta\omega_{\mathrm{cav}} = g_{0,\mathrm{high}} \cdot N_{100\,\mathrm{nW}} \approx 100\,\mathrm{MHz} \tag{4.33}$$

which is on the same order of magnitude as the cavity linewidth of $\kappa = 740\,\mathrm{MHz}$. This effect can be strong enough to modulate the reflection signal that is acquired during a homodyne calibration scan at a frequency $2\omega_{\mathrm{m}}$ (a qualitative analysis of this behavior can be found in Appendix D.2) defying a proper calibration measurement. The effect can be circumvented by using small beam powers and high scanning frequencies of $\approx 100\,\mathrm{Hz}$ for both cavity piezos. At the same time, the resonance is very narrow, requiring for a high bandwidth photo detector to accurately resolve the feature. This leads to a significant variance in the calibration measurements and consequently a relatively large error on the homodyne calibration which is $c_{\mathrm{HD,15k}} = (170 \pm 40)\frac{\mathrm{rad}}{\mathrm{nm}}$.

Another issue is the increased sensitivity of the cavity to angular misalignment. We pre-aligned the cavity at room temperature achieving a reflectivity on resonance of $\sigma = (0.62 \pm 0.02)$. The experiments presented in this section were conducted at $T_{\mathrm{MiM}} = 11\,\mathrm{K}$ after the dilution unit was repaired[84]. After cooldown we found a change in angular alignment which reduced the reflectivity on resonance due to worse mode match to $\sigma = (0.20 \pm 0.04)$. We tried to compensate the angular misalignment with the angular goniometer stepper motors but found them to be non functional[85]. Since active cooling techniques cannot be applied, we have to rely on passive effects that cool the resonator in between the individual measurements.

[84] Even though the dilution unit was fully functional, pollution of the liquid Helium disallowed proper operation of the 1K-pot.

[85] The angular positioners have to be adjusted with the tightest tolerances. Due to the multiple warm up cycles and the required disassembly of the goniometer for the cavity exchange, the pre-tension of the goniometer springs was likely too high. Since readjustment requires full disassembly of the system, which was not feasible in the short time, we decided to measure in this configuration nonetheless.

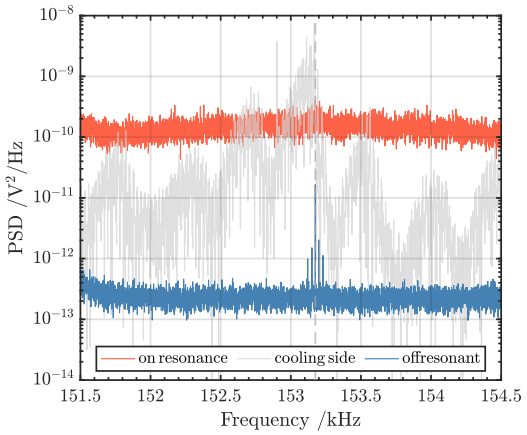

Figure 4.11: Mechanical PSD when approaching the cavity resonance:
The plots show qualitatively the systems behavior when approaching resonance. (Dark blue) Far off-resonant configuration. (Light grey) Close to resonance from the side of optomechanical cooling. The mechanical PSD of the resonator begins to develop an asymmetric shape and modulates the noise floor. This can be attributed to nonlinear effects arising in the resonator-lightfield interaction [170]. (Red) On resonance, the resonator modulates the cavity on the order of its optical linewidth. This lifts the noise floor until the resonator peak vanishes.

Pulsed state tomography in this regime requires many measurements to acquire the necessary statistics such that the repetition rate of the pulse trains has to be carefully balanced. Choosing a too high repetition rate leads to heating in between the pulse trains, disallowing for meaningful results. We worked at a measurement rate of 50 Hz and recorded 20000 pulse-trains traces per angle θ_t. The AWG and digitzer operate at the maximum resolution of 1.8 GSa/s.
Another difference to previous pulsed measurements is that it is not possible to tune the system on resonance in a continuous measurement. This is depicted in Fig. 4.11. It shows the PSD of the mechanical resonator with the cavity far off-resonant, close to resonance on the cooling side and on resonance. If tuned on resonance, the resonator starts to modulate the cavity frequency and thus periodically tuning it on- and off-resonant which leads to a rise in the noise floor that eventually buries the resonator PSD signal. This can be observed for signal beam powers as low as 100 nW.
To conduct measurements, we tune the system close to resonance using the piezo tubes until we observe the mechanical resonance peak of the oscillator in a PSD measurement behaving like in Fig. 4.11 (light blue spectrum). From here on the light is switched off by applying a bias voltage to the fiber EOM to minimize the signal beam transmission. According to the previously determined piezo calibration[86] we apply an additional offset to the fiber and "blindly" tune the system on resonance. In this configuration the pulse trains are applied. Due to the small pulse width, we can resolve the state much finer. Since the excitation of higher vibrational modes of the resonator feeds back into both quadratures we expect the highest resolution with the least back-action induced broadening for low tomography angles. Thus, we measure the region of small angles with fine resolution (θ_t = 3°, 4°, 5°, 6°, 7°, 8°, 9°, 10°) followed by a coarser spacing (θ_t = 20°, 30°, 40°, 50°, 60°, 70°, 80°, 90°). The presented measurements were conducted at a signal beam power of 14 μW and an LO power of 20 mW at repetition rate of 50 Hz. For each tomography angle 20000 traces were measured.

[86] $c_{\text{upper}} = (1.50 \pm 0.01)\,\frac{\text{nm}}{\text{V}}$ and $c_{\text{lower}} = (1.42 \pm 0.01)\,\frac{\text{nm}}{\text{V}}$. These values were acquired at a system temperature of 4 K. The calibration for the upper fiber is different from previous theses because the piezo had to be exchanged shortly before the measurements were conducted.

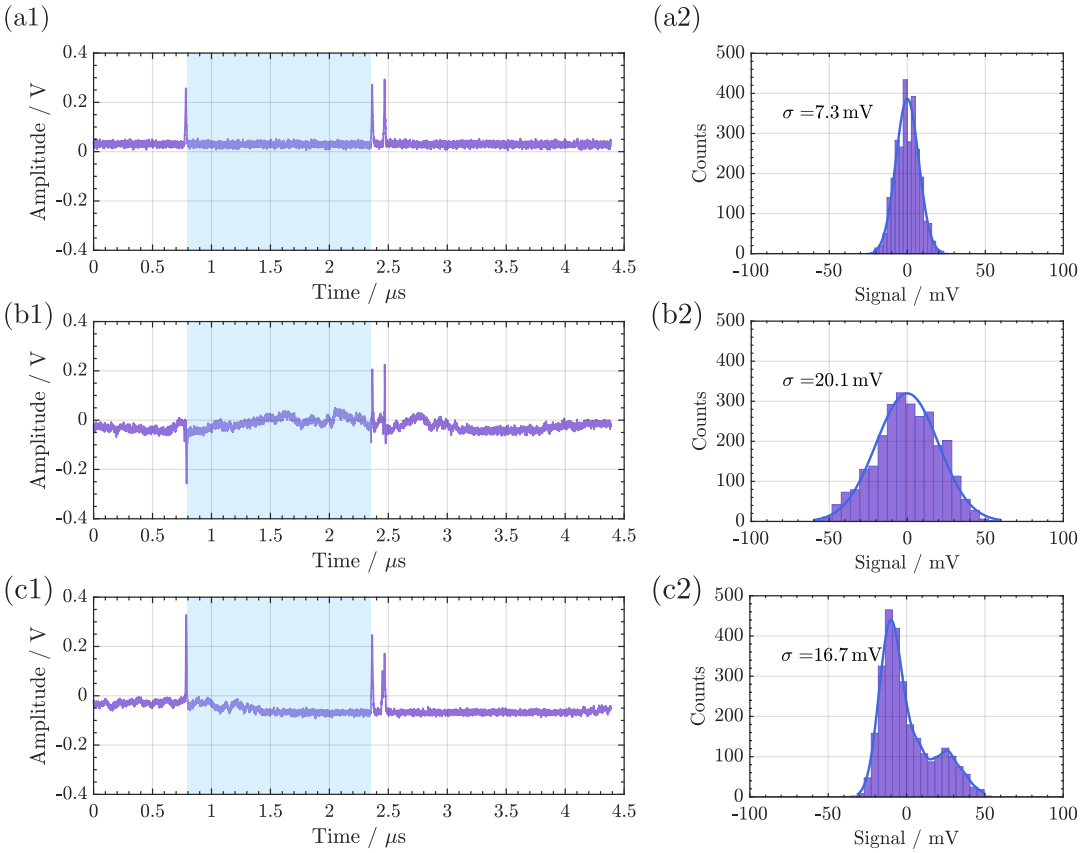

Figure 4.12: Different measurement scenarios at $\mathcal{F} = 14500$:
(a1) Measured signal of a pulse train when the cavity is off-resonant. (a2) Variance of the baseline of the signal measured within the blue shaded area. (b1,b2) Measured pulse train signal and variance for an on-resonant cavity. (c1,c2) The system is partly on-resonant but is tuned off-resonant during the measurements. Only the scenario depicted in (b1) is used for evaluation.

Evaluation of measurement data

The non-linearity of the system requires us to perform a more elaborate post-selection of the acquired data. In contrast to the previous configuration, the phase modulation from the resonator is strong enough to tune the cavity on- and off-resonant at a modulation frequency of $2\omega_m$[87]. During the first measurements we tried to use the transmission signal of the cavity, which is enhanced due to the use of a multi-mode fiber, as indicator whether the system is resonant during a pulse train. Nevertheless, the signal showed to be of insufficient strength to qualify as a selection criterion. Instead, we found the baseline of the recorded pulse trains to be a good measure.

[87] This behavior can also be qualitatively observed when slowly scanning over the cavity resonance. A corresponding measurement is depicted in Appendix D.2.

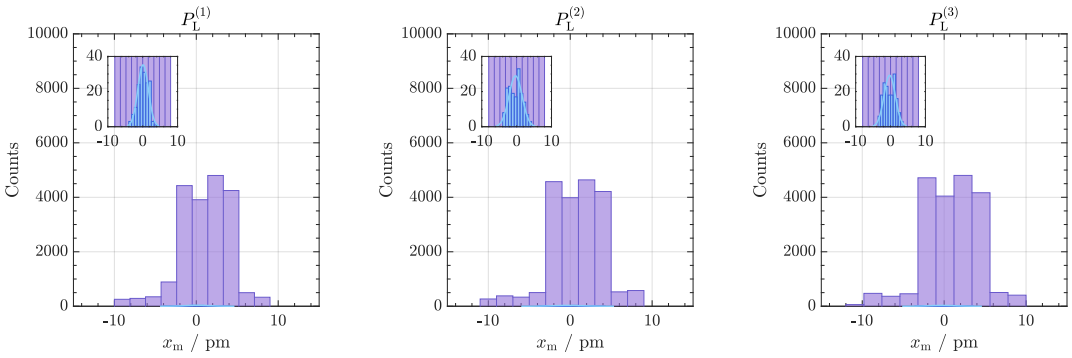

Figure 4.13: Postselection of data for $\mathcal{F} = 14500$:
(Histograms of the measurement outcomes for each pulse at $\theta_t = 80°$ prior (violet) and after (blue) postselection. Inset: Zoom into the post selected data sets after applying all selection criteria. The homodyne signal is converted to the displacement via the homodyne calibration which is $c_{HD,15k} = (170 \pm 40)\frac{rad}{nm}$ in this configuration.

Suppose we find the system in an unknown state and apply a pulse train. Then we can distinguish between three different measurement scenarios that are also depicted in Fig. 4.12:

- Scenario 1: The system is off-resonant (Fig. 4.12(a1,a2)). In this case the signal baseline is flat due to the high CMRR of the homodyne detection. This is the most common scenario to find during a measurement.
- Scenario 2: The system is on resonance (Fig. 4.12(b1,b2)) and the baseline significantly varies due to the modulation by the resonator.
- Scenario 3: The system is partly on resonance (Fig. 4.12(c1,c2)) and is shifted off-resonant during the measurement.

We want to only consider data as described by scenario 2. For this we determine the variance of the baseline between the first and the second pulse and during the last 500 ns of the pulse train. Based on the average variance of all measurements $\sigma = (8 \pm 2)\,\mathrm{mV}$ we require the variance in both regions to exceed $\sigma > 10\,\mathrm{mV}$ to be considered in the further evaluation. Together with the requirement that all data points are within the linear range of the homodyne signal, an average of 160 usable traces (0.8%) remains from initially 20000.
We further impose the requirement for the data to contain only information about the X_M quadrature by using the method presented in Fig. 4.8 of the previous evaluation. This results in a further reduction to an average of 50 (0.25%) data sets that qualify for quantum state tomography. A comparison between the data sets prior and after the post-selection is depicted in Fig. 4.13. Due to the selection criteria some tomography angles contain only a single-digit amount of data. We depict the histograms for the angles $\theta = 5°$, $\theta = 60°$ and $\theta = 80°$ as an example in Fig. 4.14. Due to the small number the data sets do not qualify for a evaluation via the fit of a statistical function as in the previous section. Instead, we determine the variance σ_N of the calculated conditional states for each measurement.

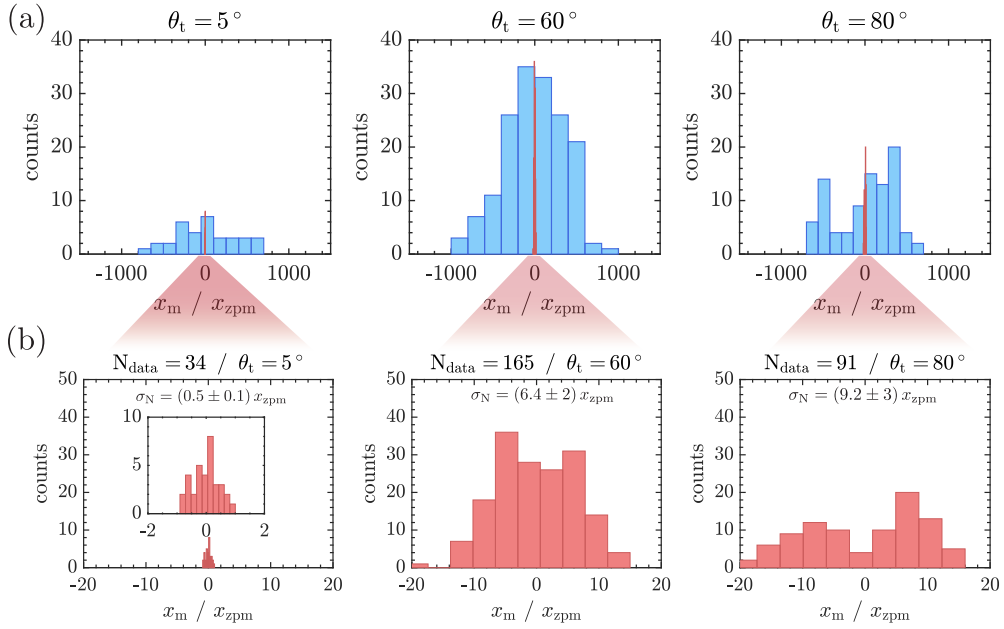

Figure 4.14: Marginal distributions at different tomography angles:
(a) Mechanical marginals at different tomography angles as determined in 4.13 (blue histograms) The conditional state (red histograms) calculated by equation 4.30 does not resemble a thermal state. Likely due to insufficient statistics. (b) Zoom into the conditional state histogram with the calculated variance of the conditional state widths.

The only data set that hints towards a normal distribution could be identified at $\theta = 60°$ where $\sigma_N = (6.4 \pm 2)\, x_{zpm}$. The results at low tomography angles suggest that the system is in principle capable of resolving the ground state with sub-SQL precision. Nonetheless more data would be necessary to assess this property with statistical significance[88].

4.3.3 Conclusion

In this chapter we implemented a QND measurement technique to realize rapid state tomography of our resonator. We investigated the degree of state-squeezing dependent on the cavity finesse.
With the medium finesse cavity, we reached a minimum state width of $\sigma = (16 \pm 1)\, x_{zpm}$ at a measurement strength of $\chi = 0.021\,(+0.012\,/\,-0.005)$. Compared to the acquired measurement strength at $\mathcal{F} = 140$ ($\chi_{140} = 0.002\,(+0.002\,/\,-0.001)$) this results verified that the measurement strength scales with the finesse according to theory within the error margins.
Experiments with the high-finesse cavity put the system into a regime where the resonator motion tuned the cavity off-resonant at twice its eigenfrequency. This required for the introduction of new postselection techniques and rendered the overwhelming part of the data unusable. The data that qualified for further evaluation hints that the system is capable to resolve the state with sub-SQL precision. Nevertheless, the statis-

[88] Similar measurements were conducted at signal beam powers of ($P_{SIG} = 0.9\,\mu W$, $P_{SIG} = 7\,\mu W$, $P_{SIG} = 20\,\mu W$, $P_{SIG} = 30\,\mu W$, $P_{SIG} = 150\,\mu W$). All show a similar behavior due to the large number of rejections.

tics were insufficient to deduct a measurement strength with statistical significance. The current results indicate, that the measurement procedure has to be further optimized. Without further modifications on the current setup this could be realized by the following measures:

- Acquisition of more data. Assuming that 0.25% of the data are usable we would require for at least 100 000 traces to acquire an average of 250 usable data sets. This is possible with the used UHF AWG but inefficient as it leads to large amounts of data (for 20000 traces a full state tomography produces approx. 40-60 GB data).

- Taking into account the higher vibrational modes of the oscillator. The pulses can excite higher incommensurate vibrational modes that broaden the conditional distribution. To account for these modes, optimal-state-estimation methods could be implemented. A promising approach are Kalman-filters [171] that were applied on optomechanical systems before during Refs. [71, 172, 173] and lead to realizations of feedback control loops on the quantum level. These methods would require for enhanced knowledge over the excited modes and thus for different preparation protocols.

Possible experimental modifications are:

- Enhancement of the measurement efficiency. The low reflectivity on resonance due to angular misalignment poses a reduction in measurement efficiency by a factor of 3 when compared to the empty cavity value. This makes a readjustment of the angular piezo motors of the goniometer necessary to control the cavity to its full extent.

- Furthermore, an additional length stabilization of the system could allow for more accurate alignment of the cavity on resonance. Since we cannot apply continuous measurements in the MiM system, such a stabilization would require for a second, empty high finesse fiber cavity which is connected to the MiM-cavity. This cavity could be stabilized via a PDH signal, allowing for a more accurate alignment and better knowledge of the system.

Conclusion and Outlook

Since its beginning, the NanoBEC project aimed for the ambitious and technically demanding goal of realizing strong hybrid coupling between two fundamentally different constituents. In the past years multiple endeavors, provided more insights into the physics and significant technical improvements to the system. In this thesis we pushed the technical boundaries further, by implementing optimized finesse cavities, bringing back the full functionality of the cryostat and conducting measurements in a high finesse regime that was not investigated before.

This led to an improvement of the hybrid cooperativity to $C_{\mathrm{hybrid}} \approx 5900$. We surpassed the former technical limitations and found a physical boundary in the maximal achievable cooperativity of this system caused by the high OD of the atomic cloud at low lattice powers and detunings that leads to the vanishing of the coupling lattice. Motivated by the acquired knowledge we shifted gears to use the benefits of the excellent experimental conditions the system provides for solely optomechanical experiments. We realized a QND rapid state preparation protocol for full quantum state tomography of the resonator and investigated the scaling of the measurement strength with the finesse. This modification allowed for rapid state preparation of the resonator to an effective mode temperature of $3.1 \pm 0.5\,\mathrm{mK}$ starting from room temperature which is in agreement with theoretical predictions. Motivated by this result we implemented a high finesse cavity with $\mathcal{F} = 14500$ to enable state squeezing below the zero-point motion. In this regime the resonator modulated the cavity resonance such that most of the acquired data was not usable for evaluation. Yet this does not diminish the capability of the system to reach the desired sub-SQL precision if the data acquisition and evaluation are further optimized.

The research on hybridization of quantum systems remains relevant and their realization will have a crucial influence on the development of complex quantum systems in the future. It is the fundamental researchers' privilege to try out the most various and exotic physical models and systems for the sake of "just" gaining knowledge. We used this privilege to find the physical boundaries of this experiment. Future perspectives beyond the improvements on pulsed state preparation require a redesign of the experiment, utilizing the individual strengths, the system provides and investigating new coupling mechanisms with different constituents. This could imply using an all fiber based setup where both constituents (i.e., atoms and oscillator) live in a fiber cavity or switching from nanomechanical resonators to levitated nanoparticles [174][89].

[89] A field that emerged recently and already shows impressive capabilities regarding ground-state preparation and controllability.

Appendix A

Old experimental setups

A.1 Free space detection setup

For the experiments on pump-asymmetry-compensation (PAC) and for the pulsed experiments at $\mathcal{F} = 140$ and free-space homodyne detection setup was used. The setup for the experiments on PAC is depicted in Fig. A.1 [90].

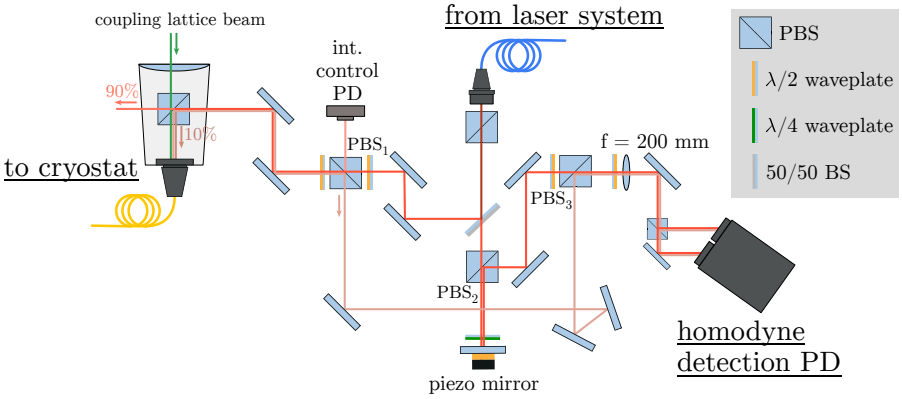

Figure A.1: Detection light from the homodyne branch of the laser system is collimated by a fiber collimator (*Schäfter & Kirchoff 60FC-L-4-M20L-02*) to a beam diameter of $d_{beam} = 3.6\,mm$ and split of by a 50/50 beamsplitter into a signal and LO branch. The LO beam transmits through PBS_2 and gets back-reflected at the piezo mirror (*Piezomechanik HPSt 150/14-10/12*) that is used for the phase adjustment between the signal and LO beam. The back-reflex is guided to PBS_3 where it is overlapped with the signal beam. The signal beam goes through PBS_1 where a fraction of the signal beam is split off and directed on a PD used for intensity control. The remaining signal light is guided to the coupling lattice telescope where a fraction of 10% is coupled together with the coupling lattice beam into the cryostat-fiber. After interaction with the resonator, the signal light is guided to PBS_3 where it is superimposed with the LO beam. Both spatially overlapped beams are split to equal parts and sent to the balanced photoreceiver (*FEMTO HCA-S, DC ... 1 MHz, gain 28.5 kV/W, NEP 1.1 pW/*$\sqrt{\text{Hz}}$). The signal is evaluated via lock-in detection. Figure from Ref. [63].

[90] The version for pulsed experiments featured an additional branch to compensate the path length difference between signal and LO branch and a 500 MHz balanced photoreceiver. Since no pulsed measurements were conducted with this setup in this thesis it is omitted here.

A.2 PAC setup

The experiments on PAC featured a special coupling lattice setup with an additional auxiliary beam to compensate for the pump-imbalance. The coupling lattice setup for PAC is depicted in Fig. A.2.

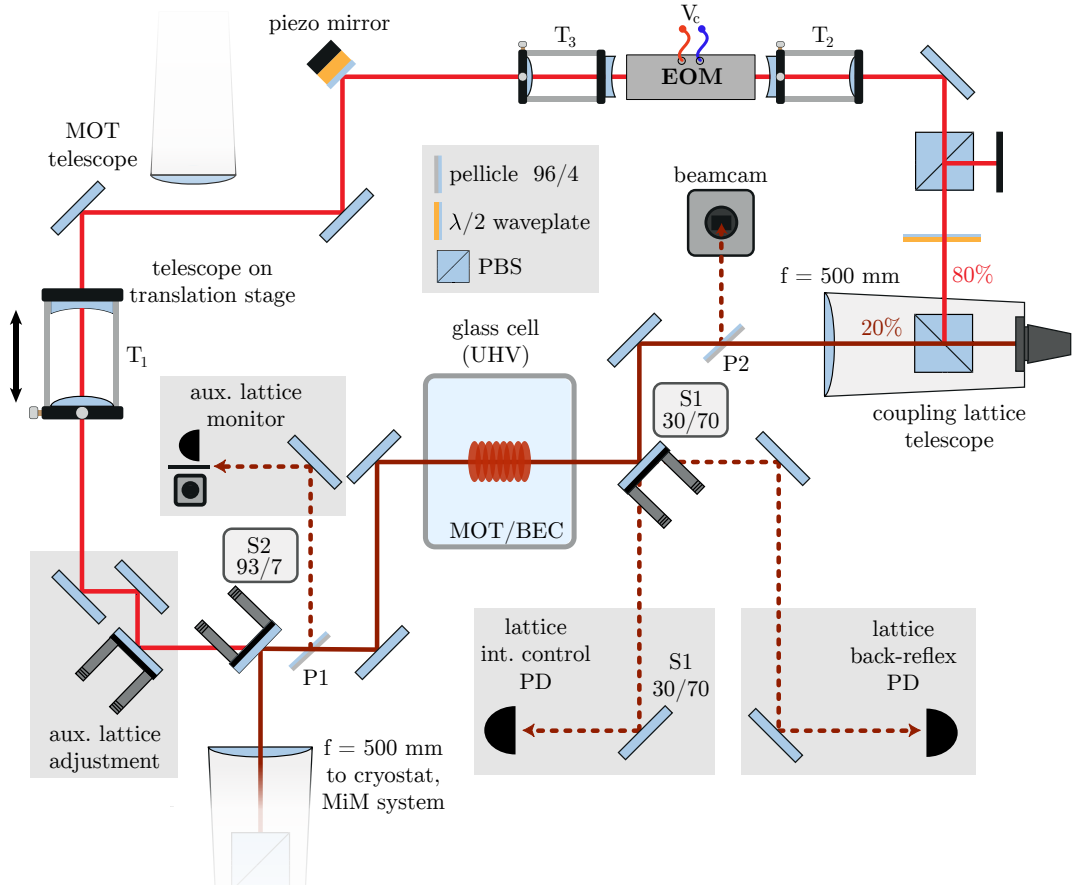

Figure A.2: The modified coupling lattice setup features an auxiliary beam that is split off from the coupling lattice beam via a PBS in the coupling lattice telescope. The auxiliary beam transmits through a PBS at which its power can be adjusted by a fine tunable $\lambda/2$-waveplate. It is guided through the telescopes T_2 and T_3 that adjust beam diameter to pass through the free space EOM (*Linos LM0202, 0.1W KD*P 3x3 400-850 nm*) and is incident on a piezo mounted mirror (*Noliac NAC2121 ring piezo*). Together the piezo and the EOM realize the auxiliary beam phase lock. The auxiliary beam is shaped by telescope T_1 to acquire optimal mode match with the back-reflected beam from the cavity. Telescope T_1 is mounted on a translation stage that allows to adjust the focus position of the auxiliary beam with micrometer precision. The auxiliary beam is superimposed with the back-reflected beam on substrate S2. Their interference signal and the spatial mode match can be monitored via an out-of-plane reflection of both beams at pellicle P1 in the near-field and at pellicle P2 in the far-field. Figure from Ref. [63].

Appendix B

Hybrid system

B.1 Overview over the optomechanical properties of the used systems

During this thesis, experiments were conducted at three different optomechanical systems at different temperatures. The tables presented here conclude the optomechanical properties for all systems used during this thesis:

- Table B.1 shows the properties of the optomechanical system used for the PAC experiments at room temperature.

- Table B.2 shows the properties of the optomechanical system used for the hybrid coupling experiments at $\mathcal{F} = 650$ and $\mathcal{F} = 1500$ at room temperature.

- Table B.3 shows the properties of the optomechanical system used for the pulsed experiments at $\mathcal{F} = 14500$ at a experiment temperature of $T_{\mathrm{MiM}} = (11 \pm 1)\,\mathrm{K}$. Although the dilution unit was fixed, impurities in the liquid Helium disallowed proper operation of the 1K-pot such that the temperature of the experiment stayed at 11 K during the measurements.

Optomechanical properties at $\mathcal{F}_{\mathrm{empty}} = (60 \pm 2)$			
ω_{m}	$2\pi \cdot 154.42\,\mathrm{kHz}$	ω_{cav}	$2\pi \cdot 384\,\mathrm{THz}$
Q	$(6.662 \pm 0.004) \times 10^6$	L_{cav}	$(21.1 \pm 0.1)\,\mu\mathrm{m}$
Γ_{m}	$2\pi \cdot (23 \pm 1)\,\mathrm{mHz}$	κ_{max}	$2\pi \cdot (50.2 \pm 0.5)\,\mathrm{GHz}$
m_{eff}	$3\,\mathrm{ng}$	x_{zpf}	$4.28\,\mathrm{fm}$
$\mathcal{F}_{\mathrm{max}}$	(140 ± 10)	G	$(111 \pm 1)\,\mathrm{GHz/nm}$
g_{m}	$(98 \pm 0.5)\,\mathrm{GHz/nm}$	g_0	$2\pi \cdot (66.8 \pm 0.3)\,\mathrm{kHz}$

Table B.1: Properties of the optomechanical system at room temperature for the cavity with $\mathcal{F}_{\mathrm{empty}} = (60 \pm 2)$. The data is from Ref. [63].

Optomechanical properties at $\mathcal{F}_{\text{empty}} = (785 \pm 15)$			
ω_{m}	$2\pi \cdot 154.41\,\text{kHz}$	ω_{cav}	$2\pi \cdot 384\,\text{THz}$
Q	$(6.662 \pm 0.004) \times 10^6$	L_{cav}	$(12.9 \pm 0.5)\,\mu\text{m}$
Γ_{m}	$2\pi \cdot (23 \pm 1)\,\text{mHz}$	κ	$2\pi \cdot (7.6 \pm 0.2) ... (17.5 \pm 0.7)\,\text{GHz}$
m_{eff}	$3\,\text{ng}$	x_{zpf}	$4.28\,\text{fm}$
$\mathcal{F}$	$(650 \pm 50) ... (1500 \pm 100)$	G	$(187 \pm 7)\,\text{GHz/nm}$
g_{m}	$(108 \pm 4)...(300 \pm 10)\,\text{GHz/nm}$	g_0	$2\pi \cdot (73 \pm 3) ... (204 \pm 7)\,\text{kHz}$

Table B.2: Properties of the optomechanical system at room temperature for the cavity with $\mathcal{F}_{\text{empty}} = (785 \pm 15)$.

Optomechanical properties at $\mathcal{F}_{\text{empty}} = (14500 \pm 1500)$			
ω_{m}	$2\pi \cdot 153.37\,\text{kHz}$	ω_{cav}	$2\pi \cdot 384\,\text{THz}$
Q	$(2.5 \pm 0.2) \times 10^7$	L_{cav}	$(14 \pm 0.5)\,\mu\text{m}$
Γ_{m}	$2\pi \cdot (6.1 \pm 0.1)\,\text{mHz}$	κ	$2\pi \cdot (740 \pm 80)\,\text{MHz}$
m_{eff}	$3\,\text{ng}$	x_{zpf}	$4.28\,\text{fm}$
$\mathcal{F}_{\text{empty}}$	(14500 ± 1500)	G	$(172 \pm 6)\,\text{GHz/nm}$
g_{m}	$(90 \pm 10)...(290 \pm 40)\,\text{GHz/nm}$	g_0	$2\pi \cdot (61 \pm 7) ... (200 \pm 30)\,\text{kHz}$

Table B.3: Properties of the optomechanical system at $T_{\text{MiM}} = 11\,\text{K}$ for the $\mathcal{F}_{\text{empty}} = (14500 \pm 1500)$ configuration. The optomechanical coupling g_{m}/G is determined from Fig. B.3. Since the system allows for no continuous optical access the linewidth had to be estimated according to equation 2.23 and could not be measured directly. Furthermore, we can only state the empty cavity finesse. We had to exchange the trampoline resonator for this system. Thus, a new quality factor was determined for the system which differs from previously stated values.

B.2 Homodyne phase-lock bandwidth estimation

To implement a phase-lock into the fiber-based homodyne detection setup we built a fiber stretcher by winding 10 m of glas-fiber[91] around a large diameter piezo ceramic cylinder[92] and implemented it into the LO branch. This system is supposed to have a high bandwidth and can be operated at low voltages.

A thorough characterization of the lock bandwidth required for a phase modulating fiber EOM that was not available at that time. Thus, we estimate the lock- bandwidth by measurement of the optical path displacement (OPD) the fiber stretcher causes at a given modulation frequency and by measurement of the amplitude response of driving signal.

The measurement of the modulation frequency dependent OPD is depicted in Fig. B.1. We set up a Mach-Zehnder interferometer with the fiber stretcher placed in one branch and observe the interference signal at one interferometer port with a photodiode[93]. We apply a sinusoidal[94] voltage to the fiber stretcher and measure the distance between the interference signal minima in the linear range of the scan signal. This allows to determine the optical path displacement per volt. Up to a modulation frequency of 4

[91] *Thorlabs HP780SM*

[92] *STEMINC SMC4037T50111 with d = 40* mm.

[93] *Thorlabs PDA36*

[94] We use a sinusoidal signal as the high capacity of the piezo leads to delayed discharge effects when using a triangular scan ramp at frequencies in the kHz regime.

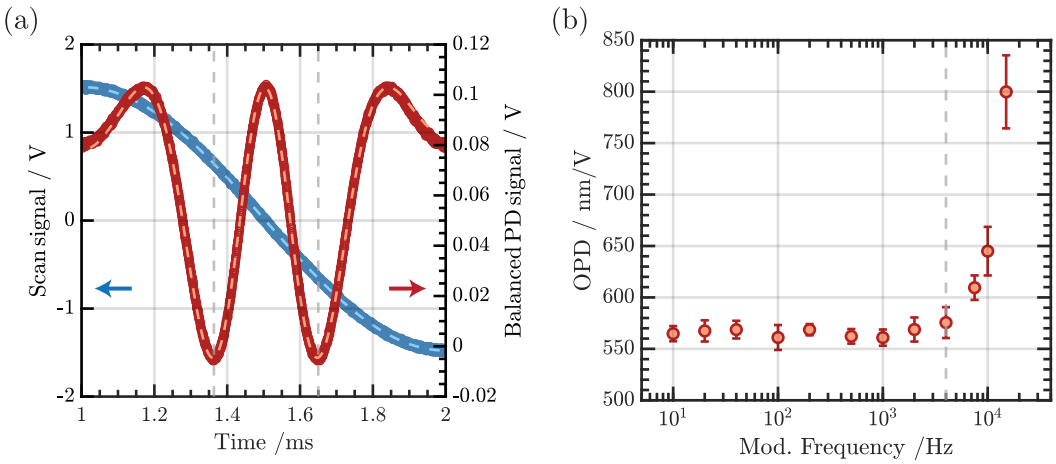

Figure B.1: (a) Interference signal (red) on the measurement PD for a sinusoidal scan signal (blue) of $V_{PP} = 3\,V$ at 500 Hz. The dashed lines denote sinusoidal fits to the data. Within the linear region of the scan signal (grey dashed vertical lines) the distance between the interference fringes is measured to determine the OPD per volt. (b) OPD for different modulation frequencies. The grey dashed line denotes the modulation frequency of 4 kHz after which the OPD significantly increases.

kHz the OPD stays constant at $(570 \pm 10)\,nm/V$. We recognize a significant increase in the OPD for higher frequencies up to 15 kHz which suggests a resonance of the system in this region. At frequencies above 15 kHz we observe a nonlinear response that renders it impossible to assign an OPD. To investigate the resonance behavior for higher frequencies, we measure the amplitude of the driving signal of the piezo for different modulation frequencies up to a modulation frequency of 90 kHz. The results are depicted in Fig. B.2.

The measurement confirms the nonlinear behavior and shows a suppression of the driving amplitude of $-18\,dB$ at a modulation frequency of 30 kHz. The measurements suggest a linear response of the system for drive voltages of 3 V up to 4 kHz.

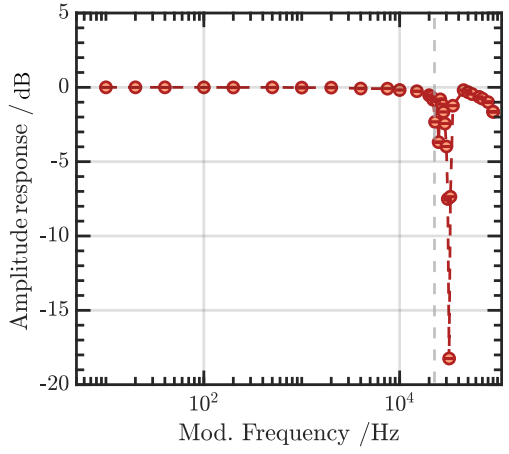

Figure B.2: Amplitude response of the fiber stretcher. The peak-to-peak signal of the driving voltage is measured for modulation frequencies up to 90 kHz. The initial signal has $V_{PP} = 3\,V$. The grey dashed line denotes a modulation frequency of 22 kHz where the amplitude is reduced by 3 dB.

B.3 g_m measurements for $\mathcal{F} = 14500$

We conducted a measurement of g_m with the high finesse cavity at an experiment temperature of $T_{MiM} = (11 \pm 1)\,K$ with the method described in Chapter 2.3.2. This became possible after the exchange of the piezo that held the upper fiber because it had a much larger travel range than the old model. Nevertheless, the scan range is smaller at low temperatures such that it was only possible to scan the piezos over one FSR of the cavity resonance. The measurement is depicted in Fig. B.3.

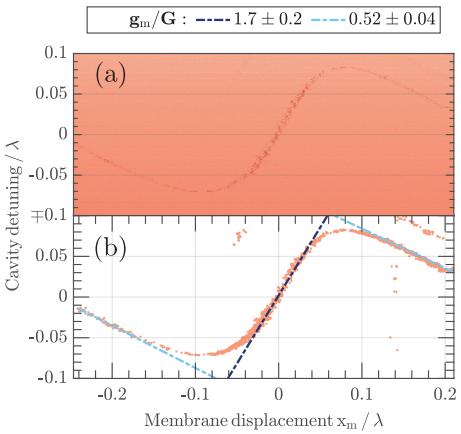

Figure B.3: (a) Raw data of the cavity transmission signal for a symmetric scan of both fibers around the resonator with a slow modulation of the cavity detuning. The red shades indicate the cavity transmission (dark corresponds to high transmission) at a resonator position x_m. (b) Extracted resonance curve from upper plot by identifying the points of highest transmission. The optomechanical coupling at each slope is determined by a linear fit (dashed blue lines) through the individual turning points.

B.4 Piezo calibration

Previously the piezos that were used to move the upper and lower fibers of the cavity had significantly different calibration factors. Prior to the pulsed measurements the upper fiber piezo broke and had to be replaced. After the replacement we observed both calibrations to be more similar. The piezo calibration was acquired by scanning the cavity over as many FSR as possible and subsequent measurement of the distances of the cavity resonances. Since the resonances are a distance $\lambda/2$ apart, the piezo travel range per volt can be deducted. Figure B.4 shows the calibration measurement for configuration with the old (Figure B.4(a)) and new piezo configuration (Figure B.4(b)) .

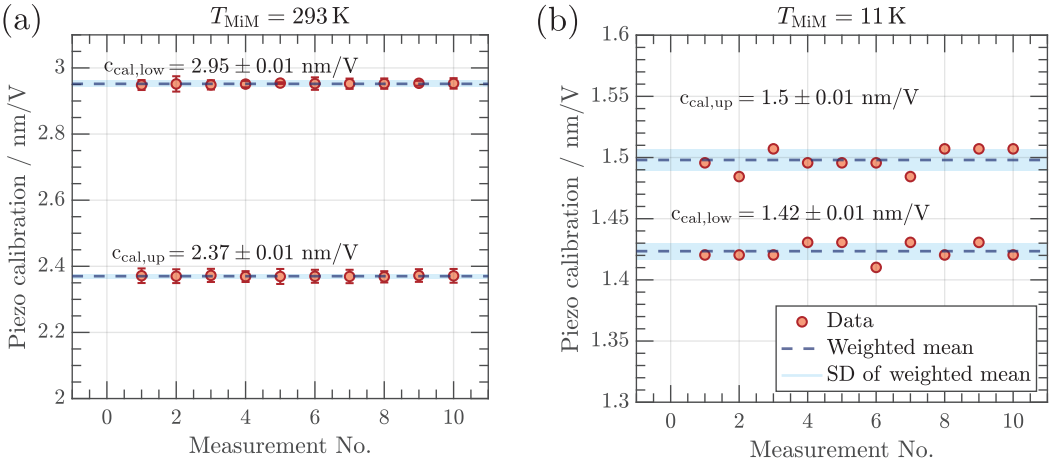

Figure B.4: (a) Piezo calibration measurement at room temperature before the upper piezo was exchanged. Each datapoint is determined from the averaged distances of multiple FSR. (b) Piezo calibration measurement at $T_{\mathrm{MiM}} = 11\,\mathrm{K}$ after the upper piezo was exchanged. Due to the low temperature the calibration constants are lower which allowed to only scan over a distance of one FSR.

B.5 Production of high finesse fiber cavities

B.5.1 CO_2 laser characterization

During this thesis we produced new fiber cavities at a finesse of $\mathcal{F} = 14500$. Our facilities allow for the production of fiber cavities with concave profiles. The setup for fiber cavity production was initially set up during Ref. [175] and further improved in Ref. [100]. When starting the production of the new cavities we found that the CO_2 laser[95] malfunctioned due to degradation of the laser-medium gas and replaced it with a new CO_2 laser[96]. The new laser has a operating wavelength of $\lambda = 10.2\,\mu$m and is specified for a maximum output power of 20 W with a relative power stability of $\pm 10\%$.

[95] *Access Laser AL30*
[96] *Coherent Diamond C20*

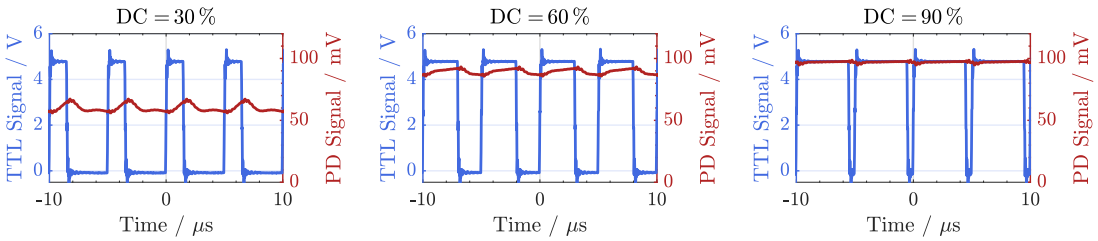

Figure B.5: Output power of the laser at different duty cycles for a repetition rate of 200 kHz. For higher duty cycles the modulation of the laser power from the switching of the laser gets less pronounced.

It can operate at repetition rates between 25 and 200 kHz. We characterized the laser to assess whether it fulfills these specifications and to find a regime where it operates most stable. This is important to get reproducible results in the manufacturing process.

The laser power is regulated by a TTL pulse-width-modulation (PWM) signal. This signal gates the RF-source that excites the laser. By operating the laser at different duty cycles (DC)[97] the output power can be adjusted. Figure B.5 shows the measured output power of the laser for different DCs on the order of the TTL signal time. The output power was measured with a high-speed IR photodiode[98]. We measured the absolute power and the relative power stability of the laser over a time of 20 s for different repetition rates and duty cycles. Figure B.6 depicts an overview over the power at different DCs and repetition rates. We observe a similar relation between the output power of the laser and the applied DC for all repetition rates. Furthermore, the laser reaches output powers above 20 W for DCs above 50%. Except for the DC of 10% the relative power fluctuations fulfill the manufacturers specifications. For DCs above 50% the relative power fluctuations are below 5% which is better than specified.

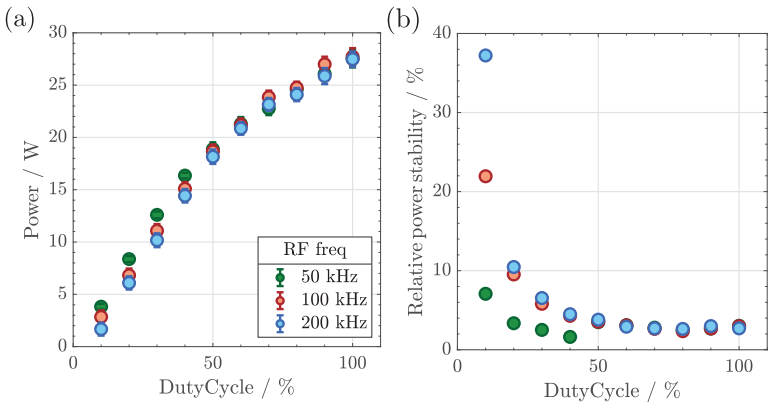

Figure B.6: (a) Output power for different repetition rates as a function of the DC. Each data point depicts the average value of a 20 s power measurement. (b) Relative power stability acquired from the data depicted in (a).

[97] The duty cycle denotes the ratio between the TTL-high and the TTL-low signal.
[98] *VIGO PVM-10.6*

For the processing of the fibers, we apply pulses on the with pulse lengths between 5 and 40 ms. To determine the stability of the laser between individual pulses we measured the power fluctuations between multiple pulses at different DCs and repetition rates. The results are depicted in Fig. B.7. In contrast to the long-term power fluctuations there are notable differences between the individual settings of operation. The highest overall stability can be observed for a repetition rate of 200 kHz at a DC of 60 %. For the cavity production we operate in this regime.

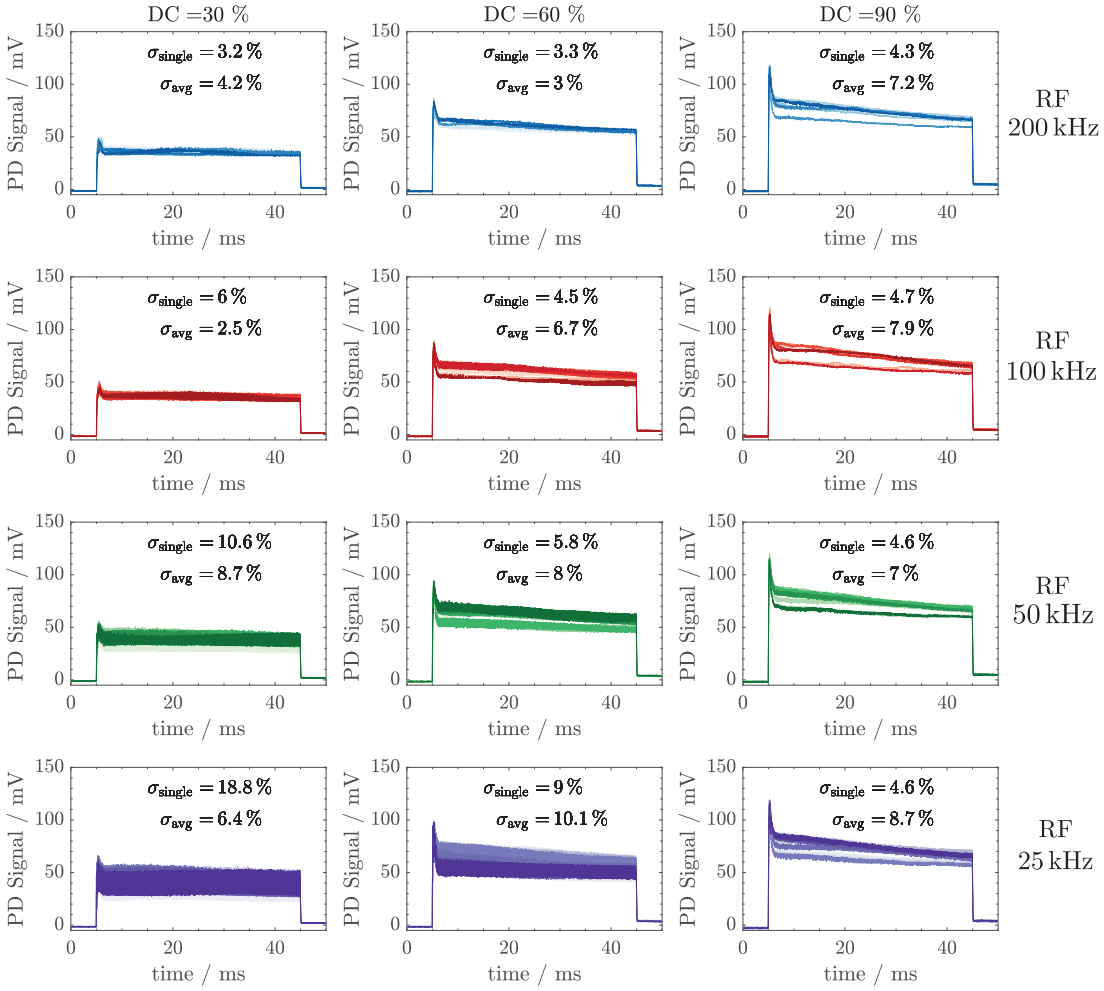

Figure B.7: Shot-to-shot fluctuations for 40 ms pulses at different DCs and repetition rates. For each setting the single pulse variance and the variance between 10 pulses is depicted. For all applied settings the laser fulfills the manufacturers specifications. In most cases the power stability is better than specified.

B.5.2 Properties of the new high finesse cavities

We produced 17 curved fiber profiles in this thesis and prepared 15 plane fibers. The reflectivity on resonance and the finesse are dependent on the reflectivities of the individual mirrors an on the quality of the curved profiles. For each curved fiber we determined the finesse and the reflectivity on resonance by measurement of the resonance peak width and the FSR. The corresponding signal is depicted in Fig. B.8.

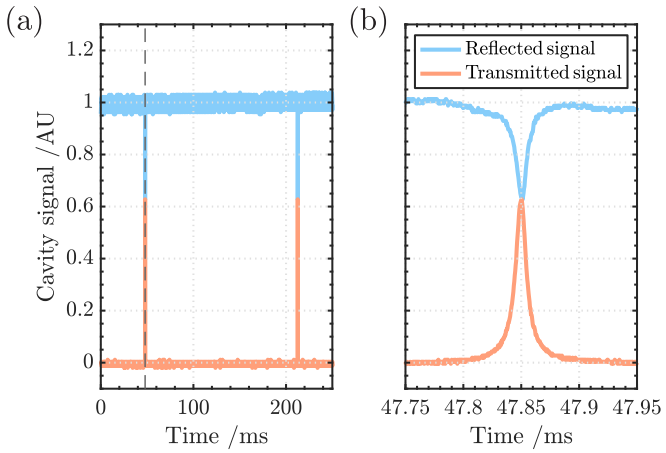

Figure B.8: (a) Normalized cavity signal in reflection (light blue) and transmission (light red) for a triangular length scan of the plane fiber. The distance between two peaks yields the FSR. (b) Zoom into one resonance peak. The minimum in reflection yields the reflectivity on resonance.

Figure B.9 shows an overview over the measured finesses and reflectivities on resonance for all produced fibers. For each measurement we adjusted the cavity to the length which had the highest reflectivity on resonance (between 12 μm and 16 μm).

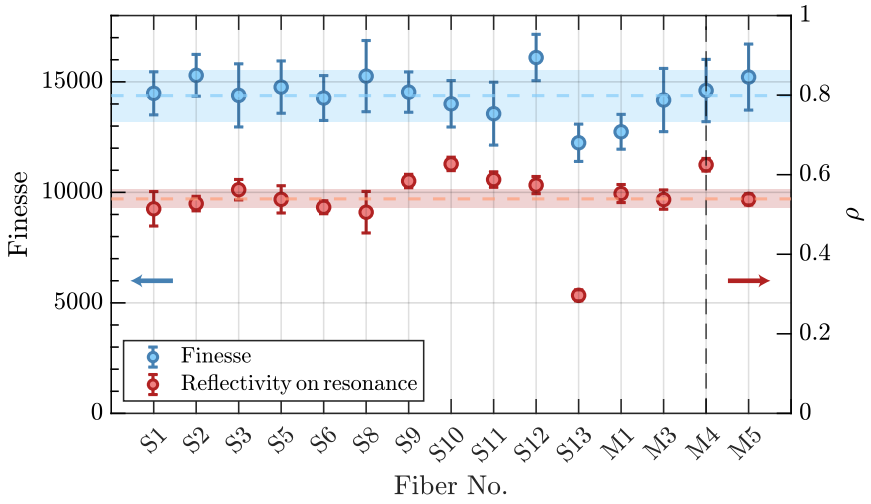

Figure B.9: Overview over the finesse (left) and reflectivity on resonance (right) of the produced fiber cavities for the pulsed experiments. The prefix "S" denotes single-mode fibers, the prefix "M" denotes multi-mode fibers. The dashed lines show the average values of the achieved finesses and reflectivities on resonance while the lighter shades depict the variance. For the pulsed experiments we used fiber M4 (black dashed line) since it showed the highest reflectivity on resonance $\sigma = (0.62 \pm 0.02)$ at a finesse of $\mathcal{F} = (14500 \pm 1500)$. Each datapoint is created from the average of 1000 scans over one FSR at a scan frequency of 20 Hz.

B.5.3 Profile analysis of the high finesse cavity

Figure B.10 depicts the profile analysis of the fiber M4 used for the cavity in the pulsed experiments.

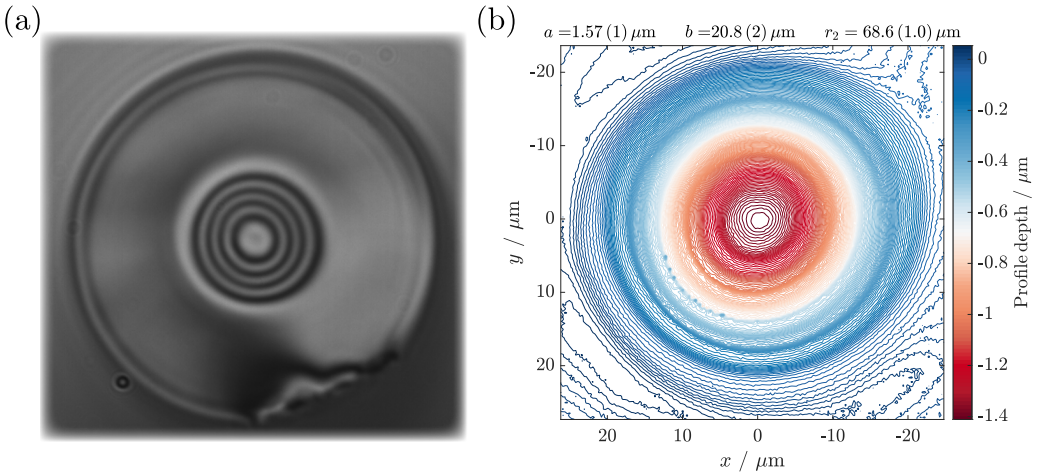

Figure B.10: (a) Interferogram of a fiber facet that was prepared by multiple CO_2 laser pulses. One interference fringe (black to black) corresponds to a height difference of 325 nm. (b) Profile evaluation using a phase shifting interferometry (PSI) algorithm. The plot shows a 2D Gaussian fit onto the profile depicted in (a). The image and the analysis are from the curved mirror of the $\mathcal{F}_{\text{empty}} = 14500$ cavity used for the new coupling experiments. $r_2 = 68.6\mu$m differs from $r_{\text{opt}} = 65.4\,\mu$m by 5%.

Appendix C

Feedback cooling

Feedback cooling is a powerful technique to control systems[95] on the quantum level and has been investigated in numerous experiments [176–180]. It is often referred to throughout this thesis and was used during the measurements on pump-asymmetry-compensation. Since its performance is strongly dependent on the signal-to-noise ratio and the bath temperature, we wanted to use the advantages of the new detection system and the repaired cryostat to measure the feedback cooling performance for the system with the new cavity at $\mathcal{F} = 650$ and possibly reach the ground state. The benchmark is the formerly measured lowest phonon occupation by T. Wagner in [62] of $n_{\mathrm{m}} = 3.8 \pm 0.1$ phonons.
Because referenced in the main chapters, we will briefly introduce the theory of feedback cooling alongside the description in previous theses [57, 62, 63] and present the feedback cooling performance with the new system at base temperature.

C.1 Theory of radiation pressure cooling

We start from the vibrational ground mode of the resonator with the mechanical linewidth $\Gamma_{\mathrm{m}} = \omega_{\mathrm{m}}/Q$ and effective mass m_{eff} and consider the application of a feedback force F_{fb}. The dynamics of the system can then be described by the Langevin equation with the stochastic thermal forces F_{th} and the back-action force F_{ba} [95]:

$$m_{\mathrm{eff}}(\ddot{x} + \Gamma_{\mathrm{m}}\dot{x} + \omega_{\mathrm{m}}^2 x) = F_{\mathrm{th}} + F_{\mathrm{ba}} + F_{\mathrm{fb}} \tag{C.1}$$

$$\overset{FT}{\Rightarrow} \underbrace{m_{\mathrm{eff}}(\omega_{\mathrm{m}}^2 - \omega^2 - i\omega\Gamma_{\mathrm{m}})}_{:=\chi_{\mathrm{m}}(\omega)^{-1}} \tilde{x} = \tilde{F}_{\mathrm{th}} + \tilde{F}_{\mathrm{ba}} + \tilde{F}_{\mathrm{fb}} \tag{C.2}$$

The Fourier transform (FT) of equation C.1 yields an expression in the frequency domain with the mechanical susceptibility $\chi_{\mathrm{m}}(\omega)$. In Fourier space the back-action and feedback force acquire the following form [95]:

$$\tilde{F}_{\mathrm{ba}} = -\chi_{\mathrm{ba}}(\omega)^{-1}\tilde{x} + \tilde{F}_{\mathrm{ba,th}} \tag{C.3}$$

$$\tilde{F}_{\mathrm{fb}} = -\chi_{\mathrm{fb}}(\omega)^{-1}\tilde{y} + \tilde{F}_{\mathrm{fb,th}} \tag{C.4}$$

Both forces include a thermal and a dynamical contribution. In case of the back-action force, the dynamical contributions $\chi_{\mathrm{ba}}(\omega)^{-1}\tilde{x}$ are the previously introduced phe-

nomenons of cold damping and the optical spring effect[99]. If we assume operation on resonance ($\Delta_{\mathrm{cav,laser}} = 0$) this contribution can be neglected. The dynamical quantity of the feedback force acts like a filter that affects the measured position $\tilde{y} = \tilde{x} + \tilde{x}_{\mathrm{imp}}$ relative to the real position $\tilde{x}$. Here $\tilde{x}_{\mathrm{imp}}$ denotes measurement imprecision added by the detection. When combining C.3 and C.4 with expression C.2, $\tilde{x}$ and $\tilde{y}$ yield [179]:

$$\left(\chi_{\mathrm{m}}^{-1} + \chi_{\mathrm{fb}}^{-1}\right)\tilde{x} = \tilde{F}_{\mathrm{th}} + \tilde{F}_{\mathrm{ba,th}} + \tilde{F}_{\mathrm{fb,th}} - \chi_{\mathrm{fb}}^{-1}\tilde{x}_{\mathrm{imp}} \tag{C.5}$$

$$\underbrace{\left(\chi_{\mathrm{m}}^{-1} + \chi_{\mathrm{fb}}^{-1}\right)}_{\chi_{\mathrm{eff}}^{-1}}\tilde{y} = \underbrace{\tilde{F}_{\mathrm{th}} + \tilde{F}_{\mathrm{ba,th}} + \tilde{F}_{\mathrm{fb,th}}}_{:=\tilde{F}_{\mathrm{tot}}} - \chi_{\mathrm{m}}^{-1}\tilde{x}_{\mathrm{imp}} \tag{C.6}$$

where we introduce the inverse mechanical susceptibility χ_{eff}^{-1}. It describes the change of the resonator susceptibility χ_{m} due to the influence of feedback cooling. From this the change of the mechanical properties of the resonator of χ_{fb}^{-1} can be derived from the real and imaginary parts. For the resonator spring constant $k_{\mathrm{m}} = m_{\mathrm{eff}}\omega_{\mathrm{m}}^2$ we find [95]:

$$k'_{\mathrm{m}} = k_{\mathrm{m}}\left(1 + \frac{\mathrm{Re}[\chi_{\mathrm{fb}}^{-1}]}{k_{\mathrm{m}}}\right) = k_{\mathrm{m}}(1 + g_{\mathrm{d}}) \tag{C.7}$$

This is a resonator displacement dependent effect where the strength of the influence on k is proportional to the displacement dependent feedback gain g_{d} The damping rate of the resonator with applied feedback cooling yields:

$$\Gamma'_{\mathrm{m}} = \Gamma_{\mathrm{m}}\left(1 + \frac{\mathrm{Im}[\chi_{\mathrm{fb}}^{-1}]}{\Gamma_{\mathrm{m}} m_{\mathrm{eff}}\omega}\right) = \Gamma_{\mathrm{m}}(1 + g_{\mathrm{v}}) \tag{C.8}$$

The influence of feedback cooling on Γ_{m} is proportional to the velocity dependent feedback gain g_{v}. Overall, the feedback filter function can be expressed in terms of the respective feedback gains via [95]:

$$\chi_{\mathrm{fb}}^{-1} = k_{\mathrm{m}} g_{\mathrm{d}} - i m_{\mathrm{eff}}\Gamma_{\mathrm{m}} g_{\mathrm{v}} \tag{C.9}$$

The previously found expressions allow to describe the complete control system which is depicted in Fig. C.1. We can calculate the single-sided power spectral density (PSD) $S_{\mathrm{x}}(\omega) = \langle\tilde{x}(\omega)\tilde{x}^*(\omega)\rangle$ of the real resonator displacement $\tilde{x}$. Here we use equations C.5 and C.6 and the definition of χ_{eff}^{-1} and $\tilde{F}_{\mathrm{tot}}$ to acquire[95]:

$$\begin{aligned} S_{\mathrm{x}}(\omega) &= \langle\tilde{x}(\omega)\tilde{x}^*(\omega)\rangle \\ &= |\chi_{\mathrm{eff}}(\omega)|^2\left(\langle\tilde{F}_{\mathrm{tot}}(\omega)\tilde{F}^*_{\mathrm{tot}}(\omega)\rangle + |\chi_{\mathrm{fb}}(\omega)|^{-2}\langle\tilde{x}_{\mathrm{imp}}(\omega)\tilde{x}^*_{\mathrm{imp}}(\omega)\rangle\right) \\ &= |\chi_{\mathrm{eff}}(\omega)|^2\left(S_{\mathrm{F}}^{\mathrm{tot}}(\omega) + |\chi_{\mathrm{fb}}(\omega)|^{-2}S_{\mathrm{x}}^{\mathrm{imp}}(\omega)\right) \end{aligned} \tag{C.10}$$

[99] That is, if we consider a high Q resonator ($\Gamma_{\mathrm{m}} \ll \omega_{\mathrm{m}}$) in the bad cavity regime ($\kappa \gg \omega_{\mathrm{m}}$).

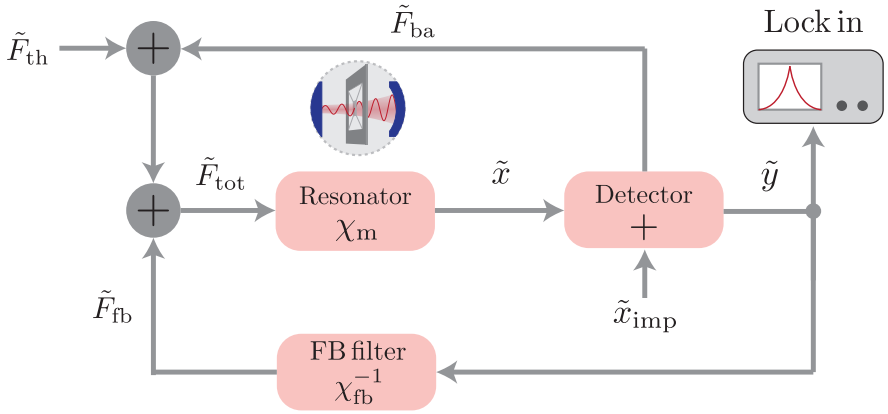

Figure C.1: Schematic of the feedback cooling mechanism. We consider a thermal force noise $\tilde{F}_{\mathrm{th}}$ coupling to the system. According to its susceptibility χ_{m} it is converted into a displacement $\tilde{x}$. The detector measures $\tilde{x}$ adding imprecision noise $\tilde{x}_{\mathrm{imp}}$ which results in the measured displacement $\tilde{y} = \tilde{x} + \tilde{x}_{\mathrm{imp}}$ and in a back-action force $\tilde{F}_{\mathrm{ba}}$ which feeds back onto the resonator. The signal $\tilde{y}$ is used by the feedback filter to derive a feedback force dependent on χ_{fb}^{-1}. All three forces yield the total force $\tilde{F}_{\mathrm{tot}}$ which acts on the resonator. Figure adapted from Ref. [57].

Equation C.10 shows the dependency of resonator displacement PSD on the thermal force noise $S_{\mathrm{F}}^{\mathrm{tot}}(\omega)$ and on the detection induced imprecision noise $S_{\mathrm{x}}^{\mathrm{imp}}$. Using the same relations as for C.10, we can calculate the $\tilde{y}$ displacement PSD to [95]:

$$S_{\mathrm{y}}(\omega) = |\chi_{\mathrm{eff}}(\omega)|^2 \left(S_{\mathrm{F}}^{\mathrm{tot}}(\omega) + |\chi_{\mathrm{m}}(\omega)|^{-2} S_{\mathrm{x}}^{\mathrm{imp}}(\omega) \right) \tag{C.11}$$

The derived expressions for S_{x} and S_{y} allow to describe the influence of feedback cooling on the acquired mode temperature. Using equation C.9 we arrive at [95]:

$$|\chi_{\mathrm{fb}}(\omega)|^{-2} = (k_{\mathrm{m}} g_{\mathrm{d}})^2 + (m_{\mathrm{eff}} \omega \Gamma_{\mathrm{m}} g_{\mathrm{v}})^2 \tag{C.12}$$

$$|\chi_{\mathrm{eff}}(\omega)|^2 = \frac{1}{m_{\mathrm{eff}}^2 \left[(\omega_m^2 (1 + g_{\mathrm{d}}) - \omega^2)^2 + (\omega \Gamma_{\mathrm{m}} (1 + g_{\mathrm{v}}))^2 \right]} \tag{C.13}$$

By using the equipartition theorem from [95]:

$$T_{\mathrm{mode}} = \frac{m_{\mathrm{eff}} \omega_{\mathrm{m}}^2}{k_{\mathrm{B}}} \langle x_{\mathrm{m}}^2 \rangle = \frac{m_{\mathrm{eff}} \omega_{\mathrm{m}}^2}{k_{\mathrm{B}}} \cdot \frac{1}{2\pi} \int_0^\infty S_{\mathrm{x}}(\omega) \mathrm{d}\omega \tag{C.14}$$

and substitute S_{x} with the expressions found in the equations C.10, C.12 and C.13 this expression yields [95]:

$$T_{\mathrm{mode}} = \frac{\omega_{\mathrm{m}}^2}{2\pi m_{\mathrm{eff}} k_{\mathrm{B}}} S_{\mathrm{F}}^{\mathrm{tot}} \int_0^\infty \frac{1}{(\omega_{\mathrm{m}}'^2 - \omega^2)^2 + (\omega \Gamma_{\mathrm{m}}')^2} \mathrm{d}\omega \tag{C.15}$$

$$+ \frac{\omega_{\mathrm{m}}^2}{2\pi m_{\mathrm{eff}} k_{\mathrm{B}}} S_{\mathrm{x}}^{\mathrm{imp}} \int_0^\infty \frac{g_{\mathrm{d}}^2 k_{\mathrm{m}}^2 + g_{\mathrm{v}}^2 (m \omega \Gamma_{\mathrm{m}})^2}{(\omega_{\mathrm{m}}'^2 - \omega^2)^2 + (\omega \Gamma_{\mathrm{m}}')^2} \mathrm{d}\omega \tag{C.16}$$

The quantities $\omega_{\mathrm{m}}' = \omega_{\mathrm{m}} \sqrt{1 + g_{\mathrm{d}}}$ and $\Gamma_{\mathrm{m}}' = \Gamma_{\mathrm{m}}(1 + g_{\mathrm{v}})$ are the feedback gain dependent

resonator frequency and linewidth. The spectral densities S_x and S_tot can be assumed as constant for our resonator parameters. The integral in equation C.15 can be solved to arrive at the final expression for the mode temperature [95]:

$$T_\mathrm{mode} = \underbrace{\frac{T_\mathrm{bath}}{(1+g_\mathrm{d})(1+g_\mathrm{v})}}_{\text{cold spring/damping}} + \left[\underbrace{\frac{k_\mathrm{m}\omega_\mathrm{m}Q}{4k_\mathrm{B}} \frac{g_\mathrm{d}^2}{(1+g_\mathrm{d})(1+g_\mathrm{v})}}_{T\propto g_\mathrm{d}} + \underbrace{\frac{k_\mathrm{m}\omega_\mathrm{m}}{4k_\mathrm{B}Q} \frac{g_\mathrm{v}^2}{1+g_\mathrm{v}}}_{T\propto g_\mathrm{v}} \right] S_\mathrm{x}^\mathrm{imp} \quad \text{(C.17)}$$

The first term of equation C.17 yields the reduction of the mode temperature dependent on the feedback gains and the bath temperature. When it approaches zero for large feedback gains, the two terms in the brackets proportional to g_d^2 and g_v^2 become dominant and cause an increase in temperature due to detection noise entering the feedback loop. Thus, the mode temperature achievable with feedback cooling exhibits a lower limit.
In Ref. [57] it was found that the displacement proportional feedback term introduces a parasitic heating effect to our system. Thus, we aim to perform solely velocity dependent feedback cooling which corresponds to a feedback phase of $\phi_\mathrm{fb} = \pi/2$. Experimentally we have to account for additional phase delays in the system due to capacities in the loop. These can be measured and compensated when adjusting the feedback loop phase in the lock in amplifier.
Assuming $g_\mathrm{d} = 0$ we can calculate the minimal mode temperature that we can achieve with velocity dependent feedback cooling to:

$$\frac{\partial T_\mathrm{mode}}{\partial g_\mathrm{v}} = 0 \rightarrow g_\mathrm{v,opt} \approx \sqrt{\frac{4k_\mathrm{B}QT_\mathrm{bath}}{k_\mathrm{m}\omega_\mathrm{m}S_\mathrm{x}^\mathrm{imp}}} \quad \text{(C.18)}$$

and arrive at the final expression:

$$T_\mathrm{mode}(g_\mathrm{v,opt}) \approx \frac{2T_\mathrm{bath}}{g_\mathrm{v,opt}} = \omega_\mathrm{m}\sqrt{\frac{m_\mathrm{eff}\Gamma_\mathrm{m}S_\mathrm{x}^\mathrm{imp}}{k_\mathrm{B}}} \quad \text{(C.19)}$$

This equation supports the use of high Q low effective mass resonators for feedback cooling. It furthermore shows the requirement of low detection noise. The modifications made on the system and the new fiber cavity motivated us to repeat feedback measurements at the new system. The results are discussed briefly in the following section.

C.2 Feedback cooling experiments with $\mathcal{F} = 650$

The experimental details on feedback cooling are described in very detail in the theses of P. Christoph [57] and T.Wagner [62]. We want to concentrate to the results with the new cavity after the repair of the cryostat at $T_\mathrm{MiM} = 4\,\mathrm{K}$ and will not discuss experimental details. For the measurements conducted we determined the system phase delay by performing feedback cooling at a fixed gain while varying the feedback loop phase $\Delta\Phi$.

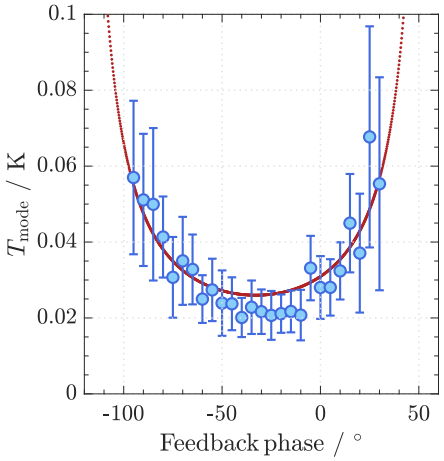

Figure C.2: Acquired mode temperatures at different feedback phase settings $\Delta\Phi$. Each data point is acquired by averaging over a one minute zero span trace of the displacement PSD. The red line is a fit of equation C.20 to the data. We determine the optimal feedback phase to $\Delta\Phi_{\mathrm{opt}} = 30° \pm 5°$.

The phase dependent minimal mode temperature can be found to fulfill [57]:

$$T_{\mathrm{mode}}(\Delta\Phi) = \frac{T_{\mathrm{bath}}}{1 + g_{\mathrm{v}}^{\mathrm{max}} \sin(\phi_0 + \Delta\Phi)} \tag{C.20}$$

The quantity ϕ_0 is the of all phase delays in the feedback loop. It changes for any modification on the feedback setup. Figure C.2 shows the measurement to determine the optimal feedback phase. The measurements presented in this section were conducted at a feedback phase $\Delta\Phi = 30°$. We operate the system at a signal/LO ratio of 10000:1 and investigate LO powers of 2.5 mW, 5 mW and 10 mW. Because it yielded the best cooling performance, we present the data for 5 mW LO power. We acquire the feedback gain and the mode temperature by measuring the spectra $S_{\mathrm{y}}(f)$ for different P-gains[100] and fitting expression C.11 to determine the in-loop displacement PSD.

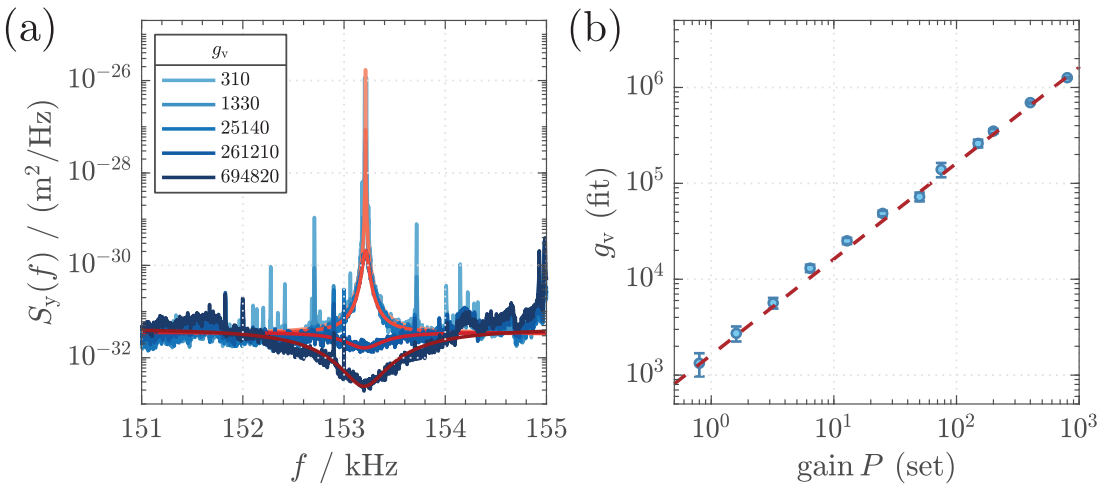

Figure C.3: (a) Measured in loop displacement spectra $S_{\mathrm{y}}(f)$ for different P-gains with fits of expression C.11. Each trace consists of 50 averaged spectra and was acquired at a demodulator frequency of 153.157 kHz and at a demodulator bandwidth of 1.6 kHz with a measurement resolution of 432 mHz. (b) Feedback gains obtained from the fits in (a) for different P-gains.

[100]The P-gain is the electronic loop gain set in the lock-in amplifier. It is an arbitrary quantity in the context of feedback cooling has no physical meaning on its own.

Using expression C.17 it is then possible to acquire the respective mode temperatures. Figure C.3 shows the measured in-loop displacement PSD with the respective fits (Fig. C.3(a)) and the derived velocity dependent feedback gain g_v (Fig. C.3(b)).
For high gains the spectra show noise squashing, a regime in which the detector noise gets canceled by the feedback loop [109]. Using equation C.19 we can calculate the mode temperatures and the effective phonon occupation of the resonator from the acquired gains. The result is presented in Fig. C.4. With the new setup we reach a final minimal mode temperature of $T_\mathrm{mode,min} = 27 \pm 1\,\mu\mathrm{K}$ which corresponds to a phonon occupation of $n_\mathrm{min,5} = 3.2 \pm 0.1$. This yields only a slight improvement over the former minimal value $n_\mathrm{min,old} = 3.8 \pm 0.1$.
This indicates slightly better noise properties of the new system over the old setup. Experiments at 10 mW (2.5 mW) LO power showed inferior cooling performance and yield a minimal phonon occupation of $n_\mathrm{min,10} = 4.7$ ($n_\mathrm{min,2.5} = 30$) phonons.

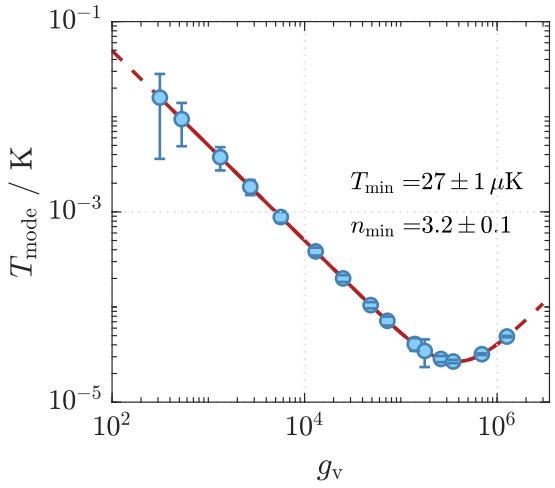

Figure C.4: Mode temperatures (blue points) at different feedback gains acquired from the fits of equation C.11 onto the spectra in Fig. C.3 with a fit of equation C.19 (red line). We reach a minimal mode temperature of $T_\mathrm{mode,min} = 27 \pm 1\,\mu\mathrm{K}$ corresponding to a phonon occupation of $n_\mathrm{min} = 3.2 \pm 0.1$.

Appendix D

Pulsed state preparation

D.1 Verification of shot-noise limited detection

Figure D.1 (a) depicts the frequency dependent common-mode-rejection-ratio (CMRR) of the used detector. The frequency response was measured with the LO beam ($P_{\mathrm{LO}} = 200\,\mu\mathrm{W}$) which was modulated via a fiber EOM at a modulation depth of $V_\pi/20$ to simulate noise. The detector shows a CMRR $> 45\,\mathrm{dB}$ on the differential output compared to individual detector port outputs for frequencies up to 10 MHz. At higher frequencies it decreases to a minimum value of 20 dB at 500 MHz[101].
In Fig. D.1 (b) the linear increase in noise variance for LO powers up to 20 mW is presented which verifies the detection to be shot noise limited.

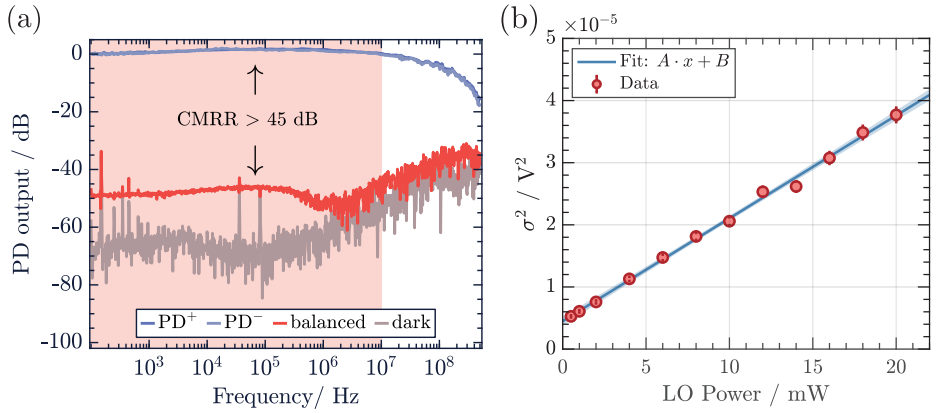

Figure D.1: (a) Frequency response of the balanced photo receiver used for the pulsed experiments (*FEMTO HBPR500-FST*). We measure a common-mode-rejection-ratio (CMRR) over 45 dB for frequencies up to 10 MHz. For frequencies above 10 MHz the CMRR decreases to a minimum value of 20 dB at 500 MHz. Subfigure from Ref. [63]. (b) Measurement of the noise variance for LO powers from 0.5 to 20 mW. The LO noise variance scales linearly over the whole range of applicable LO powers which shows that the detection is shot-noise limited.

[101] The decrease can likely be accounted by the decreasing intensity modulation depth of the EOM at these frequencies and is not to a property of the detector itself. This was verified by the manufacturer, However, this assumption could not be tested independently.

D.2 Cavity frequency modulation at high finesses

The strong effect the resonator has on the cavity frequency, modulating it on the order of the cavity linewidth can be observed when slowly scanning over the cavity resonance while observing the cavity reflection signal. Dependent on the chosen scan ramp the cavity resonance is approached from the side of optomechanical heating or cooling. When approaching from the side of optomechanical heating, even small amounts of light suffice to observe the cavity frequency modulation by the resonator which causes a modulation of the reflection signal intensity with twice the resonators eigenfrequency $\omega_{\mathrm{mod}} = 2\omega_{\mathrm{m}}$. This effect is depicted in Fig. D.2. A Fourier analysis of this signal reveals the modulation frequency to be the doubled resonator eigenfrequency.

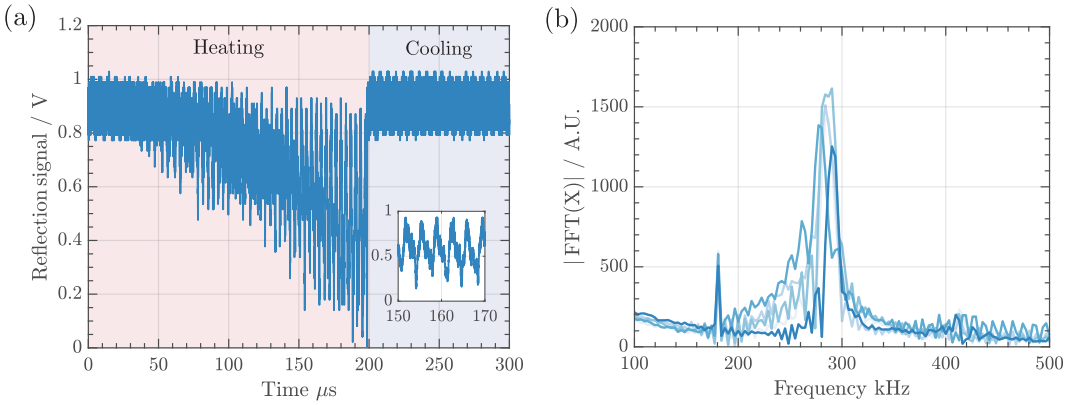

Figure D.2: (a) Reflection signal when scanning over the cavity resonance. When approaching from the side of optomechanical heating (red shaded area) the resonator modulates the reflected signal until the modulation rapidly stops once the system reaches the side of optomechanical cooling. Inset: Zoom into the modulation of the reflection signal. (b) FFT of 5 scans over the cavity resonance all starting from the side of optomechanical heating. The FFT shows the modulation in (a) to have a frequency of approximately $2\omega_{\mathrm{m}}$.

D.3 Influence of the measurement on the resonator state

Suppose we find the resonator in an initial thermal state at a bath temperature T_{bath}. The position and momentum distribution resembles a Gaussian profile [59]:

$$\sigma_x^2 = \frac{\hbar}{m_{\mathrm{eff}}\omega_{\mathrm{m}}}\left(n+\frac{1}{2}\right) = \frac{k_B T_{\mathrm{bath}}}{m\mathrm{eff}\omega_{\mathrm{m}}^2} = 2n_{\mathrm{th}}x_{\mathrm{zpm}}^2 \tag{D.1}$$

$$\sigma_p^2 = \hbar m_{\mathrm{eff}}\omega_{\mathrm{m}}\left(n+\frac{1}{2}\right) = m_{\mathrm{eff}}k_B T_{\mathrm{bath}} = \frac{\hbar^2 n_{\mathrm{th}}}{2x_{\mathrm{zpm}}^2} \tag{D.2}$$

According to [59] the interaction between the light pulse and the mechanical resonator can be described in terms of non-unitary Kraus-operators Υ that selectively narrow the wavefunction of a mechanical state in dependence of χ^{-2}. When acting on a thermal gaussian state, they create the marginal distribution [59]:

$$\langle X_{\mathrm{M}}|\rho_{\mathrm{M}}^{\mathrm{in}}(\theta_{\mathrm{t}})|x_{\mathrm{M}}\rangle \propto \exp\left[-\frac{(X_{\mathrm{M}}-\langle X_{\mathrm{M}}^{\theta_t}\rangle)^2}{2\sigma_{\theta_{\mathrm{t}}}^2}\right] \tag{D.3}$$

with the mean of the resulting conditional state $\langle X_{\mathrm{M}}^{\theta_{\mathrm{t}}}\rangle$, its variance $\sigma_{\theta_{\mathrm{t}}}^2$ and the transferred momentum Ω_{L} [59]:

$$\langle X_{\mathrm{M}}^{\theta_{\mathrm{t}}}\rangle = \frac{\chi P_{\mathrm{L}}}{\chi^2+\frac{1}{1+2n\mathrm{th}}}\cos(\theta_{\mathrm{t}}) - \Omega_{\mathrm{L}}\sin(\theta_{\mathrm{t}}) \tag{D.4}$$

$$\sigma_{\theta_{\mathrm{t}}}^2 = \frac{1}{2}\frac{\cos^2(\theta_{\mathrm{t}})}{\chi^2+\frac{1}{1+2n_{\mathrm{th}}}} + \frac{1}{2}\left(\chi^2+1+2n_{\mathrm{th}}\right)\sin^2(\theta_{\mathrm{t}}) \tag{D.5}$$

Equation D.5 contains the property of the state squeezing dependent on the tomography angle. For small θ_{t}, the first term proportional to $\cos(\theta_{\mathrm{t}})$ becomes dominant and shows squeezing of the state proportional to χ^{-2} at the cost of anti-squeezing proportional to χ^2 for $\theta_{\mathrm{t}} \to \pi/2$.
For large initial phonon occupations, which we can assume for our system even at base temperature, both expressions simplify to [59]:

$$\begin{aligned}
\theta_{\mathrm{t}} = 0 \quad &\rightarrow \quad \langle X_{\mathrm{M}}^{\mathrm{out}}\rangle \approx \frac{P_{\mathrm{L}}}{\chi} \ \text{ and } \ \sigma_{X_{\mathrm{M}}^{\mathrm{out}}}^2 \approx \frac{1}{2\chi^2} \\
\theta_{\mathrm{t}} = \frac{\pi}{2} \quad &\rightarrow \quad \langle P_{\mathrm{M}}^{\mathrm{out}}\rangle = \Omega_{\mathrm{L}} \ \text{ and } \ \sigma_{P_{\mathrm{M}}^{\mathrm{out}}}^2 \approx \frac{\chi^2+1+2n_{\mathrm{th}}}{2}
\end{aligned} \tag{D.6}$$

The found expressions show that the ground state can be resolved for $\chi \to 1$ and that the measurement drastically reduces the state width in X_{M} while the momentum and the measurement induced uncertainty get completely transferred into P_{M}. It is further notable, that ground state squeezing can be achieved regardless of the initial phonon occupation, as long as X_{M} qualifies as back-action evading QND observable.

D.4 Calculations on the optimal pulse shape for pulsed measurements

In Section 4.1.3 we introduced the measurement strength χ and distinguished between two measurement scenarios in which the probing pulse time is on the order of the cavity linewidth, or much longer. For both scenarios we introduced different measurement strengths and claimed an optimal pulse shape for pulses on the timescales of the cavity linewidth. The expression for the measurement strength can be derived for different scenarios when investigating the cavity-lightfield interaction. This derivation was outlined in the original publication by Vanner et al. [59]. To gain a profound understanding about the quantity of the measurement strength χ and to verify the influence of the pulse shape on the measurement strength, we conducted a detailed theoretical derivation of the relevant quantities alongside the outline presented in [59]. This will be presented in the following section, starting from a fundamental description of the cavity-light interaction.

Derivation of the parameter χ

We start with the intra-cavity optomechanical Hamiltonian in the rotating frame at the cavity frequency ω_{cav} [59]:

$$H = \hbar\omega_{\mathrm{M}} b^\dagger b - \hbar g_0 a^\dagger a (b + b^\dagger) \tag{D.7}$$

a is the optical field operator. b is the mechanical field operator. κ describes the cavity decay rate and a_{in} the optical input drive. The cavity field dynamics are described by [59]:

$$\frac{da}{dt} = i g_0 (b + b^\dagger) a - \kappa a + \sqrt{2\kappa} a_{\mathrm{in}} \tag{D.8}$$

We assume $\kappa^{-1} \ll \omega_{\mathrm{M}}^{-1}$ thus the mechanical position is treated as constant during the interaction [59]:

$$\frac{db}{dt} \simeq i g_0 a^\dagger a \tag{D.9}$$

This means that the mechanical evolution at t is fully described by the cavity light field and its single photon coupling rate. The mechanical motion is completely neglected. All following considerations are done at timescales of the cavity linewidth κ (in our system $\kappa = 2\pi \cdot 750$ MHz).

We separate the individual optical cavity field operators into one part that describes the pulse shape (envelope denoted as $\alpha(t)$) and a second part that describes the cavity field (using an adapted operator $\tilde{a}(t)$). Thereby we require for normalization reasons $\int dt\ \alpha_{\mathrm{in}}^2 = 1$ [59]:

$$a_{\mathrm{in}}(t) = \sqrt{N_p}\alpha_{\mathrm{in}}(t) + \tilde{a}_{\mathrm{in}}(t) \qquad\qquad a(t) = \sqrt{N_p}\alpha(t) + \tilde{a}(t) \tag{D.10}$$

Since the interaction of the cavity light field is very fast with respect to the mechanical

evolution, interactions that describe an exchange between the systems are neglected. We can assume $ig_0(b+b^\dagger)\tilde{a} \to 0$.

We plug in equation D.10 into equation D.8:

$$\begin{aligned}\frac{d}{dt}\left(\sqrt{N_p}\alpha(t)+\tilde{a}(t)\right) &= ig_0(b+b^\dagger)\left(\sqrt{N_p}\alpha(t)+\tilde{a}(t)\right)-\kappa\left(\sqrt{N_p}\alpha(t)+\tilde{a}(t)\right)\\ &\quad+\sqrt{2\kappa}\left(\sqrt{N_p}\alpha_{\mathrm{in}}(t)+\tilde{a}_{\mathrm{in}}(t)\right)\\ &= ig_0(b+b^\dagger)\sqrt{N_p}\alpha(t)+ig_0(b+b^\dagger)\tilde{a}(t)-\kappa\sqrt{N_p}\alpha(t)-\kappa\tilde{a}(t)\\ &\quad+\sqrt{2\kappa N_p}\alpha_{\mathrm{in}}(t)+\sqrt{2\kappa}\tilde{a}_{\mathrm{in}}(t)\end{aligned} \tag{D.11}$$

We sort the equation such that operators and pulse envelopes are located together:

$$\begin{aligned}\sqrt{N_p}\frac{d}{dt}\alpha(t)+\frac{d}{dt}\tilde{a}(t) &= \sqrt{N_p}\left(-\kappa\alpha(t)+\sqrt{2\kappa}\alpha_{\mathrm{in}}(t)\right)\\ &\quad\times\left(ig_0\sqrt{N_p}(b+b^\dagger)\alpha(t)-\kappa\tilde{a}(t)+\sqrt{2\kappa}\tilde{a}_{\mathrm{in}}(t)\right)\end{aligned} \tag{D.12}$$

The separation of both equations leads to [59]:

$$\sqrt{N_p}\frac{d}{dt}\alpha(t)=\sqrt{N_p}\left(-\kappa\alpha(t)+\sqrt{2\kappa}\alpha_{\mathrm{in}}(t)\right) \quad\Longleftrightarrow\quad \frac{d\alpha}{dt}=\sqrt{2\kappa}\alpha_{\mathrm{in}}(t)-\kappa\alpha(t) \tag{D.13}$$

$$\frac{d}{dt}\tilde{a}(t)=ig_0\sqrt{N_p}(b+b^\dagger)\alpha(t)+\sqrt{2\kappa}\tilde{a}_{\mathrm{in}}(t)-\kappa\tilde{a}(t) \tag{D.14}$$

Equation D.12 and D.13 are the equations of motion that describe the dynamics of the interaction of the cavity field with a input light field with pulse shape $\alpha_{\mathrm{in}}(t)$. For a complete description we have to solve both equations. Since $\alpha(t)$ is used in equation D.13 we solve equation D.12 first, by using an appropriate integration factor $\mu(t)$ and the separation of variables:

$$\frac{d\alpha}{dt}=\sqrt{2\kappa}\alpha_{\mathrm{in}}(t)-\kappa\alpha(t) \quad\Longleftrightarrow\quad \frac{d\alpha}{dt}+\kappa\alpha(t)=\sqrt{2\kappa}\alpha_{\mathrm{in}}(t) \tag{D.15}$$

$$\mu(t)\frac{d\alpha(t)}{dt}+\mu(t)\kappa\alpha(t)=\mu(t)\sqrt{2\kappa}\alpha_{\mathrm{in}}(t) \tag{D.16}$$

We find a similarity of this equation with the differential $d/dt(\mu(t)\alpha(t))$:

$$\frac{d(\mu(t)\alpha(t))}{dt}=\mu(t)\frac{d\alpha(t)}{dt}+\alpha(t)\frac{d\mu(t)}{dt} \tag{D.17}$$

Now we set the left side of equation D.15 equal to the right side of equation D.16:

$$\mu(t)\frac{d\alpha(t)}{dt}+\mu(t)\kappa\alpha(t)=\mu(t)\frac{d\alpha(t)}{dt}+\alpha(t)\frac{d\mu(t)}{dt} \tag{D.18}$$

$$\Longrightarrow \frac{d\mu(t)}{dt} = \kappa\mu(t) \quad \Longleftrightarrow \quad \mu(t) = e^{\kappa t} \tag{D.19}$$

We use the integration factor from equation D.19 in equation D.15 and obtain:

$$e^{\kappa t}\frac{d\alpha(t)}{dt} + e^{\kappa t}\kappa\alpha(t) = e^{\kappa t}\sqrt{2\kappa}\alpha_{\mathrm{in}}(t) \quad \Longleftrightarrow \quad \frac{d(e^{\kappa t}\alpha(t))}{dt} = e^{\kappa t}\sqrt{2\kappa}\alpha_{\mathrm{in}}(t) \tag{D.20}$$

Now, we can use the separation of variables:

$$\begin{aligned} d(e^{\kappa t}\alpha(t)) &= e^{\kappa t}\sqrt{2\kappa}\alpha_{\mathrm{in}}(t)dt \\ e^{\kappa t}\alpha(t) &= \sqrt{2\kappa}\int e^{\kappa t'}\alpha_{\mathrm{in}}(t')dt' + C_1 \end{aligned} \tag{D.21}$$

Since we want to learn something about the time evolution of the system we integrate from the start ($t \to -\infty$) of the evolution to t and omit the integration constant:

$$\begin{aligned} e^{\kappa t}\alpha(t) &= \sqrt{2\kappa}\int_{-\infty}^{t} e^{\kappa t'}\alpha_{\mathrm{in}}(t')dt' \\ \alpha(t) &= \sqrt{2\kappa}e^{-\kappa t}\int_{-\infty}^{t} e^{\kappa t'}\alpha_{\mathrm{in}}(t')dt' \end{aligned} \tag{D.22}$$

We solve equation D.13 using the same approach. Since the equation is of a similar form we can use the same steps as shown from equations D.14 - D.18. Then we receive:

$$e^{\kappa t}\frac{d\tilde{a}(t)}{dt} + e^{\kappa t}\kappa\tilde{a}(t) = e^{\kappa t}ig_0\sqrt{2}\sqrt{N_p}(b+b^\dagger)\alpha(t) - e^{\kappa t}\sqrt{2\kappa}\tilde{a}_{\mathrm{in}}(t) \tag{D.23}$$

$$d(e^{\kappa t}\tilde{a}(t)) = e^{\kappa t}\left(ig_0\sqrt{2}\sqrt{N_p}(b+b^\dagger)\alpha(t) - \sqrt{2\kappa}\tilde{a}_{\mathrm{in}}(t)\right)dt \tag{D.24}$$

Integrate both sides of equation D.23. We now use the relation $X_{\mathrm{M}}^{\mathrm{in}} = (b+b^\dagger)/\sqrt{2}$ and receive:

$$e^{\kappa t}\tilde{a}(t) = ig_0 2\sqrt{N_p}X_{\mathrm{M}}^{\mathrm{in}}\int e^{\kappa t'}\alpha(t')dt' - \sqrt{2\kappa}\int e^{\kappa t'}\tilde{a}_{\mathrm{in}}(t')dt' + C_1 \tag{D.25}$$

This yields an expression for $\tilde{a}(t)$:

$$\tilde{a}(t) = ig_0 2\sqrt{N_p}X_{\mathrm{M}}^{\mathrm{in}}e^{-\kappa t}\int e^{\kappa t'}\alpha(t')dt' - \sqrt{2\kappa}e^{-\kappa t}\int e^{\kappa t'}\tilde{a}_{\mathrm{in}}(t')dt' + C_1 \tag{D.26}$$

We simplify the first part of equation D.25 by using the following definition [59]:

$$\phi(t) = e^{-\kappa t}\int_{-\infty}^{t} e^{\kappa t'}\alpha(t')dt' \tag{D.27}$$

This leads to:

$$\tilde{a}(t) = ig_0 2\sqrt{N_p}\phi(t)X_{\mathrm{M}}^{\mathrm{in}} - \sqrt{2\kappa}e^{-\kappa t}\int e^{\kappa t'}\tilde{a}_{\mathrm{in}}(t')dt' + C_1 \tag{D.28}$$

Use the definition of the output field $\tilde{a}_{\text{out}} = \sqrt{2\kappa}\tilde{a} - \tilde{a}_{\text{in}}$ to get $P_{\text{L}}^{\text{out}}$:

$$\tilde{a}_{\text{out}} = \sqrt{2\kappa}\tilde{a}(t) - \tilde{a}_{\text{in}} = ig_0 2^{\frac{3}{2}}\sqrt{\kappa}\sqrt{N_p}\phi(t)X_{\text{M}}^{\text{in}} - 2\kappa e^{-\kappa t}\int_{-\infty}^{t} e^{\kappa t'}\tilde{a}_{\text{in}}(t')dt' - \tilde{a}_{\text{in}}(t) \quad \text{(D.29)}$$

While using $\sqrt{\kappa} = \frac{\kappa^{\frac{3}{2}}}{\kappa}$ we define $\varphi(t) = (2\kappa)^{\frac{3}{2}}\phi(t)$ and get [59]:

$$P_{\text{L}}^{\text{out}} = \frac{g_0}{\kappa}\sqrt{N_p}\varphi(t)X_{\text{M}}^{\text{in}} - 2\kappa e^{-\kappa t}\int_{-\infty}^{t} e^{\kappa t'}P_{\text{L}}^{\text{in}}(t')dt' - P_{\text{L}}^{\text{in}}(t) \quad \text{(D.30)}$$

Equation D.29 describes the output phase quadrature from the cavity. It is very dependent on the pulse shape ($\alpha_{\text{in}}(t)$) and the cavity linewidth κ. Note that this is not necessarily equivalent to the measured quadrature (P_L). The measured quadrature depends on the overlap between the signal and the local oscillator beam which we will consider in the following. Overall, the goal is to maximize the overlap between the cavity output field shape and the LO shape. Assume the LO pulse has an envelope of the form $\alpha_{LO}(t)$. The measured cavity field P_L is the convolution between $\alpha_{LO}(t)$ and $P_{\text{L}}^{\text{out}}$ [59]:

$$P_{\text{L}} = \sqrt{2}\int \alpha_{LO}(t)P_{\text{L}}^{\text{out}}dt \quad \text{(D.31)}$$

Since $\varphi(t) \propto \int e^{\kappa t}\alpha(t)dt$ describes the shape of the pulse coming out of the cavity for a certain $\alpha_{\text{in}}(t)$ we choose $\alpha_{LO}(t)$ with a similar shape upon a certain normalization factor $1/N_\varphi$ [59]:

$$\alpha_{LO}(t) = N_\varphi\varphi(t) \quad \text{(D.32)}$$

We plug equation D.31 into expression D.30 and only look at the mechanical component of $P_{\text{L}}^{\text{out}} \propto X_{\text{M}}^{\text{in}}$:

$$P_{\text{L}} = \sqrt{2}\frac{g_0}{\kappa}\sqrt{N_p}X_{\text{M}}^{\text{in}}\int N_\varphi\varphi(t)^2dt \quad \text{(D.33)}$$

Using the relation $N_\varphi^{-2} = \int \varphi(t)^2dt$ we get [59]:

$$P_{\text{L}} = \underbrace{\sqrt{2}\frac{1}{N_\varphi}\frac{g_0}{\kappa}\sqrt{N_p}}_{\chi}X_{\text{M}}^{\text{in}} \quad \Longleftrightarrow \quad P_{\text{L}} = \chi X_{\text{M}}^{\text{in}} \quad \text{(D.34)}$$

This aligns with the calculations of Vanner et al. and explains the definition of χ which is the contribution of X_{M}^{in} to the signal $P_{\text{L}}^{\text{out}}$.

Optimizing χ for short pulses

One can now look at different $\alpha_{\text{in}}(t)$ and $\alpha_{LO}(t)$ and calculate the reaction of the system for different signal/LO pulse shapes. When the optimal drive is applied, we expect this to result in the optimal achievable strength χ_{opt}. Vanner *et al.* propose the optimal input drive to have a Lorentzian spectrum. We assume the input drive to be [59]:

$$\alpha_{\text{in}}(t) = \sqrt{\kappa}e^{-\kappa|t|} \quad \text{(D.35)}$$

As we Fourier-transform this expression we see that is has Lorentzian spectrum.

$$FT[\alpha_{\text{in}}(t)] = \int_{-\infty}^{\infty} \sqrt{\kappa} e^{-\kappa|t|} e^{i\omega x} dx = \frac{\sqrt{\frac{2}{\pi}}\kappa^{\frac{3}{2}}}{\kappa^2 + \omega^2} \tag{D.36}$$

We recall equation D.21 and plug it into equation D.34. We get an expression for $\alpha(t)$:

$$\alpha(t) = \sqrt{2\kappa} e^{-\kappa t} \int e^{\kappa t'} \sqrt{\kappa} e^{-\kappa|t'|} dt' \tag{D.37}$$

$$\alpha(t) = \sqrt{2\kappa} e^{-\kappa t} \left(\frac{1 + 2\kappa t + e^{2\kappa t} + (2\kappa t - e^{2\kappa t} + 1)\text{sgn(t)}}{4\sqrt{\kappa}} \right) \tag{D.38}$$

The shapes of $\alpha(t)$ and $\alpha_{\text{in}}(t)$ are depicted in Fig. D.3. These are the basic shapes that occur in the system if we apply optimized pulses at timescales of κ.

To understand why this pulse shape yields the optimal measurement strength we calculate χ for the assumption that $\alpha_{\text{in}}(t)$ is described by equation D.34. Using equation D.37 we calculate $\varphi(t)$.

$$\begin{aligned}
\varphi(t) &= (2\kappa)^{\frac{3}{2}} e^{-\kappa t} \int_{-\infty}^{t} e^{\kappa t'} \alpha(t') dt' \\
&= (2\kappa)^{\frac{3}{2}} e^{-\kappa t} \int_{-\infty}^{t} e^{\kappa t'} \sqrt{2\kappa} e^{-\kappa t'} \int_{-\infty}^{t'} e^{\kappa t''} \sqrt{\kappa} e^{-\kappa|t''|} dt'' dt' \\
&= (2\kappa)^{3/2} e^{-\kappa t} \int_{-\infty}^{t} \sqrt{2\kappa} \int_{-\infty}^{t'} \sqrt{\kappa} e^{\kappa t'' - \kappa|t''|} \, dt'' \, dt'
\end{aligned} \tag{D.39}$$

We use the definition $N_\varphi^{-2} = \int_{-\infty}^{\infty} dt \varphi(t)^2$ and get a general form for N_φ.

$$\frac{1}{N_\varphi^2} = \int_{-\infty}^{\infty} 8k^3 e^{-2\kappa t} \left(\int_{-\infty}^{t} \sqrt{2\kappa} \int_{-\infty}^{t'} \alpha_{\text{in}}(t) e^{\kappa t''} \, dt'' \, dt' \right)^2 dt \tag{D.40}$$

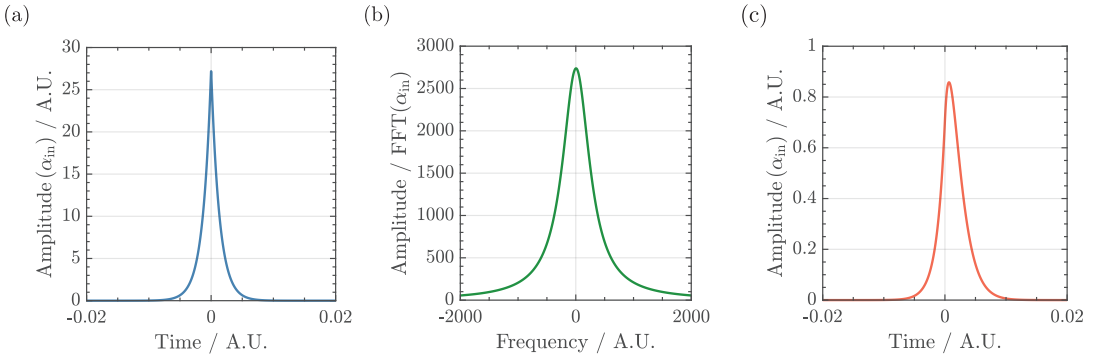

Figure D.3: (a) Input drive $\alpha_{\text{in}}(t)$ according to equation D.35. (b) Spectrum FFT($\alpha_{\text{in}}(t)$) according to equation D.36. The input pulse has a Lorentzian spectrum. (c) After interaction with the cavity, the output pulse has an envelope described by equation D.38. The traces are examples that just resemble the shape of the applied light fields for visualization.

In our particular case this yields:

$$\begin{aligned}\frac{1}{N_\varphi^2} &= \int_{-\infty}^{\infty}\left((2\kappa)^{3/2}e^{-\kappa t}\int_{-\infty}^{t}\sqrt{2\kappa}\int_{-\infty}^{t'}\sqrt{\kappa}e^{\kappa t''-\kappa|t''|}\,dt''\,dt'\right)^2 dt \\ &= \int_{-\infty}^{\infty}8k^3e^{-2\kappa t}\left(\int_{-\infty}^{t}\sqrt{2\kappa}\int_{-\infty}^{t'}\sqrt{\kappa}e^{kt''-\kappa|t''|}\,dt''\,dt'\right)^2 dt\end{aligned} \tag{D.41}$$

This integral can be solved numerically. Independent of a chosen κ its result is [59]:

$$\frac{1}{N_\varphi^2} = 10 \quad\Longleftrightarrow\quad \frac{1}{N_\varphi} = \sqrt{10} \tag{D.42}$$

By plugging this result into the definition of χ in equation D.33 we get:

$$\chi = \sqrt{2}\frac{1}{N_\varphi}\frac{g_0}{\kappa}\sqrt{N_p} = \sqrt{2}\sqrt{10}\frac{g_0}{\kappa}\sqrt{N_p} \quad\Longrightarrow\quad \underline{\underline{\chi_{opt} = 2\sqrt{5}\frac{g_0}{\kappa}\sqrt{N_p}}} \tag{D.43}$$

This is similar to the expression we introduced in Section 4.1.3.

χ for short rectangular pulses

Considering these calculations, we now investigate how system behaves if we apply rectangular pulses with $t_{\text{pulse}} \approx 1/\kappa$. We assume a rectangular pulse $\alpha_{\text{in}}(t)$ with a length of 10κ.

$$\alpha_{\text{in}}(t) = \frac{1}{N_\alpha}\Pi\left(\frac{10t}{\kappa}\right) \tag{D.44}$$

Here N_α ensures normalization and (since $\int dt\ \alpha_{\text{in}}^2 = 1$) can be calculated via:

$$N_\alpha = \sqrt{\int_{-\infty}^{\infty}\alpha_{\text{in}}(t)^2 dt} \tag{D.45}$$

We plug these relations into equation D.21 to receive $\alpha(t)$:

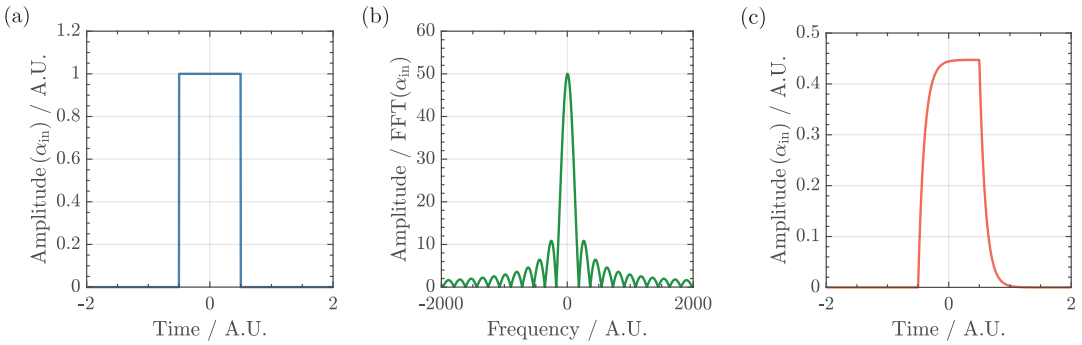

Figure D.4: (a) Input drive $\alpha_{\text{in}}(t)$ according to equation D.44. (b) Spectrum FFT($\alpha_{\text{in}}(t)$) of the input pulse. (c) After interaction with the cavity, the output pulse has an envelope described by equation D.46. The traces are examples that just resemble the shape of the applied light fields for visualization.

$$\alpha(t) = \frac{\sqrt{2\kappa}}{N_\alpha} e^{-\kappa t} \int_{-\infty}^{t} \Pi\left(\frac{10'}{\kappa}\right) e^{\kappa t'} dt' \tag{D.46}$$

As done in equation D.38 we can calculate $\varphi(t)$:

$$\varphi(t) = (2\kappa)^{\frac{3}{2}} e^{-\kappa t} \int_{-\infty}^{t} \frac{\sqrt{2\kappa}}{N_\alpha} e^{-\kappa t'} \int_{-\infty}^{t'} \Pi\left(\frac{10''}{\kappa}\right) e^{\kappa t''} dt'' dt' \tag{D.47}$$

And from $\varphi(t)$ we get N_φ:

$$\frac{1}{N_\varphi^2} = \int_{-\infty}^{\infty} \left((2\kappa)^{\frac{3}{2}} e^{-\kappa t} \int_{-\infty}^{t} \frac{\sqrt{2\kappa}}{N_\alpha} e^{-\kappa t'} \int_{-\infty}^{t'} \Pi\left(\frac{10''}{\kappa}\right) e^{\kappa t''} dt'' dt' \right) dt \tag{D.48}$$

This integral converges to a fixed value when choosing high κ. As a result, we receive as long as $\kappa \gg 1$:

$$\frac{1}{N_\varphi^2} = \frac{68}{5}\left(+\frac{52}{5e^{10}}\right) \quad \Longrightarrow \quad \frac{1}{N_\varphi} = \sqrt{\frac{68}{5}} \simeq 3.69 \tag{D.49}$$

We can calculate a maximum χ now and compare rectangular pulses with the pulses proposed by Vanner *et al.* [59]. Here we assume $P_{\mathrm{SIG}} = 4\,\mu\mathrm{W}$, $g_0 = 2\pi \cdot 204\,\mathrm{kHz}$ and $\kappa = 2\pi \cdot 750\,\mathrm{MHz}$:

$$\chi_{opt}^{\mathrm{Lorentz}} = 2\sqrt{5}\frac{g_0}{\kappa}\sqrt{N_p} \simeq 1.11 \qquad \chi_{opt}^{\mathrm{Rect}} = 3.69\frac{g_0}{\kappa}\sqrt{N_p} \simeq 0.92 \tag{D.50}$$

This means we achieve an approximately 10 percent higher χ_{opt} when choosing an optimized high-power Lorentzian pulse. However, this only applies in a regime of very short pulses.

If we assume the pulse to be very long (i.e. $t \to \infty$) we observe $1/N_\varphi \to 4$. This is the case for rectangular pulses and pulses with Lorentzian spectrum. This means the maximum χ we can achieve in a long pulse regime is independent on the pulse shape and yields:

$$\chi_{\mathrm{long}} = 4\frac{g_0}{\kappa}\sqrt{N_p} \simeq 1 \tag{D.51}$$

Appendix E

Leak detection and repair of the cryostat

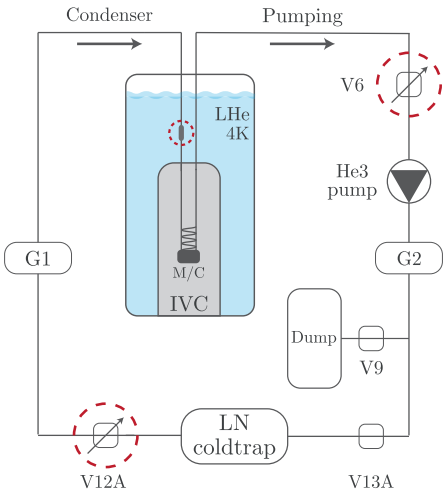

Figure E.1: Simplified sketch of the dilution refrigerator in operation. The He3/He4 mixture is circulated clockwise by a high-power rotary pump (*Pfeiffer Duos 62*). The valve V6 and V12A can be gradually opened. During normal operation both valves are fully opened. The valves V9 and V13A allow to stop the circulation and guide the mixture into the dump. G1 and G2 are pressure gauges. The dilution unit is placed inside the inner vacuum chamber (IVC) inside a bath of liquid helium. The red circles denote malfunctioning parts or leaks that were identified and repaired during this thesis. The valves and pressure gauges are named according to the original technical drawings for comparability.

Beginning in October 2023, we started an extensive investigation on the state of the dilution refrigerator. In the past, the system showed regular blockages occurring after only hours of operation. This forced us to stop its operation end of 2022 and store the mixture safely in the systems dump. Beginning in this state, the leak checks were conducted. Prior to any venting we cryo-pumped the whole system. To reduce the volume to check and reduce the chance of measuring virtual leaks, we disconnected the individual parts of the system and checked complex components separately.

The most prominent leak was found at valve V12A. With the intelligent gas handling system (IGH) separated from the other parts of the system we recognize a rapid increase in pressure starting from an evacuated system. This is presented in Fig. E.2 where a rapid increase in G1 of 300 mbar in under 10 minutes indicates a leak in this branch of the IGH.

Although very large, this leak remained undetected for a long time because its effect is

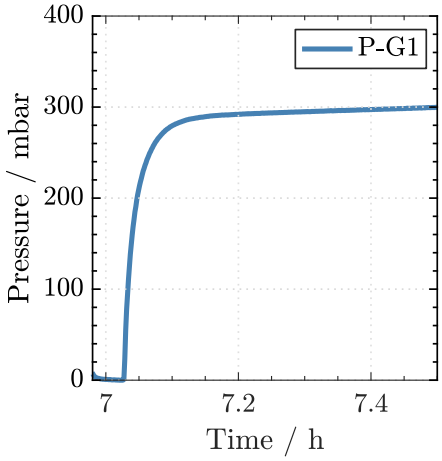

Figure E.2: Rapid increase in G1 after the system was evacuated. The intelligent gas handling system (IGH) is detached from the remaining pipe system and sealed on its outlets, thus having a very small volume. V12A is fully closed in this system configuration.

not as visible during normal operation. With fully operational cold traps, and attached to the large volume of the whole system the pressure increase is much less prominent. Furthermore, it is dependent on the opening state of the valve V12A. The exact localization of the leak turned out to be challenging due to the very high leak rates that defied the use of a leak detector. Application of local sealant on the suspected part verified the localization at V12A. In the context of regular blockages this leak might have been most influential, and prevented any long-term operation. After consultation with *Oxford Instruments* we found this valve to regularly malfunction due to carbon deposits from the LN cold-trap. During a field service the valve was removed.
A manual valve behind the LN cold trap was installed to fulfill role of the valve during condensation of the mixture. In the near future the installation of a new valve could increase the degree of automation again. The taken measures are shown in Fig. E.3.

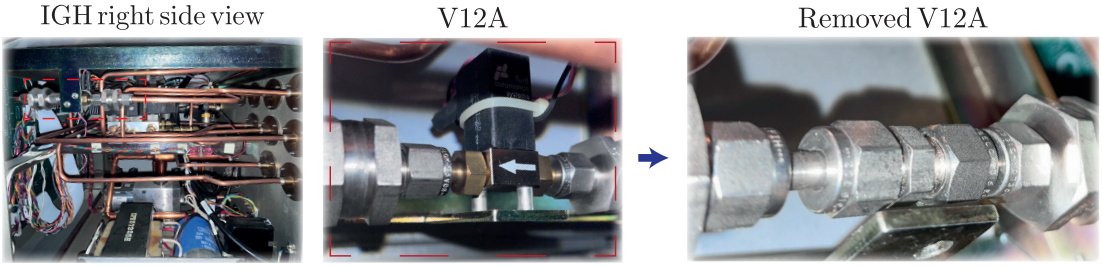

Figure E.3: Localization of the leak in the intelligent gas handling system (IGH). V12A is a magnetic valve that can be opened gradually. It is included between two 15 micron filters that are installed to prevent carbon from the LN cold trap to enter the system. Sealing the valve with high vacuum epoxy (VacSeal) did not yield a permanent repair due to the moving parts in place. During a field service by *Oxford Instruments* the valve was removed.

After the localization of the leak in V12A, we leak checked the remaining system and found a second leak in the insert that contains the He3/He4 dilution unit. This part is particularly delicate to repair as it is submerged in liquid He4 during normal operation. For an exact localization of the leak, we disassembled the whole dilution unit and identified a leak at the bottom of a hard solder joint in the condenser line that exhibited a leak rate of $Q_{\mathrm{L}} > 1 \cdot 10^{-5}\,\mathrm{mbar\,l/s}$. Although smaller than the leak on V12A, it directly allows He4 and other gases to enter the dilution unit which operates at an under

pressure and thus changing or polluting the mixture, diminishing the overall cooling performance or leading to a blockage.
The repair of this joint turned out to be technically demanding due to the location at the bottom of the joint and the requirement of using hard solder[102]. This posed the risk of solder flowing down the condenser line and widen the leak. Since further disassembly came at the high risk of damaging the dilution unit, we mounted a plate below the joint and could seal the system after a third repair attempt. The proceeding is depicted in Fig. E.4. Leak rate measurements on the whole system after the repairs at insert

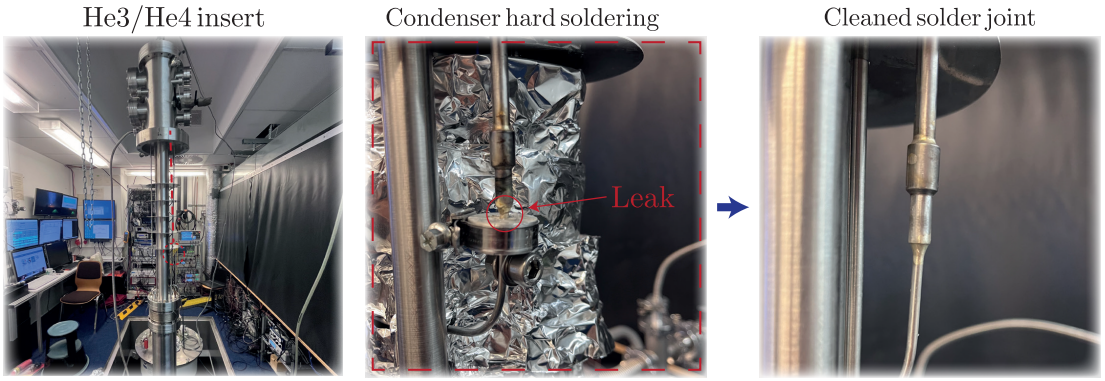

Figure E.4: Localization of the leak on the condenser line of the insert. The leak was located at the bottom of a hard solder joint which connects the straight part of the condenser line with a part winded around the still. It is submerged in liquid He4. After consultation with the mechanical workshop we mounted a disk below the joint to prevent hard solder flowing downwards. To prevent solder to clog or oxidize the condenser line a slight overpressure with Helium gas was applied to the vessel. The hard soldering was done by the mechanical workshop using an oxygen-acetylene mixture. The result after cleaning is depicted on in the right side.

temperatures of 4K verified the success of the repairs as we measured overall leak rates of[103]:

$$Q_{\mathrm{L,all}} \approx 5 \cdot 10^{-8\ (+1/-0)} \frac{\mathrm{mbar\,l}}{\mathrm{s}} \quad \text{and} \quad Q_{\mathrm{L,insert}} \approx 5 \cdot 10^{-10\ (+1/-0)} \frac{\mathrm{mbar\,l}}{\mathrm{s}} \tag{E.1}$$

Here the sub-index "all" refers to the complete line system (insert, lines, and IGH) while "insert" refers only to the dilution unit. The leak rates match with the specifications Oxford guarantees upon delivery of a new system.
Lastly we found a malfunction during the initialization of the mixture circulation due to degraded lubricant in the valve V6. Due to the large circulation flow in the system V6 is a large area valve that is moved by a 50 mNm motor via a 1:100 gear. The motor showed to produce considerable amount of heat, which lead to the hardening of the gears lubricant. Cleaning the gear using and ultrasound bath and application of new lubricant solved the issue as depicted in Fig. E.5. After these repairs we cooled

[102] In total two attempts, one of which executed during an *Oxford* field service, failed. Measuring the insert leak rate during cooldown showed the leaks to break open around LN2 temperature. Each attempt requires a complete dis- and reassembly of the system.
[103] During this time a malfunction of the leak-detector required us to operate it in an uncalibrated mode. A field service by *Pfeiffer* revealed afterwards that the measured leak rates were inaccurate on one order of magnitude.

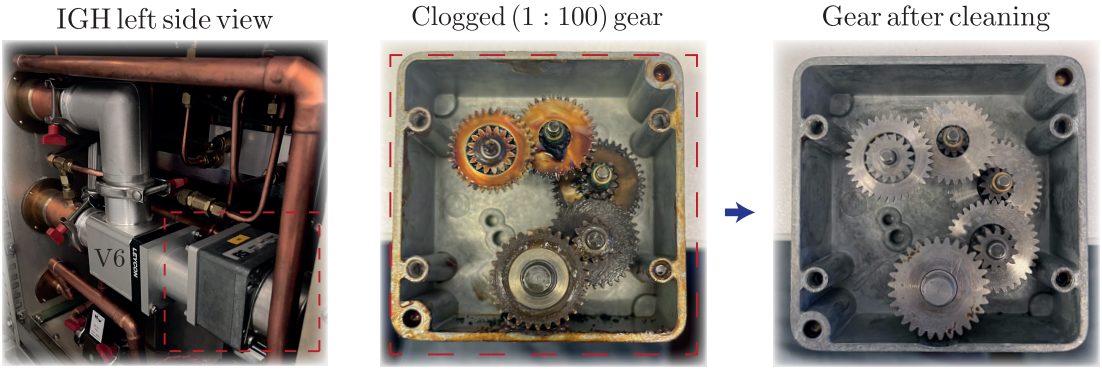

Figure E.5: Malfunction of valve V6 which regulates the circulation of the mixture. A 50 mNm motor is connected to a 1:100 gear that turns the valve. The lubricant in the gear degraded over the years. Cleaning it in an ultrasound bath and application of new lubricant resolved the malfunction.

down the system to base temperature and observe the temperature stability and the final mixing chamber temperature. We found the system to operate at mixing chamber temperatures between 100 mK and 300 mK (dependent on the still heater power) which is similar to the values acquired in the previous years. The high temperature compared to the specification of 30 mK can be explained by the large thermal load of the attached experiment, that is not shielded to the full possible extent. We were able to operate the system at stable temperatures for multiple days and were limited by the supply of liquid He4.

To assess whether any mixture got lost in the past years we conducted a single shot measurement. During operation the main circulating gas in the system is He3. This property can be used to do a rough measurement of the amount of He3 in the system by rapidly stopping the circulation (by closing V13A) and guiding all the mixture into the dump (by opening V9). Upon the point where all He3 has left the system, the warmup behavior and the pressure increase in the dump is suspected to change. This is shown in Fig. E.6 where we find roughly 10.5 L of He3 remaining in the mixture.

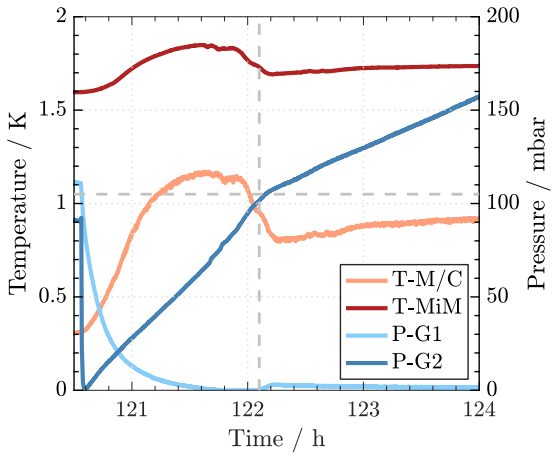

Figure E.6: Single shot measurement to assess the amount of He3 in the mixture with the mixing chamber (light red) and experiment (dark red) temperature on the left axis and the pressure readings on G1 (light blue) and G2 (dark blue) on the right axis. The point of transition in warm-up behavior and dump pressure change is marked by the grey dashed lines. At a dump volume of 100 L we can guess roughly 10.5 L of He3 to be still in the system of formerly 15 L. Note that this measurement yields only a rough estimate of the amount of He3.

Bibliography

[1] W. Heisenberg: *Quantentheorie und Philosophie*, Philipp jun. GmbH Verlag (1986), ISBN 978-3150099483. 1

[2] H. Hertz: "Ueber einen Einfluss des ultravioletten Lichtes auf die electrische Entladung", Annalen der Physik **267**, 983–1000 (1887), ISSN 0003-3804. 1

[3] M. Planck: "Ueber das Gesetz der Energieverteilung im Normalspectrum", Annalen der Physik **309**, 553–563 (1901), ISSN 0003-3804.

[4] A. Einstein: "Über einen die Erzeugung und Verwandlung des Lichtes betreffenden heuristischen Gesichtspunkt", Annalen der Physik **322**, 132–148 (1905), ISSN 0003-3804.

[5] C. Joensson: "Elektroneninterferenzen an mehreren kuenstlich hergestellten Feinspalten", Zeitschrift fuer Physik **161**, 454–474 (1961), ISSN 1434-6001. 1

[6] E. W. Mueller: "Resolution of the Atomic Structure of a Metal Surface by the Field Ion Microscope", Journal of Applied Physics **27**, 474–476 (1956), ISSN 0021-8979. 1

[7] G. Binnig and H. Rohrer: "Scanning tunneling microscopy", Surface Science **126**, 236–244 (1983), ISSN 00396028. 1

[8] E. Y. Andrei and A. H. MacDonald: "Graphene bilayers with a twist", (2020). 1

[9] X. Huang, R. Xiong, C. Hao, W. Li, B. Sa, J. Wiebe and R. Wiesendanger: "Experimental Realization of Monolayer alpha-Tellurene", Advanced Materials **36** (2024), ISSN 15214095. 1

[10] C. Degen, F. Reinhard and P. Cappellaro: "Quantum sensing", Reviews of Modern Physics **89**, 035002 (2017), ISSN 0034-6861. 1, 5

[11] V. Giovannetti, S. Lloyd and L. Maccone: "Quantum-Enhanced Measurements: Beating the Standard Quantum Limit", Science **306**, 1330–1336 (2004), ISSN 0036-8075. 5

[12] V. Giovannetti, S. Lloyd and L. Maccone: "Advances in quantum metrology", Nature Photonics **5**, 222–229 (2011), ISSN 1749-4885. 1

[13] P. C. Maurer, G. Kucsko, C. Latta, L. Jiang, N. Y. Yao, S. D. Bennett, F. Pastawski, D. Hunger, N. Chisholm, M. Markham, D. J. Twitchen, J. I. Cirac and M. D. Lukin: "Room-Temperature Quantum Bit Memory Exceeding One Second", Science **336**, 1283–1286 (2012), ISSN 0036-8075. 1

[14] J. J. Pla, K. Y. Tan, J. P. Dehollain, W. H. Lim, J. J. L. Morton, F. A. Zwanenburg, D. N. Jamieson, A. S. Dzurak and A. Morello: "High-fidelity readout and control of a nuclear spin qubit in silicon", Nature **496**, 334–338 (2013), ISSN 0028-0836. 1

[15] M. Schlosshauer: *Decoherence and the Quantum-To-Classical Transition*, Springer Berlin Heidelberg (2007), ISBN 978-3-540-35773-5. 1

[16] W. H. Zurek: "Decoherence, einselection, and the quantum origins of the classical", Reviews of Modern Physics **75**, 715–775 (2003), ISSN 0034-6861. 1

[17] A. Aspuru-Guzik and P. Walther: "Photonic quantum simulators", Nature Physics **8**, 285–291 (2012), ISSN 1745-2473. 1

[18] R. Blatt and C. F. Roos: "Quantum simulations with trapped ions", Nature Physics **8**, 277–284 (2012), ISSN 1745-2473.

[19] A. A. Houck, H. E. Türeci and J. Koch: "On-chip quantum simulation with superconducting circuits", Nature Physics **8**, 292–299 (2012), ISSN 1745-2473.

[20] I. Bloch, J. Dalibard and S. Nascimbène: "Quantum simulations with ultracold quantum gases", Nature Physics **8**, 267–276 (2012), ISSN 1745-2473.

[21] I. Georgescu, S. Ashhab and F. Nori: "Quantum simulation", Reviews of Modern Physics **86**, 153–185 (2014), ISSN 0034-6861. 1

[22] J. H. Wesenberg, A. Ardavan, G. A. D. Briggs, J. J. L. Morton, R. J. Schoelkopf, D. I. Schuster and K. Mølmer: "Quantum Computing with an Electron Spin Ensemble", Physical Review Letters **103**, 070502 (2009), ISSN 0031-9007. 1

[23] T. D. Ladd, F. Jelezko, R. Laflamme, Y. Nakamura, C. Monroe and J. L. O'Brien: "Quantum computers", Nature **464**, 45–53 (2010), ISSN 0028-0836.

[24] E. Grumbling and M. Horowitz (editors): *Quantum Computing*, National Academies Press (2019), ISBN 978-0-309-47969-1.

[25] I. H. Deutsch: "Harnessing the Power of the Second Quantum Revolution", PRX Quantum **1**, 020101 (2020), ISSN 2691-3399.

[26] A. J. Daley, I. Bloch, C. Kokail, S. Flannigan, N. Pearson, M. Troyer and P. Zoller: "Practical quantum advantage in quantum simulation", Nature **607**, 667–676 (2022), ISSN 0028-0836. 1

[27] J. Chen: "Review on Quantum Communication and Quantum Computation", Journal of Physics: Conference Series **1865**, 022008 (2021), ISSN 1742-6588. 2

[28] N. Gisin, G. Ribordy, W. Tittel and H. Zbinden: "Quantum cryptography", Reviews of Modern Physics **74**, 145–195 (2002), ISSN 0034-6861. 2

[29] C. S. Adams, J. D. Pritchard and J. P. Shaffer: "Rydberg atom quantum technologies", Journal of Physics B: Atomic, Molecular and Optical Physics **53** (1), 012002 (2019). 2

[30] T. E. Northup and R. Blatt: "Quantum information transfer using photons", (2014). 2

[31] J. J. Morton and B. W. Lovett: "Hybrid solid-state qubits: The powerful role of electron spins", Annual Review of Condensed Matter Physics **2**, 189–212 (2011), ISSN 19475454. 2

[32] L. Tian, P. Rabl, R. Blatt and P. Zoller: "Interfacing Quantum-Optical and Solid-State Qubits", Physical Review Letters **92**, 247902 (2004), ISSN 0031-9007. 2

[33] T. A. Palomaki, J. W. Harlow, J. D. Teufel, R. W. Simmonds and K. W. Lehnert: "Coherent state transfer between itinerant microwave fields and a mechanical oscillator", Nature **495**, 210–214 (2013), ISSN 0028-0836. 7

[34] D. Petrosyan, G. Bensky, G. Kurizki, I. Mazets, J. Majer and J. Schmiedmayer: "Reversible state transfer between superconducting qubits and atomic ensembles", Physical Review A **79**, 040304 (2009), ISSN 1050-2947.

[35] A. P. Reed, K. H. Mayer, J. D. Teufel, L. D. Burkhart, W. Pfaff, M. Reagor, L. Sletten, X. Ma, R. J. Schoelkopf, E. Knill and K. W. Lehnert: "Faithful conversion of propagating quantum information to mechanical motion", Nature Physics **13**, 1163–1167 (2017), ISSN 1745-2473.

[36] K. Hammerer, M. Aspelmeyer, E. S. Polzik and P. Zoller: "Establishing Einstein-Poldosky-Rosen Channels between Nanomechanics and Atomic Ensembles", Physical Review Letters **102**, 020501 (2009), ISSN 0031-9007.

[37] F. Momeni and M. H. Naderi: "Atomic quadrature squeezing and quantum state transfer in a hybrid atom–optomechanical cavity with two Duffing mechanical oscillators", Journal of the Optical Society of America B **36**, 775 (2019), ISSN 0740-3224.

[38] T. M. Karg, B. Gouraud, C. T. Ngai, G.-L. Schmid, K. Hammerer and P. Treutlein: "Light-mediated strong coupling between a mechanical oscillator and atomic spins 1 meter apart", Science **369**, 174–179 (2020), ISSN 0036-8075. 2, 48

[39] T. M. Karg: "Strong light-mediated coupling between a membrane oscillator and an atomic spin ensemble", Universität Basel, PhD Thesis (2020). 2

[40] K. Hammerer, M. Wallquist, C. Genes, M. Ludwig, F. Marquardt, P. Treutlein, P. Zoller, J. Ye and H. J. Kimble: "Strong Coupling of a Mechanical Oscillator and a Single Atom", Physical Review Letters **103**, 063005 (2009), ISSN 0031-9007. 2

[41] A. D. Armour, M. P. Blencowe and K. C. Schwab: "Entanglement and Decoherence of a Micromechanical Resonator via Coupling to a Cooper-Pair Box", Physical Review Letters **88**, 148301 (2002), ISSN 0031-9007. 2

[42] A. S. Sørensen, C. H. van der Wal, L. I. Childress and M. D. Lukin: "Capacitive Coupling of Atomic Systems to Mesoscopic Conductors", Physical Review Letters **92**, 063601 (2004), ISSN 0031-9007.

[43] C. Genes, H. Ritsch, M. Drewsen and A. Dantan: "Atom-membrane cooling and entanglement using cavity electromagnetically induced transparency", Physical Review A **84**, 051801 (2011), ISSN 1050-2947. 2, 4

[44] T. A. Palomaki, J. D. Teufel, R. W. Simmonds and K. W. Lehnert: "Entangling Mechanical Motion with Microwave Fields", Science **342**, 710–713 (2013), ISSN 0036-8075. 2

[45] S. Chu: "Cold atoms and quantum control", Nature **416**, 206–210 (2002), ISSN 00280836. 2

[46] Y.-J. Wang, M. Eardley, S. Knappe, J. Moreland, L. Hollberg and J. Kitching: "Magnetic Resonance in an Atomic Vapor Excited by a Mechanical Resonator", Physical Review Letters **97**, 227602 (2006), ISSN 0031-9007. 2, 7

[47] P. Rabl, P. Cappellaro, M. V. G. Dutt, L. Jiang, J. R. Maze and M. D. Lukin: "Strong magnetic coupling between an electronic spin qubit and a mechanical resonator", Physical Review B **79**, 041302 (2009), ISSN 1098-0121. 2

[48] C. Montoya, J. Valencia, A. A. Geraci, M. Eardley, J. Moreland, L. Hollberg and J. Kitching: "Resonant interaction of trapped cold atoms with a magnetic cantilever tip", Physical Review A **91**, 063835 (2015), ISSN 1050-2947. 2

[49] F. Bariani, S. Singh, L. F. Buchmann, M. Vengalattore and P. Meystre: "Hybrid optomechanical cooling by atomic Λ systems", Physical Review A **90**, 033838 (2014), ISSN 1050-2947. 2

[50] F. Bariani, J. Otterbach, H. Tan and P. Meystre: "Single-atom quantum control of macroscopic mechanical oscillators", Physical Review A **89**, 011801 (2014), ISSN 1050-2947. 2

[51] K. Hammerer, K. Stannigel, C. Genes, P. Zoller, P. Treutlein, S. Camerer, D. Hunger and T. W. Hänsch: "Optical lattices with micromechanical mirrors", Physical Review A **82**, 021803 (2010), ISSN 1050-2947.

[52] B. Vogell, K. Stannigel, P. Zoller, K. Hammerer, M. T. Rakher, M. Korppi, A. Jöckel and P. Treutlein: "Cavity-enhanced long-distance coupling of an atomic ensemble to a micromechanical membrane", Physical Review A - Atomic, Molecular, and Optical Physics **87**, 23816 (2013), ISSN 10502947. 12, 48, 49, 53, 54, 85, 93

[53] J. S. Bennett, L. S. Madsen, M. Baker, H. Rubinsztein-Dunlop and W. P. Bowen: "Coherent control and feedback cooling in a remotely coupled hybrid atom–optomechanical system", New Journal of Physics **16**, 083036 (2014), ISSN 1367-2630. 2, 8, 49, 50, 51, 55

[54] Z. Yi, G. xiang Li, S. ping Wu and Y. ping Yang: "Ground-state cooling of an oscillator in a hybrid atom-optomechanical system", Optics Express **22**, 20060 (2014), ISSN 1094-4087. 2

[55] B. Vogell, T. Kampschulte, M. T. Rakher, A. Faber, P. Treutlein, K. Hammerer and P. Zoller: "Long distance coupling of a quantum mechanical oscillator to the

internal states of an atomic ensemble", New Journal of Physics **17**, 043044 (2015), ISSN 1367-2630. 2, 4

[56] J. Bennett: "Quantum optomechanics in the unresolved sideband regime", University of Queensland, PhD Thesis (2017). 2, 97, 102

[57] P. Christoph: "Feedback-assisted sympathetic cooling in a hybrid atomic-mechanical system", Universität Hamburg, PhD Thesis (2018), ISBN 978-3-8439-3596-8. 2, 3, 13, 14, 17, 18, 19, 25, 38, 40, 48, 57, 136, 138, 139, 140

[58] A. Jöckel: "Sympathetic cooling of a membrane oscillator in a hybrid mechanical-atomic system", Universität Basel, PhD Thesis (2014). 2, 7, 8, 49, 50, 51, 52, 53, 57, 86

[59] M. R. Vanner, I. Pikovski, G. D. Cole, M. S. Kim, C. Brukner, K. Hammerer, G. J. Milburn and M. Aspelmeyer: "Pulsed quantum optomechanics", Proceedings of the National Academy of Sciences of the United States of America **108**, 16182–16187 (2011), ISSN 00278424. 3, 5, 35, 101, 102, 103, 105, 117, 144, 145, 146, 147, 148, 150, 151

[60] H. Zhong, A. Schwarz and R. Wiesendanger: "Miniaturized high-precision piezo driven two axes stepper goniometer", Citation: Review of Scientific Instruments **85** (2014). 3, 19

[61] H. Zhong, G. Fläschner, A. Schwarz, R. Wiesendanger, P. Christoph, T. Wagner, A. Bick, C. Staarmann, B. Abeln, K. Sengstock and C. Becker: "A millikelvin all-fiber cavity optomechanical apparatus for merging with ultra-cold atoms in a hybrid quantum system", Review of Scientific Instruments **88**, 023115 (2017), ISSN 10897623. 3, 19, 21

[62] T. Wagner: "Realization of a Hybrid Quantum System Consisting of Ultra-cold Atoms and a Nanomechanical Oscillator", Universität Hamburg, PhD Thesis (2020), ISBN 978-3-8439-4599-8. 3, 5, 13, 15, 25, 26, 28, 37, 56, 57, 58, 66, 77, 80, 85, 136, 139

[63] J. J. Butlewski: "Pump asymmetry compensation in an atom-optomechanical hybrid system", PhD Thesis . 3, 4, 5, 9, 11, 15, 19, 21, 22, 25, 26, 28, 30, 36, 48, 49, 52, 53, 57, 58, 64, 66, 67, 69, 70, 72, 73, 74, 75, 76, 77, 78, 85, 104, 106, 108, 110, 111, 125, 126, 127, 136, 142

[64] A. Vochezer, T. Kampschulte, K. Hammerer and P. Treutlein: "Light-Mediated Collective Atomic Motion in an Optical Lattice Coupled to a Membrane", Physical Review Letters **120**, 073602 (2018), ISSN 0031-9007. 3, 54, 55, 57, 58

[65] J. K. Asbóth, H. Ritsch and P. Domokos: "Collective Excitations and Instability of an Optical Lattice due to Unbalanced Pumping", Physical Review Letters **98**, 203008 (2007), ISSN 0031-9007. 3, 57, 58, 65

[66] J. K. Asbóth, H. Ritsch and P. Domokos: "Optomechanical coupling in a one-dimensional optical lattice", Physical Review A **77**, 063424 (2008), ISSN 1050-2947. 3, 57, 58, 59, 60, 61, 62, 63, 64, 65, 69

[67] C. F. Klein: “Herstellung und Charakterisierung von Fasercavities zum Einsatz in MiM-Systemen”, Universität Hamburg, Bachelor Thesis (2018). 4, 19, 40, 43, 44, 56, 79, 80

[68] M. Wallquist, K. Hammerer, P. Rabl, M. Lukin and P. Zoller: “Hybrid quantum devices and quantum engineering”, Physica Scripta **T137**, 014001 (2009), ISSN 0031-8949. 4

[69] R. Riedinger, A. Wallucks, I. Marinković, C. Löschnauer, M. Aspelmeyer, S. Hong and S. Gröblacher: “Remote quantum entanglement between two micromechanical oscillators”, Nature **556**, 473–477 (2018), ISSN 14764687. 4

[70] C. F. Ockeloen-Korppi, E. Damskägg, J.-M. Pirkkalainen, M. Asjad, A. A. Clerk, F. Massel, M. J. Woolley and M. A. Sillanpää: “Stabilized entanglement of massive mechanical oscillators”, Nature **556**, 478–482 (2018), ISSN 0028-0836. 4

[71] W. Wieczorek, S. G. Hofer, J. Hoelscher-Obermaier, R. Riedinger, K. Hammerer and M. Aspelmeyer: “Optimal State Estimation for Cavity Optomechanical Systems”, Physical Review Letters **114**, 223601 (2015), ISSN 0031-9007. 4, 123

[72] M. R. Vanner, J. Hofer, G. D. Cole and M. Aspelmeyer: “Cooling-by-measurement and mechanical state tomography via pulsed optomechanics”, Nature Communications **4**, 2295 (2013), ISSN 2041-1723. 5, 35, 96, 103, 105, 116

[73] J. T. Muhonen, G. R. L. Gala, R. Leijssen and E. Verhagen: “State preparation and tomography of a nanomechanical resonator with fast light pulses”, Physical Review Letters **123**, 113601 (2019), ISSN 10797114. 5, 105

[74] J. T. Muhonen, G. R. la Gala, R. Leijssen and E. Verhagen: “Supplementary: State preparation and tomography of a nanomechanical resonator with fast light pulses”, Physical Review Letters **123**, 1–8 (2019), ISSN 23318422. 5

[75] L. Pezzè, A. Smerzi, M. K. Oberthaler, R. Schmied and P. Treutlein: “Quantum metrology with nonclassical states of atomic ensembles”, Reviews of Modern Physics **90**, 035005 (2018), ISSN 0034-6861. 5

[76] P. Christoph, T. Wagner, H. Zhong, R. Wiesendanger, K. Sengstock, A. Schwarz and C. Becker: “Combined feedback and sympathetic cooling of a mechanical oscillator coupled to ultracold atoms”, New Journal of Physics **20**, 093020 (2018), ISSN 1367-2630. 5, 28, 47, 55, 57, 58, 63, 66, 71, 72, 78, 81, 90, 94

[77] A. D. O’Connell, M. Hofheinz, M. Ansmann, R. C. Bialczak, M. Lenander, E. Lucero, M. Neeley, D. Sank, H. Wang, M. Weides, J. Wenner, J. M. Martinis and A. N. Cleland: “Quantum ground state and single-phonon control of a mechanical resonator”, Nature **464**, 697–703 (2010), ISSN 00280836. 7, 96

[78] J.-M. Pirkkalainen, S. U. Cho, J. Li, G. S. Paraoanu, P. J. Hakonen and M. A. Sillanpää: “Hybrid circuit cavity quantum electrodynamics with a micromechanical resonator”, Nature **494**, 211–215 (2013), ISSN 0028-0836. 7

[79] I. Yeo, P.-L. de Assis, A. Gloppe, E. Dupont-Ferrier, P. Verlot, N. S. Malik, E. Dupuy, J. Claudon, J.-M. Gérard, A. Auffèves, G. Nogues, S. Seidelin, J.-P. Poizat, O. Arcizet and M. Richard: "Strain-mediated coupling in a quantum dot–mechanical oscillator hybrid system", Nature Nanotechnology **9**, 106–110 (2014), ISSN 1748-3387. 7

[80] M. Montinaro, G. Wüst, M. Munsch, Y. Fontana, E. Russo-Averchi, M. Heiss, A. F. i Morral, R. J. Warburton and M. Poggio: "Quantum Dot Opto-Mechanics in a Fully Self-Assembled Nanowire", Nano Letters **14**, 4454–4460 (2014), ISSN 1530-6984. 7

[81] D. Hunger, S. Camerer, T. W. Hänsch, D. König, J. P. Kotthaus, J. Reichel and P. Treutlein: "Resonant Coupling of a Bose-Einstein Condensate to a Micromechanical Oscillator", Physical Review Letters **104**, 143002 (2010), ISSN 0031-9007. 7

[82] S. Camerer, M. Korppi, A. Jöckel, D. Hunger, T. W. Hänsch and P. Treutlein: "Realization of an optomechanical interface between ultracold atoms and a membrane", Physical Review Letters **107**, 223001 (2011), ISSN 00319007. 7, 49

[83] W. Happer: "Optical Pumping", Reviews of Modern Physics **44**, 169–249 (1972), ISSN 0034-6861. 7

[84] H. F. Hess: "Evaporative cooling of magnetically trapped and compressed spin-polarized hydrogen", Physical Review B **34**, 3476–3479 (1986), ISSN 01631829. 7

[85] C. Chin, R. Grimm, P. Julienne and E. Tiesinga: "Feshbach resonances in ultracold gases", Reviews of Modern Physics **82**, 1225–1286 (2010), ISSN 00346861. 7

[86] R. Grimm, M. Weidemüller and Y. B. Ovchinnikov: "Optical Dipole Traps for Neutral Atoms", Advances in Atomic, Molecular and Optical Physics **42**, 95–170 (2000), ISSN 1049250X. 7, 17

[87] R. Norte, J. Moura and S. Gröblacher: "Mechanical Resonators for Quantum Optomechanics Experiments at Room Temperature", Physical Review Letters **116**, 147202 (2016), ISSN 0031-9007. 7, 20

[88] C. Reinhardt, T. Müller, A. Bourassa and J. C. Sankey: "Ultralow-Noise SiN Trampoline Resonators for Sensing and Optomechanics", Physical Review X **6**, 021001 (2016), ISSN 2160-3308. 20

[89] T. P. Purdy, K. E. Grutter, K. Srinivasan and J. M. Taylor: "Quantum correlations from a room-temperature optomechanical cavity", Science **356**, 1265–1268 (2017), ISSN 10959203. 7

[90] A. Bick: "Interfacing Ultracold Atoms and a Cryogenic Micromechanical Oscillator", Universität Hamburg, PhD Thesis (2015), ISBN 978-3-8439-2106-0. 8

[91] C. Staarmann: "Towards a Hybrid Quantum System", Universität Hamburg, PhD Thesis (2016), ISBN 978-3-8439-3050-5. 8, 10, 42, 45

[92] D. A. Steck: “Rubidium 87 D Line Data”, pages 1–29 (2003). 13, 16, 17

[93] H. P. Yuen and V. W. S. Chan: “Noise in homodyne and heterodyne detection”, Optics Letters **8**, 177 (1983), ISSN 0146-9592. 13, 32

[94] R. Kumar, E. Barrios, A. MacRae, E. Cairns, E. Huntington and A. Lvovsky: “Versatile wideband balanced detector for quantum optical homodyne tomography”, Optics Communications **285**, 5259–5267 (2012), ISSN 00304018. 13, 109

[95] M. Poot and H. S. van der Zant: “Mechanical systems in the quantum regime”, Physics Reports **511**, 273–335 (2012), ISSN 03701573. 14, 19, 20, 31, 136, 137, 138, 139

[96] O. Morsch and M. Oberthaler: “Dynamics of Bose-Einstein condensates in optical lattices”, Reviews of Modern Physics **78**, 179–215 (2006), ISSN 00346861. 16

[97] P. L. Kapitza and P. A. Dirac: “The reflection of electrons from standing light waves”, Mathematical Proceedings of the Cambridge Philosophical Society **29**, 297–300 (1933), ISSN 14698064. 17

[98] M. Greiner: “Ultracold quantum gases in three-dimensional optical lattice potentials”, Ludwig-Maximilians-Universität München, PhD Thesis (2003). 17

[99] H. Andersen: “Bose–Einstein condensates in optical lattices”, University of Aarhus, PhD Thesis (2008). 17, 18

[100] J. Petermann: “Simulations and Fabrication of Optical Fiber Cavities for a Quantum Hybrid Experiment”, Universität Hamburg, Master Thesis (2017). 19, 40, 42, 131

[101] A. Jöckel, A. Faber, T. Kampschulte, M. Korppi, M. T. Rakher and P. Treutlein: “Sympathetic cooling of a membrane oscillator in a hybrid mechanical–atomic system”, Nature Nanotechnology **10**, 55–59 (2015), ISSN 1748-3387. 20, 30, 47, 51, 116

[102] M. Aspelmeyer, T. J. Kippenberg and F. Marquardt: *Cavity Optomechanics*, Springer-Verlag Berlin Heidelberg (2014), ISBN 978-3-642-55311-0. 20, 22, 28, 49

[103] S. A. Saarinen, N. Kralj, E. C. Langman, Y. Tsaturyan and A. Schliesser: “Laser cooling a membrane-in-the-middle system close to the quantum ground state from room temperature”, Optica **10** (3), 364–372 (2023). 20

[104] J. C. Sankey, C. Yang, B. M. Zwickl, A. M. Jayich and J. G. Harris: “Strong and tunable nonlinear optomechanical coupling in a low-loss system”, Nature Physics **6**, 707–712 (2010), ISSN 17452481. 20, 24, 25, 29

[105] C. F. Klein: “The role of pump asymmetry compensation in quantum hybrid systems”, Universität Hamburg, Master Thesis (2020). 20, 60

[106] D. J. Griffiths: *Quantenmechanik Eine Einführung*, Pearson Deutschland (2012), ISBN 9783868941142. 22

[107] D. J. Wilson: “Cavity Optomechanics with High-Stress Silicon Nitride Films”, California Institute of Technology, PhD Thesis (2012). 23, 24, 26, 29

[108] D. J. Wilson, C. A. Regal, S. B. Papp and H. J. Kimble: “Cavity optomechanics with stoichiometric SiN films”, Physical Review Letters **103** (2009), ISSN 00319007. 24

[109] M. Aspelmeyer, T. J. Kippenberg and F. Marquardt: “Cavity optomechanics”, Reviews of Modern Physics **86**, 1391–1452 (2014). 28, 141

[110] P. Rohse, J. Butlewski, F. Klein, T. Wagner, C. Friesen, A. Schwarz, R. Wiesendanger, K. Sengstock and C. Becker: “A cavity optomechanical locking scheme based on the optical spring effect”, Review of Scientific Instruments **91** (2020), ISSN 10897623. 30, 70, 86

[111] R. Hui: *Introduction to Fiber-Optic Communications* (2020), ISBN 978-0-12-805345-4. 31, 32

[112] H. Bachor and T. C. Ralph: *A Guide to Experiments in Quantum Optics*, Wiley (2019), ISBN 9783527411931. 32, 34

[113] A. A. Clerk, M. H. Devoret, S. M. Girvin, F. Marquardt and R. J. Schoelkopf: “Introduction to quantum noise, measurement, and amplification”, Reviews of Modern Physics **82**, 1155–1208 (2010), ISSN 00346861. 35

[114] V. B. Braginsky, Y. I. Vorontsov and K. S. Thorne: “Quantum Nondemolition Measurements”, Science **209**, 547–557 (1980), ISSN 0036-8075. 35, 95

[115] M. R. Vanner: “Continuous and Pulsed Cavity Quantum Optomechanics”, Universität Wien, PhD Thesis (2013). 36

[116] O. Svelto: *Principles of Lasers*, Springer New York, NY (2009), ISBN 978-1-4419-1301-2. 40

[117] D. Ristau and T. Gross: “Ion beam sputter coatings for laser technology”, **5963**, 596313 (2005). 40

[118] D. Hunger, T. Steinmetz, Y. Colombe, C. Deutsch, T. W. Hänsch and J. Reichel: “A fiber Fabry–Perot cavity with high finesse”, New Journal of Physics **12**, 065038 (2010), ISSN 1367-2630. 40, 42

[119] A. Bick, C. Staarmann, P. Christoph, O. Hellmig, J. Heinze, K. Sengstock and C. Becker: “The role of mode match in fiber cavities”, Review of Scientific Instruments **87**, 013102 (2016), ISSN 0034-6748. 40, 41

[120] J. M. Bennett: “Recent developments in surface roughness characterization”, Measurement Science and Technology **3** (12), 1119 (1992). 43

[121] D. J. Larson, J. C. Bergquist, J. J. Bollinger, W. M. Itano and D. J. Wineland: “Sympathetic cooling of trapped ions: A laser-cooled two-species nonneutral ion plasma”, Physical Review Letters **57**, 70–73 (1986), ISSN 0031-9007. 47

[122] C. J. Myatt, E. A. Burt, R. W. Ghrist, E. A. Cornell and C. E. Wieman: "Production of Two Overlapping Bose-Einstein Condensates by Sympathetic Cooling", Phys. Rev. Lett. **78**, 586–589 (1997). 47

[123] I. Bloch, M. Greiner, O. Mandel, T. W. Hänsch and T. Esslinger: "Sympathetic cooling of ^{85}Rb and ^{87}Rb", Phys. Rev. A **64**, 021402 (2001).

[124] G. Modugno, G. Ferrari, G. Roati, R. J. Brecha, A. Simoni and M. Inguscio: "Bose-Einstein Condensation of Potassium Atoms by Sympathetic Cooling", Science **294** (5545), 1320–1322 (2001).

[125] J. Schmidt, P. Weckesser, F. Thielemann, T. Schaetz and L. Karpa: "Optical Traps for Sympathetic Cooling of Ions with Ultracold Neutral Atoms", Physical Review Letters **124**, 053402 (2020), ISSN 0031-9007. 47

[126] F. Schreck, G. Ferrari, K. L. Corwin, J. Cubizolles, L. Khaykovich, M.-O. Mewes and C. Salomon: "Sympathetic cooling of bosonic and fermionic lithium gases towards quantum degeneracy", Physical Review A **64**, 011402 (2001), ISSN 1050-2947. 47

[127] P. Treutlein, C. Genes, K. Hammerer, M. Poggio and P. Rabl: *Hybrid Mechanical Systems*, pages 327–351, Springer Berlin Heidelberg, Berlin, Heidelberg (2014), ISBN 978-3-642-55312-7. 47

[128] E. R. Hudson: "Sympathetic cooling of molecular ions with ultracold atoms", EPJ Techniques and Instrumentation **3** (2016). 47

[129] X. Tong, A. H. Winney and S. Willitsch: "Sympathetic Cooling of Molecular Ions in Selected Rotational and Vibrational States Produced by Threshold Photoionization", Phys. Rev. Lett. **105**, 143001 (2010). 47

[130] N. V. Morrow, S. K. Dutta and G. Raithel: "Feedback Control of Atomic Motion in an Optical Lattice", Physical Review Letters **88**, 4 (2002), ISSN 10797114. 49

[131] A. Faber: "Sympathetic cooling and self-oscillations in a hybrid atom-membrane system", Universität Basel, PhD Thesis (2016). 57, 58, 60, 63, 64, 65, 66, 69, 78

[132] I. H. Deutsch, R. J. C. Spreeuw, S. L. Rolston and W. D. Phillips: "Photonic band gaps in optical lattices", Physical Review A **52**, 1394–1410 (1995), ISSN 1050-2947. 59, 60, 61

[133] G. Birkl, M. Gatzke, I. H. Deutsch, S. L. Rolston and W. D. Phillips: "Bragg Scattering from Atoms in Optical Lattices", Physical Review Letters **75**, 2823–2826 (1995), ISSN 0031-9007. 59

[134] M. Weidemüller, A. Görlitz, T. W. Hänsch and A. Hemmerich: "Local and global properties of light-bound atomic lattices investigated by Bragg diffraction", Physical Review A **58**, 4647–4661 (1998), ISSN 1050-2947. 59

[135] A. Xuereb, P. Domokos, J. Asbóth, P. Horak and T. Freegarde: "Scattering theory of cooling and heating in optomechanical systems", Physical Review A **79**, 053810 (2009), ISSN 1050-2947. 61

[136] J.-M. Courty, A. Heidmann and M. Pinard: "Quantum limits of cold damping with optomechanical coupling", (2001). 80

[137] C. Genes, D. Vitali, P. Tombesi, S. Gigan and M. Aspelmeyer: "Ground-state cooling of a micromechanical oscillator: Comparing cold damping and cavity-assisted cooling schemes", Physical Review A - Atomic, Molecular, and Optical Physics **77** (2008), ISSN 10502947. 80

[138] V. B. Braginsky and Y. I. Vorontsov: "Quantum-mechanical limitations in macroscopic experiments and modern experimental technique", Soviet Physics Uspekhi **17**, 644–650 (1975), ISSN 0038-5670. 95

[139] V. B. Braginsky, V. Y. I. and K. F. Y.: "Optimal quantum measurements in detectors of gravitation radiation", JETP Letters **27**, 276–280 (1978). 95

[140] K. S. Thorne, R. W. P. Drever, C. M. Caves, M. Zimmermann and V. D. Sandberg: "Quantum Nondemolition Measurements of Harmonic Oscillators", Physical Review Letters **40**, 667–671 (1978), ISSN 0031-9007. 95

[141] M. D. Levenson, R. M. Shelby, M. Reid and D. F. Walls: "Quantum Nondemolition Detection of Optical Quadrature Amplitudes", Phys. Rev. Lett. **57**, 2473–2476 (1986). 96

[142] A. La Porta, R. E. Slusher and B. Yurke: "Back-Action Evading Measurements of an Optical Field Using Parametric Down Conversion", Phys. Rev. Lett. **62**, 28–31 (1989).

[143] P. Grangier, J. A. Levenson and J.-P. Poizat: "Quantum non-demolition measurements in optics", NATURE **396** (1998). 96

[144] A. Kuzmich, L. Mandel and N. P. Bigelow: "Generation of Spin Squeezing via Continuous Quantum Nondemolition Measurement", Phys. Rev. Lett. **85**, 1594–1597 (2000). 96

[145] I. Teper, G. Vrijsen, J. Lee and M. A. Kasevich: "Backaction noise produced via cavity-aided nondemolition measurement of an atomic clock state", Phys. Rev. A **78**, 051803 (2008).

[146] T. Takano, M. Fuyama, R. Namiki and Y. Takahashi: "Spin Squeezing of a Cold Atomic Ensemble with the Nuclear Spin of One-Half", Phys. Rev. Lett. **102**, 033601 (2009).

[147] J. Appel, P. J. Windpassinger, D. Oblak, U. B. Hoff, N. Kjærgaard and E. S. Polzik: "Mesoscopic atomic entanglement for precision measurements beyond the standard quantum limit", Proceedings of the National Academy of Sciences **106** (27), 10960–10965 (2009).

[148] M. H. Schleier-Smith, I. D. Leroux and V. Vuletić: "States of an Ensemble of Two-Level Atoms with Reduced Quantum Uncertainty", Phys. Rev. Lett. **104**, 073604 (2010). 96

[149] J. Suh, A. J. Weinstein, C. U. Lei, E. E. Wollman, S. K. Steinke, P. Meystre, A. A. Clerk and K. C. Schwab: "Mechanically detecting and avoiding the quantum fluctuations of a microwave field", Science **344**, 1262–1265 (2014), ISSN 0036-8075. 96

[150] J. B. Hertzberg, T. Rocheleau, T. Ndukum, M. Savva, A. A. Clerk and K. C. Schwab: "Back-action-evading measurements of nanomechanical motion", Nature Physics **6**, 213–217 (2010), ISSN 1745-2473.

[151] G. Vasilakis, H. Shen, K. Jensen, M. Balabas, D. Salart, B. Chen and E. S. Polzik: "Generation of a squeezed state of an oscillator by stroboscopic back-action-evading measurement", Nature Physics **11**, 389–392 (2015), ISSN 1745-2473.

[152] C. Ockeloen-Korppi, E. Damskägg, J.-M. Pirkkalainen, A. Clerk, M. Woolley and M. Sillanpää: "Quantum Backaction Evading Measurement of Collective Mechanical Modes", Physical Review Letters **117**, 140401 (2016), ISSN 0031-9007.

[153] V. Sudhir, R. Schilling, S. Fedorov, H. Schütz, D. Wilson and T. Kippenberg: "Quantum Correlations of Light from a Room-Temperature Mechanical Oscillator", Physical Review X **7**, 031055 (2017), ISSN 2160-3308.

[154] N. Kampel, R. Peterson, R. Fischer, P.-L. Yu, K. Cicak, R. Simmonds, K. Lehnert and C. Regal: "Improving Broadband Displacement Detection with Quantum Correlations", Physical Review X **7**, 021008 (2017), ISSN 2160-3308.

[155] I. Shomroni, L. Qiu, D. Malz, A. Nunnenkamp and T. J. Kippenberg: "Optical backaction-evading measurement of a mechanical oscillator", Nature Communications **10**, 2086 (2019), ISSN 2041-1723. 96

[156] K. C. Lee, M. R. Sprague, B. J. Sussman, J. Nunn, N. K. Langford, X.-M. Jin, T. Champion, P. Michelberger, K. F. Reim, D. England, D. Jaksch and I. A. Walmsley: "Entangling Macroscopic Diamonds at Room Temperature", Science **334**, 1253–1256 (2011), ISSN 0036-8075. 96

[157] M. Aspelmeyer, S. Gröblacher, K. Hammerer and N. Kiesel: "Quantum optomechanics—throwing a glance [Invited]", Journal of the Optical Society of America B **27**, A189 (2010), ISSN 0740-3224. 96

[158] J. D. Teufel, T. Donner, D. Li, J. W. Harlow, M. S. Allman, K. Cicak, A. J. Sirois, J. D. Whittaker, K. W. Lehnert and R. W. Simmonds: "Sideband cooling of micromechanical motion to the quantum ground state", Nature **475**, 359–363 (2011), ISSN 00280836. 96

[159] J. Chan, T. P. Alegre, A. H. Safavi-Naeini, J. T. Hill, A. Krause, S. Gröblacher, M. Aspelmeyer and O. Painter: "Laser cooling of a nanomechanical oscillator into its quantum ground state", Nature **478**, 89–92 (2011), ISSN 00280836. 96

[160] M. D. LaHaye, O. Buu, B. Camarota and K. C. Schwab: "Approaching the Quantum Limit of a Nanomechanical Resonator", Science **304** (5667), 74–77 (2004). 96

[161] V. B. Braginsky, F. Y. Khalili and K. S. Thorne: *Quantum Measurement*, Cambridge University Press (1992). 96

[162] P. Meystre and M. O. Scully: *Quantum optics, experimental gravity, and measurement theory*, volume 94, Springer Science & Business Media (2012). 96, 97, 98, 99, 100, 102

[163] G. L. Wick: "Gravitational Waves: The Evidence Mounts", Science **167**, 1237–1239 (1970), ISSN 0036-8075. 96

[164] W. Heisenberg: *Physikalische Prinzipien der Quantentheorie*, S.Hirzel Verlag GmbH (5. Auflage 2008), ISBN 978-3-7776-1616-2. 98

[165] H. M. Wiseman and G. J. Milburn: *Quantum Measurement and Control*, Cambridge University Press (2009), ISBN 978-0-521-80442-4. 104

[166] G. R. L. Gala: "Glancing at tiny vibrations", Eindhoven University of Technology (2020), ISBN 9783540773405. 104, 105

[167] A. I. Lvovsky and M. G. Raymer: "Continuous-variable optical quantum-state tomography", Reviews of Modern Physics **81**, 299–332 (2009), ISSN 00346861. 105

[168] U. Leonhardt: *Measuring the Quantum State of Light*, Cambridge University Press (1997), ISBN 0-521-49730-2. 105

[169] M. Fox: *Quantum Optics - An Introduction*, Oxford University Press (2006), ISBN 978–0–19–856672–4. 105

[170] R. Leijssen, G. R. L. Gala, L. Freisem, J. T. Muhonen and E. Verhagen: "Nonlinear cavity optomechanics with nanomechanical thermal fluctuations", Nature Communications **8** (2017), ISSN 20411723. 118, 119

[171] K. Ma, J. Kong, Y. Wang and X.-M. Lu: "Review of the Applications of Kalman Filtering in Quantum Systems", Symmetry **14**, 2478 (2022), ISSN 2073-8994. 123

[172] W. Wieczorek, S. G. Hofer, J. Hoelscher-Obermaier, R. Riedinger, K. Hammerer and M. Aspelmeyer: "Optimal State Estimation for Cavity Optomechanical Systems - Supplementary", Physical Review Letters **114**, 223601 (2015), ISSN 0031-9007. 123

[173] L. Magrini, P. Rosenzweig, C. Bach, A. Deutschmann-Olek, S. G. Hofer, S. Hong, N. Kiesel, A. Kugi and M. Aspelmeyer: "Real-time optimal quantum control of mechanical motion at room temperature", Nature **595**, 373–377 (2021), ISSN 14764687. 123

[174] F. Tebbenjohanns, M. L. Mattana, M. Rossi, M. Frimmer and L. Novotny: "Quantum control of a nanoparticle optically levitated in cryogenic free space", Nature **595**, 378–382 (2021), ISSN 14764687. 124

[175] P. Christoph: "Fiber Cavities for Quantum Optomechanics : Concepts , Manufacturing and Characterization", (2013). 131

[176] A. C. Doherty, A. Szorkovszky, G. I. Harris and W. P. Bowen: "The quantum trajectory approach to quantum feedback control of an oscillator revisited", **370**, 5338–5353 (2012), ISSN 1364503X. 136

[177] R. Vijay, C. MacKlin, D. H. Slichter, S. J. Weber, K. W. Murch, R. Naik, A. N. Korotkov and I. Siddiqi: "Stabilizing Rabi oscillations in a superconducting qubit using quantum feedback", Nature **490**, 77–80 (2012), ISSN 00280836.

[178] M. Montinaro, A. Mehlin, H. S. Solanki, P. Peddibhotla, S. Mack, D. D. Awschalom and M. Poggio: "Feedback cooling of cantilever motion using a quantum point contact transducer", Applied Physics Letters **101** (13), 133104 (2012), ISSN 0003-6951.

[179] D. J. Wilson, V. Sudhir, N. Piro, R. Schilling, A. Ghadimi and T. J. Kippenberg: "Measurement-based control of a mechanical oscillator at its thermal decoherence rate", Nature **524**, 325–329 (2015). 137

[180] J. Guo, R. Norte and S. Gröblacher: "Feedback Cooling of a Room Temperature Mechanical Oscillator close to its Motional Ground State", Physical Review Letters **123**, 223602 (2019), ISSN 10797114. 136

Danksagung

An dieser Stelle möchte ich mich bei all jenen bedanken, die diese Arbeit möglich gemacht und mich auf meinem Weg bis zu ihrer Fertigstellung unterstützt haben.
Dieser Dank gilt unter anderem meinem Doktorvater Klaus Sengstock, der es mir ermöglicht hat, diese Arbeit unter finanziell sehr sicheren Bedingungen und stets mit hervorragendem Equipment anzufertigen. Klaus, diese Sicherheit verbunden mit dem großen Vertrauen das Du mir entgegengebracht hast, sind nicht selbstverständlich und ich werde Dir dafür immer dankbar sein. Des Weiteren möchte ich mich bei Herrn Prof. Wiesendanger für die Übernahme des Zweitgutachtens sowie für die Unterstützung und finanziellen Aufwendungen für die Reparatur und den Betrieb unseres Kryostaten bedanken. So war es trotz zunächst widriger Umstände möglich, mit dem System im kalten Zustand zu arbeiten.
Das NanoBEC-Projekt hat mich seit meiner Zeit als Bachelor Student fasziniert und es war ein Privileg mit so vielen inspirierenden Menschen an diesem Projekt zu arbeiten. Daher gilt mein Dank auch allen, mit denen ich, teilweise auch nur kurz, Zeit am Projekt verbringen durfte - Vielen Dank and Philipp Rohse, Tobias Wagner, Hai Zhong, Cody Friesen und Alexander Schwarz.
Zu ganz besonderem Dank verpflichtet bin ich Christoph Becker und Jakob Butlewski:

Lieber Christoph, in den nun schon 7 Jahren an deinem Projekt durfte ich Dich als sehr engagierten und und ambitionierten Teamleiter kennenlernen, der trotz großen physikalischen Fachwissens und einer erstaunlichen Intuition, nie den Blick für die menschliche Seite eines solchen Projektes verliert. Deine motivierende und humorvolle Art konnten mir selbst bei den frustrierendsten Laborerfahrungen ein Lächeln entlocken. Du hast mein Arbeiten und meine Entwicklung als Wissenschaftler nachhaltig geprägt. Vielen Dank! Lass uns jetzt zusammen einen Quantencomputer bauen.

Lieber Jakob, ich glaube ich hätte mir keinen besseren Laborpartner in den ersten Jahren meiner Promotion wünschen können als Dich. Deine Beständigkeit und die große Gewissenhaftigkeit mit der Du arbeitest haben mich immer beeindruckt und Du warst darin stets ein Vorbild für mich. Ich habe mir ganz sicher etwas von Deiner, für einen Wissenschaftler wichtigen, Skepsis gegenüber der eigenen Arbeit angeeignet. Auch wenn Du im letzten Jahr nicht mehr am Projekt warst, habe ich von unserer gemeinsamen Zeit im Labor und unseren Gesprächen danach sehr profitiert. Vielen Dank für die großartige Unterstützung auch gegen Ende meiner Promotion.

Ich möchte allen Mitgliedern aus meiner Arbeitsgruppe für die tolle Gruppenatmosphäre danken und insbesondere Ortwin Hellmig, für seine Unterstützung in allen faseroptischen Belangen. Ortwin Du bist klasse!
Großer Dank gilt auch meiner Familie, insbesondere meinen Eltern. Ihr habt mich in allen Belangen immer vollumfänglich unterstützt, ohne diese Unterstützung an spezifische Erwartungen zu knüpfen. Diese Freiheit zu jeder Zeit meines Lebens habe ich immer genossen und sie bereitet mir bis heute Freude. Ich bedanke mich auch bei all meinen Freunden für die stets willkommene Ablenkung vom Laboralltag und die stetige, moralische Unterstützung trotz gelegentlichen Untertauchens meinerseits. Zuletzt möchte ich mich bei meiner Freundin Sweta bedanken, die mir eine große Unterstützung war und das sehr intensive, letzte Jahr für mich unglaublich bereichert hat.

Eidesstattliche Erklärung / Declaration on oath

Hiermit versichere ich an Eides statt, die vorliegende Dissertationsschrift selbst verfasst und keine anderen als die angegebenen Hilfsmittel und Quellen benutzt zu haben. Sofern im Zuge der Erstellung der vorliegenden Dissertationsschrift generative Künstliche Intelligenz (gKI) basierte elektronische Hilfsmittel verwendet wurden, versichere ich, dass meine eigene Leistung im Vordergrund stand und dass eine vollständige Dokumentation aller verwendeten Hilfsmittel gemäß der guten, wissenschaftlichen Praxis vorliegt. Ich trage die Verantwortung für eventuell durch die gKI generierte fehlerhafte oder verzerrte Inhalte, fehlerhafte Referenzen, Verstöße gegen das Datenschutz- und Urheberrecht oder Plagiate.

Hamburg, den 8. Oktober 2024

Christian Felix Klein